



Universitat Autònoma de Barcelona

Escola d'Enginyeria

Departament d'Enginyeria Electrònica

**Classical and Quantum
Trajectory-based Approaches to
Electron Transport with full Coulomb
Correlations**

**PhD Thesis written by
Guillermo Albareda Piquer**

**Under the supervision of
Xavier Oriols Pladevall**

Bellaterra (Cerdanyola del Vallès), June 2010

G. Albareda

**Classical and Quantum Trajectory-based Approaches to Electron
Transport with full Coulomb Correlations.**



Universitat Autònoma de Barcelona

**Classical and Quantum Trajectory-based Approaches to
Electron Transport with full Coulomb Correlations**

by
Guillermo Albareda Piquer

B.S. in Physics, 2006
M.S. in Micro & Nanoelectronics, 2007

Submitted to the
Departament d'Enginyeria Electrònica
in partial fulfillment of the requirements for the degree
of
PhD in Electronic Engineering
at the
Universitat Autònoma de Barcelona
June 2010

Certified by.....

Xavier Oriols Pladevall
Catedràtic d'Escola Universitària, Departament d'Enginyeria Electrònica
Thesis Supervisor

El Dr. Xavier Oriols Pladevall, professor del departament d'Enginyeria Electrònica de la Universitat Autònoma de Barcelona:

CERTIFICA:

Que el treball titulat “**Classical and Quantum Trajectory-based Approaches to Electron Transport with full Coulomb Correlations**”, presentat per Guillermo Albareda Piquer per a optar al grau de Doctor en Enginyeria Electrònica, ha estat realitzat sota la seva direcció.

Bellaterra (Cerdanyola del Vallès), 30 de Juny de 2010

Dr. Xavier Oriols Pladevall

Classical and Quantum Trajectory-based Approaches to Electron Transport with full Coulomb Correlations

by

Guillermo Albareda Piquer

Submitted to the Departament d'Enginyeria Electrònica
on July 5, 2010, in partial fulfillment of the
requirements for the degree of
PhD in Electronic Engineering

Abstract

The exact computation of a system of interacting electrons is an extremely complicated issue because the motion of one electron depends on the positions of all the others (i.e. electrons are correlated). The accurate treatment of the electron-electron correlations in electron devices is even a more difficult issue because we deal with non-equilibrium open systems. For classical electron transport approaches, the electrostatic interaction among electrons is commonly obtained from an explicit solution of the mean-field Poisson (Coulomb) equation. However, this does not provide an exact treatment of the classical Coulomb electron-electron correlations, but only an average estimation. The explicit consideration of the wave nature of electrons implies an additional computational burden, and the difficulties in treating the Coulomb interaction among electrons increase. The mean-field approximation appears again as an improvement of electron-electron correlations. In this dissertation, a classical and quantum time-dependent many-particle approach to electron transport is developed in terms of a Hamiltonian that describes a set of particles with Coulomb interaction inside an open system without any perturbative or mean-field approximation. The boundary conditions of the Hamiltonian on the borders of the open system are discussed in detail to include the Coulomb interaction between particles inside and outside of the open system. Classically, the solution of this time-dependent many-particle Hamiltonian is obtained via a coupled system of Newton-like equations with a different electric field for each particle. The quantum mechanical solution of this many-particle Hamiltonian is achieved using a time-dependent quantum (Bohm) trajectory algorithm. The validity of the classical and quantum electron transport approaches to compute observable results is also discussed in detail. A rigorous formulation of the expectation values of a measurement in terms of classical and quantum trajectories is provided. The computation of the current density is presented as a particularly relevant example of the ability of the presented theoretical approaches to predict the functionality of nanoscale electron devices. Furthermore, a reformulation of the electric power for many-particle open systems is presented. It is shown that the power consumption differs in general from the standard textbook expressions. Finally, the computational viability of the algorithms to build a powerful nanoscale device simulator is demonstrated by simulating some interesting aspects of advanced nanoscale structures provides new valuable information on the role played by electron Coulomb correlations in the establishment of macroscopic characteristics such as the electrical current, power consumption, current and voltage fluctuations, etc.

A la memòria dels meus avis, Yuyu i Buelanna.

Acknowledgments

El meu primer agraïment va dirigit al Xavier Oriols, el meu director de tesis, no només per la seva paciència i el seu afany pedagògic, sinó també per les llargues i interessants discussions compartides al llarg d'aquests darrers quatre anys. També vull donar les gràcies al Jordi Suñé, amb qui vaig començar aquesta etapa que ja acaba.

En segon lloc, i d'una manera molt especial, vull dedicar el més sincer agraïment als meus companys de fatigues: Isaak, Fito, Gerard, Hender, Jordi, Ferran, Núria, Javi, Alfonso, Abdelilah, Esteve, Mario i tots els que em deixo, sobretot per haver convertit el lloc de treball en molt més que això.

No vull oblidar tota la gent del departament amb qui he compartit hores de cantimplora i fiambrrera al menjador del departament.

També vull fer arribar el meu reconeixement als amics i amigues que han estat al meu costat durant aquests anys. A tots ells, infinites gràcies pels mil moments inoblidables que hem passat junts.

La família és mereix un reconeixement especial. Sobretot perquè la confiança fa fàstic i han hagut d'aguantar-me durant aquest últim mes en que, com sempre desorganitzadament, he anat més atabalat del previst.

Finalment, dedico el meu més sentit agraïment a la Gemma, a qui s'han de reconèixer una paciència i amor incondicionals, pels quals li estaré agraït tota la vida. Amb ella és amb qui he compartit el dia a dia durant aquests quatre anys.

Guillem Albareda.
Barcelona, 2010.

Contents

Acknowledgments	v
Preface	xiii
1 The Electron Transport Problem at the Nanoscale	1
1.1 Introduction	1
1.2 The electron transport problem at the nanoscale	3
1.3 Different approaches to treat electron-electron Coulomb correlations	10
2 Electron Transport Beyond the Mean-field Approximation	21
2.1 Introduction	21
2.2 The many-electron open system Hamiltonian	25
2.3 Boundary conditions for the many-particle open system Hamiltonian	35
2.4 Numerical solution of the many-particle open system Hamiltonian	45
2.5 A simple example: Simulation of a two-electron system	49
3 The prediction of measurable results	57
3.1 Observable results from stochastic simulations	57
3.2 Expectation values from stochastic simulations	59
3.3 Computation of the electrical current	65
3.4 Computation of the electrical power	72
4 Application to the simulation of electron devices	81
4.1 Simulation models for state-of-the-art nanoelectronic devices	81
4.2 Many-particle transport in the channel of quantum wire DG-FETs with charged atomistic impurities	84
4.3 Electric power in nanoscale electron devices with full coulomb interaction	85
4.4 Intrinsic noise in aggressively scaled DG-FETs	86
4.5 Semi-classical simulation of a N^+NN^+ structure with time-dependent boundary conditions including lead-sample Coulomb correlations	87

4.6	Quantum simulation of a RTD structure with time-dependent boundary conditions including lead-sample Coulomb correlations	88
4.7	Many-particle semi-classical computation of the I-V characteristics of a DG-FET	89
4.8	Many-particle quantum computation of the I-V characteristics of a RTD	90
5	Conclusions	91
	Bibliography	95
A	A Primer on Bohmian Mechanics	107
A.1	Introduction	107
A.2	The basic postulates	111
A.3	Bohmian Mechanics for 1D many-particle non-relativistic systems	116
B	Electron injection model for non zero-external impedance systems	123
C	Classical and quantum expectation values for mixed open systems	129
D	Publications, Conferences and Book chapters	135

List of Figures

1.2.1 Schematic view of a whole closed circuit.	5
1.2.2 Schematic view of our open system. A common strategy to study electron transport is to reduce the involved degrees of freedom. Instead of trying to describe a whole <i>closed</i> circuit, classical and quantum transport approaches reduce the number of variables to be explicitly described to deal with simplified <i>open</i> systems.	7
1.3.1 Once the transport has been transformed into an ideally stationary one, the dynamical coupling with the reservoirs can be replaced with scattering boundary conditions at infinity.	14
2.2.1 Schematic description of the different parts of the electron device. In section 2.3, an analytical parametric 1D solution is deduced for the (blue) dashed region, while a numerical 3D solution is obtained in the (yellow) solid central region defined as the simulation box. A small part of the highly doped leads is included into the simulation box in order to account for complex phenomena appearing at the interface. The definition of the variables in the figure are introduced in section 2.3 when discussing the boundary condition algorithm. Subsets refer to schematic representation of the (a) scalar potential, (b) electric field, (c) total charge density and (d) doping density.	32
2.2.2 Schematic representation of the open volume $\Omega = Lx \cdot Ly \cdot Lz$ and its limiting surface $S = \{S^1, S^2, \dots, S^6\}$. There are $N(t)$ particles inside and $M - N(t)$ outside this volume. The vector \vec{r}^l points to an arbitrary position at the boundary surface S^l	33
2.3.1 Schematic representation of the volume $\Omega = Lx \cdot Ly \cdot Lz$. Only S^1 and S^4 , corresponding to the drain and source surfaces respectively, are opened to electron flow. On the rest of surfaces standard Neumann boundary conditions are assumed.	36

2.3.2	The electrostatic potential $V_D(t)$ (due to internal and external electrons) measured on the surface S^1 at position \vec{r}_D and time t by an additional probe charge q_{M+1} situated on the boundary $\vec{r}_D \equiv \vec{r}_{M+1} \in S^1$	44
2.5.1	Potential energy profile $\bar{W}_{mean}(\vec{r}, t)$ computed with a 3D Poisson solver using the classical “mean-field” approximation on the plane X-Y of the active region $\Omega = (20\text{ nm})^3$ at $z=6\text{nm}$ at 0.4 fs. The solid points are electron positions.	52
2.5.2	Potential energy profile of the 1-electron, $\bar{W}_1(\vec{r}_1, t)$, with the “many-electron” algorithm in the plane X-Y of the active region $\Omega = (20\text{ nm})^3$ at $z=6\text{nm}$ at 0.4 fs. The solid point is the 1-electron position.	53
2.5.3	Potential energy profile of the 2-electron, $\bar{W}_2(\vec{r}_2, t)$, with the “many-electron” algorithm in the plane X-Y of the active region $\Omega = (20\text{ nm})^3$ at $z=6\text{nm}$ at 0.4 fs. The solid point is the 1-electron position.	53
2.5.4	Electron trajectory computed with the “mean-field” (circles) and the “many-electron” (squares) algorithms for four different mesh resolutions. a) $DX = DY = DZ = 2\text{ nm}$, b) $DX = DY = DZ = 4\text{ nm}$, c) $DX = DY = DZ = 6\text{ nm}$, and d) $DX = DY = DZ = 8\text{ nm}$	54
2.5.5	Schematic representation of the errors associated to mean-field and many-electron approaches as a function of the size of the discretization mesh.	54
3.1.1	Schematic representation of the whole closed circuit available information. The statistical description of the simulation box environment is coupled to the deterministic description of the active region by an stochastic injection process.	58
3.2.1	Schematic representation of the simulation box for a particular selection of classical trajectories during an infinite time.	61
3.2.2	Schematic representation of the simulation box for a particular selection of wave-packets and Bohmian trajectories during an infinite time.	64
3.3.1	Schematic representation of the current measurement in an electron device. Device simulators compute the current in the surface, S_D , of the device active region, while the ammeter measures the current in the surface, S_A	65
3.4.1	Schematic representation of the open volume $\Omega = Lx \cdot Ly \cdot Lz$ subject to an applied bias. Only two boundary surfaces, S^1 and S^4 , corresponding to the drain and source respectively, are opened to electron flow. For single-particle classical systems the energy of every single electron is conserved and the energy gained or loosed when traversing the open region equals $\pm e \cdot V_{applied}$	79

4.2.1	Spatial distribution of the transit times along the y direction (centred in z) when a negatively charged impurity is placed at different places of the channel.	84
4.3.1	Time evolution of the power consumption in the 1D DG-FET, (a), 2D DG-FET, (b), and 3D DG-FET, (c), for the two computational methods at $V_{\text{drain}}=1\text{V}$ and $V_{\text{gate}}=0.05\text{V}$ in (a) and (b), and $V_{\text{gate}}=0\text{V}$ in (c). Dashed line refers to the many-electrons method and solid line refers to the mean-field method.	85
4.4.1	Semi-classical results for the probability density for finding different drain voltages at 50 and 500 GHz for a 1D double-gate FET.	86
4.5.1	Pseudo-resistance of the contact plus lead computed through our boundary conditions model for the large simulation box (dashed lines) and the small simulation box (solid lines).	87
4.6.1	RTD current-voltage characteristic. Results taking into account the Coulomb correlations between the leads and the active region are presented in solid circles. Open circles refer to the same results neglecting the lead-active region interaction.	88
4.7.1	Average current for a 1D DG-FET, using the many-electron and the mean-field algorithms. The open ellipses include results with the same gate voltages indicated on the left.	89
4.8.1	Average current through surfaces S^1 and S^4 for an RTD as a function of bias, using the many-particle (solid symbols) and mean-field (open symbols) algorithms (lines are a visual help). Non-uniform voltages steps are used to focus on the resonant region. Insets show schematically the effect of an electron crossing an “empty” well on its own electrostatic potential using the mean-field a) or the many-particle b) approaches.	90
A.1.1	An ensemble of trajectories for the two-split experiment. Notice that while each trajectory passes through but one of the slits, the wave passes through both, and the interference profile that therefore develops in the wave generates a similar pattern in the trajectories guided by this wave.	108
B.0.1	Schematic description of a circuit with non-zero external impedance . . .	123

Preface

Recent advances in technology have made it possible to fabricate structures at the nanoscale ($1nm = 10^{-9}m$), this meaning that, at least, one of its dimensions is anywhere in between a few tens of nanometers and the size of an atom. Such structures have already a large range of applications in very disparate fields of science and technology (physics, chemistry, medicine, biology, electronics, ...), and day by day new proposals are being suggested. Nanostructures appear today as suitable platforms where merging *theoretical* and *applied* physics. Nanoelectronics constitutes a clear example of such a necessary mixture. In order to maintain the rapid evolution of the electronic industry, a very close and reciprocal relation between the theoretical description of *electron transport* and its practical application to study and design electron devices becomes mandatory. This dissertation, in particular, constitutes an example of such a mixture. As I will show, based on a fundamental study of electron transport at the nanoscale beyond the mean-field approximation, the ultimate pursuit of this work is the development of a powerful and versatile nanoelectronic device simulation tool to provide more accurate predictions of experimental results.

Due to the huge complexity involved on the electron transport problem at the nanoscale, the assumption of some kind of approximation is a mandatory prerequisite in order to study it. Similarly to other areas of research, although the underlying theory describing a particular problem is well stated, its complexity give rise to a wide range of different approaches dealing with a single problem. In particular, the exact computation of a system of Coulomb interacting electrons constitutes an extremely complicated problem because the motion of one electron depends on the positions of all others (i.e. electrons are correlated). Thus, the prediction of the collective behavior of many electrons is a very active field of research in nano-electronics, and several theoretical approximations have been proposed to improve the treatment of electron-electron Coulomb correlations. Such a complexity belongs to the core of the so called many-body problem.

For classical approaches to electron transport, the electrostatic interaction among electrons is commonly simplified by invoking the so called *mean field approximations*, which assume that Coulomb correlations does not play a crucial role in the description of electron dynamics. Under such an assumption the solution of the electrostatic problem is obtained from a single Poisson equation. Unfortunately, this approach does not provide an accurate treatment of the classical Coulomb correlations, but only an average estimation [1, 2]. It is well known that the solution of a classical many-particle system can always be written as a coupled system of single-particle Newton-like equations. However, a unique electrostatic potential (classical mean field approximation) is explicitly assumed in semi-classical transport simulators in order to deal with a unique average electrostatic potential for all electrons [1]. A successful application of the classical mean field approx-

imation appears, for example, in the semi-classical Boltzmann equation that describes the time-evolution of the electron distribution function in a one-electron phase-space [1]. The use of a unique electric field (i.e. a unique average electrostatic potential) in the Boltzmann equation neglects the correct electron-electron correlations, in particular because each electron “feels” its own charge [1, 3–6].

For quantum approaches, the difficulties are even greater due to the computational burden associated to deal with the wave nature of electrons. In fact, the Coulomb interaction among electrons is directly not considered in many quantum transport formalisms under the assumption that the system behaves as a Fermi-liquid [7]. The well-known Landauer-Buttiker approach is a very successful example of the applicability of this assumption [8, 9]. Nevertheless, the Fermi liquid paradigm has difficulties to deal with high-frequency, low-dimensionality or Coulomb blockade regimes [7–16]. On the other hand, the non-equilibrium Green’s functions formalism (also referred to as the Keldysh formalism) provides an interesting path to solve the Schrödinger equation with the Coulomb interaction introduced perturbatively [17]. Alternatively, under the assumption that the system behaves like a capacitor, one can use a simple linear relationship between the number of electrons and the electrostatic potential in a particular region to introduce partially Coulomb effects [7–10, 12, 13, 16]. The mean-field approximation appears again as a solution for electron transport. For example, an average single-particle time-independent potential profile can be computed, self-consistently, from the wave-function solutions of a set of single-particle time-independent Schrödinger equation [10, 11, 15, 18–24]. This represents a zero-order approximation (some times called the Hartree approximation [18]) to the complex problem of electron-electron correlations. Additionally, remarkable efforts have been done by Büttiker and co-workers to include Coulomb interaction in their scattering matrix approach by applying different many-body approximations to provide self-consistent electron transport theories with overall charge neutrality and total current conservation [25–27]. Finally, extensions of the equilibrium Density Functional Theory to deal with electron transport, by means of a time-independent formalism [28], or with a powerful time-dependent version can also be found in the literature [29–31]. The exact exchange-correlation functionals needed in both formalisms are unknown and they have to be approximated. Therefore, in all the descriptions of non-equilibrium quantum systems mentioned here, the electron-electron correlations are approximated to some extent.

In addition to the previous difficulties, due to the computational burden associated to the microscopic description of electron transport either in classical or quantum systems, it is mandatory to spatially reduce the simulated regions, i.e. we cannot deal with the whole circuit, but only with a part of it. In this regard, the simulation of the lead-sample-lead region is not always possible in modern nanoscale simulators. However, in

order to correctly model the DC and/or AC conductance of nanoscale systems, one has to assure the accomplishment of the “overall charge neutrality” and “current conservation” [11, 13]. The implementation of such requirements into modern nanoscale electron simulators demands some kind of reasonable description of the Coulomb interaction among the electrons inside and outside the simulation boxes. The boundary conditions on the borders of simulation boxes in electron transport approaches constitute, then, also a complicate and active field of research.

Educated guesses for the boundary conditions are present in the literature when describing nanoscale electron devices with simulation boxes large enough to include the leads. However, such boundary conditions are not applicable for small simulation boxes that exclude the leads. Elaborated semi-classical electron transport simulators solving the time-dependent Boltzmann equation within the Monte Carlo technique commonly fix the potential at the borders of the simulation box equal to the external bias (i.e. Dirichlet boundary conditions) and assume ad-hoc modifications of the injection rate to achieve “local” charge neutrality [32–40]. Some works do also include analytically the series resistances of a large reservoir which can be considered and improvement over the previous boundary conditions [41]. Others Monte Carlo simulators do also consider Neumann boundary conditions (i.e. a fixed zero electric-field) [42]. Such boundary conditions fix also the scalar potential (up to an arbitrary constant) so that the injected charge can also be indirectly fixed when a known electrochemical potential is assumed. Such boundary conditions are successful for large simulation boxes, but they are quite inaccurate for small simulation boxes that exclude the leads [42]. In principle, there are no much computational difficulties in applying semi-classical Monte Carlo technique in large simulation boxes when dealing with mean-field approaches. However, the possibility of using smaller boxes will be very welcomed for some intensive time-consuming simulations beyond the mean-field (also for statistical ensemble simulations [43], to compute current or voltage fluctuations that need very large simulation times to obtain reasonable estimators [37–39], etc.).

Electron transport simulators accounting for the wave nature of electrons leads to an additional increase of the computational complexity. The use of the external bias as the Dirichlet boundary conditions was quite usual in the simulation of ballistic electron devices such as the resonant tunneling diode, although it neglects the lead resistances [44, 45]. The boundary conditions were directly specified from the energetic difference between the fixed scalar potential and the fixed electrochemical potential. Recently, more elaborated quantum-mechanical simulators are being used based on the self-consistent solution of the non-equilibrium Green’s functions and Poisson equation [46–51]. They use either Dirichlet-type boundary conditions [46, 48] or Neumann’s ones [47, 49–51]. All these boundary algorithms are very successful because they are implemented into

simulation boxes large enough to explicitly include the leads. However, such algorithms are basically developed for static scenarios within a mean-field treatment of the Coulomb interaction. Its extension to time-dependent scenarios or the inclusion of correlations beyond the mean-field approximation has many computational difficulties that will certainly benefit from the possibility of smaller simulation boxes. Büttiker and co-workers were the first to study quantum AC conductances with both “overall charge neutrality” and “current conservation” requirements. They applied different many-body approximations to provide self-consistent theories for the AC conductance of mesoscopic systems. However, the practical implementation of Büttiker theory for AC conductance in real resonant tunneling diodes (with 2D or 3D treatments) has many computational difficulties because of the use of large simulation boxes including the leads [25–27, 52–57]. There are even more computational difficulties in using large simulation boxes to include the leads in the so-called “first-principle” electron transport simulators, because of its huge demand of computational resources for their atomistic description [28, 30, 58–64].

In this dissertation, I am interested in revisiting the computation of an ensemble of Coulomb interacting particles in an open system without any of the approximations mentioned in the previous paragraphs. In the first section of **chapter 1**, I briefly describe the evolution of electronics from its birth, 100 years ago, till present days, where theoretical predictions have become, somehow, a valuable guiding tool preparing the ground for new generations of electronic devices. In the second section, I will extendedly discuss the main problems that a theoretical approach must face up when dealing with electron transport at the nanoscale. In one hand, I will emphasize the necessity of dealing with statistical mechanics due to the unmanageable complexity of the problem. On the other hand, I will discuss the essentially correlated (and far from equilibrium) nature of the transport problem. Finally, in section 1.3, I will introduce some of the most relevant contemporary approaches to electron transport, emphasizing their abilities and limitations to deal with Coulomb correlations.

Chapter 2 constitutes the fundamental contribution of the present work to build a many-particle classical and quantum approach to electron transport [65, 66]. After a brief resume of the common strategies followed by several approaches to deal with electron-electron correlations at the nanoscale and their differences with the one that I will follow here, in section 2.2, I develop an exact many-particle Hamiltonian for Coulomb interacting electrons in open systems in terms of the solutions of multiple Poisson equations [66]. This constitutes the keystone of our approaches to electron transport. To our knowledge, the type of development of the many-particle Hamiltonian proposed here has not been previously considered in the literature because, up to now, it was impossible to handle the computational burden associated with a direct solution of a many-particle Hamiltonian.

In section 2.3, I present an original (time-dependent) boundary condition algorithm for open systems capable of accurately capturing the Coulomb correlations among the electrons inside and outside the simulation box [65]. Such boundary conditions constitute a notable improvement of standard boundary conditions used in both classical and quantum approaches. Requiring a minimum computational effort, our boundary conditions can be implemented into time-dependent simulators with large or small simulation boxes, for DC, AC conditions and even for the study of current (or voltage) fluctuations. In section 2.4, I present classical and quantum solutions of the many-particle open system Hamiltonian introduced in section 2.2 supplied with the many-particle boundary conditions discussed in section 2.3 [66]. Classically, the solution of this time-dependent many-particle Hamiltonian is obtained via a coupled system of Newton-like equations with a different electric field for each particle. This solution constitutes a generalization of the semi-classical single-particle Boltzmann distribution for many-particle systems [65, 66]. The quantum mechanical solution of the Hamiltonian is achieved using a time-dependent quantum (Bohm) trajectory algorithm [65–67]. In this quantum (Bohm) trajectory algorithm, the use of single-particle Schrödinger equations is exact to treat many-particle systems. However, similarly to Density functional theories, the formidable simplification allowing an exact treatment of the many-particle Coulomb interaction comes at price that some terms appearing in the single-particle Schrödinger equation are in general unknown.

In the firsts sections of **chapter 3**, I will focus on discussing the kind of information we can extract from our classical and quantum approaches to electron transport. Due to the stochastic nature of our simulations, it is not evident to what extent we are able to predict measurable results. Furthermore, when dealing with quantum systems, since it is still unclear how a real measurement must be theoretically reproduced in orthodox quantum mechanics, I introduce the description of the measurement process in terms of Bohmian mechanics. Such a formulation allows the extension of the classical expectation value of an observable to the quantum one in a very natural way. In section 3.3, I will demonstrate the validity of our classical and quantum approaches to compute the expectation values of the average electrical current and current noise. Finally, in section 3.4 I will reformulate the expression for the electric power consumption in many-particle open systems emphasizing their divergences from the standard definition of power as $I \cdot V$. I will recover the standard expression of the electrical power for a very particular limit, i.e. the classical single-particle one.

Finally, in **chapter 4**, our many-particle approaches to electron transport are applied to predict the behavior of certain relevant aspects of a double-gate quantum-wire transistor, a nanoresistor, and a resonant tunneling diode. The importance of accurately accounting for strongly-correlate phenomena is demonstrated when predicting several macroscopic and microscopic characteristics such as the mean current, electric power

consumption, electron transit times, current and voltage fluctuations, etc. [65, 66, 68–70].

CHAPTER 1

The Electron Transport Problem at the Nanoscale

1.1 Introduction

The rapid evolution of electronics, from its birth at the very beginning of the past century until present days, has changed our live style so much that our present society strongly dependent on electron devices. In the beginning of the present section I want to briefly describe the crucial events that has make it possible such an evolution. After that, I will comment on the role that theoretical approaches to model electron transport play in making the electronic industry to continuously growing.

1.1.1 Historical development of electronics

During the first days of the 20th, the invention of the *diode vacuum valve tube* by John Ambrose Fleming constituted the first palpable exemplification of the ability to control electron flow through different media¹. The diode valve tube constituted the ancestor of all electronic tubes, and its evolution gave birth not only to radio communications (its first application) but to the entire *electronics* industry.

In 1947, 50 years after Fleming's discovery, William Shockley, John Bardeen and Walter Brattain fabricated the first solid-state transistor, which made them deserving the Nobel price nine years later. The solid-state transistor constituted the fundamental element of the whole electronic technology in the second half of the 20th century, and gave rise to *consumer electronics*. The dimensions of the transistor were rapidly shrunk down, and in 1958 Jack S. Kilby, at Texas Instruments, fitted a whole circuit in a single silicon

¹We assume a difference between electricity and electronics: while electric circuits are connections of conductive wires and other devices whereby the uniform flow of electrons occurs, electronic circuits add a new dimension to electric circuits in that some means of control is exerted over the flow of electrons by another electrical signal, either a voltage or a current.

substrate. This was not only the birth of the integrated circuits (i.e. the microchip), but also the birth of *microelectronics*. Jack S. Kilby received the Nobel Prize in Physics in 2000 for his contribution on the invention of the integrated circuit.

Since the commercialization of the first integrated circuit in 1961, the number of integrated components on a chip was doubled every year, and based on such an empirical evidence, Gordon Moore stated that the number of components per integrated circuit would double in performance every two years² [71].

Today, the electronics industry has already entered the *nanoscale*. Intel's latest silicon process, 32nm technology, is now in full volume production, and the world's first 2-billion³ transistor microprocessor has been realized. The minimum feature size of integrated circuits has been continuously reduced in the past decades and, as predicted by the ITRS⁴ and supported by the demonstration of a MOSFET⁵ with a gate length as short as 6 nm, this trend is expected to continue in the next decade [73]. Technological progress continues to deliver the promise of Moore's Law while transforming the way we live, work, and communicate. It is not strange, hence, that one of the commonly used adjectives to refer to present society is "the information society" of the "third industrial revolution". A society that rises and expands with everyday new advances on electronic technology, but whose present way of live would just vanish on its absence.

1.1.2 The simulation of electronic devices

The success of micro and nanoelectronics technology has been supported by sophisticated physical theories on electron transport, usually implemented on computer-aided simulation tools. Specially, during the last decades, due to the increase of the complexity and cost of the technological processes necessary to fabricate electron device prototypes, precise predictions of their functionality allowing to rule out certain designs, are constituting at this moment a research and development cost reduction amount to 35 %, which is expected to increase up to 40% in the next future [74]. But more importantly, beyond the *supporting role* in the progress of electronics, theoretical approaches to electron transport constitute today a *necessary tool to guide* the continuous breakthroughs of the electronic industry.

Although analytical approaches to electron transport has been developed since the invention of the first vacuum valve [75–78] (see Ref. [79] for an extensive discussion of the first stage investigations on this area), the improvement of electronics itself has make it

²In fact, it was not Gordon Moore but David House, an Intel colleague of Gordon, who concluded a few years later that integrated circuits would double in performance every 18 months, which represents de Moore's law written exactly as we now it today.

³American billion = 2 thousand million.

⁴Acronym for International Technology Roadmap for Semiconductors [72].

⁵Acronym for Metal-oxide-semiconductor field-effect transistor.

possible to intensify the research on electron transport through computational numerical simulators. With the aid of large and fast computers, it became possible to obtain exact numerical solutions of microscopic physical models of considerable complexity⁶. The first fully numerical transport description was already suggested in 1964 by Gummel [80] for the one-dimensional bipolar transistor. The approach was further developed and applied to pn junctions [81] and to avalanche transit-time diodes by Scharfetter and Gummel [82]. The first application of a solution of the two-dimensional Poisson equation to metal–oxide–semiconductor (MOS) structures was performed by Loeb [83], and Schroeder and Muller [84]. The first application of the Monte Carlo method to the solution of the Boltzmann transport equation was proposed by T. Kurosawa in 1966 [85], and the first simultaneous solutions of the coupled continuity and Poisson equations applied to junction field effect transistors [86] and to bipolar transistors [87] date back to 1969. Since these pioneering works on device modeling many different approaches have been applied to practically all important devices, and the number of papers in the field has grown exponentially [74, 88, 89].

Electron transport theory and its application to electron device modeling has matured into a well-established field with active research, intensive software development, and vast commercial applications. Many textbooks, monographs, and reviews devoted to theoretical and computational aspects of electron transport and device modeling have been published. However, since the costs of development and maintenance of today’s theoretical simulation tools software have significantly increased, only few large semiconductor companies can support their own development team. Nonetheless, there is a fairly large number of commercial software products available on the market which serve most of the industrial demands. Numerous electron transport approaches developed at universities have the advantage that they are freely distributed. Semiconductor manufacturing companies which need more refined simulations of complex phenomena often consult researchers from universities.

1.2 The electron transport problem at the nanoscale

In the present section I want to discuss what are the main difficulties that one must face up when dealing with the tremendous complexity of the electron transport problem. After that I will also argue about two distinctive properties of electron transport at the nanoscale, i.e. its strongly-correlated and its far from equilibrium character.

⁶Numerical simulators are usually referred as computer-aided tools.

1.2.1 On the many-body statistical problem

The main difficulties that one encounters when describe electron transport at the nanoscale arise from the necessity of making reasonable approximations to an essentially untractable problem, i.e. the many-body description of electron transport.

A many-body problem

Consider, for instance, the Hamiltonian describing a whole closed circuit, i.e. including the battery, the contacts, the leads, the active region and all the constituting elements therein (see figure 1.2.1). If we assume that it contains M_T electrons and $W - M_T$ atomic cores, the Hamiltonian of the system can be written as

$$\begin{aligned}
 H_{circuit}(\vec{r}_1, \dots, \vec{r}_G, \vec{p}_1, \dots, \vec{p}_G) = & \sum_{k=1}^{M_T} \left\{ K(\vec{p}_k) + \frac{1}{2} \sum_{\substack{j=1 \\ j \neq k}}^{M_T} eV_0(\vec{r}_k, \vec{r}_j) \right\} \\
 & + \sum_{k=M_T+1}^W \left\{ K(\vec{p}_k) + \frac{1}{2} \sum_{\substack{j=M_T+1 \\ j \neq k}}^W eZ_k Z_j V_0(\vec{r}_k, \vec{r}_j) \right\} \\
 & + \sum_{k=1}^{M_T} \sum_{j=M_T+1}^W eZ_j V_0(\vec{r}_k, \vec{r}_j) \quad (1.1)
 \end{aligned}$$

In (1.1), $K(\vec{p}_k)$ is the kinetic energy of the k -th particle with a momentum \vec{p}_k , e is the electron charge, \vec{r}_k is the vector position of the k -th particle, and Z_k is the atomic number of the k -th atom. The term $V_0(\vec{r}_k, \vec{r}_j) = \frac{e}{4\pi\epsilon_0|\vec{r}_k - \vec{r}_j|}$ is the Coulomb potential (with ϵ_0 the vacuum permittivity).

Along the whole dissertation I will assume that all involved electrons are traveling at velocities much lower than light's, c (nonrelativistic approximation). Moreover, I will consider that we can neglect the electron spin-orbit coupling and a quasi-static electromagnetic regime⁷ (see ref. [65]).

Notice that both the classical and the quantum solution of the Hamiltonian (1.1) constitute an insurmountable challenge. The reason, however, does not only reside on the huge number of variables conforming the system ($W \rightarrow \infty$), but mainly on their *correlations*. Consider, for a moment, the same system without the interaction terms in (1.1), this is making $V_0(\vec{r}_k, \vec{r}_j) \rightarrow 0$. Now the dynamics of every electron and nuclei become independent on the rest of particles, i.e. their dynamics get *uncorrelated* and their solution becomes much easier. The interaction terms in (1.1) are the responsible

⁷Such a simplification assumption, however, does not means that we are considering spinless electrons. Indeed, when computing some relevant magnitudes we will account for the electron spin just by an additional factor 2.

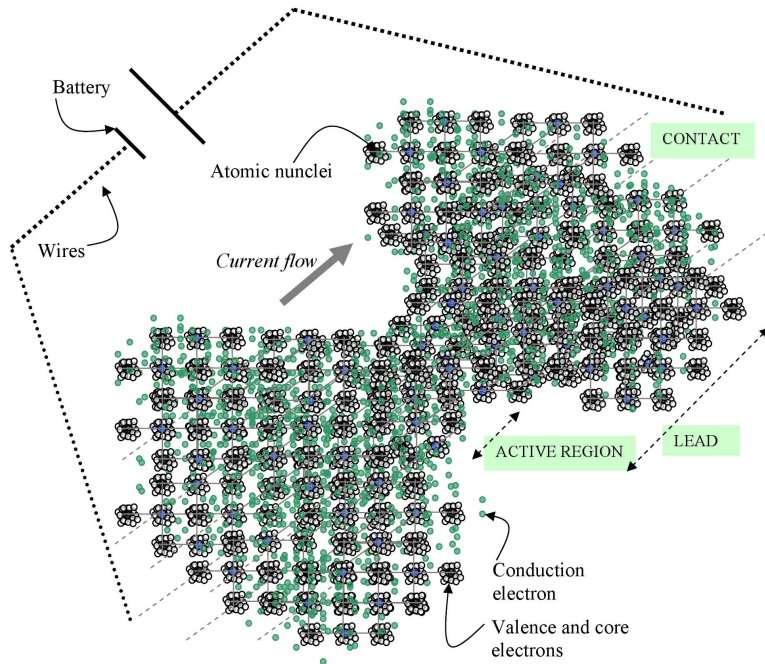


Figure 1.2.1: Schematic view of a whole closed circuit.

of coupling each particle dynamics to the rest of particle dynamics in the system, and then, are also the responsible of making their solution so difficult [90]. Such a very hard problem, known as the *many-body* problem, is the core of a long series of unsolvable problems in nature:

It would indeed be remarkable if Nature fortified herself against further advances in knowledge behind the analytical difficulties of the many-body problem. — Max Born, 1960.

The Hamiltonian (1.1) is thus not solvable, and we need to simplify it with some kind of approximation. A common strategy is to reduce the involved degrees of freedom as much as possible. Instead of trying to describe a whole *closed* circuit, both classical and quantum transport approaches must reduce the number of variables to be explicitly described to deal with *open* systems.

Internal and external opening of the system

A first step can be done by restricting our study to a spatially reduced region. Rather than taking into account the whole circuit, we focus on that particular region that we want to describe in detail. If we choose, for example, the *active region* of an electron device, then, we *externally* open it by “decoupling” its degrees of freedom from those remaining in the external environment, i.e. the rest of the circuit (see figure 1.2.2). After such a first spatial reduction of variables, the complexity of the problem usually remains

unaffordable, and some additional effort must be done in order to get a manageable system. We can, then, *internally* open the reduced region of space by “decoupling” those degrees of freedom that we want to explicitly account for, and those we do not (see figure 1.2.2). A very common example of such an internal opening of the system is that of the Born-Oppenheimer approximation, in which the explicit description of the atomic cores dynamics can be avoided. It is assumed that the electron-ion interaction does not constitute a many body problem because the ions are essentially stationary on the time-scale of the motion of the electrons (i.e. the electronic and ionic degrees of freedom are not coupled). Another common approach is to eliminate the valence and core electrons from the solution of the transport problem (see figure 1.2.2). In this case, it is assumed that non-conductive electrons are also essentially stationary on the time-scale of the motion of the conduction ones.

Statistical nature of electron transport

The previous external and internal separation of the degrees of freedom is, however, always traumatic since it causes a degradation of the description of the system correlations. This is usually referred as a degradation of the whole system’s available information, which becomes at best, known *statistically*⁸.

Those degrees of freedom that are not explicitly accounted for in the remaining open system Hamiltonian, are usually reintroduced on the solution of the electron dynamics in a rather statistical way. Let me explain it through a few examples. Consider, first, the example depicted in figure 1.2.2. There, valence and core electrons are not considered any more as actual degrees of freedom. However, they can be reincorporated in the open system Hamiltonian through the well-known relative permittivity, this is through an essentially statistical quantity. I have in mind also the electron injection models. Although the conduction electrons outside the active region are no longer considered as actual variables, we need an educated guess about how (with which position and momentum) they enter the open system. In this regard, they are commonly assumed to follow an equilibrium Fermi-Dirac statistical distribution. Another clear example is again that one of the Born-Oppenheimer approximation. There, the suppression of the nucleus dynamics in front of the electrons ones can be later statistically reintroduced through an effective interaction between electrons and phonons, an essentially statistical entity. Finally, let me recall the so called mean-field approaches. There, the Coulomb interaction terms are first neglected and then reintroduced through an statistical or mean value effective electrostatic potential.

⁸Notice that while the reduction of degrees of freedom is a common source of information degradation in both classical and quantum systems, there exists an additional source of information uncertainty

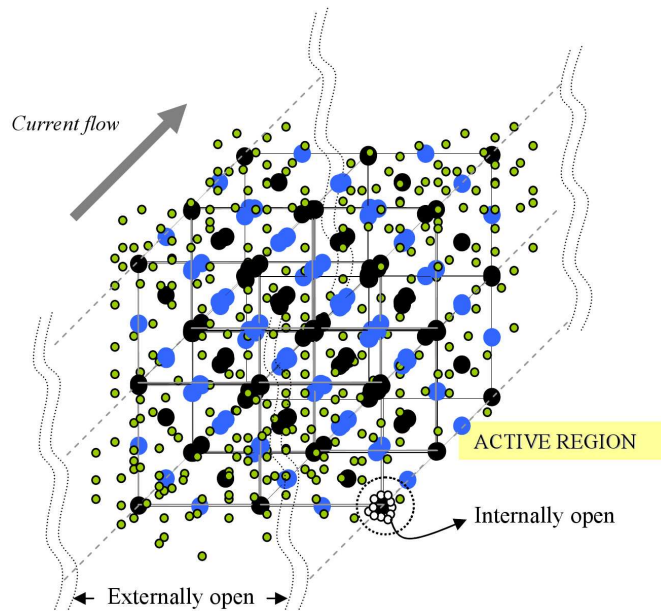


Figure 1.2.2: Schematic view of our open system. A common strategy to study electron transport is to reduce the involved degrees of freedom. Instead of trying to describe a whole *closed* circuit, classical and quantum transport approaches reduce the number of variables to be explicitly described to deal with simplified *open* systems.

Unfortunately, opening a system does entail some difficulties that must be bear in mind. From the physical point of view, a system is closed if neither energy nor particles enters or leaves it, and it is open if there is at least an export or import of energy or particles. Then, the total energy of a truly closed electron system is conserved, and its dynamics becomes deterministic⁹. In particular, the *Poincare recurrence theorem*¹⁰ holds, and the system is then wholly time-reversal¹¹. Contrarily, since open systems are exchanging energy and/or particles with its “environment”, they do not necessarily conserve its energy, and moreover, since a finite amount of degrees of freedom has been neglected, a finite amount of information is lost irreversibly in the degrees of freedom of the “environment”. For example, on the already referred case of the Born-Openheimer approximation, once we have abandoned the explicit description of the atomic cores dynamics, we can perturbatively introduce an effective potential accounting for an statistical description of the vibrations of the crystal mesh and their interaction with the

belonging exclusively to the nature of quantum mechanics, i.e. quantum mechanics assigns probabilities to events not merely because we do not know what their outcome will be, but because we cannot know what their outcome will be [91].

⁹Even the Schrödinger equation deterministically defines the time-evolution of the wavefunction

¹⁰There exists a time - called the recurrence time - after which the system will return to the neighborhood of its initial conditions. Here “neighborhood” means as close as possible to the initial conditions.

¹¹This is a result that applies to statistical mechanics, i.e. for microstates, but its extrapolation to macrostates, which will ultimately obey the second law of thermodynamics, is not obvious at all. See Refs. [92–94]

unbounded electrons. Such a perturbative technique, however, besides from being an approximate one, introduces a clear source of time irreversibility on the system dynamics due to its stochastic nature. In this regard, it seems that the elimination of degrees of freedom from an originally closed system is not innocuous at all, and even more, a simplified or statistical reintroduction of them in the description of the system dynamics has very relevant consequences.

This matter constitutes a boundary conditions problem on its broader sense, i.e. not only a spatial boundary conditions problem, but also an internal one. The external boundary conditions are imposed on the spatial borders of the open system and are the responsible of properly coupling it to the “external environment” (an example of them are the already mentioned electron injection models). The internal boundary conditions, on the other hand, are imposed through the values of certain “coupling constants” (such as the effective mass, the relative permittivity, etc...) in the equations describing electron dynamics, and are the responsible of properly coupling the open system to the “internal environment”.

1.2.2 On the non-equilibrium strongly-correlated nature

Once we accept the necessity of reducing the complexity of the electron transport problem, the question about what is the best way to do it arises.

Electron transport theory persecutes not only reproducing the exact underlying microstate of the system but specially predicting a series of macroscopic properties characterizing it. Unfortunately, constructing a standard procedure to correctly predict measurable quantities is rather a nontrivial pursuit. Probably, the most difficult part is that of recognizing those microscopical processes that strongly conditionate a subsequent macroscopical behavior. Of course all microscopical processes influence on determining how the whole system evolves from a macroscopical point of view. Every individual variable, whether it is a particular core electron, an specific nuclei or a conduction electron, has an ultimate effect on the whole system dynamics (here resides the huge complexity of the problem). However, it is also true that we can define a hierarchy in relation with the importance that such effects have on the measurable magnitudes¹². Therefore, a natural question is which are those microscopic processes that can not be underestimate in order to predict measurable quantities such as electrical current.

¹²Consider, for instance, that, under certain non-equilibrium conditions, we want to estimate the electrical current across a nanostructure, and we must neglect either the dynamics of the conduction band electrons or the dynamics of the nucleus. Since ignoring conduction electron dynamics directly sets current to zero, it is not difficult to conclude that the best choice is to omit nucleus dynamics.

A non-equilibrium problem

Once the active region of the system has been separate from its *external* environment, it can be regarded as an open system coupled to, at least, two particle and energy *reservoirs*¹³, the responsables of impinging electrical current across the channel of an electron device. Such an electron flow is a process that could never occur under *equilibrium* conditions. Since equilibrium corresponds to that state of the system where there is no net flow of particles or energy in any direction that can be identified at a macroscopic level, electrical current can be defined as a fundamentally non-equilibrium process.

A non-equilibrium state can be set near or far from equilibrium. Given an applied bias across the active region of an electron device, depending on its length, the system will attain either a near-equilibrium state or a far from equilibrium state¹⁴. In particular, electron devices at the nanoscale, are subject to large electric fields placing the nanostructures and the conducting electrons therein in *far from equilibrium* states.

The combination of such a far from equilibrium regime and the openness of the system comes out into a very complicate problem. Concepts, theorems and results that make equilibrium statistical mechanics a well-stated theoretical framework, cannot be straightforwardly carried over to the non-equilibrium case [95].

A strongly-correlated problem

There is no doubt that there exist systems in nature where correlations are not crucial in the description of their dynamics. As I have already advanced in the preface, a common way of reducing the complexity of these systems are the so called *mean-field approaches*. The main idea of mean-field theories is to replace all interactions by an average or effective interaction, thence reducing a many-body problem into an effective one-body or *single-particle* problem. The ease of solving mean-field problems means that some insight into the behavior of the system can be obtained at a relatively low cost.

Contrarily, there exist systems where mean-field approaches are not appropriate. Nanoscale electronic systems are an example of such kind of systems. Due to its aggressively scaled dimensions, nanostructures are in general characterized by simultaneously holding a small number of electrons (\sim a few tens) in a very reduced spatial region (\sim a few nanometers). The interaction among electrons becomes particularly important in this regime because the motion of one electron strongly depends on the motion of all the others and viceversa, i.e. their dynamics get *strongly correlated*.

Consider, for a moment, a very narrow (a few nanometers) junction between two electrodes. Assuming that we can roughly write the Poisson equation as $\Delta V = \frac{Q}{C}$, where

¹³i.e. an “ideal” system that can supply and receive an arbitrary amount of carriers and energy without changing its internal state.

¹⁴Such a statement can be identically argued if we assume a fixed active region length and we increase the applied bias.

V is the electrostatic potential, Q is the total charge in the junction and $C = \frac{\epsilon S}{L}$ is the capacity of the nanojunction (with ϵ the permittivity of the material, S the delimiting surface of the junction and L its length). Then, since the capacity of the junction is very small, a little variation of the charge density within the junction will produce a large amount of change in the potential energy, and consequently also a large variation of the force field distribution within the junction. In other words, a particular electron dynamics is there strongly influenced by little variations of the charge distribution around him. An extreme but really illustrative example of what such a particular regime constitutes is that of the single-electron devices¹⁵. It seems, then, that any mean-field approach to study such kind of systems will not lead to reasonable results. In particular, these particular systems can not be treated in terms of a single-particle transport problem and must account accurately for electron-electron Coulomb correlations.

Unfortunately, as I have already announced, accounting for electron-electron Coulomb correlations in a detailed way constitutes, for systems of more than three or four particles in quantum mechanics, and of more than a few tens in classical mechanics, an enormous source of complexity. In this regard, in the next section I will introduce a few examples of how different electron transport approaches tackle this problem.

1.3 Different approaches to treat electron-electron Coulomb correlations

As I have already noticed, a standard procedure to predict measurable quantities is rather a nontrivial pursuit. Indeed, higher the complexity of a problem is, larger the number of approximations that must be accounted for in order to make the system manageable, and then, larger is the number of existing approaches to address the same problem. In particular, the notable complexity of electron transport phenomena has led to a large range of disparate approaches, every one contributing in a different way to its understanding.

In this section I would like to briefly introduce some of the approaches to electron transport that can be found in the literature. The degree of complexity of these theories is broad, and it is not my intention to describe them in a detailed and rigorous way. However, on behalf of the importance of accurately treating Coulomb correlations, I will try to pay attention on stating how and to what extent these approaches account for the

¹⁵These device are based on the controllable transfer of single electrons between small conducting “islands”. Once an electron tunnels into the island, the first allowed quantum level (the only one attainable due to the small dimensions of the island) becomes occupied and moved upward. The displacement of the quantum level has a pure electrostatic origin that reads $\Delta E = \frac{e^2}{C}$, where C is the capacity of the “island” structure. Such a phenomenon is not casually called Coulomb blockade.

strongly-correlate and non-equilibrium nature of electron transport at the nanoscale.

Boltzmann formalism

To completely specify electron transport, we should know the state of each carrier within the device. In particular, if the carriers behave as classical particles, we should know each carrier position and momentum as a function of time. Alternatively, we can ask also what is the probability of finding a carrier distribution with momentums centered at $(\vec{p}_1, \dots, \vec{p}_N, t)$, locations centered at $(\vec{r}_1, \dots, \vec{r}_N, t)$, and time t . The answer is the *many-particle distribution function*:

$$f(\vec{r}_1, \dots, \vec{r}_N, \vec{p}_1, \dots, \vec{p}_N, t) d\Omega, \quad (1.2)$$

where $d\Omega$ is an infinitesimal element of the phase space spanned by the coordinates and momenta of all carriers. For most of the systems of interest, however, the many-particle distribution function, $f(\vec{r}_1, \dots, \vec{r}_N, \vec{p}_1, \dots, \vec{p}_N, t)$, is too difficult to be determined since it contains all possible *correlations* among particles, i.e. how each particle motion depends on the other particles. A simplified distribution function is the *one-particle distribution function*:

$$f(\vec{r}, \vec{p}, t) \propto \int \prod_{i=2}^N d\vec{r}_i d\vec{p}_i f(\vec{r}, \vec{p}; \vec{r}_2, \dots, \vec{r}_N, \vec{p}_2, \dots, \vec{p}_N, t). \quad (1.3)$$

Given the phase-space volume $d\vec{r}d\vec{p}$, the quantity $f(\vec{r}, \vec{p}, t) d\vec{r}d\vec{p}$ is the average number of particles that at time t is found in a phase-space volume $d\vec{r}d\vec{p}$, around the phase-space point \vec{r}, \vec{p} [88].

The Boltzmann transport equation is precisely a semiclassical equation of motion for the single-particle distribution function, also known as the Boltzmann distribution function [96]. More precisely

$$\frac{\partial f(\vec{r}, \vec{p}, t)}{\partial t} + \frac{\vec{p}}{m} \cdot \vec{\nabla}_r f(\vec{r}, \vec{p}, t) + \vec{F} \cdot \vec{\nabla}_p f(\vec{r}, \vec{p}, t) = \left(\frac{\partial f(\vec{r}, \vec{p}, t)}{\partial t} \right)_{coll}, \quad (1.4)$$

where \vec{F} is an external force and $\left(\frac{\partial f(\vec{r}, \vec{p}, t)}{\partial t} \right)_{coll}$ is the so called collision integral, which contains the description of interaction processes. In most of practical cases, the collision integral is approached through the standard perturbation theory using scattering rates calculated at a two-particle level.

The Monte Carlo technique applied to the solution of the Boltzmann equation has been one of the most successful tools chosen by the international scientific community to simulate electronic devices. It consists on simulating charge dynamics within a semiconductor crystal under the action of electric (and magnetic) fields computed self-consistently through a *mean-field* Poisson equation. Charges are represented as classical punctual

particles, and the influence of the atomic mesh over them is considered through the effective mass approximation and a set of scattering mechanisms obeying the Fermi's golden rule. The great popularity of the Monte Carlo method lies on its microscopic description of electron transport by means of intuitive trajectories obeying Newton's laws, which make it possible to obtain relevant information about the microscopical processes related with the charge transport. Furthermore, its random nature allows to study stochastic phenomena such as current noise.

Although the Boltzmann transport equation (and the Monte Carlo method) accounts for far from equilibrium conditions, its fundamental limitation comes from its single particle formulation, that is, it describes a many particle system of carriers in terms of a *single particle* distribution function. More precisely, electrostatic electron-electron interactions are described again by means of a mean-field Poisson equation. This does not provide an exact treatment of the classical electron-electron correlations but only an average estimation [1, 2]. Attempts to improve correlations among carriers are usually considered through the statistical collision integral, which, due to the tremendous analytical complexity associated with the many-body problem becomes in practice a two-body formula.

Other obvious limitations of the Boltzmann transport equation are its classical nature and the instantaneous localized in space binary collisions. On the other hand, however, its formulation takes into account in a rather easier way far from equilibrium situations and transient regimes.

Drift-diffusion and hydrodynamic approaches

Although the Boltzmann transport equation constitutes a single-particle treatment of the electron transport problem, it is still time consuming. Simpler and less demanding approaches are often required depending on the purposes of each study. The use of balance equations [97] derived from the BTE is a common procedure to obtain simplified kinetic equations. There are infinite balance equations or moments of the Boltzmann equation, however the first three are probably the most known¹⁶, i.e. the carrier density continuity equation, the momentum conservation equation and the energy density conservation equation. These equations constitute the basis of the so called hydrodynamic transport equations [99]. Assuming the relaxation time approximation for the collision terms and neglecting generation-recombination processes, the hydrodynamic carrier density continuity equation, the hydrodynamic momentum conservation equation, and the hydrodynamic energy conservation equations, respectively read as follows:

$$\frac{\partial n}{\partial t} + \vec{\nabla} \cdot (n\vec{v}) = 0, \quad (1.5)$$

¹⁶Higher order moments are discussed for example in Ref. [98]

$$\frac{\partial \vec{v}}{\partial t} + \left(\vec{v} \vec{\nabla} \right) \vec{v} + \frac{\vec{F}}{m} + \frac{1}{mn} \vec{\nabla} (n K_B T_e) = -\frac{\vec{v}}{\tau_n(\varepsilon)}, \quad (1.6)$$

$$\frac{\partial \varepsilon}{\partial t} + \vec{v} \vec{\nabla} \varepsilon + \vec{v} \vec{F} + \frac{1}{n} \vec{\nabla} (n \vec{v} K_B T_e) = -\frac{\varepsilon - \varepsilon_0}{\tau_e(\varepsilon)}, \quad (1.7)$$

where n , \vec{v} and ε are the average carrier density, velocity and energy of the electrons respectively, m is the effective mass, K_B and T_e are the Boltzmann constant and the temperature of the carriers, and τ_n and τ_e are the momentum and energy relaxation times respectively. Equations (1.5) till (1.7), together with the solution of the mean-field Poisson equation constitute the mathematical formulation of the hydrodynamic model.

Needless to say that such a simplification of the BTE, besides other additional limitations, still suffers from the same limitations as the BTE, this is from being a *single-particle* approach.

The hydrodynamic model has been used extensively to analyze and design electron devices, however, probably, more widely used is the “first order” drift-diffusion model, which, accounting only for the first two moments of the BTE, has been the basis of the classical electron device analysis during several years and still constitutes a very useful technique [43, 100, 101].

Departing again from the first three moments of the Boltzmann transport equation, but now assuming that the gradient of the carrier’s temperature is negligible, that the carriers are always in equilibrium with the crystal, that the term $\left(\vec{v} \vec{\nabla} \right) \vec{v}$ is small enough in comparison with the other terms, and finally assuming a quasi-stationary regime, the equations to be solved are reduced to the drift-diffusion carrier density continuity equation and the drift-diffusion momentum conservation equation, i.e.

$$\frac{\partial n}{\partial t} = \frac{1}{e} \vec{\nabla} \cdot \vec{J} + \left(\frac{\partial n}{\partial t} \right)_{coll}, \quad (1.8)$$

$$\vec{J} = n \mu \vec{F} + e D \vec{\nabla} n, \quad (1.9)$$

and the mean-field Poisson equation. In (1.9) D is the diffusion coefficient defined through the Einstein relation $D = \frac{K_B T \mu}{e}$, $\mu = \frac{e \tau_n}{m}$ is the electron mobility, and $\vec{J} = e \cdot \vec{v}$.

Besides from still suffering from a *single-particle* treatment of electron dynamics, the drift-diffusion equations assume thermal equilibrium between the crystal and the conducting electrons, which constitutes a strong approximation that forces the system to remain under *near-equilibrium* conditions.

Landauer approach

The Landauer approach probably constitutes the simplest quantum description of electron transport. Nonetheless, its ingenious and intuitive formulation has made it possible to understand several quantum transport phenomena. It supposes that the current

through a conductor is only expressed in terms of the transmission probability of carriers injected from the external contacts. Assuming an ideal steady state, the role of the reservoirs is simply to continually prepare electrons in the distant past (and far from the nanoscale junction) in one-dimensional scattering states entering a particular n channel with a particular wave vector k , i.e. $\varphi_n(x) = e^{ikx}$. The scattering states move towards the junction from the leads, scatter on the junction (time-independent) *mean-field* potential, and subsequently move far away from it without further scattering (see figure 1.3.1). These are known as *scattering states*. The current density of the state is computed ap-

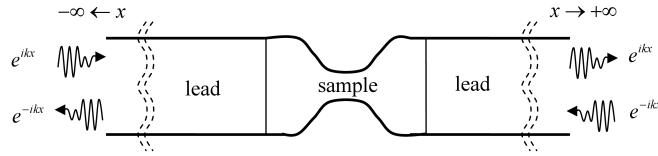


Figure 1.3.1: Once the transport has been transformed into an ideally stationary one, the dynamical coupling with the reservoirs can be replaced with scattering boundary conditions at infinity.

plying the standard current operator. On the other hand, the total steady-state current is computed as a sum over the current of each scattering state weighted by distribution functions, $T(k)$ or $R(k)$, statistically describing the transmission and the reflection probabilities respectively.

Probably, the main result of the Landauer approach is the conductance formula (i.e. the conductance quantization), which constitutes one of the most important achievements in quantum electron transport theory. In particular, the initial “four terminals” conductance proposed by Landauer [9, 102] was

$$G^{4t} = I/V^{4t} = 2 \cdot q^2/h \cdot (T/R). \quad (1.10)$$

Equation (1.10) relates the conductance to the total transmission and reflection coefficients of the electron device, and provides a conceptual framework of thinking about conductance. But another conclusion can be extracted from (1.10). Electrostatic potential is dropped locally around the scattering center (see ref. [65] for a deeper discussion on this point). In section 2.3 I will return to this point in order to discuss the boundary conditions of our approach to electron transport.

The original formulation of the Landauer approach neglects electron-electron interaction, i.e. it assumes that the systems behaves as a Fermi liquid [7]. In particular, the two-terminal version of (1.10) is

$$G^{4t} = I/V^{4t} = 2 \cdot q^2/h \cdot (T). \quad (1.11)$$

The popularity and the main virtues of the Landauer approach are due to its simplicity, the relatively low computational requirements and its rather intuitive picture of quantum electron transport. However, since continuous particles (scattering states) are assumed throughout the system, transient simulations are difficult or impossible to implement using the Landauer approach, i.e. it is a *steady-state formalism*. But moreover, Landauer approach, although accounting for far from equilibrium regimes, constitutes a *single-particle* scattering approach to steady-state transport, that is, the Landauer approach can, by definition, only capture *mean-field* properties of the electron dynamics even if it is accompanied by the use of ground-state DFT¹⁷.

Wigner function formalism

The quantum analogous of the classical many-particle distribution function (1.2), is the *generalized Wigner pseudo-distribution*, also called Wigner function. It was introduced by Eugene Wigner in 1932 to study quantum corrections to classical statistical mechanics [103]. The goal was to link the wave function that appears in the Schrödinger equation to a probability distribution in phase space.

It was firstly introduced by Wigner as:

$$f_w(\vec{r}_1, \dots, \vec{r}_N, \vec{k}_1, \dots, \vec{k}_N, t) \propto \sum_j \int_{-\infty}^{+\infty} \Psi_j(\vec{r}_1 + \vec{y}_1, \dots, \vec{r}_N + \vec{y}_N, t) \cdot \Psi_j^*(\vec{r}_1 - \vec{y}_1, \dots, \vec{r}_N - \vec{y}_N, t) \cdot \prod_{k=2}^N d\vec{y}_k e^{2i\vec{k}_i \vec{y}_i}. \quad (1.12)$$

Nonetheless, the Wigner function is today understood as the *one-reduced Wigner pseudo-distribution*. Analogously to the deduction of the *one-particle distribution function* $f(\vec{r}, \vec{p}, t)$ from the classical *many-particle distribution function* $f(\vec{r}_1, \dots, \vec{r}_N(t), \vec{p}_1, \dots, \vec{p}_N(t), t)$, from the *density matrix*

$$\rho(\vec{r}_1, \dots, \vec{r}_N, t) = \sum_j p_j |\Psi_j(\vec{r}_1, \dots, \vec{r}_N, t)\rangle \langle \Psi_j(\vec{r}_1, \dots, \vec{r}_N, t)|, \quad (1.13)$$

we can obtain a *reduced density matrix* as follows

$$\rho(\vec{r}, \vec{r}', t) \propto \sum_j \int \Psi_j(\vec{r}, \vec{r}_2, \dots, \vec{r}_N, t) \Psi_j^*(\vec{r}', \vec{r}_2, \dots, \vec{r}_N, t) \prod_{i=2}^N d\vec{r}_i. \quad (1.14)$$

¹⁷The exact exchange-correlation functionals needed in density functional formalisms are unknown and they have to be approximated. Therefore, the electron-electron correlations are approximated to some extent.

The *Wigner function*, can be then calculated from the *reduced density matrix* as

$$f_w(\vec{r}, \vec{k}, t) \propto \int_{-\infty}^{+\infty} \rho(\vec{r} + \vec{y}, \vec{r} - \vec{y}, t) d\vec{y} e^{2i\vec{k}\vec{y}}. \quad (1.15)$$

The kinetic equation for the Wigner function, reads very similar to the Boltzmann one, i.e. [74]

$$\begin{aligned} \frac{\partial f_w(\vec{r}, \vec{k}, t)}{\partial t} + \frac{\hbar \vec{k}}{m} \vec{\nabla}_r f_w(\vec{r}, \vec{k}, t) + \frac{1}{2\pi\hbar} \int d\vec{k}' V_w(\vec{r}, \vec{k} - \vec{k}') f_w(\vec{r}, \vec{k}', t) = \\ = \left(\frac{\partial f_w(\vec{r}, \vec{k}, t)}{\partial t} \right)_{coll}, \end{aligned} \quad (1.16)$$

where the Wigner potential V_w is defined as

$$V_w(\vec{r}, \vec{k}) = \frac{1}{i\hbar(2\pi)^3} \int (V(\vec{r} - \vec{y}) - V(\vec{r} + \vec{y})) \exp(-i\vec{k}\vec{y}) d\vec{y}. \quad (1.17)$$

In this regard, the Wigner formalism is based on solving the Wigner function transport equation in the same way as the Boltzmann transport equation does for classical systems.

The Wigner formalism has several virtues. It constitutes a time-dependent approach to electrical transport accounting for far from equilibrium conditions in a rather natural way. However, the limitations of the Wigner function method are very similar to those of the BTE. In the same way as the collision integral in the BTE, the Wigner's one can account, in principle, for all the many-body interactions. Unfortunately, obtaining analytical expressions for the collision integral is a very complicate job, and in practice, interactions are included just at a two-particle level. In this sense, the Wigner function constitutes in practice a *mean-field* approach to quantum electron transport.

Non-equilibrium Green's functions formalism

Non-equilibrium Green's functions (NEGF), also referred as *Keldysh formalism* [104, 105], constitutes perse a many-body technique which allows us, at least in principle, to solve the time-dependent Schrödinger equation for an interacting many-body system exactly. This is done by solving equations of motion for specific time-dependent single-particle Green's functions. However, NEGF are deduced from perturbation theory¹⁸, so they can be strictly applied only to those systems where many-body perturbation theory holds¹⁹

¹⁸NEGF formalism follows steps similar to those of the Kubo approach to determine the response of a closed system to an external time-dependent perturbation. However, the major difference with the Kubo approach is that it do not limits to weak perturbations.

¹⁹Examples of problems beyond standard many—body perturbation techniques are the Kondo effect [106] or the Luttinger liquid [107].

[88].

A rigorous introduction of the basis of NEGF requires a basic knowledge on the second quantization formalism [10, 88], so it becomes difficult to introduce them in a self-contained way without introducing some concepts that would extend unnecessarily this rather informal resume. However, another way of introducing NEGF is through the quantum kinetic equation (1.16) for the Wigner function. There, the collision term $\left(\frac{\partial f_w(\vec{r}, \vec{k}, t)}{\partial t}\right)_{coll}$ can be defined in terms of the lesser $\Sigma^<$ and greater $\Sigma^>$ self-energies as

$$\left(\frac{\partial f_w(\vec{r}, \vec{k}, t)}{\partial t}\right)_{coll} = -\frac{i}{\hbar} \left[f_w(\vec{r}, \vec{k}, t) \Sigma^> + (1 - f_w(\vec{r}, \vec{k}, t)) \Sigma^< \right]. \quad (1.18)$$

In (1.18), the self energies, which can be understood as in and out scattering rates, contain all many-body correlations. However, its exact solution is in general unknown and mean-field assumptions must be taken into account.

Despite the powerful and rigorous character of non-equilibrium Green's functions, they are in general accompanied by a rather nonintuitive and hard mathematical formulation. Even more, although electron-electron interactions beyond the mean-field approximation can be introduced throughout the self-energies, using them, except for simple model systems, it is a huge computationally demanding task, and most of the time outright impossible.

Density functional theories

The ground-state density functional theory (DFT) was originally formulated by Hohenberg and Kohn in 1964 [19]. Starting from an N -electron Hamiltonian

$$\hat{H}(\vec{r}_1, \dots, \vec{r}_N, \vec{p}_1, \dots, \vec{p}_N) = \hat{T} + \hat{W} + \hat{V}, \quad (1.19)$$

where \hat{T} is the kinetic energy operator and \hat{W} is the electron-electron interaction operator. Defining the density operator n as the reduced density operator (1.14) evaluated at $\vec{r}' = \vec{r}$:

$$n(\vec{r}) = N \int |\Psi(\vec{r}, \vec{r}_2, \dots, \vec{r}_N, t)|^2 \prod_{i=2}^N d\vec{r}_i, \quad (1.20)$$

and satisfying

$$\int n(\vec{r}) d\vec{r} = N, \quad (1.21)$$

then, the operator \hat{V} , describing a local static potential (like the electron-ion potential), can be written as

$$\hat{V} = \int d\vec{r} V(\vec{r}) n(\vec{r}). \quad (1.22)$$

If it is assumed now that for a given $V(\vec{r})$ we have found a density $n(\vec{r})$, satisfying (1.21), which corresponds to the *ground state* of the Hamiltonian (1.19), then the Hohenberg-Kohn theorem states that two external potentials, which differ by more than a constant, cannot give the same ground-state density. This establishes a one-to-one correspondence between the external potential and the ground-state density [19].

Inspired on the above theorem, Kohn and Sham deduced in 1965 their famous equations [22]:

$$\left[-\frac{\hbar^2}{2m} \vec{\nabla}^2 + V_H(\vec{r}) + V_{xc}(\vec{r}) + V(\vec{r}) \right] \phi_k^{KS}(\vec{r}) = \varepsilon_k \phi_k^{KS}(\vec{r}), \quad (1.23)$$

corresponding to the solution of the time-independent Schrödinger equation of auxiliary non-interacting electrons in the presence of the potential $V_{KS}(\vec{r}) = V_H(\vec{r}) + V_{xc}(\vec{r}) + V(\vec{r})$, where

$$V_H(\vec{r}) = e^2 \int d\vec{r}' \frac{n(\vec{r}')}{|\vec{r} - \vec{r}'|}, \quad (1.24)$$

is the Hartree potential, and $V_{xc}(\vec{r})$ is the *unknown exchange-correlation* potential including all the many-body correlation effects.

Solving the above equations yields the wavefunctions $\phi_k^{KS}(\vec{r})$, from which the ground-state density is

$$n(\vec{r}) = \sum_{k=1}^N |\phi_k^{KS}(\vec{r})|^2. \quad (1.25)$$

All properties of the ground-state system can be then extracted from (1.25). Unfortunately, since the exchange-correlation potential is unknown, some kind of educated guess must be formulated.

The main limitation of the ground-state density functional theory in order to describe electron transport, is precisely its ground-state nature. In other words, such a theory assumes that the system under study occupies a *time-independent equilibrium state*. This seems to be not a good starting point in order to describe electron transport. However, there exists some generalizations of the above theory. For instance, Runge and Gross generalized DFT to its time-dependent version in 1984 [31]. Time-dependent density functional theory (TDDFT) includes time in the previous results in a very natural way, and more importantly, it is capable of describing *non-equilibrium* scenarios.

Including a time-dependence into the Kohn-Sham potential, i.e. $V_{KS}(\vec{r}, t) = V_H(\vec{r}, t) + V_{xc}(\vec{r}, t) + V(\vec{r}, t)$, the time-dependent version of the Kohn-Sham equations becomes

$$\left[i\hbar \frac{\partial}{\partial t} + \frac{\hbar^2}{2m} \vec{\nabla}^2 - V_H(\vec{r}, t) - V_{xc}(\vec{r}, t) - V(\vec{r}, t) \right] \phi_k^{KS}(\vec{r}, t) = 0. \quad (1.26)$$

And the charge density is then

$$n(\vec{r}, t) = \sum_{k=1}^N |\phi_k^{KS}(\vec{r}, t)|. \quad (1.27)$$

TDDFT is in principle capable of accounting for both, far from equilibrium conditions and many-body phenomena. There exist, too, a series of theorems based on some reformulations of the TDDFT²⁰ guaranteeing that, if we know the exact dynamical functional $V_{xc}(\vec{r}, t)$, all many-body dynamical effects can be evaluated using effective single-particle equations. In other words, they guarantee that if we knew the exact functionals of the dynamical density-functional theories, we would obtain the exact current of the many-body system with all electron-electron interactions included [88].

Unfortunately, although such theorems constitute a formal demonstration of the validity of dynamical density-functional theories on predicting the macroscopic electrical current, the true is that we do not know the exact functionals, and some *mean-field* approximations must be used.

²⁰There exist two modifications of the TDDFT called time-dependent current density functional theory, TDCDFT [14], and stochastic time-dependent current density functional theory, STDCDFT [108].

CHAPTER 2

Electron Transport Beyond the Mean-field Approximation

2.1 Introduction

Along this chapter I will introduce the main contributions of this dissertation in the construction of a many-particle approach to classical and quantum electron transport. Before introducing the fundamental pieces of our approaches, however, I want to briefly argue why they constitute a significant change on the way of describing electron-electron Coulomb correlations.

2.1.1 Preliminary Discussion

As I have already pointed out, electron dynamics becomes strongly-correlated at the nanoscale. However, although interacting many-electron systems are well assessed through the exact expression of the system's Hamiltonian, its exact solution is a very hard problem when the number of interacting electrons increase farther than a few tens in semi-classical approaches and farther than 3 or 4 for quantum approaches. Let me put some numbers on the table in order to see that. Consider a three-dimensional system with a spatial mesh discretization containing 100 nodes on each three-dimensional spatial direction. In the quantum case, this means that a single-particle wavefunction would be defined by a matrix containing 10^6 elements. Moreover, if we have 10 electrons, then the complexity of the problem grows up exponentially, and the number of elements contained in the matrix defining the wavefunction becomes 10^{60} . Assuming now that we can store the information of each matrix element using numbers contained in 10 bits, we then need 10^{61} bits to describe the system's wavefunction. Current hard drives have storage capacities of the order of 1Tbyte= $8 \cdot 10^9$ bits, so, in order to manipulate a simple wavefunction with the above characteristics, we need at least 10^{50} computers!. Although the classical counterpart of this example is much less demanding, dealing with a few tens of electrons

start to be a very hard problem to solve. In this regard, the treatment of the many-body problem in electron devices constitutes a huge challenge, and mean-field approaches to electron transport appears as a really helpful simplification of the problem [2].

In the previous chapter (see section 1.3), for example, we have seen that in classical approaches based on the Boltzmann equation or its moments, the electrostatic interaction among electrons is obtained from the solution of a single-particle Poisson (Coulomb) equation [1, 3–6]. In order to read a deeper discussion on the use of mean-field approximation in semi-classical electron transport approaches the reader is referred to Refs. [65, 66, 68] and [1, 3–6].

Due to its additional complexity, quantum approaches can deal with even more simplified descriptions of electrostatic correlations. The Coulomb interaction among electrons is directly not considered in many quantum transport formalisms [10, 11]. As I have already pointed out in Section 1.3, the well-known Landauer approach is a very successful example of the applicability of this assumption. The Fermi-liquid paradigm has, however, important difficulties when dealing with high-frequency [11, 13] low-dimensionality [14, 15] or Coulomb blockade regimes [11, 16]. Improvements of the description of electron correlation are encountered in the Wigner and nonequilibrium Greens function formalisms introduced in the previous chapter. They provides an interesting path to solve the Schrödinger equation with the many-body Coulomb interaction introduced perturbatively [17, 103]. However, although both treatments can deal, in principle, with many-body electron dynamics, the mean-field approximation appears again as a solution for realistic electron transport situations. Finally, in extensions of the equilibrium density-functional theory to deal with electron transport by means of a time-independent formalism [28] or with a powerful time-dependent version [29–31], the exact exchange-correlation functionals needed in both formalisms are unknown and they have to be approximated to some extent.

All the above approaches to electron transport share a *common strategy* to describe electron-electron interactions. Instead of directly dealing with electron-electron Coulomb interactions, they first reduce them to a single-particle scenario for later recovering a many-body problem by means of an “effective” potential. Notice for example the case of the approaches based on the semi-classical Boltzmann distribution function. There, the *many-body phase density* (see expression (1.2)), is firstly reduced to the *one-particle reduced density* (see expression (1.3)), and then, many-body phenomena are reincorporated, in principle, through the collision integral of the kinetic transport equation. A very similar situation is that of the Wigner function, whose derivation depends on firstly reducing the *many-body density matrix* to the *reduced density matrix* (see equation (1.14)). Non-equilibrium Green’s functions are not so different. The *many-body time-dependent Schrödinger equation* is there solved in terms of *time-dependent single-particle Green’s*

functions containing the self-energies which include, in principle, all many-body correlations. Density functional theories proceeds in a very similar way. Many-body phenomena are reintroduced in this case through the *exchange-correlation* potentials.

In what follows I will follow a different strategy. Instead of trying to reduce the problem to a single-particle one, I will directly work with a many-particle description of the Coulomb electron-electron correlations. Throughout this chapter, I am interested in revisiting the computation of an ensemble of Coulomb-interacting particles in an open system without any mean-field or perturbative approximation. With this goal, I will develop a many-particle Hamiltonian for open systems in terms of the solutions of multiple Poisson equations. This Hamiltonian will be supported with a sort of boundary conditions, one for each electron inside the open system, accounting for Coulomb correlations among them and the non simulated electrons in the leads. After this, I will present a classical and also a quantum solution of the many-particle Hamiltonian, both applicable to realistic three-dimensional simulations of electron devices. I will present the classical and quantum algorithms together because they solve the same many-particle Hamiltonian and moreover both share many technical details. The use of a common classical and quantum language based on Hamiltonians, is however not casual. It is my intention to emphasize the similarities between classical and quantum mechanics. I will give some arguments about this point in the next subsection.

2.1.2 Coulomb correlations: A classical or quantum phenomena?

A common way of classifying electron transport approaches is that one in terms of their capability of accounting for quantum phenomena. Of course it is important whether a particular approach can deal or not with quantum phenomena, but depending on the particular structure we want to deal with, it can be equally important if such an approach can deal with single-particle or many-particle correlations, or furthermore, if such an approach can deal with equilibrium or non-equilibrium conditions. In order to appreciate this, let me compare classical and quantum mechanics in a rather uncommon way.

It would be indeed very illustrative if we could write quantum mechanics in terms of quantum trajectories comparable to classical ones. This is what Louis de Broglie and later David Bohm suggested some time ago (in Appendix A I present an introduction to the formulation of Bohmian mechanics) [109, 110]. For instance, the quantum Newton's like equation corresponding to the closed Hamiltonian (1.1) can be written in terms of

bohmian trajectories as:

$$m \frac{d\vec{v}_k(\vec{r}_k[t], t)}{dt} = \left[-e\vec{\nabla}_k \left\{ \sum_{\substack{j=1 \\ j \neq k}}^{M_T} V_0(\vec{r}_k, \vec{r}_j) + \sum_{j=M_T+1}^W Z_j V_0(\vec{r}_k, \vec{r}_j) + \sum_{\substack{j=1 \\ j \neq k}}^{M_T} Q_j(\vec{r}_1, \dots, \vec{r}_W, t) \right\} \right]_{\substack{\vec{r}_1 = \vec{r}_1[t] \\ \vdots \\ \vec{r}_W = \vec{r}_W[t]}}, \quad (2.1)$$

where

$$Q_j(\vec{r}_1, \dots, \vec{r}_W, t) = -\frac{\hbar^2}{2m} \frac{\vec{\nabla}_j^2 R(\vec{r}_1, \dots, \vec{r}_W, t)}{R(\vec{r}_1, \dots, \vec{r}_W, t)}, \quad (2.2)$$

is the quantum potential (see Appendix A for a detailed explanation on its origin) associated with the j -th trajectory. If we compare now the previous quantum equation with its classical counterpart, i.e.

$$m \frac{d\vec{v}_k(\vec{r}_k[t], t)}{dt} = \left[-e\vec{\nabla}_k \left\{ \sum_{\substack{j=1 \\ j \neq k}}^{M_T} V_0(\vec{r}_k, \vec{r}_j) + \sum_{j=M_T+1}^W Z_j V_0(\vec{r}_k, \vec{r}_j) \right\} \right]_{\substack{\vec{r}_1 = \vec{r}_1[t] \\ \vdots \\ \vec{r}_W = \vec{r}_W[t]}}, \quad (2.3)$$

it can be easily concluded that the ultimate origin of quantum phenomena can be represented by just an additional potential term¹, i.e. Q .

A reasonable question arises, then, if we wonder about why such an additional potential term, Q , should be more “important” than the Coulomb one, V_0 , in (2.1). Indeed, if we could exactly solve (2.1), then this question would be easily answered by simply analyzing the results. Unfortunately, as I have already argued, due to computational limitations, we cannot do that. So, we must decide which term in (2.1) deserves more attention, or, in other words, what level of accuracy we want to assign to each term in (2.1). This is not an easy decision to take, and in general one must think about it carefully. Indeed, it seems that, depending on the particular scenario we are dealing with, quantum potential correlations and Coulomb correlations does not take equal “weights”, and then, the adjectives quantum and strongly-correlate will not acquire the same importance. In fact, during this dissertation I will use both a semi-classical and a quantum approach to electron transport presented in a very similar way, and depending on the particular system under study, in chapter 4 I will use one or the other. In summary, from the above discussion I want to emphasize the idea that differences between a classical and a quantum description of electron transport can be less important, depending on the system

¹Let me clarify that the exchange interaction is always present in a system of identical particles (electrons), but it will not be mentioned in this section because it does not affect explicitly the expression of the (first-quantization) many-particle Hamiltonians discussed here. The exchange interaction is introduced into the symmetry (when electron positions are interchanged) of the many-body wavefunction. We will briefly revisit this issue in section 2.4.2, when dealing with the quantum solution of the many-particle Hamiltonian.

under study, than the differences between single-particle and many-particle approaches.

2.2 The many-electron open system Hamiltonian

I proceed here with the deduction of an expression for the many-particle open system Hamiltonian.

2.2.1 Towards a many-electron single-band effective mass equation

Some electron transport approaches, spend much effort on formulating a rigorous treatment of the effect of the electron correlations on the description of the *band structure* of the nanostructure, and much less effort on providing a reasonable description of the correlation among *transport* electrons, i.e. carriers. Here, with the aim of accurately describe the dynamical electron correlations I will took the opposite direction.

Suppose the whole closed circuit described in section 1.2.2. The Hamiltonian of such a system can be defined as

$$\begin{aligned}
 H_{circuit}(\vec{r}_1, \dots, \vec{r}_W, \vec{p}_1, \dots, \vec{p}_W) = & \sum_{i=1}^{M_T} \left\{ K(\vec{p}_i) + \frac{1}{2} \sum_{\substack{j=1 \\ j \neq i}}^{M_T} eV_0(\vec{r}_i, \vec{r}_j) \right\} \\
 & + \sum_{i=M+1}^W \left\{ K(\vec{p}_i) + \frac{1}{2} \sum_{\substack{j=M+1 \\ j \neq i}}^W eZ_i Z_j V_0(\vec{r}_i, \vec{r}_j) \right\} \\
 & + \sum_{i=1}^{M_T} \sum_{j=M_T+1}^W eZ_j V_0(\vec{r}_i, \vec{r}_j) \quad (2.4)
 \end{aligned}$$

where $K(\vec{p}_i)$ is the kinetic energy of the i -th particle with a momentum \vec{p}_i , e is the electron charge, \vec{r}_i is the vector position of the i -th particle, and Z_i is the atomic number of the i -th atom. The term

$$V_0(\vec{r}_i, \vec{r}_j) = \frac{e}{4\pi\epsilon_0 |\vec{r}_i - \vec{r}_j|} \quad (2.5)$$

is the Coulomb potential with ϵ_0 the vacuum permittivity.

The time-dependent Schrödinger equation that describes the evolution of the circuit wave function, $\Psi_{circuit}$, is

$$i\hbar \frac{\partial \Psi_{circuit}}{\partial t} = H_{circuit} \Psi_{circuit}, \quad (2.6)$$

The adiabatic and the bounded electrons approximation

Unfortunately, the solution of the Hamiltonian (2.4) is unaffordable, and we must simplify it. In order to reduce the degrees of freedom involved in (1.1), we first remove its explicit dependence on the valence and core electrons by modifying the vacuum permittivity ($\varepsilon_0 \rightarrow \varepsilon = \varepsilon_r \cdot \varepsilon_0$, where ε_r is the relative permittivity) and account for an average induced polarization between the bounded electrons and the nuclei [111]). Furthermore, we assume the *adiabatic approximation*² [10, 112–114] (also called Born-Oppenheimer approximation) under which conducting electrons are moving in a quasi-static atomic potential defined by the fixed positions of the atoms³.

The original Hamiltonian (1.1), has been reduced to the carrier's one:

$$H_{\text{carriers}}(\vec{r}_1, \dots, \vec{r}_M, \vec{p}_1, \dots, \vec{p}_M) = \sum_{i=1}^M \left\{ K(\vec{p}_i) + \frac{1}{2} \sum_{\substack{j=1 \\ j \neq i}}^M eV(\vec{r}_i, \vec{r}_j) + \sum_{j=M_T+1}^W eZ_j V(\vec{r}_i, \vec{R}_j) \right\} \quad (2.7)$$

where M is now the total number of unbounded electrons, and R_j are now the fixed positions of the atoms. The Coulomb potential,

$$V(\vec{r}_i, \vec{r}_j) = \frac{e}{4\pi\varepsilon|\vec{r}_i - \vec{r}_j|} \quad (2.8)$$

has been properly redefined accordingly to the effective value of the dielectric permittivity.

From now on, the dynamics of the nucleus and the bounded electrons are not anymore explicitly accounted for, and hence, we do not deal anymore with the circuit wavefunction, Ψ_{circuit} , but with the wavefunction of the M ($M = M_T - N_b$) unbounded electrons (i.e. carriers), Ψ_{carriers} , obeying the next Schrödinger equation

$$i\hbar \frac{\partial \Psi_{\text{carriers}}}{\partial t} = H_{\text{carriers}} \Psi_{\text{carriers}} \quad (2.9)$$

Single-band effective mass approximation for many-particle systems

Despite the previous approximations, we are still dealing with an insolvable problem. In order to continue reducing the degrees of freedom, an important decision to be made is that of the energy band model that will be used. Two choices have become popular for

²While the nuclei mass is much larger than the electron's one, the mean value of their equilibrium kinetic energy is comparable. Thus the electron's velocities are much larger than those of the nucleus and a new spatial electron distribution is established within a negligible time lapse in comparison with that of the nucleus.

³An effective potential $U_S(\vec{r}_i, t)$ describing the interaction of the unbounded electrons with the vibrations of the crystal mesh can be introduced ad-hoc by using perturbation theory

electron device modeling: the “tight-binding” model⁴ [115] and the “envelope-function” model⁵ [114]. Here the electron-atom interaction potential is assumed to be an average over a unit cell of the atomic lattice of the semiconductor, and the carrier kinetics, leaving electron-electron interactions aside, is treated almost the same as a free carrier, but with a modified mass called the effective mass, denoted m^* . The envelope-function model is thus often called the effective mass model. The tight-binding approach, as its name indicates, takes the opposite extreme of a nearly-bound carrier. The electron-atom interaction potential is periodic, with deep energy wells at the atomic cores. The tight-binding approach is theoretically more accurate, but it is significantly more computationally demanding. This presents another trade-off choice of accuracy versus computation time. Here, the tight-binding approach was rejected in favor of the envelope-function potential model.

In order to further simplify the previous Hamiltonian (2.7), we define H_0 as that part of the whole Hamiltonian containing the kinetic terms and the interaction among electrons and atoms. Hence, we can rewrite (2.7) as

$$\hat{H}_{\text{carriers}} = \hat{H}_0 + \frac{1}{2} \sum_{i=1}^M \sum_{\substack{j=1 \\ j \neq i}}^M eV(\vec{r}_i, \vec{r}_j), \quad (2.10)$$

where

$$\hat{H}_0 = \sum_{i=1}^M H_{0i} = \sum_{i=1}^M \left\{ K(\vec{p}_i) + \sum_{j=M_T+1}^G eZ_j V(\vec{r}_i, \vec{R}_j) \right\}. \quad (2.11)$$

On one hand, H_0 is separable, and hence, we can find mono-electronic eigenstates for every one of the M Hamiltonians H_{0i} . Moreover, if we assume an ideal periodic atomic structure, solutions of these mono-electronic Hamiltonians are the Bloch states.

Since the M Hamiltonians included in H_0 are all identical, we can solve them in one go by using a generic variable \vec{r} instead of \vec{r}_i . Consider the solution of the time-independent Schrödinger equation for every H_{0i} in (2.11):

$$\left[-\frac{\hbar^2}{2m_e} \vec{\nabla}_{\vec{r}} + \sum_{j=M_T+1}^G eZ_j V(\vec{r}, \vec{R}_j) \right] \phi_{n,k}(\vec{r}) = E(\vec{k}) \phi_{n,k}(\vec{r}), \quad (2.12)$$

where k refers to the wavevector of the well known Bloch wave functions, $\phi_{n,k}(\vec{r})$, defined as

$$\phi_{n,k}(\vec{r}) = u_{n,k}(\vec{r}) \exp(i\vec{k}\vec{r}), \quad (2.13)$$

where $u_{n,k}$ are periodic functions with the same period of the lattice defined by the vector

⁴Also known as the LCAO (linear combination of atomic orbitals) model.

⁵Also known as the nearly-free carrier model or the effective mass approximation.

\vec{a} ,

$$u_{n,k}(\vec{r} + \vec{a}) = u_{n,k}(\vec{r}), \quad (2.14)$$

and satisfy

$$\int_{\text{unit-cell}} u_{n,k}(\vec{r}) \cdot u_{n',k}^*(\vec{r}) d^3r = \delta_{n,n'}. \quad (2.15)$$

For each value of \vec{k} there exist an infinite number of eigenstates $\phi_{n,k}$ with $n = 1, 2, 3, \dots$. Every eigenstate $\phi_{n,k}$ is associated to a different band n , i.e. when \vec{k} varies, the eigenstates cross a series of band energies [115]. In the present discussion I will assume that electrons can be described by linear combinations of Bloch states of *one single band*, neglecting inter-band transitions.

Since the eigenvalues, $E(\vec{k})$ in (2.12) are also periodic

$$E(\vec{k}) = E(\vec{k} + \vec{K}), \quad (2.16)$$

with

$$K_j = j \frac{2\pi}{a}, \quad j = 1, 2, \dots, \quad (2.17)$$

then all the information related with the band structure can be spatially reduced to the first Brillouin zone [115]. Moreover, if we develop (2.16) in second order Taylor series around the band minimum \vec{k}_0 , then we can write

$$E(\vec{k}) = E(\vec{k}_0) + \frac{1}{2} m_{\alpha\beta}^{-1} (\vec{k}_\alpha - \vec{k}_{\alpha,0}) \cdot (\vec{k}_\beta - \vec{k}_{\beta,0}). \quad (2.18)$$

The quantities $m_{\alpha\beta}^{-1}$ have the dimensions of an inverse mass, and represent the second derivative of the energy with respect to the wave vector components α and β , i.e.

$$m_{\alpha\beta}^{-1} = \frac{1}{\hbar^2} \left. \frac{\partial^2 E(\vec{k})}{\partial k_\alpha \partial k_\beta} \right|_{\vec{k}=\vec{k}_0}. \quad (2.19)$$

As the value of a second derivative does not depend on the differentiation order near the band minimum, $m_{\alpha\beta}^{-1}$ represent a symmetric tensor. The components of this tensor depend on the coordinate system. In particular, the coordinate system can be chosen so that the non-diagonal components vanish (we call this components x , y and z for simplicity), that is, $m_{\alpha\beta}^{-1} = 0$ for $\alpha \neq \beta$. Then, we can rewrite expression (2.18) as

$$E(\vec{k}) = E(0) + \frac{\hbar^2 (k_x - k_{x,0})^2}{2m_x^*} + \frac{\hbar^2 (k_y - k_{y,0})^2}{2m_y^*} + \frac{\hbar^2 (k_z - k_{z,0})^2}{2m_z^*}, \quad (2.20)$$

where

$$\frac{1}{m_j^*} = \frac{1}{\hbar^2} \left. \frac{\partial^2 E(\vec{k})}{\partial k_j^2} \right|_{k_j=k_{j,0}}, \quad (2.21)$$

is the electron effective mass associated with the spatial direction j with $j = x, y, z$.

Let me recall that we are looking for a solution of the whole Hamiltonian in (2.10) instead of a solution of H_0 . Although the electron-electron interaction term appearing in (2.10) does not allow a single-particle description of the problem, we can use the Bloch states as an orthonormal basis for any M -particle wave function $\Psi_{carriers}$. Hence, we can write $\Psi_{carriers}$ as:

$$\Psi_{carriers}(\vec{r}_1, \dots, \vec{r}_M, t) = \sum_{k_1, \dots, k_M} a(k_1, \dots, k_M, t) \phi_{k_1}(\vec{r}_1) \phi_{k_2}(\vec{r}_2) \cdots \phi_{k_M}(\vec{r}_M), \quad (2.22)$$

where $\phi_{k_i}(\vec{r}_i)$ is the Bloch wavefunction associated to the i -th electron with a wave vector \vec{k}_i , solution of the Hamiltonian H_{0i} defined in (2.11). Then, we can introduce (2.22) into the carriers Hamiltonian (2.10) to write

$$i \hbar \frac{\partial \Psi_{carriers}(\vec{r}_1, \dots, \vec{r}_M, t)}{\partial t} = \sum_{i=1}^M H_{0i} \Psi_{carriers}(\vec{r}_1, \dots, \vec{r}_M, t) + \frac{1}{2} \sum_{i=1}^M \sum_{\substack{j=1 \\ j \neq i}}^M eV(\vec{r}_i, \vec{r}_j) \Psi_{carriers}(\vec{r}_1, \dots, \vec{r}_M, t). \quad (2.23)$$

The first term in the right hand of equation (2.23) as

$$\left[\sum_{i=1}^M H_{0i} \right] \Psi_{carriers}(\vec{r}_1, \dots, \vec{r}_M, t) = \sum_{k_1, \dots, k_M} a(k_1, \dots, k_M, t) \left[(H_{01} \phi_{k_1}(\vec{r}_1)) \phi_{k_2}(\vec{r}_2) \cdots \phi_{k_M}(\vec{r}_M) + \cdots + \phi_{k_1}(\vec{r}_1) \cdots \phi_{k_{M-1}}(\vec{r}_{M-1}) (H_{0M} \phi_{k_M}(\vec{r}_M)) \right]. \quad (2.24)$$

Now, using the periodicity of $E(\vec{k})$, it can be demonstrate that an operator $\hat{E}(-i\vec{\nabla}_{\vec{r}_j})$ involving the derivatives $\vec{\nabla}_{\vec{r}_j}$ has the same eigenstates and eigenvalues as the mono-electronic Hamiltonian \hat{H}_{0j} . That is

$$\hat{E}(-i \nabla_{\vec{r}_i}) \cdot \phi_{k_i}(\vec{r}_i) = \hat{H}_{0i} \cdot \phi_{k_i}(\vec{r}_i) = E(\vec{k}_i) \cdot \phi_{k_i}(\vec{r}_i). \quad (2.25)$$

Using this property, we can write

$$\left[\sum_{i=1}^M \hat{H}_{0i} \right] \Psi_{carriers}(\vec{r}_1, \vec{r}_2, \dots, \vec{r}_M, t) = \left[\sum_{i=1}^M \hat{E}(-i \nabla_{\vec{r}_i}) \right] \Psi_{carriers}(\vec{r}_1, \vec{r}_2, \dots, \vec{r}_M, t), \quad (2.26)$$

and equation (2.23) can be finally written as:

$$i \hbar \frac{\partial \Psi_{carriers}(\vec{r}_1, \vec{r}_2, \dots, \vec{r}_M, t)}{\partial t} = \left[\sum_{i=1}^M \hat{E}(-i \nabla_{\vec{r}_i}) + \frac{1}{2} \sum_{i=1}^M \sum_{\substack{j=1 \\ j \neq i}}^M eV(\vec{r}_i, \vec{r}_j) \right] \Psi_{carriers}(\vec{r}_1, \vec{r}_2, \dots, \vec{r}_M, t). \quad (2.27)$$

The previous equation is a single-band effective mass equation for many-particle systems, and constitute an important simplification of equation (2.9). The complicate lattice potential has been described by means of a single number: the effective mass.

The electron-electron interaction potential usually varies slowly in comparison with the lattice one, and the wave function $\Psi_{carriers}(\vec{r}_1, \vec{r}_2, \dots, \vec{r}_M, t)$ can be written as the product of an envelope function slowly varying and a product of Bloch functions evaluated at the band minimum rapidly varying. Assuming that the Bloch functions can be written as

$$\phi_{\vec{k}}(\vec{r}) = \exp(i \vec{k} \cdot \vec{r}) \cdot u_{\vec{k}}(\vec{r}) \approx \exp(i \vec{k} \cdot \vec{r}) \cdot u_{\vec{k}_0}(\vec{r}) = \exp(i(\vec{k} - \vec{k}_0) \cdot \vec{r}) \cdot \phi_{\vec{k}_0}(\vec{r}), \quad (2.28)$$

then the many-electron wavefunction (2.22) becomes

$$\Psi_{carriers}(\vec{r}_1, \dots, \vec{r}_M, t) = \sum_{k_1, \dots, k_M} a(k_1, \dots, k_M, t) \cdot \exp(i(\vec{k}_1 - \vec{k}_0) \cdot \vec{r}_1) \cdot \phi_{\vec{k}_0}(\vec{r}_1) \cdot \dots \cdot \exp(i(\vec{k}_M - \vec{k}_0) \cdot \vec{r}_M) \cdot \phi_{\vec{k}_0}(\vec{r}_M). \quad (2.29)$$

This means that $\Psi_{carriers}(\vec{r}_1, \vec{r}_2, \dots, \vec{r}_M, t)$ can be defined as the product of an envelope function $F(\vec{r}_1, \dots, \vec{r}_M, t)$ and M Bloch functions evaluated at the momentum origin \vec{k}_0 :

$$\begin{aligned} \Psi_{carriers}(\vec{r}_1, \vec{r}_2, \dots, \vec{r}_M, t) &= \\ &= \phi_{\vec{k}_0}(\vec{r}_1) \cdot \phi_{\vec{k}_0}(\vec{r}_M) \sum_{k_1, \dots, k_M} a(k_1, \dots, k_M, t) \exp(i(\vec{k}_1 - \vec{k}_0) \cdot \vec{r}_1) \cdot \dots \cdot \exp(i(\vec{k}_M - \vec{k}_0) \cdot \vec{r}_M) \\ &= \phi_{\vec{k}_0}(\vec{r}_1) \cdot \phi_{\vec{k}_0}(\vec{r}_M) \cdot F(\vec{r}_1, \dots, \vec{r}_M, t) \end{aligned} \quad (2.30)$$

Using again the periodicity of $E(\vec{k})$ it can be demonstrated that:

$$\hat{E}(-i \vec{\nabla}_{\vec{r}_j}) \cdot (\phi_{\vec{k}_0}(\vec{r}_j) \cdot F(\vec{r}_1, \dots, \vec{r}_M, t)) = \phi_{\vec{k}_0}(\vec{r}_j) \hat{E}(\vec{k}_0 - i \vec{\nabla}_{\vec{r}_j}) \cdot F(\vec{r}_1, \dots, \vec{r}_M, t), \quad (2.31)$$

If we develop now $E(\vec{k}_0 - i\vec{\nabla}_{\vec{r}_j})$ in Taylor series around \vec{k}_0 as in (2.20), we can write

$$\hat{E}(\vec{k}_0 - i\vec{\nabla}_{\vec{r}_j}) = E(\vec{k}_0) + \frac{\hbar^2}{2} \left(-i \frac{\partial^2}{m_x^* \partial^2 x_j} - i \frac{\partial^2}{m_y^* \partial^2 y_j} - i \frac{\partial^2}{m_z^* \partial^2 z_j} \right). \quad (2.32)$$

where $E(\vec{k}_0)$ can be set to zero since it does only defines an energy reference origin. Then we can write a many-particle envelope equation

$$i\hbar \frac{\partial F(\vec{r}_1, \dots, \vec{r}_M, t)}{\partial t} = \left[\sum_{j=1}^M -\frac{\hbar^2}{2} \left(\frac{\partial^2}{m_x^* \partial x_j^2} + \frac{\partial^2}{m_y^* \partial y_j^2} + \frac{\partial^2}{m_z^* \partial z_j^2} \right) + \frac{1}{2} \sum_{i=1}^M \sum_{\substack{j=1 \\ j \neq i}}^M eV(\vec{r}_i, \vec{r}_j) \right] F(\vec{r}_1, \dots, \vec{r}_M, t). \quad (2.33)$$

Since the envelope function is roughly constant along a single unit cell, using the orthonormality of the functions $u_k(\vec{r})$ defined in (2.15), it can be easily demonstrate that the computation of the current and charge densities *averaged over a unit cell* can be obtained either from the whole carriers wave function or simply from the many-particle envelope function in expression (2.33). Therefore, if we do not care about the ultimate atomistic detail of the shape of the current and charge densities, we can directly deal with the envelope function instead of the carriers one. In this regard, references to the wave function will denote references to the envelope function from now on.

Therefore, by simply redefining $K(\vec{p}_k)$ as:

$$K(\vec{p}_k) = -\frac{\hbar^2}{2} \left(\frac{\partial^2}{m_x^* \partial x_j^2} + \frac{\partial^2}{m_y^* \partial y_j^2} + \frac{\partial^2}{m_z^* \partial z_j^2} \right), \quad (2.34)$$

our initial Hamiltonian (2.4) can be finally reduced to the next one:

$$\hat{H}_{env} = \sum_{j=1}^M \left[K(\vec{p}_k) + \frac{1}{2} \sum_{i=1}^M eV(\vec{r}_i, \vec{r}_j) \right]. \quad (2.35)$$

2.2.2 Many-electron open system Hamiltonian

The Hamiltonian in (2.35) is still computationally unaffordable because it involves a huge number of degrees of freedom (those of the battery, contacts, leads, etc...). We must reduce the described space region (see figure 2.2.1).

From now on we externally open the system and focus only on the active region⁶ of the electron device we want to study in detail. This is indeed a fundamental approach that any electron transport simulator must assume (regardless the approximations considered

⁶I will refer to the *sample* or *active region* indistinctly.

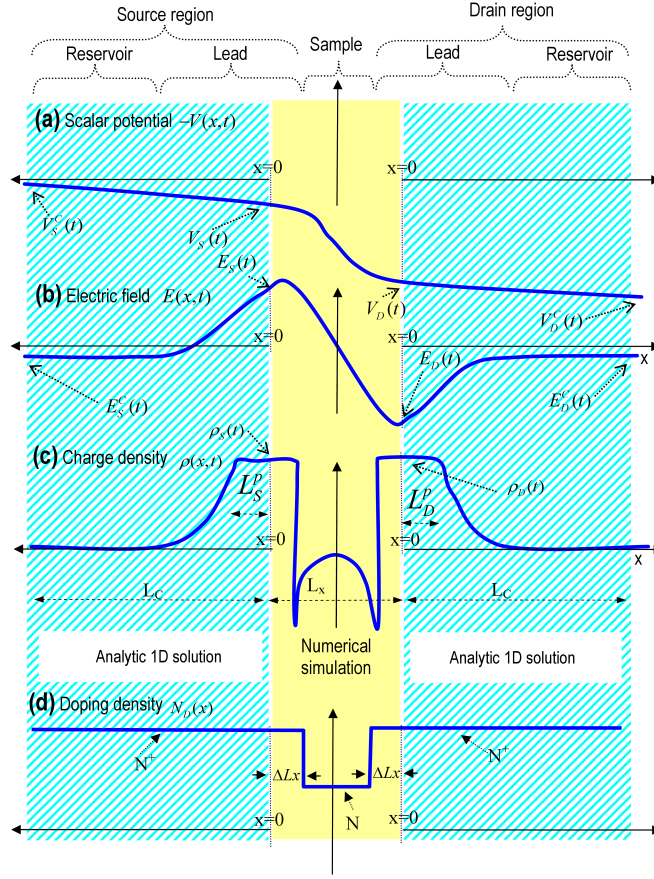


Figure 2.2.1: Schematic description of the different parts of the electron device. In section 2.3, an analytical parametric 1D solution is deduced for the (blue) dashed region, while a numerical 3D solution is obtained in the (yellow) solid central region defined as the simulation box. A small part of the highly doped leads is included into the simulation box in order to account for complex phenomena appearing at the interface. The definition of the variables in the figure are introduced in section 2.3 when discussing the boundary condition algorithm. Subsets refer to schematic representation of the (a) scalar potential, (b) electric field, (c) total charge density and (d) doping density.

up to this point) in order to be able to solve the Schrödinger equation for quantum systems or the Hamilton-Jacobi (Newton) equations for semi-classical systems.

We divide, then, the previous ensemble of M particles into a sub-ensemble of $N(t)$ particles whose positions are inside the volume Ω and a second sub-ensemble, $\{N(t) + 1, \dots, M\}$ which are outside⁷ (see figure 2.2.2). We assume that the number of particles

⁷For a quantum system, the number of particles inside the volume $N(t)$ has not only a dependence on time, but a dependence on all particle positions $N(\vec{r}_1, \dots, \vec{r}_k, \dots, \vec{r}_M, t)$. Let me assume a wave-function whose probability presence occupies regions inside and outside Ω . Then, the limit of the sum in the Hamiltonian (2.35) depends on the exact value of the variable \vec{r}_k . In principle, the k -particle have to be included into the first sub-ensemble when the Hamiltonian deals with $\vec{r}_k \in \Omega$ and into the second sub-ensemble when $\vec{r}_k \notin \Omega$. In order to avoid a very complicated notation, we do only write the time dependence of $N(t)$ for either classical or quantum systems. In any case, since our quantum solution will deal with quantum (Bohm) trajectories (rather than wave-functions), the simpler notation mentioned

inside, $N(t)$, is a time-dependent function that provides an explicit time-dependence to the many-particle (open-system) Hamiltonian. As drawn in figure 2.2.2, we assume a parallelepiped where the six rectangular surfaces $S = \{S^1, S^2, \dots, S^6\}$ are the boundaries of Ω . I use \vec{r}^l as the “boundary” vector representing an arbitrary position on the surfaces S^l . Now, the number of carriers in the system $N(t)$ will vary with time, i.e.

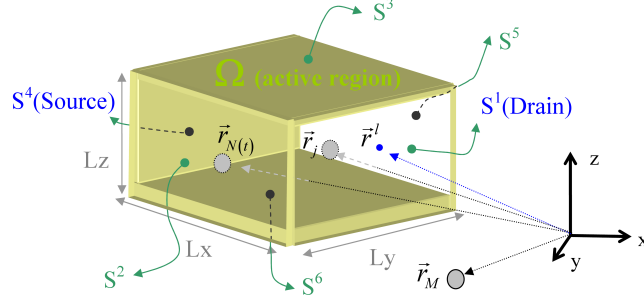


Figure 2.2.2: Schematic representation of the open volume $\Omega = Lx \cdot Ly \cdot Lz$ and its limiting surface $S = \{S^1, S^2, \dots, S^6\}$. There are $N(t)$ particles inside and $M - N(t)$ outside this volume. The vector \vec{r}^l points to an arbitrary position at the boundary surface S^l .

$$\hat{H}_{env}^{open}(\vec{r}_1, \dots, \vec{r}_M, \vec{p}_1, \dots, \vec{p}_{N(t)}, t) = \sum_k^{N(t)} \left\{ K(\vec{p}_k) + \frac{1}{2} \sum_{\substack{k=1 \\ k \neq j}}^{N(t)} eV(\vec{r}_k, \vec{r}_j) + \sum_{j=N(t)+1}^M eV(\vec{r}_k, \vec{r}_j) \right\} \quad (2.36)$$

Since throughout this dissertation I will work continuously with the many-particle open system Hamiltonian (2.36), in order to simplify its notation, let me simply refer to it as \hat{H} .

As I will show in the next section, the third term in (2.36) can be included in the Hamiltonian of the open system through the boundary conditions of the Poisson equation. The roughness of the approximation bringing together the effects of all the external particles over the $N(t)$ carriers will depend on our ability of formulating the boundary conditions at the borders of the active region of the electron device (see section 2.3 for an extent discussion on this point).

In the previous paragraphs, the assumption of a series of approximations have make it possible to go from the complex circuit Hamiltonian described in equation (2.4), to the much more simple one describing the “interesting” region of the circuit (2.36). However, although up to this point we have discussed the many-particle Hamiltonian in terms of the Coulomb force, this approach is inconvenient to deal with solid-state scenarios with a spatial-dependent permittivity [116]. For this reason, we rewrite here our many-particle Hamiltonian in terms of the more generic Poisson equation, which can be applied

here is appropriate for the classical and quantum algorithms.

to systems with (or without) a spatial-dependent permittivity (by simply substituting $\varepsilon \rightarrow \varepsilon(\vec{r})$ in the Poisson equation).

I start the discussion rewriting the previous many-particle open system Hamiltonian (2.36) as:

$$H(\vec{r}_1, \dots, \vec{r}_M, \vec{p}_1, \dots, \vec{p}_{N(t)}, t) = \sum_{k=1}^{N(t)} \left\{ K(\vec{p}_k) + \sum_{\substack{j=1 \\ j \neq k}}^{N(t)} e \cdot V(\vec{r}_k, \vec{r}_j) + \sum_{j=N(t)+1}^M e \cdot V(\vec{r}_k, \vec{r}_j) - \frac{1}{2} \sum_{\substack{j=1 \\ j \neq k}}^{N(t)} e \cdot V(\vec{r}_k, \vec{r}_j) \right\} \quad (2.37)$$

Each term $V(\vec{r}_k, \vec{r}_j)$ that appears in (2.37) can be explicitly obtained from a Poisson (or Laplace) equation inside the volume Ω . Using the superposition property of the Poisson equation, we can rewrite (2.37) as:

$$H(\vec{r}_1, \dots, \vec{r}_{N(t)}, \vec{p}_1, \dots, \vec{p}_{N(t)}, t) = \sum_{k=1}^{N(t)} \left\{ K(\vec{p}_k) + e \cdot W_k(\vec{r}_1, \dots, \vec{r}_{N(t)}, t) - \frac{1}{2} \sum_{\substack{j=1 \\ j \neq k}}^{N(t)} e \cdot V(\vec{r}_k, \vec{r}_j) \right\}, \quad (2.38)$$

where the term $W_k(\vec{r}_1, \dots, \vec{r}_k, \dots, \vec{r}_{N(t)})$ is a particular solution of the following Poisson equation:

$$\nabla_{\vec{r}_k}^2 (\varepsilon \cdot W_k(\vec{r}_1, \dots, \vec{r}_{N(t)})) = \rho_k(\vec{r}_1, \dots, \vec{r}_{N(t)}) \quad (2.39)$$

The term $\rho_k(\vec{r}_1, \dots, \vec{r}_{N(t)})$ in (2.39) depends on the position of the first $N(t)$ electrons:

$$\rho_k(\vec{r}_1, \dots, \vec{r}_k, \dots, \vec{r}_{N(t)}) = \sum_{\substack{j=1 \\ j \neq k}}^{N(t)} e \cdot \delta(\vec{r}_k - \vec{r}_j) \quad (2.40)$$

but (2.40) is independent of the position of the external particles because they only affect the boundary conditions of (2.39). Let me notice that there are still terms, $V(\vec{r}_k, \vec{r}_j)$, in (2.38) that are not computed from Poisson equations in (2.39), but from (2.8). However, we will show that these terms $V(\vec{r}_k, \vec{r}_j)$ have no role in the classical (i.e. section 2.4.1) or quantum (i.e. section 2.4.2) solutions of (2.38).

By construction, comparing (2.37) and (2.38), the term $W_k(\vec{r}_1, \dots, \vec{r}_{N(t)}, t)$ can be rewritten as:

$$W_k(\vec{r}_1, \dots, \vec{r}_{N(t)}, t) = \sum_{\substack{j=1 \\ j \neq k}}^{N(t)} V(\vec{r}_k, \vec{r}_j) + \sum_{i=N(t)+1}^M V(\vec{r}_k, \vec{r}_i) \quad (2.41)$$

The dependence of $W_k(\vec{r}_1, \dots, \vec{r}_{N(t)}, t)$ on the positions of the external particles is explic-

itly written in the last sum in (2.41), while in (2.39) this dependence is hidden in the boundary conditions of $W_k(\vec{r}_1, \dots, \vec{r}_k, \dots, \vec{r}_{N(t)})$ on the surface $S = \{S^1, S^2, \dots, S^6\}$. In fact, the boundary conditions are a delicate issue that we will discuss in next section.

2.3 Boundary conditions for the many-particle open system Hamiltonian

Since we want to deal with solutions of the Poisson equation (2.39), the boundary conditions for the $N(t)$ terms $W_k(\vec{r}_1, \dots, \vec{r}_k, \dots, \vec{r}_{N(t)})$ must be specified on the border surfaces $S = \{S^1, S^2, \dots, S^6\}$ of figure 2.2.2. Such boundary conditions will provide, somehow, information on the electrostatic effect that outside particles (i.e. $N(t) + 1, \dots, M$) have on the electrons inside Ω .

In practical situations, the volume Ω describes the active region of some kind of electron device. I will assume here a two-terminal device (source and drain) to explain our boundary conditions algorithm⁸. This means that only two, S^1 and S^4 , of the six border surfaces $S = \{S^1, S^2, \dots, S^6\}$ are really opened to the flow of carriers (see figure 2.3.1). These opened surfaces represent indeed, the most complicated boundary conditions to be modeled, and are the ones I will discuss in detail in this section (see also [65]). On the “closed” non-metallic surfaces⁹, Neumann boundary conditions are used with the educated guess that the component of the electric field normal to that surfaces is zero. The continuity of the displacement vector normal to surfaces justifies this assumption on “closed” boundaries when the relative permittivity inside is much higher than the corresponding value outside. On “closed” metallic surfaces⁹, we assume a many-particle version of the standard Dirichlet boundary conditions [66].

Before introducing our time-dependent boundary conditions, let me emphasize the important role that they play in modeling of electron transport at the nanoscale.

2.3.1 On the importance of boundary conditions

In order to correctly model the DC and/or AC conductance of nanoscale systems, one has to assure the accomplishment of the “overall charge neutrality” and “current conservation” [11, 13]. The implementation of such requirements into modern nanoscale electron simulators demands some kind of reasonable approximation for the Coulomb interaction.

On one hand, the importance of the “overall charge neutrality” (i.e. that the total charge in the whole device is zero) in nanoscale ballistic devices was clarified by the work

⁸In any case, the boundary conditions can be straightforwardly adapted to multi-terminal systems with an arbitrary number of “opened” borders.

⁹Here closed means that carriers do not cross that surface.

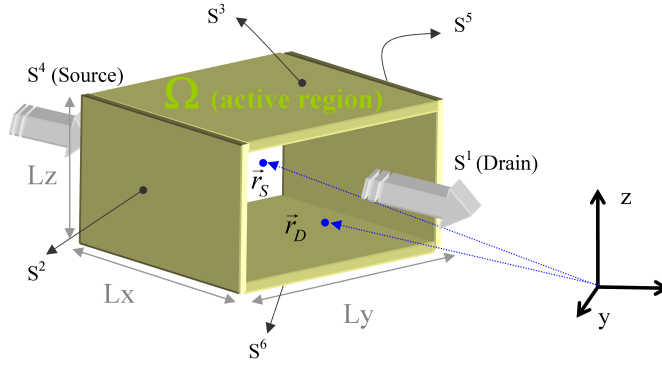


Figure 2.3.1: Schematic representation of the volume $\Omega = Lx \cdot Ly \cdot Lz$. Only S^1 and S^4 , corresponding to the drain and source surfaces respectively, are opened to electron flow. On the rest of surfaces standard Neumann boundary conditions are assumed.

of Landauer, Buttiker and co-workers on the “two-terminals” and the “four-terminals” conductance of ballistic devices [117]. The well-known standard textbook expression of the DC (zero temperature) conductance through a tunneling obstacle is known as the “two-terminal” expression because it is defined as the current divided by the voltage drop sufficiently far from the obstacle. However, the original formulation of the conductance proposed by Landauer [9, 102] in 1957 was known as the “four-terminal” conductance because its experimental validation needs two additional voltages probes to measure the voltage drop close to the tunneling obstacle. The presence of resistances in the leads¹⁰ explains the difference between both expressions. The ultimate origin of such resistances is the requirement of “overall charge neutrality” that transforms unbalanced charges in the leads into a voltage drop there, via the Poisson (Gauss) equation. See ref. [65] for a detailed discussion of such lead resistances.

On the other hand, the “current conservation” (i.e. the total current computed on any surface in the simulation box is equal to the total current measured inside an ammeter located far from the sample) is a necessary “requirement” for the prediction of AC conductances. The displacement current, i.e. the time-dependent variations of the electric field, assures that the total (conduction plus displacement) current density is a divergentless vector. Important theoretical contributions were done by Büttiker and co-workers for predicting AC properties of mesoscopic systems within a frequency-dependent scattering matrix formalism, in weakly non-linear regimes taking into account “overall charge neutrality” and “current conservation” [11, 25–27, 53, 54, 56].

In general, modern electron transport simulators do include reasonable approximations for the coulomb interactions that can guarantee the accomplishment of the “overall

¹⁰I refer to “sample” as the active region and the “leads” as the regions connecting the sample and the ideal (black body) reservoirs. The reservoirs are usually called “contacts” in mesoscopic devices. I avoid this last name here because “contacts” are usually understood as what we call here the sample in those papers related with the simulation of atomistic structures.

charge neutrality” requirement. In addition, those simulators that are developed within a time-dependent or frequency-dependent framework can also assure the “current conservation” requirement. However, the powerful treatment of quantum and atomistic effects can only be applied to a very limited number of degrees of freedom [118]. In fact, due to computational restrictions, a small simulation box is a mandatory requirement in many modern simulators. This restriction on the dimensions of the simulating-box implies that either very short leads (with screening length of few Armstrongs) are included into the small simulation box, or the leads are directly excluded from the simulation box. The first solution is only acceptable for metallic leads [28, 61] close to equilibrium, but it becomes inappropriate in general scenarios ranging from highly doped poly-silicon leads (with screening length of few nanometres) till modern junctionless devices [119]. In far-from equilibrium conditions (i.e. high bias conditions), the standard screening lengths have to be complemented by an additional depletion length in the leads. The second solution (neglecting the leads) implies serious difficulties for the achievement of “overall charge neutrality”. In any case, a possible inaccuracy in the computation of the “overall charge neutrality” affects our ability to treat the time-dependent Coulomb correlation among electrons and, therefore, the requirement of “current conservation”. In conclusion, due to computational difficulties, modern electron transport simulators have to be implemented in small simulation boxes that imply important difficulties for providing accurate simulations of the DC or AC conductances of nanoscale devices.

In principle, the problem of excluding the leads from the simulation box, while retaining the lead-sample Coulomb correlation, can be solvable by providing adequate boundary conditions on each of the “opened” borders of the simulation box. However, such boundary conditions are not easily predictable. The standard boundary conditions found in the literature for nanoscale electron device simulators are based on specifying two conditions in each of the borders of the simulation box:

(Border-potential-BC).- We have to specify the value of the scalar potential (or electric field) at the borders of the simulation box. These condition is a direct consequence of the uniqueness theorem for the Poisson equation [116] which tells that such condition are enough to completely specify the solution of Poisson equation, when the charge inside the simulation box is perfectly determined (the reason for discarding the electromagnetic vector potential in nanoscale systems is explained in ref. [65]).

(Border-charge-BC).- Contrarily to what is needed for the uniqueness solution of the Poisson equation, the charge density inside the simulation box is uncertain because it depends on the electron injected from the borders of the simulation box. Therefore, any boundary condition algorithm has to

include the information on the charge in the borders as an additional condition. In many cases, the electron injected on the borders depends, somehow, on the scalar potential there determined by the “Border-potential-BC” (and a fixed electrochemical potential). Therefore, a coupled system of boundary conditions appears.

Educated guesses for both boundary conditions (“Border-potential-BC” and “Border-charge-BC”) are present in the literature when describing nanoscale electron devices with simulation boxes large enough to include the leads. However, such boundary conditions are not applicable for small simulation boxes that exclude the leads. An extent discussion on the limitations of the standard boundary conditions when applied to small simulation boxes, in either classical or quantum electron device simulators, can be found ref. [65].

Here, I present a novel self-consistent and time-dependent definition of the boundary conditions for small simulation boxes (excluding most of the leads) that is able to capture the lead-sample Coulomb correlations.

2.3.2 Single-particle time-dependent boundary-conditions at the borders of the sample for overall charge neutrality

As explained in the previous paragraphs, all boundary condition of electrons transport simulators are based on specifying the value of the scalar potential (or the electric field) in the borders and the charge density there. Therefore, according to the levels of figure 2.2.1, we have to specify the values $V_S(t)$ and $V_D(t)$ for the “Border-potential-BC”, and $\rho_S(t)$ and $\rho_D(t)$ for the “Border-charge-BC”¹¹.

As we have explained in section 2.3.1, it is very difficult to provide an educated guess of the scalar potential, the electric field or the charge density on the borders of a small simulation box that excludes the leads. For large simulation boxes, one can assume a known value of the electrochemical potential (deep inside the reservoir) that controls the electron injection. However, close to the active region, where the far from equilibrium momentum distribution can be quite arbitrary, the prediction of any value of the electrochemical potential is quite inappropriate. Fortunately, from the results in this section we will be able to translate the “Border-potential-BC” and “Border-charge-BC” discussed in 2.3.1 for the borders of a small simulation box into simpler conditions deep inside the reservoirs. This is the key point of our boundary condition algorithm. In particular, the two new boundary conditions that we will impose at $x = \mp L_C$ are:

¹¹In section 2.3.2, I will provide analytical relationships between scalar potentials, electric fields and charge densities in the borders of the simulation box, at $x = 0$, and those values deep inside the reservoirs, at $x = \mp L_C$, which adds the unknowns $V_S^C(t)$, $V_D^C(t)$, $E_S^C(t)$ and $E_D^C(t)$. In total, for our two-terminal models, we have eight unknowns and, thus, we need eight conditions to specify the boundary conditions.

“Deep-drift-BC”: We assume that the inelastic scattering mechanisms at, both, the source $x \leq -L_C$ and the drain $x \geq L_C$ reservoirs provides a non-equilibrium position-independent “thermal” distribution of electrons there (it is implicitly assumed that the contact length L_C is large enough and the temperature Θ high enough so that inelastic scattering is relevant there). Such position-independent electron distribution is consistent with the “local” charge neutrality deduced in expression (2.47) that implies a uniform electric field there. According to the Drude’s model, the electric fields there tend both to $E_{S/D}^C(t) \rightarrow E_{S/D}^{drift}(t)$ [see expressions (2.45) and (2.46)].

“Deep-potential-BC”: We assume that electro-chemical potentials can be defined for the “thermal” distribution deep inside both reservoirs. As a consequence of the previous position-independent electron distribution deep inside the reservoirs, we can assume that the energy separation between such electro-chemical potential level and the bottom of the conduction band, in the drain and source reservoirs (at $x = \mp L_C$) are equal. Therefore, the energy separation between the bottoms of the conduction bands at both reservoirs (which coincides with the separation of the electrochemical potentials) is equal to the difference of the external voltages. Thus, $V_S^C(t) = 0$ and $V_D^C(t) = V_{external}(t)$.

These two conditions, “Deep-drift-BC” and “Deep-potential-BC” are quite reasonable deep inside the reservoirs. In fact, it can be shown that the numerical MC solution of the non-equilibrium Boltzmann equation in a large simulation box provides these scenarios in the reservoir [65].

In this subsection I will describe a formulation of the previous boundary conditions for a single-particle system. That is, I will assume that all electrons are subjected to the same boundary conditions. Again, this is a simplification of the real many-particle problem. As I have shown in the previous section (see equations (2.38), (2.39) and (2.39)), every single electron “sees” its own electrostatic potential, electric field and charge distribution. Consequently, each electron should see its own boundary conditions. In subsection 2.3.3 I will extend the boundary conditions presented here to the many-particle ones.

Time-dependent “overall charge neutrality” in nanoscale electron devices

In order to impose a time-dependent condition for the solutions of the charge density $\rho(\vec{r}, t)$, the electric field $\vec{E}(\vec{r}, t)$ and the scalar potential $V(\vec{r}, t)$, we start by integrating the local continuity equation (i.e. the condition of charge conservation implicit in Maxwell’s equations. See ref. [65]) in a large volume Ω' (see a 1D schematic representation in figure

2.2.1), that includes the sample, the leads and the reservoirs:

$$\frac{\partial}{\partial t} \int_{\Omega'} \rho(\vec{r}, t) \cdot d^3\vec{r} + \int_{S'} \vec{J}_C(\vec{r}, t) \cdot d\vec{s} = 0, \quad (2.42)$$

where the volume Ω' is limited by the surface S' .

Under some reasonable assumptions deep inside the reservoirs, expression (2.42) determines the time-evolution of the total charge $Q(t) = \int_{\Omega'} \rho(\vec{r}, t) \cdot d^3\vec{r}$ in the whole system [65]. Its solution is:

$$Q(t) = Q(t_0) \cdot \exp\left(-\frac{t-t_0}{\tau_c}\right) \quad (2.43)$$

with the dielectric relaxation time (sometimes called Maxwell relaxation time) defined as:

$$\tau_c = \varepsilon/\sigma \quad (2.44)$$

being ε the effective permittivity and σ the conductivity.

As expected, the meaning of expression (2.43) is that the total charge inside the system tends to zero in periods of time related to the dielectric relaxation time. Identically, it can be seen that the electric fields deep inside both reservoirs (see figure 2.2.1) tends to be identical and equal to the drift value¹² $E_{S/D}^{drift}(t)$ as:

$$E_S^C(t) - E_S^{drift}(t) = \left(E_S^C(t_0) - E_S^{drift}(t_0)\right) \cdot \exp\left(-\frac{t-t_0}{\tau_c}\right) \quad (2.45)$$

and

$$E_D^{drift}(t) - E_D^C(t) = \left(E_D^{drift}(t_0) - E_D^C(t_0)\right) \cdot \exp\left(-\frac{t-t_0}{\tau_c}\right) \quad (2.46)$$

The main approximation used to obtain (2.43), (2.45) and (2.46) is Drude's law. This implies that our time-dependent boundary condition algorithm is only valid for frequencies below the inverse of the average electron scattering time (see ref. [65]). In good reservoirs such frequencies are much higher than the THz range, which is high enough for most practical electronic applications.

Analytical spatial-dependent charge density, electric field, and scalar potential in the leads

In order to be able to evaluate the total charge in expression (2.43) or to apply expression (2.45) and (2.46), we need a knowledge of the charge densities or the electric fields deep inside the leads. Since we are interested in not simulating explicitly the leads, we

¹²In fact, the value of the $E_{drift}(t)$ is not a parameter, but it will be determined from the conduction current, via the Drude formula.

look for analytical expressions. Nonlinear screening theory is important, but a general analytical solution to the Poisson equation does not exist. Therefore, we have to take some simplifying assumptions. We will use the schemes depicted in figure 2.2.1 to explain our analytical solution in the leads and the simplifications that will be assumed.

We assume that all expressions in the leads depend only on the variable x along the transport direction, but are independent on the lateral directions y and z , so that a 1D scheme is appropriate. In order to develop simpler analytical expressions we consider one specific (negative) x -axis for the source and another (positive) for the drain with different origins. The point $x = 0$ is located at the interface between the numerical solution in the simulation box and the analytical solution in the lead (see figure 2.2.1). Let me notice that a small part of the lead is explicitly included into the numerical simulation box (see the length ΔLx in figure 2.2.1) in order to take into account some complex effects in the interfaces that our simple analytical model cannot capture (e.g. the presence of quasi-bound states [120] in the accumulation well that appears in the sample-lead interface or the Friedel oscillations [121]).

Then, assuming some additional approximations, a reasonable expression for the charge density, the electric field and the scalar potential at the drain are [65]:

$$\rho(x, t) = \begin{cases} \rho_D(t) \cdot \exp\left(-\frac{x-L_D^p}{l}\right); & L_D^p \leq x \leq L_C; \\ \rho_D(t); & 0 \leq x \leq L_D^p; \end{cases} \quad (2.47)$$

$$E(x, t) = \begin{cases} E_D^C(t) - \frac{\rho_D(t) \cdot l}{\epsilon} \cdot \exp\left(\frac{-x+L_D^p}{l}\right); & L_D^p \leq x \leq L_C; \\ E_D^C(t) - \frac{\rho_D(t) \cdot (l+L_D^p)}{\epsilon} + \frac{\rho_D(t) \cdot x}{\epsilon}; & 0 \leq x \leq L_D^p; \end{cases} \quad (2.48)$$

$$V(x, t) = \begin{cases} V_D^C(t) + E_D^C(t) \cdot (-x + L_C) - \frac{\rho_D(t) \cdot l^2}{\epsilon} \cdot \exp\left(\frac{-x+L_D^p}{l}\right); & L_D^p \leq x \leq L_C; \\ V_D^C(t) + E_D^C(t) \cdot (-x + L_C) - \frac{\rho_D(t) \cdot (-x+L_D^p)^2}{2 \cdot \epsilon} - \frac{\rho_D(t) \cdot l \cdot (l+L_D^p-x)}{\epsilon}; & 0 \leq x \leq L_D^p; \end{cases} \quad (2.49)$$

In the previous three equations, L_D^p is the depletion length of the drain lead indicated in figure 2.2.1 and l is the standard Debye length [122]. Analogous expressions for the source region can be identically deduced [65].

The validity of expressions (2.47) till (2.49) are limited to frequencies lower than the plasma frequency in the leads. Such frequencies will also be higher than few THz in normal highly doped leads.

Expressions (2.47) till (2.49), evaluated at $x = 0$, provides a relationship between the

values of the charge densities, the electric fields and the scalar potentials deep inside the reservoir and those in the border of the simulation box. In particular, the electric field deep inside the leads must vary in time as [65]:

$$E_{S/D}^C(t + \Delta t) = E_{S/D}(t + \Delta t) \mp \frac{\rho_{S/D}(t) \cdot (l + L_{S/D}^p(t))}{\varepsilon} \quad (2.50)$$

where we have defined $E_{S/D}(t + \Delta t) = E(0, t + \Delta t)$. The analogous expressions for the scalar potential are [65]:

$$V_{S/D}(t + \Delta t) = V_{S/D}^C(t + \Delta t) \mp E_{S/D}^C(t + \Delta t) \cdot L_C - \frac{\rho_{S/D}(t) \cdot (l + L_{S/D}^p(t))^2}{2\varepsilon} - \frac{\rho_{S/D}(t) \cdot l^2}{2\varepsilon}. \quad (2.51)$$

We fix the value $V_S^C(t + \Delta t) = 0$ and $V_D^C(t + \Delta t) = V_{external}(t + \Delta t)$. Finally the charge density at source and drain borders of the simulation box $\rho_{S/D}$ must vary in time as [65]:

$$\rho_{S/D}(t + \Delta t) = \rho_{S/D}(t) \pm \left(E_{S/D}^C(t) - E_{S/D}^{drift}(t) \right) \frac{\varepsilon \cdot \Delta T}{(l + L_{S/D}^p(t)) \cdot \tau_c}. \quad (2.52)$$

Although equations (2.52) together with the values $\rho_S(t)$ and $\rho_D(t)$ clearly defines $\rho_S(t + \Delta t)$ and $\rho_D(t + \Delta t)$ we do not have an exact control on how to increase/decrease these value in our simulator. On the contrary, we do only have the possibility of increasing/decreasing the injecting probability (see expression (B.1) in Appendix B) through the parameters of $F_S^{inj}(t + \Delta t)$ and $F_D^{inj}(t + \Delta t)$ that appear in expression (B.5) and (B.6) of Appendix (B). The exact relationship between the displacement of the injecting energy levels and the variation of the “injected” charge density in the simulation box boundaries is not trivial. We perform a pre-processing computation of the function $\rho^{inj}(F_{S,D}^{inj} + qV_{S,D})$ according to the injection model described in Appendix B. Once such a relation has been established, we can determine exactly in which way the injecting energy levels have to be displaced. There is, however, a particular scenario that can not be managed just by modifying the injecting energy levels. Very far from equilibrium, at high applied bias, we can “accumulate” electrons as much as needed to decrease $\rho_S(t)$ in order to achieve “overall charge neutrality”. However, we cannot “deplete” electrons as much as possible in the sample-lead interface. Once we arrive at zero injected electrons, we cannot decree this number any more. In such situations, the only way to decrease the negative charge is to enlarge the depleted (positive charge) region in the drain (see figure 2.2.1.c). The same “depleted” procedure could be needed in the source for a negative bias. [65]

2.3.3 Extension of the boundary conditions to many-particle Hamiltonians

In the previous subsection I have developed a single-particle algorithm describing a unique set of time-dependent boundary conditions for all electrons to account for overall charge neutrality. Here I want to extend such results to a many-particle approach where each electron has its own boundary conditions. Let me recall, that we are looking for solutions for the $N(t)$ Poisson equations (2.39). Thus, we need to specify $N(t)$ boundary conditions on the two opened border surfaces S^1 and S^4 (see figure 2.3.1) for the $N(t)$ terms $W_k(\vec{r}_1, \dots, \vec{r}_k, \dots, \vec{r}_{N(t)})$.

In order to provide a clear notation for discussing the boundary conditions of $W_k(\vec{r}_1, \dots, \vec{r}_k, \dots, \vec{r}_{N(t)})$, we distinguish between the “source” vectors $\{\vec{r}_1, \dots, \vec{r}_{k-1}, \vec{r}_{k+1}, \dots, \vec{r}_{N(t)}\}$ and the additional “observation” vector \vec{r} that runs over all space [116]. In particular, the electrostatic potential that appears in the Hamiltonian (2.37) is defined as the value of the potential $W_k(\vec{r}_1, \dots, \vec{r}_{k-1}, \vec{r}, \vec{r}_{k+1}, \dots, \vec{r}_{N(t)}, t)$ at the particular position $\vec{r} = \vec{r}_k$:

$$W_k(\vec{r}_1, \dots, \vec{r}_{k-1}, \vec{r}_k, \vec{r}_{k+1}, \dots, \vec{r}_{N(t)}, t) = W_k(\vec{r}_1, \dots, \vec{r}_{k-1}, \vec{r}, \vec{r}_{k+1}, \dots, \vec{r}_{N(t)}, t) \Big|_{\vec{r}=\vec{r}_k} \quad (2.53)$$

Our goal is to find an educated guess for all the $N(t)$ terms $W_k(\vec{r}_1, \dots, \vec{r}_{k-1}, \vec{r}, \vec{r}_{k+1}, \dots, \vec{r}_{N(t)}, t)$ at all “observation” points $\vec{r} = \vec{r}_S$ and $\vec{r} = \vec{r}_D$ on the surfaces S^1 and S^4 . The information of such boundary conditions comes from the value of the total voltage (due to internal and external electrons) at position $\vec{r}_{S/D}$ and time t . We define such a voltage as the electrostatic potential associated to an additional probe charge q_{M+1} situated on that boundary, $\vec{r}_{S/D} \equiv \vec{r}_{M+1} \in S^{4/1}$, which can be now identified with the voltages $V_{S/D}(t)$ defined in (2.51) (see fig. 2.3.2). The electrostatic potential “seen” by this extra charge due to the presence of the rest of the particles is just:

$$V_{S/D}(t) \equiv \sum_{j=1}^M V(\vec{r}_{M+1}, \vec{r}_j) \Big|_{\vec{r}_{M+1}=\vec{r}_{S/D}} \quad (2.54)$$

where the expected restriction $j \neq M + 1$ is hidden in the limit of the sum.

Once the relationship (2.54) is established, we can easily define the boundary conditions of any of the $N(t)$ electrostatic potential $W_k(\vec{r}_1, \dots, \vec{r}, \dots, \vec{r}_{N(t)})$ from the function $V_{S/D}(t)$. In particular, from (2.41), we know that:

$$W_k(\vec{r}_1, \dots, \vec{r}_{k-1}, \vec{r}, \vec{r}_{k+1}, \dots, \vec{r}_{N(t)}, t) \Big|_{\vec{r}=\vec{r}_{S/D}} = \sum_{\substack{j=1 \\ j \neq k}}^M V(\vec{r}_{S/D}, \vec{r}_j) = V_{S/D}(t) - V(\vec{r}_{S/D}, \vec{r}_k) \quad ; \quad l = 1, \dots, 6 \quad (2.55)$$

where $V(\vec{r}_{S/D}, \vec{r}_k)$ is defined according to (2.8). The discussion done here is valid for either classical or quantum systems¹³.

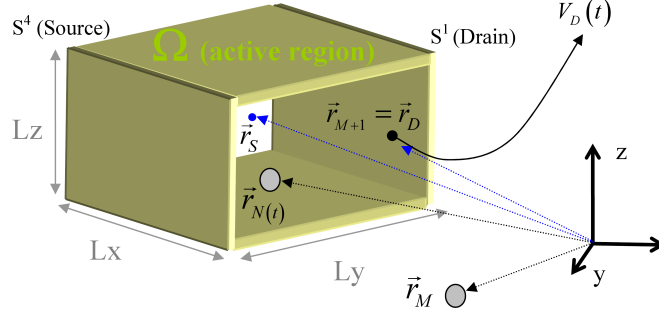


Figure 2.3.2: The electrostatic potential $V_D(t)$ (due to internal and external electrons) measured on the surface S^1 at position \vec{r}_D and time t by an additional probe charge q_{M+1} situated on the boundary $\vec{r}_D \equiv \vec{r}_{M+1} \in S^1$.

The reader can be surprised by the fact that the right hand side of expression (2.55) tend to infinite $V(\vec{r}_{S/D}, \vec{r}_k) \rightarrow \infty$ when $\vec{r}_k \rightarrow \vec{r}_{S/D}$. However, when $\vec{r}_k \rightarrow \vec{r}_{S/D}$, the extra particle at $\vec{r}_{S/D} \equiv \vec{r}_{M+1} \in S_l$ would also provide an infinite value of the electrostatic potential, i.e. $V_{S/D}(t) \rightarrow \infty$, due to the presence of the k -particle on the surface. Therefore, the first infinite, $V(\vec{r}_{S/D}, \vec{r}_k) \rightarrow \infty$, is canceled by the second infinite, $V_{S/D}(t) \rightarrow \infty$. Strictly speaking, our assumption that the potential at one particular surface is position-independent, $V_{S/D}(t)$, is not completely accurate because it should reproduce, somehow, the atomistic charge distribution and the carrier inhomogeneity on the surface. In particular, one can expect $V_{S/D}(t) \rightarrow \infty$ when the electron is close to the border, $\vec{r}_k \rightarrow \vec{r}_{S/D}$. However, due to our ignorance about the atomistic description of the contact interface, we apply the boundary conditions (2.55) assuming that the distance between \vec{r}_k and $r_{S/D}$ is always greater than 1 nm (this value is interpreted as a measure of range of the atomistic pseudo-potential [15] in the spatial-dependent permittivity scenarios discussed here).

Finally, it can be shown that the boundary conditions (2.55) developed here provides, for metallic contacts, the same electrostatic description obtained from the image-charge method. But moreover, it has the fundamental advantage that it can be directly implemented into realistic (classical or quantum) electron device simulators via a 3D Poisson solver [66].

¹³Classically, the definition of $V_{S/D}(t)$ can be directly associated to the voltage “measured” at $\vec{r}_{S/D}$ by an external meter. On the contrary, quantum mechanically, the voltage “measured” at $\vec{r}_{S/D}$ would require evaluating a bracket between the many-particle wave-function and $V_{S/D}(t)$. In this section we are not discussing the many-particle wave-function, but only an expression of the many-particle Hamiltonian. Therefore, it is important to remark that $V_{S/D}(t)$ is not defined as the voltage “measured” at $\vec{r}_{S/D}$, but as the electrostatic potential that describes the interaction of the electron at $\vec{r}_{S/D}$ with the rest of M electrons. This last definition is identical for classical and quantum cases.

2.4 Numerical solution of the many-particle open system Hamiltonian

Once I have introduced the many-particle open system Hamiltonian and its boundary conditions, we are ready to solve it. In this section I present two kind of solutions. On one hand I present a semi-classical solution based on Hamilton-Jacobi equations. On the other, I present a quantum solution based on Bohmian mechanics.

2.4.1 Semi-classical solution of the many-particle Hamiltonian

The classical description of the particle dynamics subjected to the many-particle Hamiltonian (2.38) can be computed by using the well-known Hamilton equations. In particular, we can obtain the (Newton like) description of the classical trajectory $\vec{r}_i[t]$ in the real space through:

$$\frac{d\vec{p}_i[t]}{dt} = \left[-\nabla_{\vec{r}_i} H(\vec{r}_1, \dots, \vec{r}_{N(t)}, \vec{p}_1, \dots, \vec{p}_{N(t)}, t) \right]_{\vec{r}_1=\vec{r}_1[t], \dots, \vec{p}_{N(t)}=\vec{p}_{N(t)}[t]}, \quad (2.56a)$$

$$\frac{d\vec{r}_i[t]}{dt} = \left[\nabla_{\vec{p}_i} H(\vec{r}_1, \dots, \vec{r}_{N(t)}, \vec{p}_1, \dots, \vec{p}_{N(t)}, t) \right]_{\vec{r}_1=\vec{r}_1[t], \dots, \vec{p}_{N(t)}=\vec{p}_{N(t)}[t]}. \quad (2.56b)$$

For the many-particle Hamiltonian studied in this work, expression (2.56b) gives the trivial result $m \cdot \vec{v}_i[t] = \vec{p}_i[t]$, while the evaluation of expression (2.56a) requires a detailed development. We know that the \vec{r}_i -gradient of the exact many-particle Hamiltonian (2.38) can be written as:

$$[\nabla_{\vec{r}_i} H]_{\vec{R}=\vec{R}[t]} = \left[\nabla_{\vec{r}_i} \sum_{k=1}^{N(t)} \left\{ e \cdot W_k(\vec{r}_1, \dots, \vec{r}_{N(t)}, t) - \frac{1}{2} \sum_{\substack{j=1 \\ j \neq k}}^{N(t)} e \cdot V(\vec{r}_k, \vec{r}_j) \right\} \right]_{\vec{R}=\vec{R}[t]}. \quad (2.57)$$

We define the multi-dimensional vector $\vec{R} = (\vec{r}_1, \dots, \vec{r}_{N(t)})$ to account, in a compact way, for the classical trajectories of $N(t)$ electrons $\vec{R}[t] = (\vec{r}_1[t], \dots, \vec{r}_{N(t)}[t])$. Substituting the definition of $W_k(\vec{r}_1, \dots, \vec{r}_{N(t)}, t)$ done in expression (2.41) into equation (2.57), we find:

$$[\nabla_{\vec{r}_i} H]_{\vec{R}=\vec{R}[t]} = \left[\nabla_{\vec{r}_i} \left\{ 2 \sum_{\substack{j=1 \\ j \neq i}}^{N(t)} e V(\vec{r}_j, \vec{r}_i) + \sum_{j=N(t)+1}^M e V(\vec{r}_j, \vec{r}_i) \right\} - \nabla_{\vec{r}_i} \sum_{\substack{j=1 \\ j \neq i}}^{N(t)} e \cdot V(\vec{r}_j, \vec{r}_i) \right]_{\vec{R}=\vec{R}[t]}. \quad (2.58)$$

Note the elimination of the factor $\frac{1}{2}$ in the first term of the right hand part of (2.58) that accounts for those terms $e \cdot V(\vec{r}_k, \vec{r}_j)$ in (2.57) where $\vec{r}_k \neq \vec{r}_i$ and $\vec{r}_j = \vec{r}_i$, that are identical to the term $e \cdot V(\vec{r}_i, \vec{r}_k)$ in (2.58). For the same reason, we include a factor 2

on the first term of right hand of (2.58). From expressions (2.41) and (2.58), we realize that:

$$[\nabla_{\vec{r}_i} H]_{\vec{R}=\vec{R}[t]} = [\nabla_{\vec{r}_i} W_i(\vec{r}_1, \dots, \vec{r}_{N(t)})]_{\vec{R}=\vec{R}[t]}. \quad (2.59)$$

Only the term $W_i(\vec{r}_1, \dots, \vec{r}_{N(t)})$ of the whole Hamiltonian (2.38) becomes relevant for a classical description of the i -particle. In fact, since we only evaluate a \vec{r}_i -gradient, the rest of particle positions can be evaluated at their particular value at time t , i.e. $\vec{r}_k \rightarrow \vec{r}_k[t]$ for all $k \neq i$. Therefore, we define the single-particle potential $\bar{W}_i(\vec{r}_i, t)$ from the many-particle potential as:

$$\bar{W}_i(\vec{r}_i, t) = W_i(\vec{r}_1[t], \dots, \vec{r}_{i-1}[t], \vec{r}_i, \vec{r}_{i+1}[t], \dots, \vec{r}_{N(t)}[t]). \quad (2.60)$$

We use a “hat” to differentiate the (time-dependent) single-particle electrostatic potential from the many-particle potential. Each i -term of the single-particle electrostatic potential, $\bar{W}_i(\vec{r}_i, t)$, is a solution of one particular 3D-Poisson equation:

$$\nabla_{\vec{r}_i}^2 (\varepsilon(\vec{r}_i) \cdot \bar{W}_i(\vec{r}_i, t)) = \bar{\rho}_i(\vec{r}_i, t), \quad (2.61)$$

where the single-particle charge density is defined as:

$$\bar{\rho}_i(\vec{r}_i, t) = \sum_{\substack{j=1 \\ j \neq i}}^{N(t)} e \delta(\vec{r}_i - \vec{r}_j[t]), \quad (2.62)$$

and the boundary conditions are adapted here as:

$$\bar{W}_i(\vec{r}_i, t) \Big|_{\vec{r}_i=\vec{r}_{S/D}} = V_{S/D}(t) - V(\vec{r}_{S/D}, \vec{r}_i[t]). \quad (2.63)$$

Let me remind that expressions (2.60), (2.61) and (2.62) together with the boundary conditions in (2.63), provide an exact treatment of the many-particle correlations in classical scenarios. The $N(t)$ Newton equations are coupled by $N(t)$ Poisson equations. Therefore, the many-particle Hamiltonian of (2.38) can be written exactly (without mean-field approximation) as a sum of single particle Hamiltonian for classical scenarios:

$$H(\vec{r}_1, \dots, \vec{r}_{N(t)}, \vec{p}_1, \dots, \vec{p}_{N(t)}, t) = \sum_{k=1}^{N(t)} \{K(\vec{p}_k) + e \cdot \bar{W}_k(\vec{r}_k, t)\}. \quad (2.64)$$

As I have already argued, our many-electron method applied to semiclassical devices cannot be considered as a solution of the Boltzmann equation because the latter is developed within a classical mean-field approximation. The term $\bar{W}_k(\vec{r}_k, t)$ in the Hamiltonian of expression (2.64) means that each particle “sees” its own electrostatic potential which is

different to that of the others. Apart from the scattering rates, this is the fundamental difference between our “many-electron” method applied to classical transport and the standard Monte Carlo solution of the Boltzmann equation method for electron devices.

2.4.2 Quantum Solution of the many-particle Hamiltonian

The many-particle open-system Hamiltonian developed in expression (2.38) is also valid for quantum systems. In this section, I will explain its practical quantum solution using a quantum (Bohm) trajectory formalism discussed in Appendix A. For convenience, we rewrite the many-particle Hamiltonian in (2.38) as:

$$H(\vec{r}_1, \dots, \vec{r}_{N(t)}, t) = \left\{ \sum_{k=1}^{N(t)} -\frac{\hbar^2}{2 \cdot m_k} \nabla_{\vec{r}_k}^2 + U(\vec{r}_1, \dots, \vec{r}_{N(t)}, t) \right\}, \quad (2.65)$$

where we explicitly write the electron momentum as $\vec{p}_k = -i\hbar\nabla_{\vec{r}_k}$ in the kinetic energy. According to eq. (2.38), the many-particle electrostatic potential $U(\vec{r}_1, \dots, \vec{r}_{N(t)}, t)$ is defined as:

$$U(\vec{r}_1, \dots, \vec{r}_{N(t)}, t) = \sum_{k=1}^{N(t)} \left\{ e \cdot W_k(\vec{r}_1, \dots, \vec{r}_{N(t)}, t) - \frac{1}{2} \sum_{\substack{j=1 \\ j \neq k}}^{N(t)} e \cdot V(\vec{r}_k, \vec{r}_j) \right\}. \quad (2.66)$$

Then, the time-dependent Schrödinger equation that provides the many-particle wave-function, $\Phi(\vec{r}_1, \dots, \vec{r}_{N(t)}, t)$, that describes the electron dynamics associated to our many-particle (open-system) Hamiltonian is:

$$i\hbar \frac{\partial \Phi(\vec{r}_1, \dots, \vec{r}_{N(t)}, t)}{\partial t} = \left\{ \sum_{k=1}^{N(t)} -\frac{\hbar^2}{2 \cdot m} \nabla_{\vec{r}_k}^2 + U(\vec{r}_1, \dots, \vec{r}_{N(t)}, t) \right\} \cdot \Phi(\vec{r}_1, \dots, \vec{r}_{N(t)}, t). \quad (2.67)$$

The practical utility of expression (2.67) in understanding quantum scenarios can seem quite doubtful because its direct solution becomes computationally inaccessible for more than very few electrons [14, 15, 123]. However, we can use a transport formalism based on Bohm trajectories that simplifies the complexity of evaluating (2.67) (see appendix A and [67]). Here, I go directly to the main result of Ref. [67] (see also Appendix A), where it is shown that a many-particle electron Bohm trajectory $\vec{r}_a[t]$ computed from the many-particle wave-function, $\Phi(\vec{r}_1, \dots, \vec{r}_{N(t)}, t)$, solution of the equation (2.67) can be equivalently computed from the single-particle wave-function $\Psi_a(\vec{r}_a, t)$ solution of the

following single-particle Schrödinger equation:

$$i\hbar \frac{\partial \Psi_a(\vec{r}_a, t)}{\partial t} = \left\{ -\frac{\hbar^2}{2 \cdot m} \nabla_{\vec{r}_a}^2 + U_a(\vec{r}_a, \vec{R}_a[t], t) + G_a(\vec{r}_a, \vec{R}_a[t], t) + i \cdot J_a(\vec{r}_a, \vec{R}_a[t], t) \right\} \Psi_a(\vec{r}_a, t), \quad (2.68)$$

where I have defined $\vec{R}_a[t] = \{\vec{r}_1[t], \vec{r}_{a-1}[t], \vec{r}_{a+1}[t], \vec{r}_N[t], t\}$ as a vector that contains all Bohm trajectories except $\vec{r}_a[t]$. The exact definition of the other potentials that appear in (2.68), $G_a(\vec{r}_a, \vec{R}_a[t], t)$ and $J_a(\vec{r}_a, \vec{R}_a[t], t)$, can be found in Appendix A (see also [67]). The total many-particle electrostatic potential in (2.67) can be divided into two parts:

$$U(\vec{r}_a, \vec{R}_a[t], t) = U_a(\vec{r}_a, \vec{R}_a[t], t) + U_b(\vec{R}_a[t], t). \quad (2.69)$$

From expressions (2.41) and (2.66), we realize that can be greatly simplified as:

$$U_a(\vec{r}_a, \vec{R}_a[t], t) = 2 \sum_{\substack{j=1 \\ j \neq a}}^{N(t)} q_a \cdot V(\vec{r}_a, \vec{r}_j[t]) + \sum_{i=N(t)+1}^M q_a \cdot V(\vec{r}_a, \vec{r}_i[t]) - \sum_{\substack{j=1 \\ j \neq a}}^{N(t)} q_a \cdot V(\vec{r}_a, \vec{r}_j[t]) = \bar{W}_a(\vec{r}_a, \vec{R}_a[t], t). \quad (2.70)$$

The rest of the terms $V(\vec{r}_j[t], \vec{r}_i[t])$ of expression (2.70) appear in $U_b(\vec{R}_a[t], t)$ and they are included in the potential $G_a(\vec{r}_a, \vec{R}_a[t], t)$. However, the term $U_b(\vec{R}_a[t], t)$ has no role on the single-particle wave-function $\Psi_a(\vec{r}_a, t)$ because it has no dependence on \vec{r}_a and it only introduces an irrelevant global phase on $\Psi_a(\vec{r}_a, t)$.

Let me notice that, in the right hand side of expression (2.70), we have used the same definition of the potential profile as in the classical expression (2.60). The only difference here is that $\vec{R}_a[t]$ are not classical trajectories, but quantum (Bohm) trajectories. Therefore, the computation of the potential profile $\bar{W}_a(\vec{r}_a, \vec{R}_a[t], t)$ that appears in the single-particle Schrödinger equation (2.68) just needs a 3D Poisson equation (2.61), (2.62) with the boundary conditions (2.63). Interestingly, since the term $\bar{W}_a(\vec{r}_a, \vec{R}_a[t], t)$ is computed from a Poisson equation, our quantum-trajectory algorithm can also be directly extended to spatial dependent permittivity systems.

In fact, in order to effectively solve the Schrödinger equation (2.68), we need to know the position of the rest of Bohm particles $\vec{R}_a[t] = \{\vec{r}_1[t], \vec{r}_{a-1}[t], \vec{r}_{a+1}[t], \vec{r}_N[t], t\}$. Therefore, all $N(t)$ Bohm trajectories have to be computed simultaneously within a system of $N(t)$ Schrödinger equations coupled by $N(t)$ Poisson equations. The keystone of our

quantum trajectory algorithm is that, in order to find $\vec{r}_a[t]$, we do not have to evaluate the electrostatic potential, $U(\vec{r}_1, \dots, \vec{r}_{N(t)}, t)$, and the wave-function, $\Phi(\vec{r}_1, \dots, \vec{r}_{N(t)}, t)$, everywhere in the N-multidimensional configuration space $\{\vec{r}_1, \dots, \vec{r}_a, \dots, \vec{r}_{N(t)}, t\}$, but only over a smaller number of configurations points where all positions of electrons are fixed, $\vec{R}_a[t]$, except \vec{r}_a , i.e. $\{\vec{r}_1[t], \dots, \vec{r}_a, \dots, \vec{r}_{N(t)}[t], t\}$. We want to remark that the full (short and long range) Coulomb interaction present in (2.38) is considered explicitly in (2.68) without any (mean-field or perturbative) approximation. In particular, defining $\Psi_a(\vec{r}_a, t) = r_a(\vec{r}_a, t) \exp\left[\frac{is_a(\vec{r}_a, t)}{\hbar}\right]$ from the many-particle wave function $\Phi(\vec{r}_1, \dots, \vec{r}_{N(t)}, t)$ evaluated at $\{\vec{r}_a, \vec{R}_a[t]\}$, we can write the trajectory $\vec{r}_a[t]$ (see appendix A) as

$$\vec{r}_a[t] = \vec{r}_a[t_0] + \int_{t_0}^t \vec{v}_a(\vec{r}_a[t'], t') dt', \quad (2.71a)$$

$$\vec{v}_a(\vec{r}_a[t], t) = \frac{1}{m} \vec{\nabla}_{\vec{r}_a} s_a(\vec{r}_a, t). \quad (2.71b)$$

In this quantum (Bohm) trajectory algorithm, the use of single-particle Schrödinger equations (2.68) is exact to treat many-particle system as demonstrated in [67]. However, the exact values of the terms $G_a(\vec{r}_a, \vec{R}_a[t], t)$ and $J_a(\vec{r}_a, \vec{R}_a[t], t)$ that appear in the Hamiltonian (2.68) are unknown (because they require the partial knowledge of the shape of the many-particle wave-function). Thus, from a practical point of view, they need to be approximated by some educated guess. In addition, the exchange interaction among the (fermions) electrons can also be considered in the present quantum algorithm. A brief explanation of how the exchange interaction can be introduced in the present quantum (Bohm) trajectory algorithm is mentioned in Ref. [67]. Here we will use a particular algorithm, discussed at the end of Appendix A, which let us avoid the computation of $G_a(\vec{r}_a, \vec{R}_a[t], t)$ and $J_a(\vec{r}_a, \vec{R}_a[t], t)$.

2.5 A simple example: Simulation of a two-electron system

In this sub-section I will explain the origin of the important differences appearing between a time-dependent mean-field algorithm described below and our time-dependent many-particle algorithm. Although I will use here a simple semi-classical two-electron system, the conceptual differences remarked here between the mean-field and the many-particle approaches, can be extrapolated not only to quantum simulations but also to much complex systems. Let me first introduce the mean-field version of expression (2.38), and then analyze some remarkable results for a simple two-electron system.

2.5.1 Semi-classical solution of the mean-field Hamiltonian

As described in the introduction of this chapter, the mean-field approximation provides a single average potential for computing the dynamics of all electrons. This average potential, that we label here by the suffix “mean” $\bar{W}_{mean}(\vec{r}, t)$, is still capable of preserving most of the collective effects of the Coulomb interaction. Here, I compare this approximation with our exact many-particle Hamiltonian. The term $\bar{W}_{mean}(\vec{r}, t)$ is computed by taking into account all charges inside the volume Ω . However, since one particle can not “feel” its own charge, in fact, $\bar{W}_{mean}(\vec{r}, t)$ can be interpreted as the electrostatic potential “seen” by an additional probe charge whose position is \vec{r} .

$$\bar{W}_{mean}(\vec{r}, t) = \bar{W}_{M+1}(\vec{r}_1[t], \dots, \vec{r}_{N(t)}[t], \vec{r}). \quad (2.72)$$

This term $\bar{W}_{mean}(\vec{r}, t)$ is a solution of a unique 3D-Poisson equation:

$$\nabla_{\vec{r}}^2 \bar{W}_{mean}(\vec{r}, t) = \bar{\rho}_{mean}(\vec{r}, t), \quad (2.73)$$

where the charge density is defined as:

$$\bar{\rho}_{mean}(\vec{r}, t) = \sum_{j=1}^{N(t)} q_j \delta(\vec{r} - \vec{r}_j[t]), \quad (2.74)$$

and, according to expression (2.54) in the previous section, the boundary conditions for this additional probe charge must be:

$$\bar{W}_{mean}(\vec{r}, t)|_{\vec{r}=\vec{r}_{S/D}} = V_{S/D}(t). \quad (2.75)$$

Let me notice that the time-dependent mean-field approximation discussed here can be applied to either the classical or quantum systems. Both approaches share expressions (2.73), (2.74) and (2.75) for the computation of the electrostatic potentials (change the classical trajectories by the quantum ones). I also want to remark the time-dependence of expression (2.73). This is a common feature for classical (semiconductor Monte Carlo [32]) simulations, but less frequent for quantum mean-field approaches.

Now, I estimate the error of our time-dependent mean-field approximation. First, I show that the mean-field potential can be written in terms of the potentials $\bar{W}_i(\vec{r}_i, t)$ mentioned in equation (2.60). In particular, we can write the mean-field potential $\bar{W}_{mean}(\vec{r}, t)$ as:

$$\bar{W}_{mean}(\vec{r}, t) = \frac{1}{N(t)} \left\{ \sum_{j=1}^{N(t)} \bar{W}_{mean}(\vec{r}, t) \right\} = \frac{1}{N(t)} \sum_{j=1}^{N(t)} \left\{ \bar{W}_j(\vec{r}, t) + V(\vec{r}, \vec{r}_j[t]) \right\}. \quad (2.76)$$

Now, I compute the error, $Error_k(\vec{r}, t)$, as:

$$Error_k(\vec{r}, t) = \bar{W}_{mean}(\vec{r}, t) - W_k(\vec{r}, t) = \frac{1}{N(t)} \left\{ \sum_{j=1}^{N(t)} \bar{W}_j(\vec{r}, t) + V(\vec{r}, \vec{r}_j[t]) \right\} - \bar{W}_k(\vec{r}, t), \quad (2.77)$$

that can be finally rewritten as:

$$Error_k(\vec{r}, t) = \frac{1}{N(t)} \sum_{j=1}^{N(t)} \left\{ (\bar{W}_j(\vec{r}, t) - \bar{W}_k(\vec{r}, t)) + V(\vec{r}, \vec{r}_j[t]) \right\} = V(\vec{r}, \vec{r}_k[t]), \quad (2.78)$$

where, according to (2.41), we have used the identity:

$$\bar{W}_j(\vec{r}, t) - \bar{W}_k(\vec{r}, t) = \sum_{\substack{i=1 \\ i \neq j}}^M V(\vec{r}, \vec{r}_i[t]) - \sum_{\substack{i=1 \\ i \neq k}}^M V(\vec{r}, \vec{r}_i[t]) = V(\vec{r}, \vec{r}_k[t]) - V(\vec{r}, \vec{r}_j[t]). \quad (2.79)$$

Expression (2.78) shows that $Error_k(\vec{r}, t) \rightarrow \infty$, when $\vec{r} \rightarrow \vec{r}_k[t]$. The mean-field approximation implies that the potential “felt” by the k -particle at $\vec{r} \rightarrow \vec{r}_k[t]$ is its own potential profile. In fact, from a numerical point of view, the use of the mean-field approximation is not so bad. For example, classical simulators uses 3D meshes with cell sizes of few nanometers, $DX \approx DY \approx DZ \gg 10 \text{ nm}$. Then, the error of the mean-field approximation is smaller than the technical error (i.e. mesh error) due to the finite size of the cells. The long range Coulomb interaction is well captured with the mean-field approximation, while this approximation is really bad strategy to capture the short range Coulomb interaction (see figure 2.5.5).

Finally, let me remark another important point about the mean-field approximation. Looking at the final expression (2.78), rewritten here as $W_k(\vec{r}, t) = \bar{W}_{mean}(\vec{r}, t) - V(\vec{r}, \vec{r}_k[t])$, it seems that $W_k(\vec{r}, t)$ can be computed from a unique mean-field solution of the Poisson equation $\bar{W}_{mean}(\vec{r}, t)$ when subtracting the appropriate two-particle potential $V(\vec{r}, \vec{r}_k[t])$. However, such a strategy is not as general as our procedure because it requires an analytical expression for the two-particle Coulomb interaction $V(\vec{r}, \vec{r}_k[t])$. The analytical expression of $V(\vec{r}, \vec{r}_k[t])$ written in expression (2.8) is only valid for scenarios with homogenous permittivity. On the contrary, our procedure with $N(t)$ electrostatic potentials computed from $N(t)$ different Poisson equations in a limited 3D volume Ω can be applied inside general scenario with (or without) spatial dependent permittivity.

2.5.2 Simulation of a two-electron system

I consider one electron (labeled as 1-electron) injected from the source surface, S_4 , at an arbitrary position. A second electron is injected, arbitrarily, from the drain surface, S_1 . A battery provides an external voltage equal to zero at the drain and source surface. A 3D cubic system with a volume of $\Omega = (20 \text{ nm})^3$ is considered as the active device region. We consider Silicon parameters for the numerical simulation. Within the mean-field approximation only the potential profile $\bar{W}_{mean}(\vec{r}, t)$ is calculated for the two electron system using expressions (2.72)-(2.75). Then, we realize from figure 2.5.1 that each electron can be reflected by an artificial alteration of the potential profile related to its own charge. In figures 2.5.2 and 2.5.3 we have plotted the energy potential profile “seen”

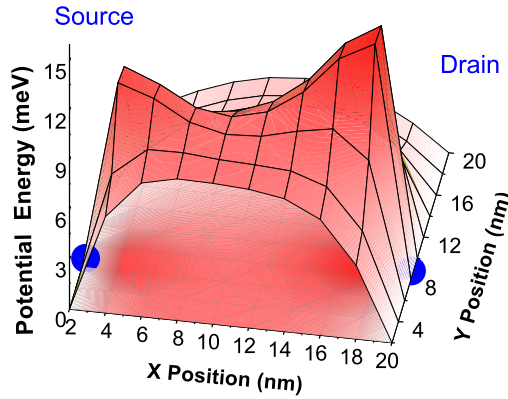


Figure 2.5.1: Potential energy profile $\bar{W}_{mean}(\vec{r}, t)$ computed with a 3D Poisson solver using the classical “mean-field” approximation on the plane X-Y of the active region $\Omega = (20 \text{ nm})^3$ at $z=6\text{nm}$ at 0.4 fs. The solid points are electron positions.

by the 1-electron, $\bar{W}_1(\vec{r}_1, t)$, and by the 2-electron, $\bar{W}_2(\vec{r}_2, t)$, using the many-particle algorithm described by expressions (2.60)-(2.63). Electrons are not affected by their own charge. We clearly see that, within the mean-field approximation, electrons can be unable to overcome the large potential barrier that appears at their own position (due to their own charge). In addition, the simple results confirm that the mean-field error is equal to expression (2.78), i.e. the error of the mean-field potential profile at each position of the active region is $Error_k(\vec{r}, t) = V(\vec{r}, \vec{r}_k[t])$. Finally, a discussion about the role of the spatial mesh used for the numerical solution of the Poisson equation is relevant. For an electron device with a length of hundreds of nanometers, we need a mesh of the 3D active region with spatial step $DX \sim DY \sim DZ > 10 \text{ nm}$ to deal with no more than one thousand nodes in the numerical solution of the Poisson equation. This

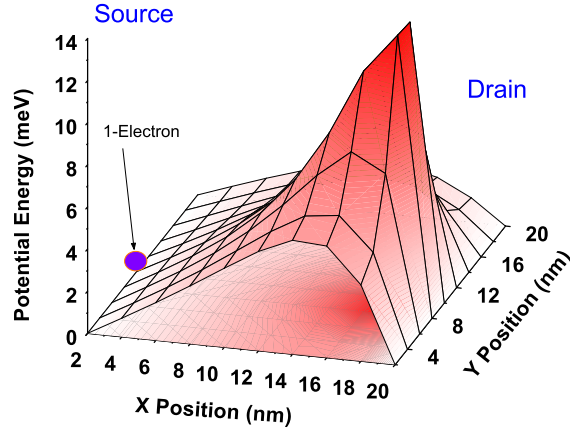


Figure 2.5.2: Potential energy profile of the 1-electron, $\bar{W}_1(\vec{r}_1, t)$, with the “many-electron” algorithm in the plane X-Y of the active region $\Omega = (20 \text{ nm})^3$ at $z=6\text{nm}$ at 0.4 fs. The solid point is the 1-electron position.

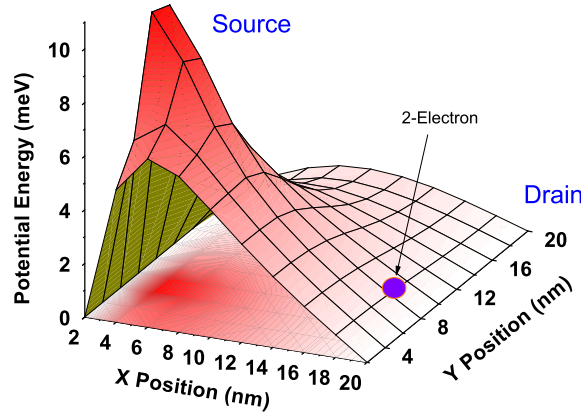


Figure 2.5.3: Potential energy profile of the 2-electron, $\bar{W}_2(\vec{r}_2, t)$, with the “many-electron” algorithm in the plane X-Y of the active region $\Omega = (20 \text{ nm})^3$ at $z=6\text{nm}$ at 0.4 fs. The solid point is the 1-electron position.

computational limitation in the resolution of the potential is present either when solving the mean-field or the many-electron algorithm. With such spatial resolution, the short-range interaction is missing in both procedures because two electrons inside the same spatial cell will not repel each other. In addition, the error between both procedures, $Error_k(\vec{r}, t) = V(\vec{r}, \vec{r}[t]_k)$, is reduced because the numerical Coulomb potential profile is smoothed due to the low resolution (i.e. the diameter of the region where $V(\vec{r}, \vec{r}[t]_k)$ has a strong influence is shorter than the cell dimensions). Therefore, we obtain roughly identical results with both schemes. In the subplots of figure 2.5.4, the same electron trajectory is presented for different mesh resolution. As can be seen, for the best mesh resolution ($DX = DY = DZ = 2 \text{ nm}$), the differences between both treatments are

maximized due to the important spurious auto-reflection effect found in the mean-field trajectory. On the other hand, as the resolution of our mesh is reduced, differences between both treatments disappear, giving roughly equal trajectories for cell dimensions above 5 nm. In summary, when the spatial cells are large, the mean-field and the many-

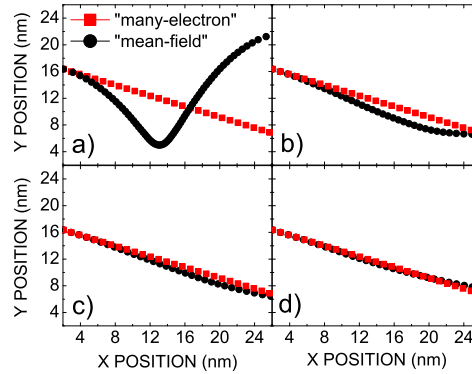


Figure 2.5.4: Electron trajectory computed with the “mean-field” (circles) and the “many-electron” (squares) algorithms for four different mesh resolutions. a) $DX = DY = DZ = 2 \text{ nm}$, b) $DX = DY = DZ = 4 \text{ nm}$, c) $DX = DY = DZ = 6 \text{ nm}$, and d) $DX = DY = DZ = 8 \text{ nm}$.

electron schemes correctly model the long-range Coulomb interaction, but both neglect the short-range component. On the contrary, with smaller spatial steps $DX \sim DY \sim DZ < 5 \text{ nm}$, the many-electron resolution takes into account long- and short- range Coulomb interaction correctly, whereas the description of the short-range component within the mean-field approximation is completely incorrect (i.e. electrons are repelled by themselves). In other words, when $DX, DY, DZ \rightarrow 0$ the mesh error in our many-electron algorithm reduces to zero, while the error in the mean-field approach tends to infinite, $Error_k(\vec{r}, t) \rightarrow \infty$. See a schematic summary of the explanation of this discussion in figure 2.5.5. Finally, it is important to remark that the electron trajectories

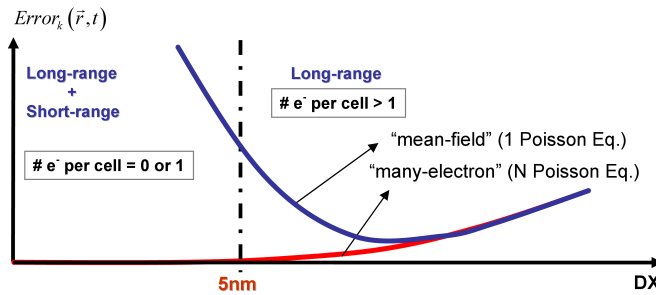


Figure 2.5.5: Schematic representation of the errors associated to mean-field and many-electron approaches as a function of the size of the discretization mesh.

in Fig. 2.5.4 are computed using the classical scheme of section 2.4.1, but the electrostatic potential profiles are computed from a 3D Poisson solver that is identical for the classical or quantum algorithms. Therefore, the conclusions drawn here for the classical algorithm can be directly extrapolated to our quantum algorithm. In the classical algorithm, the wrong potential profile of Fig. 2.5.1 affects the electric field [equations 2.56] that modifies the electron dynamics. Identically, the wrong "mean-field" potential in expression (2.68) will affect the solution of the Schrödinger equation that will modify Bohm trajectories (2.71).

CHAPTER 3

The prediction of measurable results

As I have pointed out several times along this dissertation, the exact many-body state of the system *can not* be solved. Nonetheless, from a pragmatic point of view, the knowledge of the exact microstate of the system is not useful by itself. What is really usable is to predict measurable properties such as the electrical current flowing through a particular nanostructure.

In the first section of this chapter I will argue that the kind of information extracted from our simulations that can be ultimately associated to real measurement results is that of expectation (or average) values. In section 3.2 I will discuss the definition of expectation values for classical and quantum open systems. Finally, in sections 3.3 and 3.4 I will focus on two particularly important observable measurements, that of the electrical current and that of the electric power consumption.

3.1 Observable results from stochastic simulations

It is important to recall here that the theoretical study of electron transport ultimately constitutes an statistical problem. Due to computational limitations, we have been forced to reduce the degrees of freedom of our system. Since we can only describe a very reduced number of variables in a very reduced region of space (an open system representing the active region of an electron device), we are obliged to deal with an essentially uncertain environment (see the discussion in section 1.2.2). In particular, although electron dynamics within our open system is *deterministically* described by the many-particle Hamiltonian (2.38) supplied with the Hamilton-Jacobi equations (2.56) for classical systems and the pseudo-Schrödinger equations in (2.68) for quantum systems, our simulations are subject to an *stochastic injection* of electrons describing how (i.e. in which position, time and momentum) electrons enter the simulated region, or equivalently, how are those electrons outside the open system distributed in phase space. Certainly, this is an information that can be known, at best, statistically, i.e. according to the Fermi-Dirac statistics (the reader

is referred to section 2.3 and Appendix B for a detailed discussion on this point). The injection process, is then the responsible of coupling an statistical *external* environment to our “deterministic” simulation box, and thus, it is also one of the main responsables of converting the information that we have on the dynamics occurring inside the simulation region into something statistical¹ (see figure 3.1.1 for an schematic representation of this problem).

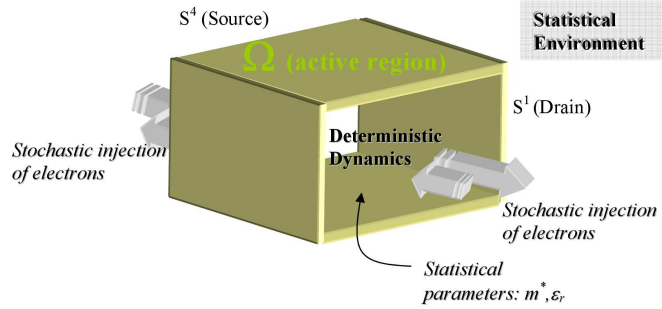


Figure 3.1.1: Schematic representation of the whole closed circuit available information. The statistical description of the simulation box environment is coupled to the deterministic description of the active region by an stochastic injection process.

Although the injection of electrons in the open system constitutes an essentially stochastic process, it is indeed capable of politely reproducing the probabilistic distribution of electrons in the spatial limits of the simulation box (see section 2.3 and Appendix B). Therefore, although we are not capable of describing at every single time which is the real microstate occupied by our open system, we do are able to predict the probability that our system occupies a particular microstate. In other words, although we cannot reproduce the result of a single *measurement* (associated to a particular microstate of the system), we can reproduce the probability of measuring such a result, and hence, we can also predict the mean value of a long series of identical measurement results, i.e. its *expectation* value². Repeating several times the same simulation, we can elaborate a list of possible outcomes a_i , e.g. $\{a_5, a_1, a_{32}, a_1, \dots\}$, of an observable $A(t)$, with an occurrence probability $P(a_i, t)$. From these data we can then compute the expectation value of the observable $A(t)$ as:

$$\langle A(t) \rangle = \sum_{i=1}^{\infty} a_i P(a_i, t). \quad (3.1)$$

¹The injection process is also the responsible of converting our open system into an irreversible system. Irreversibility of physical process is related to loss or transfer of information during time evolution from the system whose dynamics we are interested in to other degrees of freedom, that either we choose not to consider, or their number is so large that it is practically impossible to follow each and every one of them in time.

²In practice, since we simulate a single open system and we let it evolve in time, then, at time t we will deal with a single possible microstate of the system. Such a microstate is not able to give us information about the result of a real measurement.

This is the standard (either classical or quantum) definition of the expectation value of an observable measurement $A(t)$, and represents the kind of information that we can obtain from our electron transport approaches. The previous discussion is valid for both classical and quantum systems, however, when dealing with quantum systems there is an additional source of statistical uncertainty associated to the wave nature of the carriers (see section 3.2.3 for an extended discussion on this point).

In conclusion, the price that we have to pay for the reduction of the degrees of freedom is that we do not deal anymore with a *pure* many-particle microstate, but with a *mixed* many-particle microstate (the reader can find an extensive discussion on this point in Appendix C), and therefore, only that information referring to expectation values has to do with real measurable results. In the next sections I will extend the previous discussion for both classical and quantum open systems, focusing on the practical computation of expression (3.1).

3.2 Expectation values from stochastic simulations

3.2.1 The measurement as a detection of pointer positions

Clearly, in all measurements, we are not directly measuring the outcomes a_i but the position of a pointer. These data are, indeed, of a very simple nature. Usually the value of a_i can be ascribed to a detector pointer described by the positions of the particles conforming it, $\vec{r}_p[t] = \vec{r}_{p1}[t], \dots, \vec{r}_{pN}[t]$. Hence, the measurement of any magnitude is a position measurement. In this regard, the outcomes of an observable A can be always defined as a function, f_A , of the pointer positions, i.e. $f_A(\vec{r}_p[t])$. In particular, expression (3.1) can be also written as

$$\begin{aligned} \langle A(t) \rangle &= \sum_{i=1}^{\infty} a_i P(a_i, t) \\ &= \sum_{i=1}^{\infty} f_A(\vec{r}_{p,i}[t]) \cdot P(\vec{r}_{p,i}[t]), \end{aligned} \quad (3.2)$$

where $f_A(\vec{r}_{p,i}[t]) = a_i$, $\vec{r}_{p,i}[t] = \{\vec{r}_{p1,i}[t], \dots, \vec{r}_{pN,i}[t]\}$, and $P(\vec{r}_{p,i}[t]) = P(a_i, t)$. As I will show in brief, the position vectors $\vec{r}_{p,i}[t]$ can refer either to classical or quantum trajectories.

Although the previous affirmation could seem quite obvious when dealing with classical systems, as I will discuss in section 3.2.3, it is certainly a delicate issue when we discuss the measurement process within its “orthodox” formulation of quantum mechanics (i.e. the problem of the wave function collapse). Bell expressed this point in this way:

In physics the only observations we must consider are position observations, if only the positions of instrument pointers. It is a great merit of the de Broglie-Bohm picture to force us to consider this fact. If you make axioms, rather than definitions and theorems, about the “measurement” of anything else, then you commit redundancy and risk inconsistency. — John S. Bell (1987) [124].

In any case, in practical situations, accounting for the degrees of freedom of the pointer would force us to include the whole measuring apparatus, the battery and the wires into our simulations. Obviously, this is computationally unviable, and hence, we should be capable of finding a function, f'_A , relating the simulated degrees of freedom of the open system, i.e. $\{\vec{r}_1, \dots, \vec{r}_{N(t)}\}$, and the measured quantities a_i . In Appendix C I will discuss in detail how the probabilities appearing in expression (3.2) can be formally rewritten in terms of the simulated degrees of freedom and the function f'_A (for both classical and quantum systems). In the rest of this section I will explain how we can compute, in practice, the expectation value of a particular observable $A(t)$ departing from the supposition that we already know the function f'_A . In sections 3.3 and 3.4 I will provide a reasonable definition of f'_A when measuring the electrical current and power.

3.2.2 The classical expectation value of an observable result

The uncertainty associated to the electrons entering the simulation box can be practically represented by an h -ensemble of different electron characteristics. As I have already noticed, such an uncertainty, $h = 1, \dots, H$, is partially related to the lack of information we have on the energies, positions and injection times of the electrons at the borders of the simulation box.

Now, the practical procedure to compute the expectation value of the observable A at time t_1 is the following. At $t = 0$, we select a particular realization of the h -uncertainty. Then, we solve the (many-particle) Hamilton-Jacobi equations (2.56b) and (2.56b) from time $t = 0$ till $t = t_1$. Next, we compute the values $a_h(t_1)$ as

$$a_h(t_1) = A'_f(\vec{r}_{1,h}[t_1], \dots, \vec{r}_{N(t),h}[t_1]). \quad (3.3)$$

After that, we repeat the previous procedure for $h = 1, \dots, \infty$. The expectation value or the ensemble average of the observable A at time t_1 can be then computed as:

$$\langle A(t_1) \rangle = \lim_{H \rightarrow \infty} \frac{1}{H} \sum_{h=1}^H a_h(t_1). \quad (3.4)$$

The probability of each element of the h -ensemble is $1/H$.

For a stationary process, the mean value (3.4) is independent of time. Then, if the process is ergodic, we can compute the expectation value of A from the next time average expression:

$$\overline{a_h(t)} = \lim_{T \rightarrow \infty} \frac{1}{T} \int_{-T/2}^{T/2} a_h(t) dt \quad (3.5)$$

In this case, the practical procedure for the computation of the mean value of the

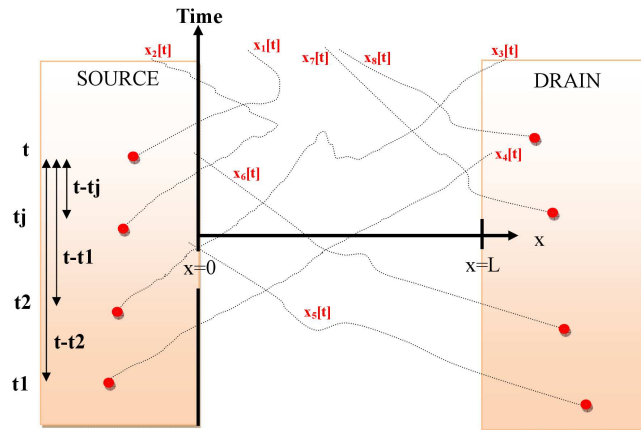


Figure 3.2.1: Schematic representation of the simulation box for a particular selection of classical trajectories during an infinite time.

observable A is the following. Before beginning the simulation, we select a particular realization of the whole h -uncertainty for an “infinite” number of electrons, that is the one of a whole closed circuit, i.e. $\{\vec{r}_{1,h}, \dots, \vec{r}_{M,h}, t_0\}$ (with M the total number of unbounded electrons in the whole circuit). In figure 3.2.1 I have represented an scheme of the simulation box in position and time. A single sample function will often provide little information about the statistics of the process. However, if the process is ergodic, that is, time averages equal ensemble averages³, then all statistical information can be derived from just one sample function.

3.2.3 The quantum expectation value of an observable result

The use of quantum mechanics is certainly a delicate issue when discussing the measurement process. In this regard, let me first introduce the measurement problem of quantum mechanics.

A measurement performed on a quantum system with a pure wave function, typically yields a random result. However, the quantum dynamics governing the evolution of the wave function over time, at least when no measurement is being performed, given by

³The trajectory of a representative point in the phase-space traverses, during a time evolution, any neighborhood of any relevant point of the phase space.

the Schrödinger's equation, is completely deterministic. Thus, insofar as the particular physical processes which we call measurements are governed by the same fundamental physical laws that govern all other processes, one is naturally led to the hypothesis that the origin of the randomness in the results of quantum measurements lies in random initial conditions, in our ignorance of the complete description of the system of interest of which we know only the wave function.

The measurement problem, however, is often expressed a little differently in the context of orthodox quantum mechanics. Textbook on quantum theory provides two rules for the evolution of the wave function of a quantum system: A deterministic dynamics given by Schrödinger's equation for when the system is not being "measured" or observed, and a random collapse of the wave function to an eigenstate of the "measured observable" for when it is^{4,5}. In short, the measurement problem of the orthodox formulation of quantum mechanics is this:

It would seem that the theory [quantum mechanics] is exclusively concerned about "results of measurement", and has nothing to say about anything else. What exactly qualifies some physical systems to play the role of "measurer"? Was the wavefunction of the world waiting to jump for thousands of millions of years until a single-celled living creature appeared? Or did it have to wait a little longer, for some better qualified system ... with a Ph.D.? If the theory is to apply to anything but highly idealized laboratory operations, are we not obliged to admit that more or less "measurement-like" processes are going on more or less all the time, more or less everywhere. Do we not have jumping then all the time? — John S. Bell (1987) [124].

From these considerations Bell has drawn the conclusion that we have only two possibilities. Either we add something to the wave function for the description of the state of the system or we modify the Schrödinger equation⁶. The former solution given by Bell fits perfectly with Bohmian mechanics, which in order to wholly describe a system adds

⁴According to orthodox quantum theory, the wave function of any individual system provides a complete description of that system.

⁵John Bell emphasized several times that the 'orthodox' formulation of the quantum theory is unprofessional. It does not explain with accuracy which parts of the whole quantum system forms the measurement apparatus and which the quantum system itself, or wheatear the measurement process requires some kind of human action or not.

⁶The allure of wave function monism (monism means here that the complete description of a system is provided by only its wave function) is so strong that some solutions to the orthodox measurement problem in fact involve the abrogation of Schrödinger's equation. There have been several recent proposals [125–129] suggesting explicitly that the quantum evolution is not of universal validity, that under suitable conditions, encompassing those which prevail during measurements, the evolution of the wave function is not governed by Schrödinger's equation. A common suggestion is that the quantum dynamics should be replaced by some sort of "nonlinear" (possibly nondeterministic) modification, to which, on the microscopic level, it is but an extremely good approximation. One of the most concrete proposals along these lines is that of Ghirardi, Rimini, and Weber [129].

the configuration space, i.e. the position of the particles are guided by the wave function (see Appendix A).

Next, I introduce the quantum expectation value of an observable in terms of Bohmian mechanics. The reader can find a particular deduction of this formulation, departing from the orthodox definition of an expectation value, in Appendix C.

The quantum expectation value of an observable result in terms of bohmian trajectories

Contrarily to orthodox quantum mechanics, the Bohmian formulation of quantum mechanics states that an observable is finally measured by an apparatus that provides a relationship between the value of a particular outcome of the observable and the position of a pointer (just as in classical mechanics). The very relevant point of the Bohmian measurement process is that it emphasizes that what we have ultimately “measured” is the position of the pointer, not the observable itself. In this regard, if we are able to find a function f'_A relating the position of the simulated bohmian trajectories (in the open system) and the positions of the pointer \vec{r}_p , then we can also compute its expectation value in terms of theses trajectories.

As I have already announced, the addition of the wave nature of the electron introduces an additional source of uncertainty in the classical definition of the expectation value, i.e. in quantum open systems there exists two types of uncertainty. One is shared with classical systems, and another one belongs exclusively to quantum systems. The former is ultimately related with the characteristics of the electrons injected into the simulation box and, as in the classical case, I will use the subindex h to refer to it. The second uncertainty, has a pure quantum mechanical origin, and it can be ultimately related with the initial positions of Bohmian trajectories. In the predictions of Bohmian mechanics concerning the result of a quantum experiment, it is assumed that, prior to the experiment, the positions of the particles involved in the system are randomly distributed according to Born’s statistical law. In this sense, according to the quantum equilibrium hypothesis (see expressions (A.14) in Appendix A and (C.14) in Appendix C), we know that there exists an ensemble $g = 1, \dots, G$ of possible distributions of Bohmian initial positions that exactly reproduce the modulus of the wave function at any time.

Therefore, similarly to its classical counterpart, the practical procedure to compute the quantum expectation value of an observable A is the following. At $t = 0$, we select a particular realization of the h -uncertainty and a particular realization of the g -uncertainty. Then, we solve the (many-particle) pseudo-Schrödinger equations (2.68) from time $t = 0$ till $t = t_1$. Next, for each particular observable A , we compute the values $a_{g,h}(t_1)$ as

$$a_{g,h}(t_1) = f'_A(\vec{r}_{1,h,g}[t_1], \dots, \vec{r}_{N(t),h,g}[t_1]). \quad (3.6)$$

Finally, we repeat the procedure for $g = 1, \dots, \infty$ and $h = 1, \dots, \infty$, and after that, the expectation value or the ensemble average of A at time t_1 can be computed as:

$$\langle A(t_1) \rangle = \lim_{G, H \rightarrow \infty} \frac{1}{GH} \sum_{h=1}^H \sum_{g=1}^G a_{g,h}(t_1) \quad (3.7)$$

The probability of each element of the g -ensemble is $1/G$. Identically, the probability of each h -element is also $1/H$.

Again, for a stationary process, the mean value (3.18) is independent of time. Then, if the process is ergodic, we can compute the expectation value of A from the next time average expression:

$$\overline{a_{g,h}(t)} = \lim_{T \rightarrow \infty} \frac{1}{T} \int_{-T/2}^{T/2} A_{g,h}(t) dt. \quad (3.8)$$

In this case, the practical procedure for the computation of the mean value of the observable is the following. Before beginning the simulation, we select a particular realization of the h -uncertainty for an “infinite” number of electrons, that is the one of a whole closed circuit, i.e. $\{\vec{r}_{1,h,g}, \dots, \vec{r}_{M,h,g}, t_0\}$ (with M the total number of unbounded electrons in the whole circuit). Simultaneously, we fix the “quantum” g -uncertainty of this particular realization (see figure 3.2.2 where I have represented an scheme of the simulation box in position and time). Again, a single sample function will often provide little information about the statistics of the process. However, if the process is ergodic, then all statistical information can be derived from just one sample function.

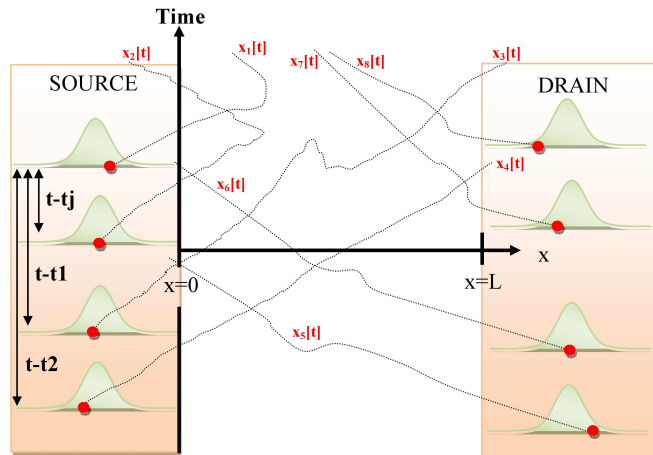


Figure 3.2.2: Schematic representation of the simulation box for a particular selection of wave-packets and Bohmian trajectories during an infinite time.

In summary, the ability of Bohmian mechanics to predict measurable results without invoking the wavefunction collapse resides in the fact that the measured quantity de-

pend, ultimately, on the distribution of positions of a set of Bohmain particles. Roughly speaking, we avoid collapsing the wavefunction to a particular position $\vec{r}[t]$ at time t because we have already “collapsed” it to $\vec{r}[t_0]$ at the initial time t_0 .

3.3 Computation of the electrical current

The functionality of any electronic device is determined by the relationship between the current measured by an ammeter and the voltage imposed at the external battery. See Fig. 3.3.1 for a description of the whole circuit that will support most of our explanations in this section. The current $I(t)$ is experimentally measured by an ammeter located far

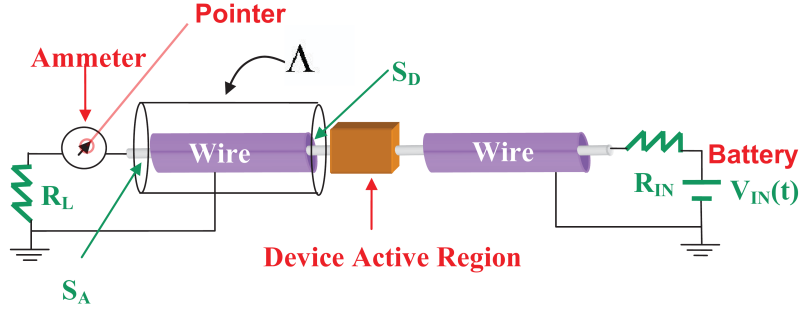


Figure 3.3.1: Schematic representation of the current measurement in an electron device. Device simulators compute the current in the surface, S_D , of the device active region, while the ammeter measures the current in the surface, S_A .

from the device active region using, for example, the magnetic deflection of a pointer⁷. We define, as in the previous section, $\vec{r}_p = \vec{r}_{p1}, \dots, \vec{r}_{pN}$ as those positions of the particles forming the pointer that completely specify its spatial location. In principle, if one solves the many-particle Hamiltonian (with classical or quantum trajectories) of the whole circuit including the measuring apparatus, the exact microstate of the system can be exactly known at every time t . Then, each possible experimental value of the current $I(t)$ is related to a particular distribution of the particles of the “pointer” at time t .

Unfortunately, the huge number of variables contained in the Hamiltonian make its solution through the many-particle Hamiltonian untractable. Instead of trying to describe a whole *closed* circuit, we have been forced to drastically reduce the number of degrees of freedom being simulated. In particular, we can only describe electron dynamics in the active region of an electron device. The elimination of all the degrees of freedom of the wire, the battery and the ammeter can seem surprising. At the end of the day, we will compare our predictions for $I(t)$ with the current measured experimentally at the

⁷A current passing through a coil in a magnetic field causes the coil to move. The position of a ‘pointer’ fixed to this coil will indicate the value of the current.

ammeter, not at the device active region. Therefore, if we eliminate the “pointer” of the ammeter from the set of simulated degrees of freedom, we need another definition of the current $I(t)$, based on the position of the simulated electron trajectories. In the next subsection I will provide a reasonable expression for such a function.

3.3.1 The relationship between currents on the ammeter and on the active region surfaces

Let us assume that we deal with a particular h -element and g -element of the Bohmian trajectories of the circuit (if we deal with a classical systems we just remove the subindex g in the next argumentation). We will keep the subindexes g and h to remind this point. Next, we show that the current $I_{S_A,g,h}(t)$ crossing a surface of the ammeter, S_A , drawn in Fig. 3.3.1 can be related to the current $I_{S_D,g,h}(t)$ on the surface of the device active region, S_D ⁸. We will provide this demonstration without simulating explicitly the dynamics of the Bohmian trajectories, but assuming that they fulfill Maxwell equations. Let us start by rewriting the current conservation in any point along the wire:

$$\vec{\nabla} \cdot \vec{j}_{c,g,h}(\vec{r}, t) + \frac{\partial \rho_{g,h}(\vec{r}, t)}{\partial t} = 0. \quad (3.9)$$

The first term of Eq. (3.9) is the divergence of the conduction current density, $\vec{j}_{c,g,h}(\vec{r}, t)$, while the other is the temporal variations of electron charge density $\rho_{g,h}(\vec{r}, t)$. The second term can be related to the electric field, $\vec{E}_{g,h}(\vec{r}, t)$, by using the Poisson (i.e. first Maxwell) equation:

$$\vec{\nabla} \cdot \left(\varepsilon(\vec{r}) \vec{E}_{g,h}(\vec{r}, t) \right) = \rho_{g,h}(\vec{r}, t), \quad (3.10)$$

where the electric permittivity, $\varepsilon(\vec{r})$, is assumed to be a time-independent scalar function. Thus, we can rewrite Eq. (3.9) as:

$$\vec{\nabla} \cdot \vec{j}_{c,g,h}(\vec{r}, t) + \vec{\nabla} \cdot \left(\varepsilon(\vec{r}) \frac{\partial \vec{E}_{g,h}(\vec{r}, t)}{\partial t} \right) = \vec{\nabla} \cdot \left(\vec{j}_{c,g,h}(\vec{r}, t) + \vec{j}_{d,g,h}(\vec{r}, t) \right) = 0. \quad (3.11)$$

where the displacement current density is $\vec{j}_{d,g,h}(\vec{r}, t) = \varepsilon(\vec{r}) \frac{\partial \vec{E}_{g,h}(\vec{r}, t)}{\partial t}$. From equation (3.11), we can define the total current $\vec{j}_{T,g,h}(\vec{r}, t) = \vec{j}_{c,g,h}(\vec{r}, t) + \vec{j}_{d,g,h}(\vec{r}, t)$ as a divergence free vector. Finally, we arrive to the following identity for the total currents:

$$\int_{\Lambda} \vec{\nabla} \cdot \vec{j}_{T,g,h}(\vec{r}, t) d\Lambda = \int_S \vec{j}_{T,g,h}(\vec{r}, t) d\vec{s} = 0, \quad (3.12)$$

⁸In principle, we do also need a demonstration that the current $I_g(t)$ indicated by the “pointer” positions can be related with the current crossing a surface of the ammeter, S_A . We avoid the explicit demonstration, which will follow the identical steps done in this section.

where the first integral is evaluated inside an arbitrary volume Λ and the second integral over the closed surface S limiting this volume Λ drawn in Fig. 3.3.1. The surface S is composed of the ammeter surface, S_A , the device surface, S_D and a lateral cylindrical surface. We assume that this lateral surface is so far away from the metallic wire, so that the electric field there is almost zero and there are no particles crossing it⁹. Thus, the integral surface of the right hand side of expression (3.12) can be rewritten as:

$$\int_{S_D} \vec{j}_{T,g,h}(\vec{r}, t) d\vec{s} + \int_{S_A} \vec{j}_{T,g,h}(\vec{r}, t) d\vec{s} = 0 \quad (3.13)$$

Expression (3.13) tells us that $I_{S_A,g,h}(t) = -I(t)_{S_D,g,h}$. There is an irrelevant sign related with the direction of the vector $d\vec{s}$. In conclusion, the current measured on the surface of an ammeter is equal to the current measured on a surface of the simulation box.

3.3.2 The relationship between the current on the active region surfaces and the simulated trajectories

Now, we determine the function f'_A between the positions of the open system trajectories $\{\vec{r}_{1,k,g}[t], \dots, \vec{r}_{N(t),k,g}[t]\}$ and the value of the current $I_{S_D,h,g}(t)$ measured on the surface S_D (recall that for recovering a classical explanation we just have to erase the subindex g in what follows).

I will discuss the charge associated with the conduction and displacement components of the total current. From the continuity equation 3.9 that accomplishes the simulated trajectories, we conclude that:

$$\int_{S_D} \vec{j}_{c,g,h}(x_D, y, z, t) d\vec{s} = \frac{d}{dt} \int_{S_D} \int_{x=-\infty}^{x=x_D} \rho_{g,h}(x, y, z, t) dx dy dz \quad (3.14)$$

We have defined x_D as the x-position of the S_D surface. In principle, we know that the density of particles at time t in the whole circuit can be written as $\rho_{g,h}(r, t) = \sum_{i=1}^{M_P} \delta(\vec{r} - \vec{r}_{i,g,h}[t])$. Then, we can define the conduction charge as:

$$Q_{c,g,h}(t) = \int_{S_D} d\vec{s} \int_{x=-\infty}^{x_D} dx \sum_{i=1}^M \delta(\vec{r} - \vec{r}_{i,g,h}[t]) = q \left(\sum_{i=1}^M u(x_{i,g,h}[t] - x_D) \right) \quad (3.15)$$

where the unit step function (Heaviside) is $u(\xi) = 1$ when $\xi > 0$ and zero elsewhere and the number of particles M accounts for all the unbounded electrons in the whole circuit.

⁹In fact, the relevant point is not only that the lateral surface is far away from the wire, but also that the difference between the relative dielectric constants in the wire and in the air tends to concentrate the electromagnetic field inside the wire

In addition, we know that the displacement current is defined as $\vec{j}_{d,g,h}(\vec{r}, t) = \varepsilon(\vec{r}) \frac{\partial \vec{E}_{g,h}(\vec{r}, t)}{\partial t}$. Therefore, we can interpret the displacement charge, as:

$$Q_{d,g,h}(t) = \int_{S_D} d\vec{s} \varepsilon(\vec{r}) \vec{E}_{g,h}(x_D, y, z, t) \quad (3.16)$$

The electric field, $\vec{E}_{g,h}(x_D, y, z, t)$ depends directly on the position of the simulated particles and the boundary conditions on the borders of our simulation box. Finally, we can interpret one particular outcomes of the total current measured by an ammeter, $I_{g,h}(t)$, as the time-derivative of the conduction plus displacement charge:

$$I_{S_D g,h}(t) = \frac{d(Q_{c,g,h}(t) + Q_{d,g,h}(t))}{dt}. \quad (3.17)$$

Notice that the title of this subsection makes reference to find a relationship between the current on the active region surfaces and the *simulated* trajectories. From the definition of the conduction charge (Eq. (3.15)), however, it could seem that what we have done is finding a relation between the trajectories (simulated and non-simulated) of the whole circuit and the current on the active region surfaces. Fortunately, the time derivative of this quantity appearing in (3.17), can be computed by simply counting the number of trajectories (all of them simulated) crossing the surface S_D [130].

In conclusion, we have found a function between one particular set of trajectories $\vec{r}_{1,h,g}[t], \dots, \vec{r}_{N(t),h,g}[t]$ and the charge $Q_{c,h,g}(t) + Q_{d,h,g}(t)$. According to expression 3.13, hereafter, we simplify our notation $I_{S_D,h,g}(t) = I_{h,g}(t)$.

3.3.3 The practical computation of DC, AC and transient currents

As discussed in subsections 3.2.2 and 3.2.3, when dealing with an open simulation box, the measured observables need one subindex for each of the two sources of uncertainty, h and g (only the subindex h when dealing with classical systems). We can determine the average value of the current at time t_1 (or the expectation value, or the mean, or the first moment) from the following ensemble average:

$$\langle I(t_1) \rangle = \lim_{G,H \rightarrow \infty} \frac{1}{GH} \sum_{g=1}^G \sum_{h=1}^H I_{g,h}(t_1) \quad (3.18)$$

As we have discussed, the probability of each element of the g -ensemble is $1/G$. Identically, the probability of each h -element is also $1/H$.

When the battery of Fig. 3.3.1 is fixed to a constant value, then, the whole circuit becomes stationary. This is the DC measurement of the current. Now, for a stationary

process, the classical mean current computed from (3.18) is independent of time. Then, if the process is ergodic, we can compute the mean current from the a time average expression:

$$\overline{I_h(t)} = \lim_{T \rightarrow \infty} \frac{1}{T} \int_{-T/2}^{T/2} I_h(t) dt. \quad (3.19)$$

Equivalently, for quantum systems, we can compute the mean current from the (first-order) time average expression:

$$\overline{I_{g,h}(t)} = \lim_{T \rightarrow \infty} \frac{1}{T} \int_{-T/2}^{T/2} I_{g,h}(t) dt. \quad (3.20)$$

Electrical engineers are not only interested in the DC behavior of nanoelectronic devices, but also in their transient or AC performance. For these time-dependent scenarios, the circuit is no longer neither stationary nor ergodic. Then, we cannot use ergodicity and we have to compute the mean value of the current at each particular time, t_1 , only from the ensemble average in (3.18).

3.3.4 The computation of the current fluctuations for a stationary and ergodic system

When we measure experimentally the current, we found a randomly varying function of time, not a constant value. We named these fluctuations of the current as noise. The characterization of the noise is a extremely important issue in electronics to understand how to avoid it in practical applications. In addition, from a physical point of view, there is a lot of useful information in the noise that is missing (because of the average) in the mean values discussed above. Before writing the mathematical expression for the practical evaluation of noise, we provide a brief summary of noise features in electronics that will be useful latter to discuss the noise results.

The thermal and shot noises

Noise in electronic devices can be understood as a consequence of uncertainties in the electron transport process. Theoretical approaches to analyze and model noise in semiconductor devices are carried out using stochastic calculus and microscopic noise sources (see for example [131] for a semi-classical treatment of noise in semiconductor devices).

There are two fundamental sources of noise in nanostructures, the thermal and the shot noise. The former is at non-zero temperature where the thermal agitation causes the occupation number of the state to fluctuate. Typically, we can characterize the presence or not of an electron in a particular region of phase-space by the occupation number n which is either zero or one, at each particular time. In simple scenarios, the average of

the occupation number $\langle n \rangle$ is determined by the Fermi distribution function f and we have simply $\langle n \rangle = f$. At equilibrium the probability that a state is empty is on the average given by $1 - f$, and occupied is on the average given by f . Taking into account that $n^2 = n$, we find immediately that the fluctuations of the occupation number are given by:

$$\langle (n - \langle n \rangle)^2 \rangle = f(1 - f) \quad (3.21)$$

At high temperatures and high enough energies f is much smaller than one and thus the factor $1 - f$ in Eq. (3.21) can be replaced by 1. Thus the fluctuations are determined by the Boltzmann distribution.

The latter noise source, namely the shot noise, can be explained with the simple case of a flux of particle incident upon a barrier. At the barrier the particle is either transmitted with probability T or reflected with probability $R = 1 - T$ (not both!). We now only consider the transmitted state characterized by the occupation numbers n_T and its average value simply given by $\langle n_T \rangle = T$. To find the mean squared fluctuations in the transmitted state, we consider the average of the product of the occupation numbers of the transmitted and reflected beam $\langle n_T(1 - n_T) \rangle$. Since in each event the particle is either transmitted or reflected, the product $n_T(1 - n_T)$ vanishes. Notice that this mechanism is essentially the particle nature of the charge as anticipated above. Hence the average $\langle n_T(1 - n_T) \rangle$ vanishes also and we find easily:

$$\langle (n_T - \langle n_T \rangle)^2 \rangle = T(1 - T) \quad (3.22)$$

Such fluctuations are called *partition noise* since the scatterer divides the incident carrier stream into two streams.

Both the thermal and shot noise at low frequencies and low voltages reflect in many situations independent quasi-particle transport. Electrons are, however, interacting entities and both the fluctuations at finite frequencies and the fluctuation properties far from equilibrium require in general a discussion of the role of the Coulomb interaction. A quasi-particle picture is no longer sufficient and collective properties of the electron system come into play. Moreover, for finite frequency the electrodynamics (Maxwell equations) must be included. Please see the review of Blanter and Büttiker [11] as a guide for theoretical approach to noise in mesoscopic devices.

The practical compaction of current fluctuations

Now, we return to the practical expressions for the computation of the current fluctuations in nanoelectronic devices with trajectories. Since we directly know all possible measurable current values $I_{g,h}(t_1)$ and their probabilities $1/(GH)$, we can use standard

techniques for characterizing the fluctuations of the current (this is a very relevant advantage of using Bohmian mechanics to study electron transport).

The fluctuating signal of the current can be defined from $\Delta I_{g,h}(t) = I_{g,h}(t) - \langle I_{g,h}(t) \rangle$. We can obtain information of the noise from the variance (or the mean square or the second moment) defined as $\langle \Delta I(t)^2 \rangle = \langle I(t)^2 \rangle - \langle I(t) \rangle^2$. However, experimentalists are interested in having information on the distribution of noise at different frequencies¹⁰. Therefore, the characterization of fluctuations of the current, i.e. the noise, are computed from the covariance:

$$\langle \Delta I(t_1) \Delta I(t_2) \rangle = \lim_{g,h \rightarrow \infty} \frac{1}{GH} \sum_{g=1}^G \sum_{h=1}^H \Delta I_{g,h}(t_1) \Delta I_{g,h}(t_2) \quad (3.23)$$

If the process is ergodic, we can compute the noise equivalently from the autocorrelation function:

$$\overline{\Delta I(t) \Delta I(t + \tau)} = \lim_{T \rightarrow \infty} \frac{1}{T} \int_{-T/2}^{T/2} \Delta I_{g,h}(t) \Delta I_{g,h}(t + \tau) dt \quad (3.24)$$

We mention ergodicity of the correlation when $\langle \Delta I_{g,h}(t) \Delta I_{g,h}(t + \tau) \rangle = \overline{\Delta I_i(t) \Delta I_i(t + \tau)}$. In addition, a process is called wide-sense (or weakly) stationary if its mean value is constant and its autocorrelation function can be defined as:

$$R(\tau) = \overline{\Delta I(t) \Delta I(t + \tau)} \quad (3.25)$$

because it depends only on $\tau = t_2 - t_1$. Wide-sense stationary processes are important because the autocorrelation function 3.24 and the power spectral density function $S(f)$ (measured by experimentalists) form a Fourier transform pair:

$$S(f) = \int_{-\infty}^{\infty} R(\tau) e^{-j2\pi f\tau} d\tau \quad (3.26)$$

This is known as the Wiener-Khinchine theorem. In many systems, without correlations one obtains the well known Schottky's result [132] for the shot noise:

$$S_{shot}(f) = 2e \langle I \rangle \quad (3.27)$$

which is also referred to in literature as *Poissonian value* of shot noise.

Our ability to make a “continuous” measurement of the time-dependent current needs, perhaps, some additional explanation. When we have considered the elimination of the degrees of freedom associated to the battery, the wire and the ammeter and re-introduce

¹⁰Most of electronic apparatuses and the ammeter itself have to be interpreted as low-pass filters. Therefore, they are able to measure the noise up to a maximum frequency

them, somehow, by the boundary conditions in our simulation box and electron injection algorithm, we have also assumed that the simulated electrons of the active region have a significant influence on the degrees of freedom of the ammeter, \vec{r}_a , but the degrees of freedom of the ammeter have small (negligible) influence on the simulated particles. In the literature, this type of measurement is called “ideal” or “weak” measurement and they are also present in the orthodox interpretation of quantum mechanics¹¹. Under the “weak” measurement done by the ammeter, we can consider the measurement of the current of one particular sample at two different times.

3.4 Computation of the electrical power

Power consumption is one of the main drawbacks when scaling down any new technology [133, 134]. In the last few years, the electronic development is being driven not only by the desire of improving circuit density and speed but also of reducing power consumption. The ITRS has identified this last constraint as one of the top three overall challenges for the next 15 years [72]. In this sense, accuracy is a mandatory requirement when predicting electric power in the active region of a FET transistor because the results of the single transistor are then extrapolated to the large number of transistors in present-day CPUs. In this section I show that the formulation of the electric power in nanoscale open classical and quantum systems can not be reduced to the standard expression $I \cdot V$ when dealing with full Coulomb correlations. Only when taking the single-particle classical limit we recover the well known textbook expression.

In the next discussion I will eliminate again the “pointer” of the measuring apparatus from the set of simulated degrees of freedom. Then, we need a definition of the electrical power $P(t)$, based on the position of the simulated electron trajectories (both classical and quantum), i.e. we must find the function f'_p . Let me notice that if we could associate the electric power to the standard expression, $I \cdot V$, we would not have major problems when comparing our theoretical predictions with the results obtained with an experimental setup. In the previous section I discussed how to associate our predictions of electric current with the measure performed in an ammeter. It is not more difficult to associate the applied voltage V with the measure performed with a voltmeter. Unfortunately, if we take a look to expressions (3.44) and (3.46), which correspond to the electrical power

¹¹The type of measurement process with orthodox quantum mechanics first introduced to students is the so-called “strong” measurement. The measurement transforms “instantaneously” the wavepacket into one of the eigenstates of an operator. However, there are many measurements that do not fit with the (von Neumann) “strong” measurement. For example, when one illuminates an object and continually detects the reflected light in order to track the object motion, or when one sees the bubbles originated by electrically charged particles (coming from cosmic reactions) moving through a bubble chamber. The ‘orthodox’ theory itself has developed its own formal formalism to discuss these new type of continuous measurements named ‘weak’ measurements [125].

for quantum and classical open systems respectively, things seem much complicated. Nonetheless, as I will show, these expressions are reasonable. Moreover, the kinetic energy gained or loosed by electrons in the open system (consider for instance the active region of a particular electron device), which is directly related to the electric power $P(t)$, could be, in principle, related to other magnitudes such as thermal dissipation in the leads. In this regard, we should be able to measure the discrepancies between the standard $I \cdot V$ electric power and expressions (3.44) and (3.46).

In section 3.4.1 I will first deduce the expression of the electrical power and the energy conservation law in a simple closed system. Such expressions will be useful later, in subsection 3.4.2, in order to identify the proper expressions of the classical and quantum electric power for open systems. Although along the whole section I will use a quantum formulation of the problem in terms of Bohmian mechanics for a pure microstate of the system, when taking the expectation values of the electric power I will assume a summation over both the h - and g -uncertainties. Moreover, I will present the classical limit of the most relevant results. Finally, in 3.4.3 I will use the measurement theory discussed at the beginning of this chapter in order to recover the standard expectation value of the electric power, $I \cdot V$, for a single-particle classical system.

3.4.1 Expectation value of the energy in closed systems

Let me start with a closed system Hamiltonian such as the one described in (2.7). The 3-dimensional generalization of the quantum Hamilton-Jacobi equation, (A.36), deduced in Appendix A reads

$$\sum_{k=1}^M \left\{ \frac{\left(\vec{\nabla}_{r_k} S(\vec{r}_1, \dots, \vec{r}_M, t) \right)^2}{2m} + \frac{1}{2} \sum_{\substack{i=1 \\ i \neq k}}^M eV(\vec{r}_k, \vec{r}_i) + Q_k(\vec{r}_1, \dots, \vec{r}_M, t) \right\} + \frac{\partial S(\vec{r}_1, \dots, \vec{r}_M, t)}{\partial t} = 0. \quad (3.28)$$

Taking the gradient, $\vec{\nabla}_{r_j}$, of (3.28) and using the hydrodynamic derivative $\frac{d}{dt} = \sum_{i=1}^{M(t)} \dot{\vec{r}}_i \cdot \vec{\nabla}_{r_i} + \frac{\partial}{\partial t}$, we obtain the quantum analogous of the Newton's second law for many-particle systems

$$m\ddot{\vec{r}}_j[t] = -\frac{1}{2} \sum_{\substack{k=1 \\ k \neq j}}^M e\vec{\nabla}_j V(\vec{r}_k[t], \vec{r}_j) - \sum_{k=1}^M \vec{\nabla}_{r_j} Q_k(\vec{r}_1[t], \dots, \vec{r}_j, \dots, \vec{r}_M[t], t), \quad (3.29)$$

where the coordinates $\vec{r}_k[t]$ are now understood as quantum trajectories. In order to do not complicate the notation, however, from now on I will omit the explicit apparition of

[t].

The first term on the right side of (3.29) is just the Lorentz force in absence of magnetic fields. The second term represents the quantum force (the reader is referred to Appendix A for a brief discussion on its significance). Except for the quantum force, which is the ultimate source of quantum phenomena, equation (3.29) is identical to the classical Newton's second law for the j -th particle.

Taking now the product of (3.29) and $\dot{\vec{r}}_j$, and then summing over all j -th terms, we finally find:

$$P(t) = \sum_{j=1}^M \frac{d}{dt} \left(\frac{1}{2} m \dot{\vec{r}}_j^2 + Q_j(\vec{r}_1, \dots, \vec{r}_M, t) \right) = -\frac{1}{2} \sum_{j=1}^M \sum_{\substack{k=1 \\ k \neq j}}^M e \dot{\vec{r}}_j \vec{\nabla}_{\vec{r}_j} V(\vec{r}_k, \vec{r}_j) + \sum_{j=1}^M \frac{\partial Q_j(\vec{r}_1, \dots, \vec{r}_M, t)}{\partial t}. \quad (3.30)$$

The term in parenthesis on the left hand of (3.30) is the total quantum kinetic energy, K , (the many-particle generalization of expression A.32), i.e. $K = \sum_{j=1}^{N(t)} K_j = \sum_{j=1}^{N(t)} \left(\frac{1}{2} m \dot{\vec{r}}_j^2 + Q_j \right)$. Then, expression (3.30) can be identified with the electric power, if we realize that it leads to the energy conservation law. In order to see it, let me use again the hydrodynamic derivative to rearrange equation (3.30) and write

$$\sum_{j=1}^M \frac{d}{dt} \left(\frac{1}{2} m \dot{\vec{r}}_j^2 + \sum_{\substack{k=1 \\ k \neq j}}^M e V(\vec{r}_k, \vec{r}_j) + Q_j(\vec{r}_1, \dots, \vec{r}_M, t) \right) = \sum_{j=1}^M \frac{\partial Q_j(\vec{r}_1, \dots, \vec{r}_M, t)}{\partial t}. \quad (3.31)$$

Since we are dealing with a closed system, it can be demonstrate that the expectation value of $\frac{\partial Q_j}{\partial t}$ vanishes [135]:

$$\begin{aligned} \left\langle \frac{\partial Q_j}{\partial t} \right\rangle &= \int_{-\infty}^{+\infty} d^3 r R^2 \frac{\partial}{\partial t} \left(\frac{\vec{\nabla}_{\vec{r}_j}^2 R}{R} \right) \\ &= \int_{-\infty}^{+\infty} d^3 r \left(R \vec{\nabla}_{\vec{r}_j}^2 \frac{\partial R}{\partial t} - \frac{\partial R}{\partial t} \vec{\nabla}_{\vec{r}_j}^2 R \right) \\ &= \int_{-\infty}^{+\infty} d^3 r \vec{\nabla}_{\vec{r}_j} \left(R \vec{\nabla}_{\vec{r}_j} \frac{\partial R}{\partial t} - \frac{\partial R}{\partial t} \vec{\nabla}_{\vec{r}_j} R \right) \\ &= \int_{-\infty}^{+\infty} d^2 r \left(R \vec{\nabla}_{\vec{r}_j} \frac{\partial R}{\partial t} - \frac{\partial R}{\partial t} \vec{\nabla}_{\vec{r}_j} R \right) \\ &= 0, \end{aligned} \quad (3.32)$$

where in the last equality I have used the boundary condition $r^2 R \rightarrow 0$ as $\vec{r} \rightarrow \infty$.

Therefore, from (3.31) and (3.32) we can identify the total energy of the system, $\epsilon(t)$, with

$$\epsilon(t) = \sum_{j=1}^M \left(\frac{1}{2} m \dot{r}_j^2 + \sum_{\substack{k=1 \\ k \neq j}}^M eV(\vec{r}_k, \vec{r}_j) + Q_j(\vec{r}_1, \dots, \vec{r}_M, t) \right). \quad (3.33)$$

Thus, the conservation law for the total energy of our closed system in terms of Bohmian mechanics reads

$$\left\langle \frac{d\epsilon(t)}{dt} \right\rangle = \sum_{j=1}^M \left\langle \frac{d}{dt} \left(\frac{1}{2} m \dot{r}_j^2 + \sum_{\substack{k=1 \\ k \neq j}}^M eV(\vec{r}_k, \vec{r}_j) + Q_j(\vec{r}_1, \dots, \vec{r}_M, t) \right) \right\rangle = 0. \quad (3.34)$$

The last term on the right hand of equation (3.30) can be interpreted as the quantum deviation from the classical electrical power, and from (3.32) we can conclude that it is both positive and negative. In other words, the system borrows energy or gives up energy per unit time to an unspecified source or sink, which is sometimes identified as the quantum field. The previous demonstration constitutes the generalization of the Donald H. Kobe's result presented for a single-particle system in Ref. [135].

From (3.34), if we let $Q \rightarrow 0$ we recover the energy conservation law for classical closed systems, i.e.

$$\left\langle \frac{d\epsilon_{class}}{dt} \right\rangle = \sum_{j=1}^M \left\langle \frac{d}{dt} \left(\frac{1}{2} m \dot{r}_j^2 + \sum_{\substack{k=1 \\ k \neq j}}^M eV(\vec{r}_k, \vec{r}_j) \right) \right\rangle = 0. \quad (3.35)$$

3.4.2 Expectation value of the energy and electric power in open systems

Let me now show what happens with the energy and the electric power when we open the previous system. Let me first recall the many-particle Schrödinger equation defined in equation 2.67, i.e.

$$i\hbar \frac{\partial \Phi(\vec{r}_1, \dots, \vec{r}_{N(t)}, t)}{\partial t} = \left\{ \sum_{k=1}^{N(t)} -\frac{\hbar^2}{2 \cdot m} \nabla_{\vec{r}_k}^2 + U(\vec{r}_1, \dots, \vec{r}_{N(t)}, t) \right\} \cdot \Phi(\vec{r}_1, \dots, \vec{r}_{N(t)}, t) \quad (3.36)$$

where

$$U(\vec{r}_1, \dots, \vec{r}_{N(t)}, t) = \sum_{k=1}^{N(t)} \left\{ e \cdot W_k(\vec{r}_1, \dots, \vec{r}_{N(t)}, t) - \frac{1}{2} \sum_{\substack{j=1 \\ j \neq k}}^{N(t)} e \cdot V(\vec{r}_k, \vec{r}_j) \right\}. \quad (3.37)$$

From (3.37), it can be deduced the next many-particle quantum Hamilton-Jacobi equation:

$$\sum_{k=1}^{N(t)} \left\{ \frac{\left(\vec{\nabla}_{r_k} S(\vec{r}_1, \dots, \vec{r}_{N(t)}, t) \right)^2}{2m_k} + U(\vec{r}_1, \dots, \vec{r}_{N(t)}, t) + Q_k(\vec{r}_1, \dots, \vec{r}_{N(t)}, t) \right\} + \frac{\partial S(\vec{r}_1, \dots, \vec{r}_{N(t)}, t)}{\partial t} = 0. \quad (3.38)$$

As in the previous subsection, taking the gradient, $\vec{\nabla}_{r_j}$, of expression (3.38) and using the hydrodynamic derivative, we obtain the quantum analogous of the Newton's second law for many-particle systems, but now for open systems:

$$m\ddot{\vec{r}}_j = -\vec{\nabla}_j U(\vec{r}_1, \dots, \vec{r}_{N(t)}, t) - \sum_{k=1}^{N(t)} \left(\vec{\nabla}_{r_j} Q_k(\vec{r}_1, \dots, \vec{r}_{N(t)}, t) \right). \quad (3.39)$$

We can now rewrite (3.39) as

$$m\ddot{\vec{r}}_j = -e\vec{\nabla}_{r_j} W_j(\vec{r}_1, \dots, \vec{r}_{N(t)}, t) - \sum_{k=1}^{N(t)} \left(\vec{\nabla}_{r_j} Q_k(\vec{r}_1, \dots, \vec{r}_{N(t)}, t) \right), \quad (3.40)$$

where I have omitted the second term on the right side of equation (3.37) using the same argument discussed in reference to equation (2.70). Except for the quantum force, equation (3.40) is again the classical Newton's second law. Taking now the product of (3.40) and $\dot{\vec{r}}_j$ and summing over the $N(t)$ particles conforming the open system, we find

$$\sum_{j=1}^{N(t)} \frac{d}{dt} \left(\frac{1}{2} m \dot{\vec{r}}_j^2 \right) = - \sum_{j=1}^{N(t)} \dot{\vec{r}}_j \vec{\nabla}_{r_j} W_j(\vec{r}_1, \dots, \vec{r}_{N(t)}, t) - \sum_{k=1}^{N(t)} \sum_{j=1}^{N(t)} \dot{\vec{r}}_j \vec{\nabla}_{r_j} Q_k(\vec{r}_1, \dots, \vec{r}_{N(t)}, t), \quad (3.41)$$

If we use once more the hydrodynamic derivative we can rearrange expression (3.41) to finally read

$$\frac{d}{dt} \sum_{j=1}^{N(t)} \left\{ \frac{1}{2} m \dot{\vec{r}}_j^2 + Q_j(\vec{r}_1, \dots, \vec{r}_{N(t)}, t) \right\} = \sum_{j=1}^{N(t)} \left(- \dot{\vec{r}}_j \vec{\nabla}_{r_j} W_j(\vec{r}_1, \dots, \vec{r}_{N(t)}, t) + \frac{\partial Q_j(\vec{r}_1, \dots, \vec{r}_{N(t)}, t)}{\partial t} \right). \quad (3.42)$$

The term in parenthesis on the left hand of (3.42) is again the total quantum kinetic energy, K . Therefore, we can identify the right hand of (3.42) as the quantum power,

$P(t)$, i.e.

$$P(t) = \sum_{j=1}^{N(t)} \frac{d}{dt} K_j = \sum_{j=1}^{N(t)} \left(-\dot{\vec{r}}_j \cdot \vec{\nabla}_{r_j} W_j(\vec{r}_1, \dots, \vec{r}_{N(t)}, t) + \frac{\partial Q_j(\vec{r}_1, \dots, \vec{r}_{N(t)}, t)}{\partial t} \right). \quad (3.43)$$

Taking the expectation value of (3.43) we find:

$$\langle P \rangle = \sum_{j=1}^{N(t)} \left\langle \frac{d}{dt} K_j \right\rangle = \sum_{j=1}^{N(t)} \left\langle -\dot{\vec{r}}_j \cdot \vec{\nabla}_{r_j} W_j(\vec{r}_1, \dots, \vec{r}_{N(t)}, t) + \frac{\partial Q_j(\vec{r}_1, \dots, \vec{r}_{N(t)}, t)}{\partial t} \right\rangle. \quad (3.44)$$

Contrarily to the previous closed case, now the expectation value of the time derivative of the quantum force, $\frac{\partial Q_j}{\partial t}$, does not vanish:

$$\begin{aligned} \left\langle \frac{\partial Q_j}{\partial t} \right\rangle &= \int_{\Omega} d^3 r R^2 \frac{\partial}{\partial t} \left(\frac{\vec{\nabla}_{r_j}^2 R}{R} \right) \\ &= \int_{-\infty}^{+\infty} d^2 r \left(R \vec{\nabla}_{r_j} \frac{\partial R}{\partial t} - \frac{\partial R}{\partial t} \vec{\nabla}_{r_j} R \right) \\ &\neq 0, \end{aligned} \quad (3.45)$$

where Ω is the volume of the active region (see figure 2.3.1). Since we are dealing now with an open system, we can not use anymore the boundary condition $\vec{r}^2 R \rightarrow 0$ as $\vec{r} \rightarrow \infty$ for the two opened surfaces.

We can probably better recognize the classical limit of expression (3.44) letting $Q \rightarrow 0$:

$$\begin{aligned} \langle P_{class}(t) \rangle &= \sum_{j=1}^{N(t)} \left\langle \frac{d}{dt} \left(\frac{1}{2} m \dot{\vec{r}}_j^2 \right) \right\rangle = \sum_{j=1}^{N(t)} \left\langle \left(-\dot{\vec{r}}_j \cdot \vec{\nabla}_{r_j} W_j(\vec{r}_1, \dots, \vec{r}_{N(t)}, t) \right) \right\rangle = \\ &= \sum_{j=1}^{N(t)} \left\langle \vec{v}_j \cdot \vec{F}_j \right\rangle, \end{aligned} \quad (3.46)$$

where $\vec{F}_j = -e\vec{E}_j$ is the Lorentz force in absence of magnetic fields. As expected, the many-particle classical limit of the electric power is nothing more but the sum over all electrons of the product of their velocities and their correspondent electrostatic forces.

3.4.3 Computing the classical single-particle limit: Recovering the standard classical $P = I \cdot V$ expression

We have still not recovered the standard expression $I \cdot V$, neither for classical nor quantum open systems. In what follows, I will demonstrate that the classical expression (3.46) leads to the standard prediction of power consumption when the single-particle limit is taken.

From expression (3.46) it is easy to realize that if we approximate the scalar potential as

$$W_j(\vec{r}_1, \dots, \vec{r}_{N(t)}, t) \rightarrow W(\vec{r}_j), \quad (3.47)$$

that is taking the single-particle limit, then $\frac{d}{dt}W(\vec{r}_j) = e\vec{r}_j \cdot \vec{\nabla}_j W(\vec{r}_j)$. In such a particular case, we can express the expected value of equation (3.46) for a mixed microstate as

$$\langle P_{class}(t) \rangle = \sum_{j=1}^{N(t)} \left\langle \frac{d}{dt} K_j \right\rangle = \sum_{j=1}^{N(t)} \left\langle e \frac{d}{dt} W_j(\vec{r}_1, \dots, \vec{r}_{N(t)}, t) \right\rangle. \quad (3.48)$$

Expression (3.48) evidences that the total energy of every single electron is conserved for single-particle systems.

If the previous process is ergodic, then we can convert this ensemble average into a time average and the expectation of the single-particle classical power can be computed from:

$$\langle P(t) \rangle = \lim_{T \rightarrow \infty} \frac{1}{T} \int_{-T/2}^{+T/2} \sum_{j=1}^{N(t)} e \frac{d}{dt} W_j(\vec{r}_1, \dots, \vec{r}_{N(t)}, t) (\vec{r}_j(t)) \cdot dt. \quad (3.49)$$

Expression (3.49) can be rewritten as

$$\langle P \rangle = \lim_{t \rightarrow \infty} \frac{e}{T} \int_{-T/2}^{+T/2} \left\{ \frac{d}{dt} W_1(\vec{r}_1(t)) \cdot \theta(t_{1o}, t_{1f}) + \dots + \frac{d}{dt} W_{\tilde{N}}(\vec{r}_{\tilde{N}}(t)) \cdot \theta(t_{\tilde{N}o}, t_{\tilde{N}f}) \right\} \cdot dt \quad (3.50)$$

where I have defined

$$\theta(t; t_{io}, t_{if}) = \begin{cases} 0 & t_{io} \leq t \leq t_{if} \\ 1 & \text{otherwise} \end{cases} \quad (3.51)$$

In (3.51), \tilde{N} is the total number of electrons that have entered the volume Ω from time $t = 0$ until $t \rightarrow \infty$. Assume now the open system subject to an applied voltage (the channel of an electron device for instance). Then, it can be easily argued that only those electrons crossing the volume Ω , from one opened surface to the other, will contribute to

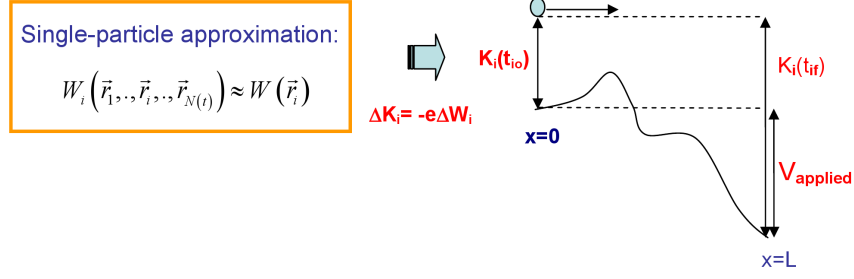


Figure 3.4.1: Schematic representation of the open volume $\Omega = Lx \cdot Ly \cdot Lz$ subject to an applied bias. Only two boundary surfaces, S^1 and S^4 , corresponding to the drain and source respectively, are opened to electron flow. For single-particle classical systems the energy of every single electron is conserved and the energy gained or loosed when traversing the open region equals $\pm e \cdot V_{applied}$.

the integral in (3.50) with exactly the amount

$$\lim_{T \rightarrow \infty} \frac{1}{T} \int_{-T/2}^{+T/2} dt \frac{d}{dt} W_i(\vec{r}_i(t)) \cdot \theta(t_{io}, t_{if}) = eW_i(\vec{r}_i(t_{if})) - eW_i(\vec{r}_i(t_{io})) = \pm e \cdot V_{applied}, \quad (3.52)$$

where the sign of the contribution depends on the direction electrons cross the volume and the polarity of the applied voltage. From (3.52) and (3.50) we can finally conclude that the expectation value of the classical electric power in the single-particle limit reduces to

$$\langle P \rangle = e \left(\frac{\tilde{N}_{SD}}{T} - \frac{\tilde{N}_{DSQ}}{T} \right) \cdot V_{applied} = \langle I \rangle \cdot V_{applied}, \quad (3.53)$$

where \tilde{N}_{SD} is the total number of electrons that have traversed the active region from source to drain, and \tilde{N}_{DSQ} is the total number of electrons that have traversed the active region from drain to source.

CHAPTER 4

Application to the simulation of electron devices

Up to now I have been mainly focused on the theoretical aspects of our trajectory-based classical and quantum approaches to electron transport. Chapters 2 and 3 constitute the keystone pieces for the development of a versatile simulation tool capable of describing electron transport including Coulomb correlations at a many-particle level. The aim of this chapter is to present some examples of the capabilities of such a simulator to predict certain relevant aspects of future nanoscale electron devices. Let me first summarize in a few paragraphs the state-of-the-art of nanoelectronic devices.

4.1 Simulation models for state-of-the-art nanoelectronic devices

For over four decades, microelectronics industry has been characterized by an exponential growth of the performance of its products [72, 136]. On one hand, the level of integration has increased (Moore’s law), as well as the switching velocity and functionality of integrated circuits. On the other hand, power consumption and cost per operation has decreased. Most of these developments have arisen as a direct consequence of the ability of the electronics industry to further reduce the size of conventional MOSFET. However, there is nowadays a broad consensus that the geometric scaling of MOSFET is not enough to provide the expected performance gain of future electronic devices [72, 136]. Given this, the scientific community has identified the “More Moore” domain, which looks for avenues to evolve traditional CMOS devices by means of a tradeoff between the traditional miniaturizing and the introduction of new technological solutions (high-k dielectric, multiple gate transistors, stressed silicon, metal gates, etc.), known as “equivalent scaling” [72]. There is a wide agreement that these are currently the best strategies for the electronics industry in the 2007-2022 period predicted by the latest ITRS [72].

However, the scientific community is searching also for completely different alternatives to CMOS, since the long-term scaling required by Moore's law (4 nm channel length transistors predicted for 2022 [72]) will be technologically and economically unattainable. In this sense, the "Beyond CMOS" domain explores emerging electronic devices whose operation is based on different physical principles than MOSFET, being able to improve at least some aspects of the FET performance. For example, devices based on the spin orientation control rather than the electron charge dynamics are being pursued ("spintronics"), as well as devices based on tunnel transport such as "Resonant Tunneling Diodes" and "single-electron devices". Building block materials different from bulk Silicon are also under investigation, such as "silicon nanowires" or "Carbonbased Nanoelectronics" (i.e. carbon nanotubes and graphene). It is currently not clear which of these proposals may replace the FET. In any case, it is believed that in the near future some of these emerging devices can coexist with nanometer CMOS structures by using technologies not necessarily based on electronics (MEMS, sensors, etc), combined with new architectures (quantum computing, bio-inspired, etc.) or new connections (3D, "Silicon-on-Package"), what has come to be known as the "More than Moore" domain [72, 136].

Here, our many-particle approaches to electron transport are applied to predict the behavior of certain relevant aspects of future nanoscale electron devices. In particular, we will study mainly two different electronic devices belonging to the transition between the "More Moore" and "Beyond CMOS" domains whose relevance is widely acknowledged in the international community. In one hand, as pointed out by subsequent ITRS predictions [72]), a considerable effort is required to understand the real limitations of the "ultimate Nanoscale MOSFETs". In this chapter we examine multi-gate FETs with channel lengths on the order of 10 nanometers or less by means of our many-particle classical simulator to explore the dynamic performance where the correlations are more relevant. Our results show, for example, that fluctuations in current can generate "BIT-errors" or intolerable "Signal-to-noise" ratios [70], or that the study of discrete doping induced fluctuations neglecting the time-dependent Coulomb correlations among (transport) electrons can lead to misleading predictions [68], or that the conventional single-particle $I \cdot V$ definition of the electric power can ultimately induce not negligible errors when computing the energetic consumption of aggressively scaled MOSFETs [69]. On the other hand, nowadays there is a revival of the interest in Resonant Tunneling Diodes, the goal not being the substitution of the MOSFET in general applications, but their use as devices that may have some niche applications of interest (such as oscillators, frequency multipliers, etc.) because their use can imply a dramatic reduction of circuit complexity when compared to the traditional CMOS implementation. Our quantum simulator provides a unique tool to describe rigorously these Resonant Tunneling devices, and its predictions shows

important divergences with respect to those of mean-field approaches [65, 66].

In summary, in this chapter, the importance of accounting for strongly-correlated phenomena is demonstrated when predicting several macroscopic and microscopic characteristics, such as the mean current, electric power consumption, electron transit times or current and voltage fluctuations, for two particularly relevant nanoelectronic devices.

4.2 Many-particle transport in the channel of quantum wire DG-FETs with charged atomistic impurities

Differences in number and the position of dopant atoms in Sub-10nm channel devices will produce important variations on the devices' microscopic behavior, and consequently, the variability of macroscopic parameters such as drive current or threshold voltage will increase. This particular phenomenon is known as discrete dopant induced fluctuations, and constitutes one of the most reported causes of variations in electron devices characteristics (coming from the atomistic nature of mater). In this work we highlight the importance of accurately accounting for (time-dependent) Coulomb correlations among (transport) electrons in the analysis of discrete doping induced fluctuations. In particular, we study the effect of single ionized dopants on the performance of a quantum wire double-gate FET, mainly when its lateral dimensions approach the effective cross section of the charged impurities. We reveal the significant impact of the sign and position of the impurity along the transistor channel on the on-current, the threshold voltage, the distribution of the current in the channel cross-section, the transmission probabilities and the distribution of transit times. We find that neglecting the (time-dependent) Coulomb correlations among (transport) electrons can lead to misleading predictions of the previous results.

G. Albareda, X. Saura, X. Oriols, and J. Suné, “Many-particle transport in the channel of quantum wire DG-FETs with charged atomistic impurities”, *Accepted for publication in J. Appl. Phys.*

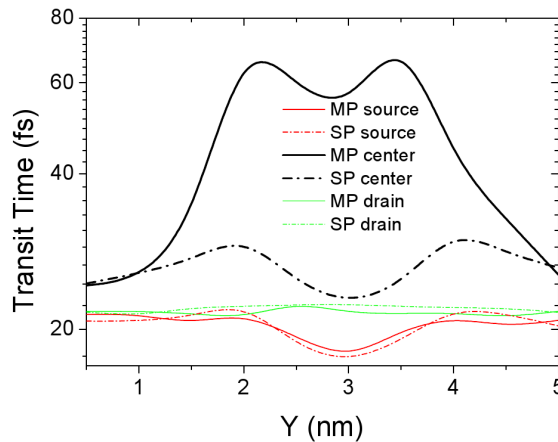


Figure 4.2.1: Spatial distribution of the transit times along the y direction (centred in z) when a negatively charged impurity is placed at different places of the channel.

4.3 Electric power in nanoscale electron devices with full coulomb interaction

Power consumption is one of the main drawbacks when scaling down any new technology. In the last few years, the electronic development is being driven not only by the desire of improving circuit density and speed but also of reducing power consumption. The ITRS has identified this last constraint as one of the top three overall challenges for the next 15 years. In this sense, accuracy is a mandatory requirement when predicting electric power in the active region of a MOS transistor because the results of the single transistor are then extrapolated to the large number of transistors in present-day CPUs. The conventional single-particle $I \cdot V$ definition of the electric power is compared here with the many-particle formulation presented in chapter 3 for classical 3D, 2D and 1D double-gate MOSFETs. The results computed with our many-particle approach show not-negligible discrepancies when compared with the conventional definition of electric power. Such small discrepancies become very important when the single-transistor power is multiplied by the huge number of transistors present in state-of-the-art integrated circuits.

G. Albareda, A. Alarcón and X. Oriols, “Electric power in nanoscale electron devices with full coulomb interaction”, *Int. J. Numer. Model.* DOI: 10.1002/jnm.748 (2010).

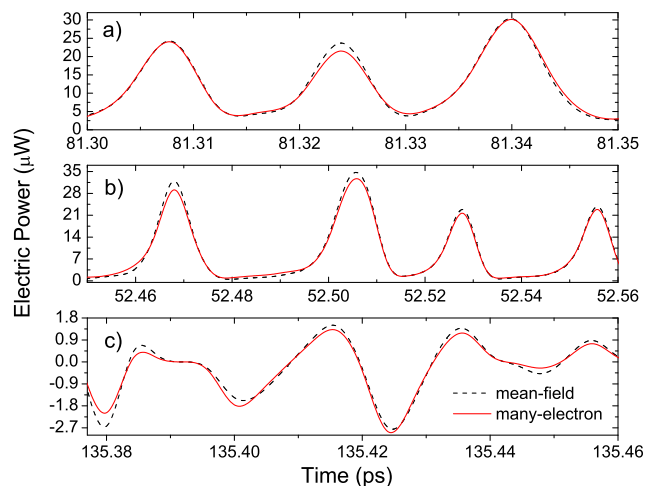


Figure 4.3.1: Time evolution of the power consumption in the 1D DG-FET, (a), 2D DG-FET, (b), and 3D DG-FET, (c), for the two computational methods at $V_{\text{drain}}=1\text{V}$ and $V_{\text{gate}}=0.05\text{V}$ in (a) and (b), and $V_{\text{gate}}=0\text{V}$ in (c). Dashed line refers to the many-electrons method and solid line refers to the mean-field method.

4.4 Intrinsic noise in aggressively scaled DG-FETs

The ITRS predicts for the near future the introduction of nanoscale field-effect transistors with channel lengths below 30 nm, including novel structures with two, three or even four gates provided in order to improve the gate control over the sourcedrain conductance. The advantages of these nanoscale FETs in overcoming the physical limits of traditional FETs are clearly established in terms of size, speed and power consumption. However, few studies deal with the noise performance of these aggressively scaled FETs. This is the main goal of this work. Here, an study of the effect of the intrinsic (thermal and shot) noise of aggressively scaled (3D and 1D) FETs on the performance of an analog amplifier and a digital inverter is carried out by means of our many-particle approach. The numerical data indicate important drawbacks in the noise performance of aggressively scaled FETs that could invalidate roadmap projections as regards analog and digital applications. In particular it is shown that smaller devices produce a smaller average current and a larger Fano factor, leading to a signal-to-noise (S/N) degradation. Moreover, the increase of the clock frequency and reduction of the FET lateral dimensions result in a drastic increase of the Bit-Error-Rate, mainly because smaller devices (with smaller capacitances) are more sensitive to electrostatics.

G. Albareda, D. Jimenez and X. Oriols, “Intrinsic noise in aggressively scaled DG-FETs”, *J. Stat. Mech.* (2009), P01044.

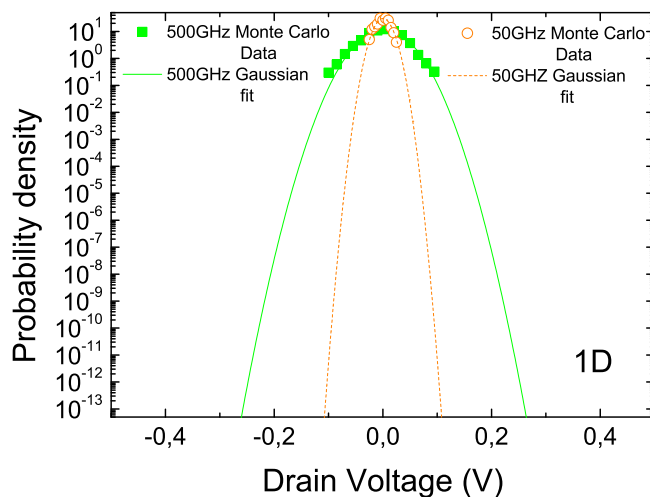


Figure 4.4.1: Semi-classical results for the probability density for finding different drain voltages at 50 and 500 GHz for a 1D double-gate FET.

4.5 Semi-classical simulation of a N^+NN^+ structure with time-dependent boundary conditions including lead-sample Coulomb correlations

In this manuscript, we consider an N^+NN^+ resistor with two different simulation boxes. First, a large simulation box ($L_x(\text{LB}) = 42\text{nm}$), that includes the leads and reservoirs (N^+ region) plus the sample (N region). Second, a smaller simulation box, ($L_x(\text{SB}) = 8\text{nm}$), that only includes the sample (N region) plus a small part of the leads. It is shown that our BC (described in section 2.3) provides an excellent description of the coulomb coupling between the sample and the leads, even at (far from equilibrium) high bias conditions for classical systems. The (reservoir plus lead) resistance obtained from a LB simulation box is practically identical to that obtained from a SB simulation. The comparison of the current voltage-characteristic are discussed in detail. We do also show numerically the enormous difficulties that the standard BC, applied to small simulation boxes that exclude the leads, have when trying to reproduce the previous set of results obtained with our algorithm. The ultimate reason why none of the standard BC types are able to produce reasonable results is because they do not achieve the “overall charge neutrality” requirement.

G. Albareda, H. López, X. Cartoixà, J. Suné, and X. Oriols, “Time-dependent boundary conditions with lead-sample Coulomb correlations: Application to classical and quantum nanoscale electron device simulators”, *Accepted for publication in Phys. Rev. B*.

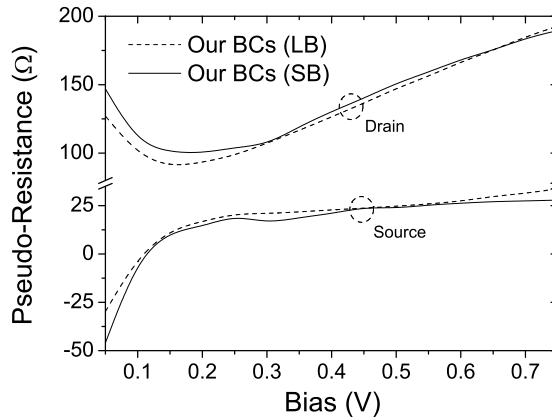


Figure 4.5.1: Pseudo-resistance of the contact plus lead computed through our boundary conditions model for the large simulation box (dashed lines) and the small simulation box (solid lines).

4.6 Quantum simulation of a RTD structure with time-dependent boundary conditions including lead-sample Coulomb correlations

Here, we provide an example of the implementation of our BC algorithm into a Resonant Tunneling Diode. In order to emphasize the relevance of taking into account the Coulomb correlations among the active region and the leads, we compare the results obtained with our BC model and those obtained through standard Dirichlet external bias at the borders of the simulation box. We emphasize the ability of our boundary conditions algorithm to assure overall charge neutrality in simulation boxes much smaller than the total lead-sample-lead length. The results are compared with those obtained with standard fixed bias boundary conditions showing relevant discrepancies. In the results of the RTD with our BC algorithm, we can guarantee that the profile of the charge density along the whole device (the reservoirs, the leads and the sample) is compatible with the requirement of “overall charge neutrality”. In addition, we can also guarantee that the profiles of the electric field and scalar potential are self-consistent with the profile of the charge density. Even more, the requirement of “overall charge neutrality” is achieved in time intervals related with the relaxation dielectric time.

G. Albareda, H. López, X. Cartoixà, J. Suné, and X. Oriols, “Time-dependent boundary conditions with lead-sample Coulomb correlations: Application to classical and quantum nanoscale electron device simulators”, *Accepted for publication in Phys. Rev. B*.

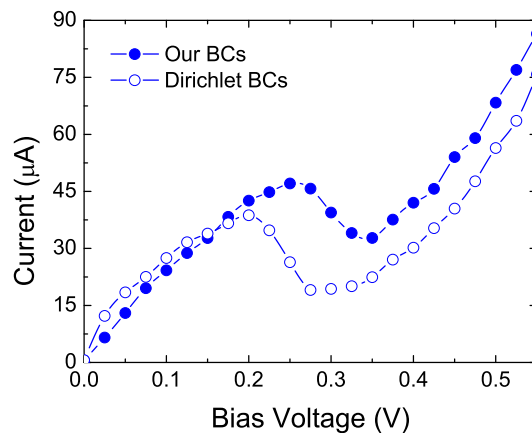


Figure 4.6.1: RTD current-voltage characteristic. Results taking into account the Coulomb correlations between the leads and the active region are presented in solid circles. Open circles refer to the same results neglecting the lead-active region interaction.

4.7 Many-particle semi-classical computation of the I-V characteristics of a DG-FET

We use the classical solution of the many-particle Hamiltonian to provide a full simulation for a nanoscale DGFET. The classical many-electron algorithm is compared with the classical mean-field one. It is shown that when the FET remains under the subthreshold region, the results are quite similar for both methods. However, interestingly, the average current of the FET system in the subthreshold region predicted by the many-electron algorithm is slightly larger than the result obtained by the mean-field approximation. In other words, the mean-field results remain in the subthreshold region, while the many-electron results show a DG-FET channel partially opened. In any case, the most important differences occur for higher gate voltages. The number of electrons inside the channel tends to be identical within both methods. However, the average current that is sensible to electron dynamics is higher with the many-electron method than with the mean-field approximation because fewer electrons are reflected in the former (i.e., there are no electrons reflected by its own charge). For the highest gate voltages, equal results for the mean current are obtained for both methods.

G. Albareda, J. Suné and X. Oriols, “Many-particle Hamiltonian for open systems with full Coulomb interaction: Application to classical and quantum time-dependent simulations of nanoscale electron devices”, *Phys. Rev. B* 79, 075315 (2009).

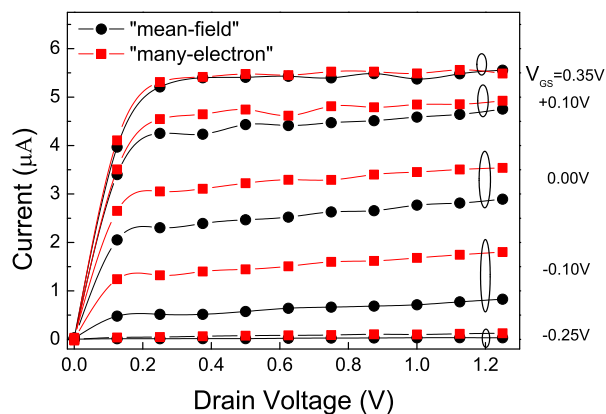


Figure 4.7.1: Average current for a 1D DG-FET, using the many-electron and the mean-field algorithms. The open ellipses include results with the same gate voltages indicated on the left.

4.8 Many-particle quantum computation of the I-V characteristics of a RTD

In this manuscript, we provide a numerical example of the solution of the quantum many-particle Hamiltonian for an ensemble of electrons in a RTD. We again compare our many-electron method with the mean-field approximation. In the resonant region, the correct consideration of the electron-electron interaction is very relevant because the quantum transport is very sensible to the quantum well electrostatics. The potential profile determines the shape of the quantum well and, therefore, the resonant energies. When a “mean-field” electron tries to traverse the “empty” double barrier structure, it “feels” a perturbation in the quantum well due to its own charge implying an increase in the resonant energy and the possibility of being finally reflected by its own charge. In other words, the “mean-field” electron can be Coulomb blockaded by itself. Our many-electron algorithm is free from this pathological behavior. This important difference explains the spurious reduction in the current with the mean-field method at resonance. It also explains the movement of the position of the resonant voltage (i.e., the voltage at the maximum current).

G. Albareda, J. Suné and X. Oriols, “Many-particle Hamiltonian for open systems with full Coulomb interaction: Application to classical and quantum time-dependent simulations of nanoscale electron devices”, *Phys. Rev. B* 79, 075315 (2009).

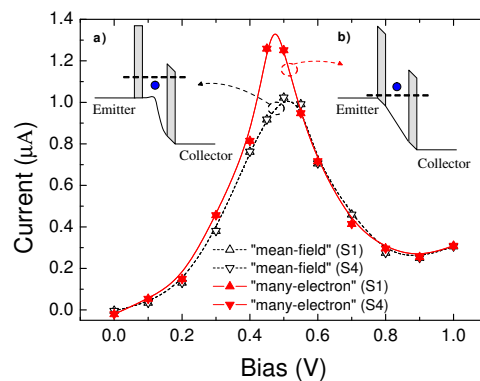


Figure 4.8.1: Average current through surfaces S^1 and S^4 for an RTD as a function of bias, using the many-particle (solid symbols) and mean-field (open symbols) algorithms (lines are a visual help). Non-uniform voltages steps are used to focus on the resonant region. Insets show schematically the effect of an electron crossing an “empty” well on its own electrostatic potential using the mean-field a) or the many-particle b) approaches.

CHAPTER 5

Conclusions

In this dissertation I have presented both a classical and a quantum trajectory-based approach to electron transport at the nanoscale without assuming any mean-field or perturbative approximation to describe the Coulomb interaction among transport electrons.

In chapter 1, I have presented an introductory motivation for the development of an electron transport simulator capable of accurately describing electron-electron Coulomb correlations beyond standard mean-field approaches. I have emphasized the essentially many-body and statistical characters of electron transport at the nanoscale. Due to the huge number of variables involved in a whole closed system, we are obliged to restrict our study to a limited number of degrees of freedom within a reduced region of space. During the process of reduction of degrees of freedom, most approaches to electron transport subjugate the role of the Coulomb correlations to different kinds of mean-field approximations. However, it is known that a very reduced number of carriers involved in nanoscale active regions are determining the ultimate functionality of an electron device. The Coulomb correlations among these carriers become, hence, critical in the establishment of a particular value of any macroscopic magnitude such as electrical current. In this regard, an improvement of the description of the electrostatic correlations among electrons would not only contribute to provide more accurate predictions of the functionality of modern electron devices, but also to understand many-body phenomena taking place at the nanoscale.

Chapter 2 constitutes the theoretical core of our classical and quantum approaches. In section 2.2, a many-particle Hamiltonian for $N(t)$ electrons inside an open system has been developed. Departing from the exact Hamiltonian of a whole closed circuit, after assuming a single-band effective mass approximation, we are capable of constructing a many-particle Hamiltonian (2.38) built of a sum of $N(t)$ electrostatic potentials, $W_k(\vec{r}_1, \dots, \vec{r}_k, \dots, \vec{r}_{N(t)})$, solutions of $N(t)$ Poisson equations (2.39). We use the Poisson equation to define $W_k(\vec{r}_1, \dots, \vec{r}_k, \dots, \vec{r}_{N(t)})$, instead of the Coulomb law, because the former is valid for scenarios with (or without) a spatial-dependent permittivity. After that, in section 2.3, I have presented a novel boundary conditions algorithm describing the Coulomb

correlations among electrons inside and outside the open system without having to enlarge the explicitly simulated degrees of freedom. Interestingly, we have seen that in terms of analytical expressions describing the charge density, the electric field and the scalar potential along the leads and reservoirs, we can transfer the assumptions about the boundary conditions at the borders of a small simulation boxes into the simpler specifications of the boundary conditions deep inside the reservoirs. In particular, the two new boundary conditions that we impose deep inside the reservoirs are, first, the electric field tends to a drift value $E_{S/D}^C(t) \rightarrow E_{S/D}^{drift}(t)$ (that we refer as Deep-drift-BC) and, second, the scalar potentials deep inside the reservoir is fixed by the external bias $V_S^C(t) = 0$ and $V_D^C(t) = V_{external}(t)$. We have highlighted that our algorithm is able to discuss far from equilibrium situations where depletion lengths in the leads have to be added to standard screening. More over, the frequency-dependent correlations included into our boundary conditions algorithm, due to sample-lead Coulomb interaction, allow us to investigate the computation of (zero-frequency or high-frequency) current fluctuations beyond the standard external zero impedance assumption (i.e. most of the computations of current fluctuations in electron devices assume that the voltage applied in the simulation box is a non-fluctuating quantity). Finally, it is shown that the boundary conditions (2.55) are different for each term $W_k(\vec{r}_1, \dots, \vec{r}_k, \dots, \vec{r}_{N(t)})$. In particular, these particle-dependent boundary conditions of the electrostatic potentials provide the same electron dynamics than the image charge method applied to electron transport. However, our many-particle approach has the fundamental advantage that it can be directly implemented into 3D realistic (classical or quantum) electron device simulators, while the image-charge method is an excellent analytical approach applicable only to very simple systems (such as one electron crossing an ideal infinite metallic surface). In section 2.4, I have present classical and quantum solutions of the many-particle open system Hamiltonian supplied with our many-particle boundary conditions. Classically, the solution of this time-dependent many-particle Hamiltonian is obtained via a coupled system of Newton-like equations with a different electric field for each particle. This solution constitutes a generalization of the Monte Carlo technique for the semi-classical single-particle Boltzmann distribution towards many-particle systems. The quantum mechanical solution of the Hamiltonian has been achieved using a time-dependent quantum (Bohm) trajectory algorithm described in appendix A and in reference [67]. In this quantum (Bohm) trajectory algorithm, the use of single-particle Schrödinger equations is exact to treat many-particle systems. However, similarly to Density functional theories, the formidable simplification allowing an exact treatment of the many-particle Coulomb interaction comes at price that some terms appearing in the single-particle Schrödinger equation are in general unknown.

In chapter 3, I have discussed in detail which kind of information is accessible through our classical and quantum approaches. The ultimate reason that determines the success

of the different approaches to electron transport is their practical ability to improve our capabilities of predicting measurable observables. Therefore, it is quite relevant to recognize the amount of information extracted from our simulations that really has to do with real experimental results. First, due to computational limitations, we have been forced to reduce the degrees of freedom of our system. Since we can only describe electron dynamics in a very reduced region of space, we are obliged to deal with an essentially statistical environment. Therefore, although electron dynamics within the open system is *deterministically* described by the many-particle Hamiltonian, our simulations are subject to an *stochastic* injection of electrons and certain statistical parameters such as the effective mass or the effective permittivity, and hence, our predictions can provide only statistical information, i.e. expectation values of observable results (see section 3.1). Second, I have emphasized the necessity of recognizing the real nature of the measurement process. In all measurements, data can be always ascribed to a detector pointer described by the positions of the particles conforming it. Hence, all detectors are ultimately position measurements. Contrarily to this simple statement, “ortodox” quantum mechanics presents several difficulties when discussing the measurement process (i.e. the problem of the wave function collapse). The Bohmian formulation of quantum mechanics, on the other hand, emphasizes that what we have ultimately “measured” is the position of the pointer, not the observable itself (see section 3.2). Unfortunately, due again to computational limitations, we can not simulate the degrees of freedom of the measuring apparatus, and then we need another definition of an observable result based on the position of the simulated electron trajectories within our open system. In section 3.3 I have demonstrate the existence of a relationship between the current on the ammeter and the simulated trajectories. Such a relationship provides a rigorous definition of the expectation values of the electrical current and noise in terms of the classical and quantum trajectories constituting our open system. In particular, it is shown that if the process is ergodic and stationary, then we can compute the expectation value of the current and its fluctuations from time average expressions. Finally, in section 3.4 I have reformulated the expression of the electric power for many-particle classical and quantum open systems with the aid of the energy conservation law for closed systems. I have shown that only when taking the single-particle limit of the classical expression for the electric power, we recover the standard textbook formula $I \cdot V$.

Finally, in chapter 4, our many-particle approaches to electron transport have been applied to predict the behavior of some relevant aspects of future nanoscale electron devices. After a brief introduction of the state-of-the-art of the nanoscale devices, I have emphasized the importance of accounting for Coulomb correlated phenomena when predicting several macroscopic and microscopic characteristics such as the mean current, electric power consumption, electron transit times or current and voltage fluctuations for

two particular devices belonging to the frontier between the “More Moore” and “Beyond CMOS” domains: a nanoscale double-gate transistor and a resonant-tunneling diode. Results in this section are simply summarized, and the reader is referred to the correspondent articles published by the author to discuss the details.

Bibliography

- [1] W. J. Gross, D. Vasileska, and D. K. Ferry, “A novel approach for introducing the electron-electron and electron-impurity interactions in particle-based simulations,” *Electron Device Letters, IEEE*, vol. 20, no. 9, pp. 463, sep 1999.
- [2] C. Jacoboni and L. Reggiani, “The monte carlo method for the solution of charge transport in semiconductors with applications to covalent materials,” *Review of Modern Physics*, vol. 55, no. 3, pp. 645, Jul 1983.
- [3] W. J. Gross, D. Vasileska, and D. K. Ferry, “Ultrasmall mosfets: the importance of the full coulomb interaction on device characteristics,” *Transactions on Electron Devices, IEEE*, vol. 47, no. 10, pp. 1831, oct 2000.
- [4] P. Dollfus, A. Bournel, S. Galdin, S. Barraud, and P. Hesto, “Effect of discrete impurities on electron transport in ultrashort mosfet using 3d mc simulation,” *Transaction on Electron Devices, IEEE*, vol. 51, pp. 749, 2004.
- [5] S. M. Ramey and D. K. Ferry, “A new model for including discrete dopant ions into monte carlo simulations,” *Transactrions on Nanotechnology, IEEE*, vol. 2, pp. 193, 2003.
- [6] S. M. Ramey and D. K. Ferry, “Modeling of quantum effects in ultrasmall fd-soi mosfets with effective potentials and three-dimensional monte carlo,” *Physica B*, vol. 314, pp. 350, 2002.
- [7] *The absence of Coulomb interaction in electron systems was explained, first, by Landau in terms of the Fermi Liquid paradigm, where the real electrons were substituted by quasi-electrons with a negligible Coulomb interaction among them: L. D. Landau, Soviet Physics JETP-USSR 8, 70 (1959); L. D. Landau, Soviet Physics JETP-USSR 3, 920 (1957).*
- [8] M. Büttiker, “Scattering theory of thermal and excess noise in open conductors,” *Physical Review Letters*, vol. 65, no. 23, pp. 2901, Dec 1990.

- [9] R. Landauer, "Spatial variation of currents and fields due to localized scatterers in metallic conduction," *IBM Journal of Research and Development*, vol. 1, pp. 223, 1957.
- [10] S. Datta, *Electronic transport in mesoscopic systems*, Cambridge University Press, 1995.
- [11] Y. M. Blanter and M. Büttiker, "Shot noise in mesoscopic conductors," *Physics Reports*, vol. 336, no. 1-2, pp. 1, 2000.
- [12] W. R. Frensley, "Boundary conditions for open quantum systems driven far from equilibrium," *Review of Modern Physics*, vol. 62, no. 3, pp. 745, 1990.
- [13] R. Landauer, "Conductance from transmission: common sense points," *Physica Scripta*, vol. T42, pp. 110, 1992.
- [14] G. F. Giuliani and G. Vignale, *Quantum Theory of electron Liquid*, Cambridge University Press, 2005.
- [15] J. M. Thijssen, *Computational Physics*, Cambridge University Press, 2003.
- [16] I. L. Aleiner, P. W. Brouwer, and L. I. Glazman, "Quantum effects in coulomb blockade," *Physics Reports*, vol. 358, no. 5-6, pp. 309, 2002.
- [17] E. N. Economou, *Green's Functions in Quantum Physics*, Springer-Verlag, 1990.
- [18] D. R. Hartree, "The wave mechanics of an atom with a non-coulomb central field. part i. theory and methods," *Proceedings of the Cambridge Philosophical Society*, vol. 24, pp. 89, 1928.
- [19] P. Hohenberg and W. Kohn, "Inhomogeneous electron gas," *Physical Review*, vol. 136, pp. B864, 1964.
- [20] R. O. Jones and O. Gunnarsson, "The density functional formalism, its applications and prospects," *Review of Modern Physics*, vol. 61, no. 3, pp. 689, Jul 1989.
- [21] R. O. Jones and O. Gunnarsson, "Density-functional formalism: Sources of error in local-density approximations," *Physical Review Letters*, vol. 55, no. 1, pp. 107, Jul 1985.
- [22] W. Kohn and L. J. Sham, "Self-consistent equations including exchange and correlation effects," *Physical Review*, vol. 140, no. 4A, pp. A1133, Nov 1965.

- [23] D. C. Langreth and M. J. Mehl, “Easily implementable nonlocal exchange-correlation energy functional,” *Physical Review Letters*, vol. 47, no. 6, pp. 446, Aug 1981.
- [24] J. C. Slater, “A simplification of the hartree-fock method,” *Physical Review*, vol. 81, pp. 385, 1951.
- [25] M. Büttiker, A. Prêtre, and H. Thomas, “Dynamic conductance and the scattering matrix of small conductors,” *Physical Review Letters*, vol. 70, no. 26, pp. 4114, Jun 1993.
- [26] M Büttiker, “Capacitance, admittance, and rectification properties of small conductors,” *Journal of Physics: Condensed Matter*, vol. 5, pp. 9361, 1993.
- [27] M. C. Goorden and M. Büttiker, “Two-particle scattering matrix of two interacting mesoscopic conductors,” *Physical Review Letters*, vol. 99, no. 14, pp. 146801, Oct 2007.
- [28] M. Brandbyge, J. Mozos, P. Ordejón, J. Taylor, and K. Stokbro, “Density-functional method for nonequilibrium electron transport,” *Physical Review B*, vol. 65, no. 16, pp. 165401, Mar 2002.
- [29] K. Burke, J. Werschnik, and E. K. U. Gross, “Time-dependent density functional theory: Past, present, and future,” *Journal of Chemical Physics*, vol. 123, pp. 062206, 2005.
- [30] S. Kurth, G. Stefanucci, C. O. Almbladh, A. Rubio, and E. K. U. Gross, “Time-dependent quantum transport: A practical scheme using density functional theory,” *Physical Review B*, vol. 72, no. 3, pp. 035308, Jul 2005.
- [31] E. Runge and E. K. U. Gross, “Density-functional theory for time-dependent systems,” *Physical Review Letters*, vol. 52, no. 12, pp. 997, Mar 1984.
- [32] C. Jacoboni and P. Lugli, *The Monte Carlo Method for Semiconductor Device Simulation*, Springer-Verlag Wien, 1989.
- [33] O. M. Bulashenko, J. Mateos, D. Pardo, T. González, L. Reggiani, and J. M. Rubí, “Electron-number statistics and shot-noise suppression by coulomb correlation in nondegenerate ballistic transport,” *Physical Review B*, vol. 57, no. 3, pp. 1366, Jan 1998.
- [34] M. V. Fischetti and S. E. Laux, “Long-range coulomb interactions in small si devices. part i: Performance and reliability,” *Journal of Applied Physics*, vol. 89, pp. 1205, 2001.

- [35] G. Gomila, I. R. Cantalapiedra, T. González, and L. Reggiani, “Semiclassical theory of shot noise in ballistic $n^+ - i - n^+$ semiconductor structures: Relevance of pauli and long-range coulomb correlations,” *Physical Review B*, vol. 66, no. 7, pp. 075302, Aug 2002.
- [36] T. Gonzalez and D. Pardo, “Physical models of ohmic contact for monte carlo device simulation,” *Solid-State Electronics*, vol. 39, pp. 555, 1996.
- [37] T. Gonzalez and D. Pardo, “Ensemble monte carlo with poisson solver for the study of current fluctuations in homogeneous gaas structures,” *Journal of Applied Physics*, vol. 73, pp. 7453, 1993.
- [38] A. Reklaitis and L. Reggiani, “Monte carlo study of shot-noise suppression in semiconductor heterostructure diodes,” *Physical Review B*, vol. 60, no. 16, pp. 11683, Oct 1999.
- [39] T. Gonzalez, O. M Bulashenko, J. Mateos, D. Pardo, and L. Reggiani, “Effect of long-range coulomb interaction on shot-noise suppression in ballistic transport,” *Physical Review B*, vol. 56, pp. 6424, 1997.
- [40] C. J. Wordelman and U. Ravaioli, “Integration of a particle-particle-particle-mesh algorithm with the ensemble monte carlo method for the simulation of ultra-small semiconductor devices,” *Transaction on Electron Devices, IEEE*, vol. 47, pp. 410, 2000.
- [41] S. Babiker, A. Asenov, N. Cameron, and S. P. Beaumont, “Simple approach to include external resistances in the monte carlo simulation of mesfets and hemts,” *Transactions on Electron Devices, IEEE*, vol. 43, pp. 2032, 1996.
- [42] C. Riddet, A. R. Brown, S. Roy, and A. Asenov, “Boundary conditions for density gradient corrections in 3d monte carlo simulations,” *Journal of Computational Electronics*, vol. 7, pp. 231, 2008.
- [43] D. Reid, C. Millar, G. Roy, S. Roy, and A. Asenov, “Analysis of threshold voltage distribution due to random dopants: A 100.000 sample 3d simulation study,” *Transactions on Electron Devices, IEEE*, vol. 56, pp. 2255, 2009.
- [44] M. O. Vasell, J. Lee, and H. F. Lockwood, “Current density for cold cathode discharge gap in rare gases,” *Journal of Applied Physics*, vol. 54, pp. 5206, 1983.
- [45] B. Ricco and M. Ya. Azbel, “Physics of resonant tunneling. the one-dimensional double-barrier case,” *Physical Review B*, vol. 29, no. 4, pp. 1970, Feb 1984.

- [46] A. Rahman, J. Guo, S. Datta, and M. S. Lundstrom, "Theory of ballistic nano-transistors," *Transaction on Electron Devices, IEEE*, vol. 50, pp. 1853, 2003.
- [47] G. C. Liang, A. W. Ghosh, M. Paulsson, and S. Datta, "Electrostatic potential profiles of molecular conductors," *Physical Review B*, vol. 69, no. 11, pp. 115302, Mar 2004.
- [48] M. J. McLennan, Y. Lee, and S. Datta, "Voltage drop in mesoscopic systems: A numerical study using a quantum kinetic equation," *Physical Review B*, vol. 43, no. 17, pp. 13846, Jun 1991.
- [49] R. Venugopal, S. Goasguen, S. Datta, and M. S. Lundstrom, "Quantum mechanical analysis of channel access geometry and series resistance in nanoscale transistors," *Journal of Applied Physics*, vol. 95, pp. 292, 2004.
- [50] R. Venugopal, Z. Ren, and M. S. Lundstrom, "Simulating quantum transport in nanoscale mosfets: ballistic hole transport, subband engineering and boundary conditions," *Transactions on Nanotechnology, IEEE*, vol. 2, pp. 135, 2003.
- [51] Z. Ren, R. Venugopal, S. Goasguen, S. Datta, and M.S. Lundstrom, "nanomos 2.5: A two-dimensional simulator for quantum transport in double-gate mosfets," *Transactions on Electron Devices*, vol. 50, pp. 1914, 2002.
- [52] T. C. Au Yeung, Yu. Yabin, W. Z. Shangguan, and W. K. Chow, "Dynamic response of a double barrier system: The effect of contacts," *Physical Review B*, vol. 68, no. 7, pp. 075316, Aug 2003.
- [53] M. Büttiker and S. E Nigg, "Mesoscopic capacitance oscillations," *Nanotechnology*, vol. 18, pp. 044029, 2007.
- [54] M. Büttiker, H. Thomas, and A. Prtre, "Mesoscopic capacitors," *Physics Letters A*, vol. 180, no. 4-5, pp. 364, 1993.
- [55] J. Gabelli, G. Fève, J. M. Berroir, B. Plaais, A. Cavanna, B. Etienne, Y. Jin, and D. C. Glattli, "Violation of kirchhoff's laws for a coherent rc circuit," *Science*, vol. 313, pp. 499, 2006.
- [56] M. Büttiker, H. Thomas, and A. Prêtre, "Current partition in multiprobe conductors in the presence of slowly oscillating external potentials," *Zeitschrift fr Physik B Condensed Matter*, vol. 94, pp. 133, 1994.
- [57] J. Quan, Y. Yu, and Y. H. Tang, "Role of wide contacts in the ac response of a double-barrier structure," *Physical Review B*, vol. 73, no. 19, pp. 195314, May 2006.

- [58] R. Baer and D. Neuhauser, “Ab initio electrical conductance of a molecular wire,” *International Journal of Quantum Chemistry*, vol. 91, pp. 524, 2003.
- [59] M. Di Ventra and N. D. Lang, “Transport in nanoscale conductors from first principles,” *Physical Review B*, vol. 65, no. 4, pp. 045402, Dec 2001.
- [60] M. Di Ventra, S. T. Pantelides, and N. D. Lang, “First-principles calculation of transport properties of a molecular device,” *Physical Review Letters*, vol. 84, no. 5, pp. 979, Jan 2000.
- [61] J. Taylor, H. Guo, and J. Wang, “Ab initio modeling of quantum transport properties of molecular electronic devices,” *Physical Review B*, vol. 63, pp. 245407, 2001.
- [62] N. D. Lang, “Resistance of atomic wires,” *Physical Review B*, vol. 52, no. 7, pp. 5335, Aug 1995.
- [63] X. Li and Y. Yan, “Quantum master equation scheme of time-dependent density functional theory to time-dependent transport in nanoelectronic devices,” *Physical Review B*, vol. 75, no. 7, pp. 075114, Feb 2007.
- [64] R. Baer, T. Seideman, S. Llani, and D. Neuhauser, “Ab initio study of the alternating current impedance of a molecular junction,” *Journal of Chemical Physics*, vol. 120, pp. 3387, 2004.
- [65] G. Albareda, H. Lopez, X. Cartoixa, J. Suñé, and X. Oriols, “Time-dependent boundary conditions with lead-sample coulomb correlations: Application to classical and quantum nanoscale electron device simulators,” Accepted for publication in *Phys. Rev. B*.
- [66] G. Albareda, J. Suñé, and X. Oriols, “Many-particle hamiltonian for open systems with full coulomb interaction: Application to classical and quantum time-dependent simulations of nanoscale electron devices,” *Physical Review B*, vol. 79, no. 7, pp. 075315, Feb 2009.
- [67] X. Oriols, “Quantum-trajectory approach to time-dependent transport in mesoscopic systems with electron-electron interactions,” *Physical Review Letters*, vol. 98, no. 6, pp. 066803, Feb 2007.
- [68] G. Albareda, X. Saura, X. Oriols, and J. Suñé, “Many-particle transport in the channel of quantum wire double-gate mosfets with charged atomistic impurities,” Accepted for publication in *J. Appl. Phys.*

- [69] G. Albareda, A. Alarcón, and X. Oriols, “Electric power in nanoscale devices with full coulomb interaction,” *International Journal of Numerical Modeling*, vol. DOI: 10.1002/jnm, 2010.
- [70] G. Albareda, D. Jiménez, and X. Oriols, “Intrinsic noise in aggressively scaled field-effect transistors,” *Journal of Statistical Mechanics*, vol. 2009, pp. 01044, 2009.
- [71] G. E. Moore, “Cramming more components onto integrated circuits,” *Electronics*, vol. 38, pp. 114, 1965.
- [72] *International Technology Roadmap for Semiconductors 2009*.
- [73] B. Doris, “Extreme scaling with ultra-thin si channel mosfets,” *IEDM Technical Digest*, p. 267, 2002.
- [74] V. Sverdlov, E. Ungersboek, H. Kpsina, and S. Selberherr, “Current transport models for nanoscale semiconductor devices,” *Materials Science and Engineering: Reports*, vol. 58, pp. 228, 2008.
- [75] *L. Landau and A. Kompanejez, Phys. Z. Sowjetunion, vol. 6, pp. 163, 1934.*
- [76] *B. Davydov, Phys. Z. Sowjetunion, vol. 9, pp. 443, 1936.*
- [77] *B. Davydov, Phys. Z. Sowjetunion, vol. 12, pp. 269, 1937.*
- [78] *W. Shockley, Bell System Technical Journal, vol. 30, pp. 990, 1951.*
- [79] E. M. Conwell, *High field transport in semiconductors, Solid-state Phys. Suppl. 9*, Academic, New York, 1967.
- [80] H. Gummel, “A self-consistent iterative scheme for one-dimensional steady state transistor calculations,” *Transaction on Electron Devices, IEEE*, vol. 11, pp. 455, 1964.
- [81] A. De Mari, “An accurate numerical steady-state one-dimensional solution of the p-n junction,” *Solid-State Electronics*, vol. 11, pp. 33, 1968.
- [82] D. Scharfetter and H. Gummel, “Large-signal analysis of a silicon read diode oscillator,” *Transaction on Electron Devices, IEEE*, vol. 16, pp. 64, 1969.
- [83] H. Loeb, R. Andrew, and W. Love, “Application of 2-dimensional solutions of the shockley-poisson equation to inversion-layer m.o.s.t. devices,” *Electronic Letters*, vol. 4, pp. 352, 1968.

- [84] J. Schroeder and R. Muller, "Igfet analysis through numerical solution of poisson's equation," *Transaction on Electron Devices, IEEE*, vol. 15, pp. 954, 1968.
- [85] T. Kurosawa, "Proceedings of the international conference on the physics of semi-conductors", Kyoto, 1966.
- [86] D. Kennedy, "On the ambipolar diffusion of impurities into silicon," *Proceedings IEEE*, vol. 57, pp. 1202, 1969.
- [87] J. Slotboom, "Iterative scheme for 1- and 2- dimensional d.c.-transistor simulation," *Electronics Letters*, vol. 5, pp. 677, 1969.
- [88] M. Di Ventra, *Electrical Transport in Nanoscale Systems*, Cambridge University Press, The Edinburgh Building, Cambridge CB2 8RU, UK, first edition, 2008.
- [89] J. P. Sun, G. I. Haddad, P. Mazumder, and J. N. Shulman, "Resonant tunneling diodes: models and properties," *Proceedings IEEE*, vol. 86, pp. 641, 1998.
- [90] *The general theory of quantum mechanics is now almost complete. The underlying physical laws necessary for the mathematical theory of a large part of physics and the whole of chemistry are thus completely known, and the difficulty is only that the exact application of these laws leads to equations much too complicated to be soluble.* — P.A.M. Dirac, 1929.
- [91] D. Dürr, S. Goldstein, and N. Zangh, "Quantum equilibrium and the origin of absolute uncertainty," *Journal of Statistical Physics*, vol. 67, pp. 843, 1992.
- [92] S. Lloyd, "Quantum thermodynamics: excuse or ignorance," *Nature Physics*, vol. 2, pp. 727, 2006.
- [93] C. Callender, "Taking thermodynamics too seriously," *Studies in History and Philosophy of Science Part B: Studies in History and Philosophy of Modern Physics*, vol. 32, no. 4, pp. 539, 2001.
- [94] S. Popescu, A. J. Short, and A. Winter, "Entanglement and the foundations of statistical mechanics," *Nature Physics*, vol. 2, pp. 754, 2006.
- [95] G. Lebon, D. Jou, and J. Casas-Vzquez, *Understanding Non-Equilibrium Thermodynamics*, Springer-Verlag, first edition, 2008.
- [96] L. W. Boltzmann, "Weitere studien uber das wrmegewicht unter gasmoleklen," *Ber. Wien. Akad.*, vol. 66, pp. 275, 1872.
- [97] M. Lundstrom, *Fundamentals of carrier transport*, Cambridge University Press, 2000.

- [98] T. Grasser, H. Kosina, C. Heitzinger, and S. Selberherr, ,” *Journal of Applied Physics*, vol. 91, pp. 3869, 2002.
- [99] K. Blotekjaer, ,” *Transaction on Electron Devices, IEEE*, vol. 17, pp. 38, 1970.
- [100] C. Millar, D. Reid, G. Roy, S. Roy, and A. Asenov, ,” *Electron Device Letters, IEEE*, vol. 29, pp. 946, 2008.
- [101] Y. Li, C. Hwang, and H. Huang, ,” *Physica Status Solidi A*, vol. 205, pp. 1505, 2008.
- [102] R. Landauer, “Electrical resistance of disordered one-dimensional lattices,” *Philosophical Magazine*, vol. 21, pp. 863, 1970.
- [103] E. Wigner, “On the quantum correction for thermodynamic equilibrium,” *Physical Review*, vol. 40, no. 5, pp. 749, Jun 1932.
- [104] L. V. Keldysh, *Zh. Eksp. Teor. Fiz.*, vol. 47, pp. 1515, 1964.
- [105] L. V. Keldysh, *Sov. Phys. JETP*, vol. 47, pp. 804, 1978.
- [106] J. Kondo, “Resistance minimum in dilute magnetic alloys,” *Progress in Theoretical Physics*, vol. 32, pp. 37, 1964.
- [107] J. M. Luttinger, “An exactly soluble model of a many fermion system,” *Journal of Mathematical Physics*, vol. 4, pp. 1154, 1963.
- [108] M. Di Ventura and R. D’Agosta, “Stochastic time-dependent current-density-functional theory,” *Physical Review Letters*, vol. 98, no. 22, pp. 226403, Jun 2007.
- [109] D. Bohm, “A suggested interpretation of the quantum theory in terms of ”hidden” variables. i,” *Physical Review*, vol. 85, no. 2, pp. 166, Jan 1952.
- [110] L. de Broglie, “La nouvelle dynamique des quanta,” *Electrons and Photons: Rapports et discussions du cinquieme conseil de physique tenu Bruxelles*, p. 105, 1927.
- [111] J. R. Reitz, F. J. Milford, and R. W. Christy, *Foundations of electromagnetic theory*, Addison-Wesley, 1992.
- [112] S. Datta, *Quantum Transport: Atom to Transistor*, Cambridge University Press, The Edinburgh Building, Cambridge CB2 2RU, UK, first edition, 2005.
- [113] M. Lundstrom and J. Guo, *Nanoscale Transistors: Device Physics, Modeling and Simulation*, Springer Science, 233 Spring Street, New York, NY 10013, USA, first edition, 2006.

- [114] S. Datta, *Quantum phenomena*, Addison-Wesley, 1989.
- [115] C. Kittel, *Introduction to Solid State Physics*, John Wiley & Sons, 1986.
- [116] M. Javid and P. M. Brown, *Field Analysis and Electromagnetics*, McGraw-Hill, 1963.
- [117] M. Büttiker, Y. Imry, R. Landauer, and S. Pinhas, “Generalized many-channel conductance formula with application to small rings,” *Physical Review B*, vol. 31, no. 10, pp. 6207, May 1985.
- [118] In principle, a formal quantum treatment of the openness of the sample requires quite elaborate formalisms to trace out the degrees of freedom not explicitly simulated⁶⁸. In this sense, the Lindblad or quantum master equations are the accurate substitutes of the Schrodinger or Liouville equations which are applicable for closed systems. This formal treatment of an open system is far from the scope of this work and we follow the standard way in of dealing with open systems by specifying educated guesses for the boundary conditions on the borders of the simulation box.
- [119] J. P. et al. Collinge, “Nanowire transistors without junctions,” *Nature Nanotechnology*, vol. 5, pp. 225, 2010.
- [120] X. Oriols, J. Suné, F. Martn, and X. Aymerich, ,” *J. Appl. Phys.*, vol. 78, pp. 2135, 1995.
- [121] G. F. Giuliani and G. E. Simion, “Friedel oscillations in a two dimensional fermi liquid,” *Solid State Communications*, vol. 127, pp. 789, 2003.
- [122] T. Ihn, *Semiconductor Nanostructures: Quantum states and electronic transport*, Oxford University Press, 2010.
- [123] W. Kohn, “Nobel lecture: Electronic structure of matter—wave functions and density functionals,” *Review of Modern Physics*, vol. 71, no. 5, pp. 1253, Oct 1999.
- [124] J. S. Bell, *Speakable and Unsayable in Quantum Mechanics*, Cambridge University Press, 1987.
- [125] K. Jacobs and D. A. Steck, “A straightforward introduction to continuous quantum measurement,” *Contemporary Physics*, vol. 47, pp. 279, 2006.
- [126] S. Weinberg, “Precision tests of quantum mechanics,” *Physical Review Letters*, vol. 62, no. 5, pp. 485, Jan 1989.
- [127] E. P. Wigner, *Review of the quantum mechanical measurement problem*, Plenum, New York, 1983.

- [128] H. P. Stapp, *Quantum Implications: Essays in honor of David Bohm*, chapter Light as foundation of being, Routledge & Kegan Paul, London and New York, 1987.
- [129] G. C. Ghirardi, A. Rimini, and T. Weber, “Unified dynamics for microscopic and macroscopic systems,” *Physical Review D*, vol. 34, no. 2, pp. 470, Jul 1986.
- [130] A. Alarcon and X. Oriols, ,” *J. Stat. Mech.*, vol. 2009, pp. P01051, 2009.
- [131] G. F. Bonani, *Noise in Semiconductors Devices, Modeling and Simulation*, Springer-Verlag Berlin Heidelberg, 2001.
- [132] W. Schottky, “Über spontane Stromschwankungen in verschiedenen elektrizitätsleitern,” *Ann. Phys. (Leipzig)*, vol. 57, pp. 541, 1918.
- [133] D. J. Frank, “Power-constrained cmos scaling limits,” *IBM Journal of Research and Development*, vol. 46, pp. 235, 2002.
- [134] M. et al. Horowitz, “Scaling, power, and the future of cmos,” *IEDM Technical Digest*, 2005.
- [135] D. H. Kobe, “Quantum power in de broglie-bohm theory,” *Journal of Physics A : Mathematical & Theoretical*, vol. 40, pp. 5155, 2007.
- [136] *ENIAC Strategic Research Agenda 2009*.
- [137] W. Heisemberg, *ber quantentheoretische Umdeutung kinematischer und mechanischer Beziehungen*, *Zeitschrift fr Physik*, 33, 879-893, 1925 (received 29 July 1925). [English translation in: B. L. van der Waerden, editor, *Sources of Quantum Mechanics (Dover Publications, 1968) ISBN 0-486-61881-1 (English title: Quantum-Theoretical Re-interpretation of Kinematic and Mechanical Relations).*].
- [138] M. Born, “Quantenmechanik der stobvorgange,” *Zeitschrift fur Physik*, vol. 38, pp. 803, 1926.
- [139] J. J. Sakurai, *Modern quantum mechanics*, Addison-Wesley, 1994.
- [140] X. Oriols, E. Fernández-Díaz, A. Álvarez, and A. Alarcón, “An electron injection model for time-dependent simulators of nanoscale devices with electron confinement: Application to the comparison of the intrinsic noise of 3d-, 2d- and 1d-ballistic transistors,” *Solid-State Electronics*, vol. 51, pp. 306, 2007.

APPENDIX A

A Primer on Bohmian Mechanics

A.1 Introduction

Early twentieth-century experiments on the physics of very small-scale phenomena led to the discovery of results that could not be explained with classical mechanics. It was mandatory a new physical theory capable of interpreting these experiments from novel, abstract and imaginative formalisms. In 1927, Louis de Broglie proposed an interpretation of these experiments based on a pilot field that guides particles towards non-classical trajectories [110]. This was the origin of the pilot-wave formulation of quantum mechanics (also referred as Bohmian mechanics to account for the posterior work of David Bohm [109]). Simultaneously, Niels Bohr, Max Born and Werner Heisenberg, in the course of their collaboration in Copenhagen, provided an original formulation of these experiments without the need of trajectories [137, 138]. This was the origin of the so-called Copenhagen interpretation of quantum phenomena. For historical reasons, the latter is widely accepted as the orthodox formulation of quantum mechanics and it is the only interpretation of quantum phenomena explained at most universities.

“Orthodox” quantum mechanics explored a route to understand quantum mechanics where waves and particles were incompatible properties of the electrons, while the Bohmian mechanics explored the compatible route.

1. .. **Wave and particle:** In this route, the wave and particle concepts are merged on atomic dimensions by assuming that a pilot-wave solution of the Schrödinger equation guides the electron trajectory. In the same manner as an electron is guided by an electromagnetic field. This is what we call the Bohmian route.
2. .. **Wave or particle?:** The successful route to merge wave and particles concepts was, however, the so called Copenhagen interpretation. Electrons are associated basically to probability (amplitude) waves. The particle nature of the electron appears when we measure the position of the electron. In Bohr’s words, an object cannot be both a wave and a particle at the same time; it must be either one or

the other, depending upon the situation.

The ability of the **wave and particle** route to explain quantum phenomena is explained in a very didactic way in the double-slit experiment (see figure A.1.1). In this particular example, a beam of electrons with low intensity (so that electrons are injected one by one) travels through a barrier with two slits removed. If one puts a detector screen on the other side, the pattern of detected particles shows interference fringes characteristic of waves; however, the detector screen responds to particles. The system exhibits behavior of both waves (interference patterns) and particles (dots on the screen). Let me summarize what is going on in such an experiment with an enlightening quotation:

“Is it not clear from the smallness of the scintillation on the screen that we have to do with a particle? And is it not clear, from the diffraction and interference patterns, that the motion of the particle is directed by a wave? De Broglie showed in detail how the motion of a particle, passing through just one of two holes in screen, could be influenced by waves propagating through both holes. And so influenced that the particle does not go where the waves cancel out, but is attracted to where they cooperate. This idea seems to me so natural and simple, to resolve the wave-particle dilemma in such a clear and ordinary way, that it is a great mystery to me that it was so generally ignored.” — John S. Bell (1987) [124].

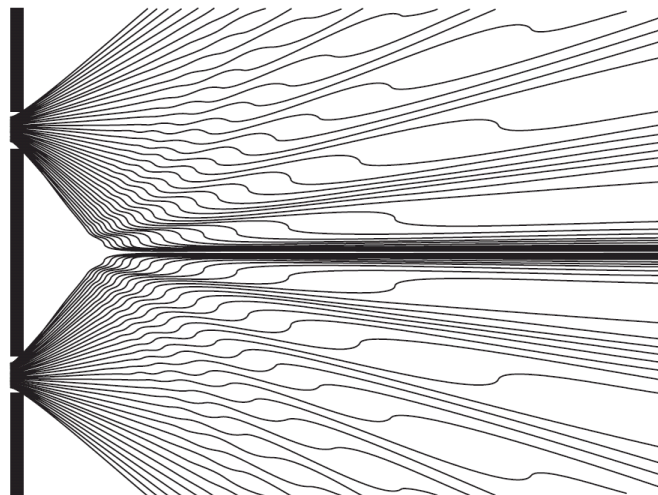


Figure A.1.1: An ensemble of trajectories for the two-slit experiment. Notice that while each trajectory passes through but one of the slits, the wave passes through both, and the interference profile that therefore develops in the wave generates a similar pattern in the trajectories guided by this wave.

A quite general way of introducing Bohmian mechanics is as the theory of motion that resolves the dilemma of the appearance of both particle and wave properties in a rather trivial manner. In Bohmian mechanics, particles are moving in a completely deterministic—but non Newtonian—way, with the wave function guiding this motion. This **wave and particle** route to quantum mechanics appears in contraposition to the standard **wave or particle** interpretation.

Bohmian Mechanics for 1D single particle non-relativistic systems

We can start from the quantum wave equation (i.e the Schrodinger equation) and arrive at a quantum Hamilton-Jacobi equation. That is, directly following the work presented by Bohm in his original paper [109]. We write the quantum (complex) wavefunction, $\psi(x, t) = \psi_r(x, t) + i\psi_i(x, t)$, in a polar form:

$$R^2(x, t) = \psi_r^2(x, t) + \psi_i^2(x, t) \quad (\text{A.1})$$

$$S(x, t) = \hbar \tan^{-1} \left(\frac{\psi_i(x, t)}{\psi_r(x, t)} \right) \quad (\text{A.2})$$

We assume that the wavefunction is single-valued so that $R(x, t)$ is also single-valued. However, the definition of $S(x, t)$ has some practical difficulties¹. Similarly, the function $S(x, t)$ can not be computed when $\psi_r(x, t) = 0$ and $\psi_i(x, t) = 0$. However, then $R(x, t) = 0$ meaning that no electrons will reach this configuration point, so that we do not need to compute the velocity.

In order to find the quantum Hamilton-Jacobi equation, we can introduce $\psi(x, t) = R(x, t)\exp(iS(x, t)/\hbar)$ into the Schrödinger equation

$$i\hbar \frac{\partial \psi(x, t)}{\partial t} = -\frac{\hbar^2}{2m} \frac{\partial^2 \psi(x, t)}{\partial x^2} + V(x, t)\psi(x, t). \quad (\text{A.3})$$

Then, the imaginary part of (A.3) gives a *local* conservation law:

$$\frac{\partial R^2(x, t)}{\partial t} + \frac{\partial}{\partial x} \left(\frac{1}{m} \frac{\partial S(x, t)}{\partial x} R^2(x, t) \right) = 0, \quad (\text{A.4})$$

¹In principle, $S(x, t)$ is a multi-valued function because the function $\tan^{-1}(x)$ itself is a multi-valued function. All action functions $S'(x, t) = S(x, t) + 2\pi n$ with an arbitrary value of n give identical wavefunction. In fact, they do also provide identical velocity because its spatial derivative is independent on the constant $2\pi n$. Therefore, such technical multi-valued value of the action function is not a practical problem for computing the Bohmian trajectories from the wavefunction. If we want to use (A.1) and (A.2) to reconstruct the wavefunction, then, the multi-valued problem can be eliminated by imposing an (arbitrary) additional restriction on the definition of S .

and the real part of (A.3) gives the following quantum Hamilton-Jacobi equation:

$$\frac{\partial S(x, t)}{\partial t} + \frac{1}{2m} \left(\frac{\partial S(x, t)}{\partial x} \right)^2 + V(x, t) + Q(x, t) = 0, \quad (\text{A.5})$$

where the term $Q(x, t)$ is the so-called quantum potential defined as:

$$Q(x, t) = -\frac{\hbar^2}{2m} \frac{\partial^2 R(x, t)/\partial x^2}{R(x, t)} \quad (\text{A.6})$$

On one hand, from the quantum Hamilton-Jacobi equation (A.5) it can be defined the velocities of an ensemble of quantum trajectories as $\partial S(x, t)/\partial x$. From A.2, it can be easily shown that this new expression of quantum velocity is:

$$\begin{aligned} v(x, t) &= \frac{\partial S(x, t)}{\partial x} = \hbar \frac{\partial}{\partial x} \tan^{-1} \left(\frac{\psi_i(x, t)}{\psi_r(x, t)} \right) \\ &= \hbar \frac{\frac{\partial \psi_i(x, t)}{\partial x} \psi_r(x, t)}{1 + \left(\frac{\psi_i(x, t)}{\psi_r(x, t)} \right)^2} \\ &= \hbar \frac{\psi_r(x, t) \frac{\partial \psi_i(x, t)}{\partial x} - \psi_i(x, t) \frac{\partial \psi_r(x, t)}{\partial x}}{\psi_r^2(x, t) + \psi_i^2(x, t)} \end{aligned} \quad (\text{A.7})$$

Using now the following identity:

$$\psi(x, t) \frac{\partial \psi^*(x, t)}{\partial x} - \psi^*(x, t) \frac{\partial \psi(x, t)}{\partial x} = \frac{2}{i} \left(\psi_r(x, t) \frac{\partial \psi_i(x, t)}{\partial x} - \psi_i(x, t) \frac{\partial \psi_r(x, t)}{\partial x} \right) \quad (\text{A.8})$$

we obtain another common way of introducing the velocity of quantum trajectories in terms of the probability current density $J(x, t)$:

$$v(x, t) = \frac{1}{m} \frac{\partial S(x, t)}{\partial x} = \frac{J(x, t)}{|\psi(x, t)|^2} \quad (\text{A.9})$$

where $J(x, t)$ is defined as

$$J(x, t) = i \frac{\hbar}{2m} \left(\psi(x, t) \frac{\partial \psi^*(x, t)}{\partial x} - \psi^*(x, t) \frac{\partial \psi(x, t)}{\partial x} \right) \quad (\text{A.10})$$

On the other hand, since the quantity $R(x, t)$ reproduces the wave function's modulus, $|\psi(x, t)|$, at time t_0 , from the local conservation law (A.4) it can be demonstrate that a set of quantum trajectories with velocities $\partial S(x, t)/\partial x$ will reproduce at any time the wave function $\psi(x, t)$.

The quantum Newton-like equation

Now, it can be interesting to compute the time-derivative of the Bohmian velocity (A.9) to realize if some kind of quantum Newton-like equation can be recovered. In particular, we compute:

$$m \frac{d}{dt} v(x[t], t) = \frac{d}{dt} \left[\frac{\partial S}{\partial x} \right]_{x=x[t]} = \left[\frac{\partial^2 S}{\partial x^2} \right]_{x=x[t]} \cdot \dot{x}[t] + \left[\frac{\partial}{\partial x} \frac{\partial S}{\partial t} \right]_{x=x[t]}, \quad (\text{A.11})$$

and rewrite (A.11) as:

$$m \frac{d}{dt} v(x[t], t) = \left[\frac{\partial}{\partial x} \left(\frac{1}{2m} \left(\frac{\partial S}{\partial x} \right)^2 + \frac{\partial S}{\partial t} \right) \right]_{x=x[t]}. \quad (\text{A.12})$$

Finally, using (A.5) we conclude:

$$m \frac{d}{dt} v(x[t], t) = \left[-\frac{\partial}{\partial x} (V(x, t) + Q(x, t)) \right]_{x=x[t]}. \quad (\text{A.13})$$

The quantum (complex) single-particle wave-function can be interpreted as an ensemble of trajectories which are all solutions of the same single-particle experiment but with different initial conditions. The quantum trajectories are not solutions of the classical Newton law with a classical potential energy, but solutions of the a “quantum” Newton law (A.13) where a quantum potential (that accounts for all non-classical effects) is added to the classical potential.

A.2 The basic postulates

Here I present the basic postulates of Bohmian mechanics. Although I present them for the single-particle case, they can be directly extended to many-particle systems. In general, the postulates of any physical theory can be presented in different alternative (and compatible) ways. For example, classical mechanics can be postulated from Newton’s laws, from Lagrange’s equations, Feynman paths, etc. We follow here the standard presentation of Bohmian mechanics that provides the smaller number of ingredients needed to present the theory.

First postulate: The dynamics of a single-particle in a quantum system comprises a wavefunction $\psi(x, t)$ plus a trajectory $x[t]$ that moves continuously under the guidance of the wave.

a.- The wavefunction $\psi(x, t)$ is a solution of the Schrödinger equation (A.3):

$$i\hbar \frac{\partial \psi(x, t)}{\partial t} = -\frac{\hbar^2}{2m} \frac{\partial^2 \psi(x, t)}{\partial x^2} + V(x, t)\psi(x, t)$$

b.- The trajectory $x[t]$ is obtained by time-integrating the particle velocity $v(t)$ defined in expression (A.9):

$$v(x, t) = \frac{J(x, t)}{|\psi(x, t)|^2}$$

where $|\psi(x, t)|^2 = \psi(x, t)\psi^*(x, t)$ is the square modulus of the wavefunction and $J(x, t)$ is the mean value of the current density defined in (A.2) as:

$$J(x, t) = i\frac{\hbar}{2m} \left(\psi(x, t) \frac{\partial \psi^*(x, t)}{\partial x} - \psi^*(x, t) \frac{\partial \psi(x, t)}{\partial x} \right)$$

The initial position $x[t_o] = x_o$ has to be specified to completely determine the trajectory $x[t]$. The initial velocity $v[t_o] = v_o$ is already determined by the knowledge of $\psi(x_o, t_o)$.

Second postulate (*Quantum equilibrium Hypothesis*) An ensemble of $N \rightarrow \infty$ trajectories, $x_i[t]$, associated to the same $\psi(x, t)$ have to be generated by varying the initial position x_{oi} of each trajectory. In particular, the number of particles of the ensemble that lies between x and $x + dx$ at the initial time t_o have to be selected proportionally to $R^2(x, t_o) = |\psi(x, t_o)|^2$. This condition can be written mathematically as:

$$R^2(x, t_o) = \lim_{N \rightarrow \infty} \frac{1}{N} \left(\sum_{i=1}^N \delta(x - x_i[t_o]) \right) \quad \text{for } t = t_o \quad (\text{A.14})$$

where $1/N$ is a constant that determine the proportionality between the number of particles and $R^2(x, t_o)$.

This second postulate has one very important corollary on how Bohmian mechanics reproduce the predictions of the “orthodox” quantum theory. It can be seen that an ensemble of Bohmian trajectories will reproduce $R(x, t)^2 = |\psi(x, t)|^2$ at any time.

The computation of the mean value of a measurement

In chapter 3 I have shown that the definition of the measurement process in terms of Bohmian mechanics can be related with the position of the pointer of a measuring ap-

paratus. In other words, in order to predict observable results, Bohmian mechanics does not require the use of Hermitian operators and the wavefunction collapse as the orthodox quantum mechanics does. Nonetheless, Bohmian mechanics can also express the expectation value of an observable in terms of “local” observables which are directly deduced from “orthodox” Hermitian operators. Indeed, this is a quite usual way of introducing the Bohmian average of a measurement. Here, contrarily to chapter 3, I will follow this path to introduce the Bohmian expectation value of an observable.

The exact outcome of a particular quantum experiment described by the pure wavefunction $\psi(x, t)$ is uncertain. If we repeat a quantum experiment many times with exactly the same wavefunction $\psi(x, t)$, we will obtain different outcomes. The probabilistic information of the experiment can be treated to obtain the mean value. There are several equivalent ways for computing the mean value of the magnitude that we are measuring. We named this magnitude as the observable \hat{A} .

1. .. **Mean value from the list of outcomes and its probabilities:** After a large number N of repetitions of the same experiment, we can elaborate a list of the possible outcomes a_i with its occurrence probability P_i . From these data we can compute the mean value as:

$$\langle \hat{A} \rangle_{\psi} = \sum_{i=1}^N a_i P_i \quad (\text{A.15})$$

This is a standard (classical or a quantum) definition of the mean value.

2. .. **Mean value from the wavefunction and the operator:** According to the orthodox quantum theory, an observable is associated to a hermitian operator \hat{A} that describes the measurement process. Such operator determines the possible outcomes a_i and the eigenstates, u_i , with $\hat{A}|u_i\rangle = a_i|u_i\rangle$.

Therefore, $P_i = \langle \psi | u_i \rangle \langle u_i | \psi \rangle$ so that we can write:

$$\langle \hat{A} \rangle_{\psi} = \langle \psi | \left(\sum_{i=1}^N a_i \cdot |u_i\rangle \langle u_i| \right) | \psi \rangle = \langle \psi | \hat{A} | \psi \rangle \quad (\text{A.16})$$

where we use $a_i|u_i\rangle = \hat{A}|u_i\rangle$ and we have identified expression $\sum_{i=1}^N |u_i\rangle \langle u_i|$ as the identity because of the orthonormality of the eigenstates. Therefore, we can compute the mean value of an ensemble of experiments from (A.16) by only knowing the wavefunction and the operator (without knowing neither the eigenstates nor the outcome values and its probabilities). The reader can be surprised because we use a bra-ket notation in (A.16) instead of our wavefunction in the position

representation. The bra-ket notation provides a more compact notation. In any case, expression (A.16), can be rewritten in the position representation by write the hermitian operator \hat{A} in the position representation. Then, the mean value of this operator over the wavefunction $\psi(x, t)$ is given by:

$$\langle \hat{A} \rangle_\psi = \int_{-\infty}^{\infty} \psi^*(x, t) \hat{A} \left(x, -i\hbar \frac{\partial}{\partial x} \right) \psi(x, t) dx \quad (\text{A.17})$$

3. .. **Mean value from the Bohmian mechanics in the position representation** We can always write the hermitian operator \hat{A} an the mean value $\langle \hat{A} \rangle_\psi$ in the position representation. Then, the mean value of this operator over the wavefunction $\psi(x, t)$ is given by:

$$\langle \hat{A} \rangle_\psi = \int_{-\infty}^{\infty} \psi^*(x, t) \hat{A} \left(x, -i\hbar \frac{\partial}{\partial x} \right) \psi(x, t) dx \quad (\text{A.18})$$

Alternatively, the same mean value can be computed from Bohmian mechanics by defining an spatial average of a “local” magnitude $A_B(x)$ weighted by $R^2(x, t)$:

$$\langle \hat{A} \rangle_\psi = \int_{-\infty}^{\infty} R^2(x, t) A_B(x) dx \quad (\text{A.19})$$

In order to obtain the same value with (A.18) and (A.19), we can easily identify the “local” mean value $A_B(x)$ as:

$$A_B(x) = \text{Real} \left(\left[\frac{\psi^*(x, t) \hat{A} \left(x, -i\hbar \frac{\partial}{\partial x} \right) \psi(x, t)}{\psi^*(x, t) \cdot \psi(x, t)} \right]_{\psi(x, t) = R(x, t) e^{i \frac{S(x, t)}{\hbar}}} \right), \quad (\text{A.20})$$

where we take only the real part, $\text{Real}()$, because we know that the mean value is real, but expression (A.20) without $\text{Real}()$ can take complex values. In any case, it is clear that the integration of the imaginary part in (A.19) would give zero.

4. .. **Mean value from the Bohmian trajectories** For practical computations, we will compute the mean value using (A.19) with a finite number of Bohmian trajectories. Let us assume that we compute N trajectories $x[t]$. We will select the initial position x_{oi} of the Bohmian trajectories $x_i[t_o]$ according to the second postulate. Therefore, we can use expression (A.14) to rewrite $R^2(x, t)$ in (A.19). Finally, we obtain:

$$\langle \hat{A} \rangle_\psi = \lim_{N \rightarrow \infty} \frac{1}{N} \sum_{i=1}^N A_B(x_i[t]) \quad (\text{A.21})$$

By construction, in the limit $N \rightarrow \infty$, the value of expression (A.21) is identical to the value of (A.19).

Now, we provide several examples on how some common mean values are computed from the orthodox quantum formalism and from Bohmian trajectories. First, we compute the mean value of the position:

$$\langle x \rangle_\psi = \int_{-\infty}^{\infty} \psi^*(x, t) x \psi(x, t) dx, \quad (\text{A.22})$$

with $x_B(x) = x$ so that

$$\langle x \rangle_\psi = \int_{-\infty}^{\infty} R^2(x, t) x dx. \quad (\text{A.23})$$

Identically, the mean value of the momentum:

$$\langle p \rangle_\psi = \int_{-\infty}^{\infty} \psi^*(x, t) (-i\hbar \frac{\partial}{\partial x}) \psi(x, t) dx, \quad (\text{A.24})$$

with $p_B(x) = \partial S(x, t) / \partial x$ is

$$\langle p \rangle_\psi = \int_{-\infty}^{\infty} R^2(x, t) \frac{\partial S(x, t)}{\partial x} dx. \quad (\text{A.25})$$

For the classical potential energy, we have:

$$\langle V \rangle_\psi = \int_{-\infty}^{\infty} \psi^*(x, t) V(x, t) \psi(x, t) dx, \quad (\text{A.26})$$

with $V_B(x) = V(x, t)$ so that:

$$\langle V \rangle_\psi = \int_{-\infty}^{\infty} R^2(x, t) V(x, t) dx. \quad (\text{A.27})$$

Now, we compute the mean value of the kinetic energy:

$$\langle K \rangle_\psi = \int_{-\infty}^{\infty} \psi^*(x, t) \left(-\frac{\hbar^2}{2m} \frac{\partial^2}{\partial x^2} \right) \psi(x, t) dx. \quad (\text{A.28})$$

It is important to notice that the local mean value of the kinetic energy takes into account the Bohmian kinetic energy plus the quantum potential energy. In particular, $K_B(x)$ can be obtained from the expression:

$$K_B(x) = \text{Real} \left(-\frac{R(x, t) e^{-iS(x, t)/\hbar} \frac{\hbar^2}{2m} \left(\frac{\partial}{\partial x} \right)^2 R(x, t) e^{iS(x, t)/\hbar}}{R^2(x, t)} \right). \quad (\text{A.29})$$

The real part² of K_B is:

$$K_B = \left(\frac{\partial S(x, t)}{\partial x} \right)^2 + Q(x, t), \quad (\text{A.30})$$

so that, finally, we obtain the Bohmian expression of the mean kinetic energy of the ensemble of trajectories:

$$\langle K \rangle_\psi = \int_{-\infty}^{\infty} R^2(x, t) \left(\left(\frac{\partial S(x, t)}{\partial x} \right)^2 + Q(x, t) \right) dx. \quad (\text{A.31})$$

Finally, we compute the mean value of the current density operator. First, let us notice that probability density operator can be written as $|x\rangle\langle x|$ and its expected mean value is $\langle \psi | x \rangle \langle x | \psi \rangle = |\psi(x, t)|^2$ or, in the Bohmian language, $\langle \psi | x \rangle \langle x | \psi \rangle = R^2(x, t)$. The (hermitian) current operator can be written as $\hat{J} = 1/(2m)(|x\rangle\langle x|\hat{p} - \hat{p}|x\rangle\langle x|)$. It can be easily demonstrated that:

$$\langle J \rangle_\psi = J(x, t) = v(x, t)R^2(x, t) = \lim_{N \rightarrow \infty} \frac{1}{N} \sum_{i=1}^N v(x_i[t]) \cdot \delta(x - x_i[t]) \quad (\text{A.32})$$

The average value of the current density depends on the position and it is equal to the average Bohmian velocity multiplied by the square modulus of R . At a particular position “ x ”, this current is just the sum of all particles that reside at this position $x = x_i[t]$ at time t multiplied by their bohmian velocities $v(x_i[t])$.

A.3 Bohmian Mechanics for 1D many-particle non-relativistic systems

Most of our knowledge about the behavior of a quantum system has been understood for a simple systems composed of just one particle (i.e. the so-called single-particle systems discussed in the previous section). However, a single particle system is some kind of idealization of real systems. A macroscopic object is composed of a very large number of particles. This is true even for an atom which is composed of several protons and neutrons, plus few electrons.

²It can be demonstrated quite easily that the imaginary part of (A.29) is equal to the spatial derivative of the current that becomes zero when integrated over all space. We use that $J(x = \pm\infty, t) = 0$ which is always valid for wavefunction that are normalized to unity, but it is not true for other types of wavefunctions such as plane wave.

Many-particle quantum Hamilton-Jacobi equation

We start by introducing the polar form of the many-particle wavefunction $\psi(x_1, \dots, x_N, t) = R(x_1, \dots, x_N, t)e^{iS(x_1, \dots, x_N, t)/\hbar}$ into the (non-relativistic) many-particle Schrödinger equation

$$i\hbar \frac{\partial \psi(x_1, \dots, x_N, t)}{\partial t} = -\frac{\hbar^2}{2m} \sum_{i=1}^N \frac{\partial^2 \psi(x_1, \dots, x_N, t)}{\partial x_i^2} + V(x_1, \dots, x_N, t)\psi(x_1, \dots, x_N, t). \quad (\text{A.33})$$

Then, after a quite simple manipulation, one obtains from the imaginary part:

$$\frac{\partial R^2(x_1, \dots, x_N, t)}{\partial t} + \sum_{i=1}^N \frac{\partial}{\partial x_i} \left(\frac{1}{m} \frac{\partial S(x_1, \dots, x_N, t)}{\partial x_i} R^2(x_1, \dots, x_N, t) \right) = 0, \quad (\text{A.34})$$

where we recognize the velocity of the x_i particle as:

$$v_i(t) = \frac{1}{m} \frac{\partial S(x_1, \dots, x_N, t)}{\partial x_i}, \quad (\text{A.35})$$

and from the real part:

$$\frac{\partial S(x_1, \dots, x_N, t)}{\partial t} + \sum_{i=1}^N \frac{1}{2m} \frac{\partial^2 S(x_1, \dots, x_N, t)}{\partial x_i^2} + V(x_1, \dots, x_N, t) + Q(x_1, \dots, x_N, t) = 0 \quad (\text{A.36})$$

where we have defined the quantum potential as

$$Q(x_1, \dots, x_N, t) = \sum_{i=1}^N Q_i(x_1, \dots, x_N, t) \quad (\text{A.37})$$

with

$$Q_i(x_1, \dots, x_N, t) = -\frac{\hbar^2}{2m} \frac{\partial^2 R(x_1, \dots, x_N, t)/\partial x_i^2}{R(x_1, \dots, x_N, t)} \quad (\text{A.38})$$

Let us emphasize the similarities and differences between the classical potential energy $V(x_1, \dots, x_N, t)$ and the quantum potential energy $Q(x_1, \dots, x_N, t)$ that appears in (A.36). In principle, both, provides correlations among electrons because the dynamics of the x_i particle depends on the positions of the rest of the particles. In general, the term $V(x_1, \dots, x_N, t)$ can produce classical correlations and the term $Q(x_1, \dots, x_N, t)$ quantum (or nonclassical) correlations which are generally refereed as entanglement. The important point is that the classical correlations will be slower than light speed because the dependence of all variables in $V(x_1, \dots, x_N, t)$ imposes such restriction. For example, the potential energy that determines the electromagnetic interaction among different particles takes into account the distance among the particles to assure that the influence of one particle into the other is not faster than the light speed. However, such restriction

is not present in the quantum potential that is directly defined from the wave-function as expression (A.38), and therefore it does not vanish at large distances. Very far particles have an “*instantaneous correlation*”. In addition, let us notice that the quantum potential obtained from (A.38) with $R(x_1, \dots, x_N, t)$, or with $a \cdot R(x_1, \dots, x_N, t)$ under the condition $a \rightarrow 0$, is exactly the same. A typical example of this nonlocal characteristic is the quantum entanglement [139].

Solution of the many-particle Schrödinger equation from a coupled system of single-particle Schrodinger equations

As we have discussed, the main reason why the many-particle Schrödinger equation is practically unsolvable is because it seeks for a unique solution within the whole configuration space of all the particles $x_1, \dots, x_i, \dots, x_N$, while the classical equations seeks for one solution for each particle using a much smaller configuration space where all other particles are assumed as “known” parameters $\{x_1[t], \dots, x_{i-1}[t], x_i, x_{i+1}[t], \dots, x_N[t]\}$. The Newton solution of $x_i[t]$ just needs the spatial dependence of $V(x_1, \dots, x_N)$ on the variable x_i to make the derivative. The rest of spatial variables can be fixed to the particle positions $x_1 = x_1[t]$ (i.e. we do not need information on its spatial dependence for computing $x_i[t]$). The main idea behind the work developed in [67] is that any trajectory $x_a[t]$ that is computed from the many-particle wave-function $\psi(x_a, \vec{x}_b, t)$, where $\vec{x}_b[t] = x_1[t], \dots, x_{a-1}[t], x_{a+1}[t], \dots, x_N[t]$, can be alternatively computed from a much simpler single-particle wave-function $\psi_a(x_a, t) = \Psi(x_a, \vec{x}_b[t], t)$. It is quite trivial to realize that this is true. By definition, the angle $S_a(x_a, t)$ of $\psi_a(x_a, t)$ is identical to the angle $S(x_a, \vec{x}_b, t)$ of $\Psi(x_a, \vec{x}_b, t)$ when evaluated at $x_a, \vec{x}_b[t]$. Therefore, since the velocity of the trajectory $x_a[t]$ is computed from the spatial dependence of $S(x_a, \vec{x}_b, t)$ on x_a when all other positions are fixed at $\vec{x}_b = \vec{x}_b[t]$, the same velocity will be obtained from the spatial dependence of $S_a(x_a, t)$. Interestingly, $\psi_a(x_a, t)$ is a solution of single-particle (pseudo) Schrodinger equation because it depends only on time t and position x_a . Next, our effort will be knowing which is such single-particle equation.

First of all, it is easily verifiable that any (single-valued) function $\psi_a(x_a, t)$ which has well-defined (i) second order spatial derivative and (ii) first order temporal derivative, can be obtained from a Schrodinger like equation when the following potential energy $W(x_a, t)$ is used:

$$W(x_a, t) = \frac{i\hbar \frac{\partial \psi_a(x_a, t)}{\partial t} + \frac{\hbar^2}{2m} \frac{\partial^2 \psi_a(x_a, t)}{\partial x_a^2}}{\psi_a(x_a, t)} \quad (\text{A.39})$$

for $\psi_a(x_a, t) \neq 0$, and $W(x_a, t) = 0$ for $\psi_a(x_a, t) = 0$. In fact, it would be interesting to rewrite the expression of $W(x_a, t)$ in terms of the polar form of the wavefunction

$\psi(x_a, t) = R(x_a, t)e^{iS(x_a, t)/\hbar}$. We obtain for the real part,

$$Re[W(x_a, t)] = - \left(K_a(x_a, t) + Q_a(x_a, t) + \frac{\partial S(x_a, t)}{\partial x_a} \right) \quad (\text{A.40})$$

the Hamilton-Jacobi equation. However, we do also obtain $Im[W(x_a, t)]$ that accounts for the “strange” wavefunctions that do not preserve its total norm:

$$Im[W(x_a, t)] = \frac{\hbar}{2R_a^2(x_a, t)} \left(\frac{\partial R_a^2(x_a, t)}{\partial t} - \frac{\partial}{\partial x_a} \left(\frac{R_a^2(x_a, t)}{m} \frac{\partial S_a(x_a, t)}{\partial x_a} \right) \right) \quad (\text{A.41})$$

It can be easily verified that $Im[W(x_a, t)] = 0$ when the wavefunctions preserve the norm. Finally, we are interested in rewriting these expressions in terms of the global many-particle wave-function. Then, we realize that the total many-particle Schrödinger equation can be written in terms of a coupled single-particle pseudo-Schrödinger equations:

$$i\hbar \frac{\partial \psi_a(x_a, t)}{\partial t} = \left(-\frac{\hbar^2}{2m} \frac{\partial^2}{\partial x_a^2} + U_a(x_a, \vec{x}_b[t], t) + G_a(x_a, \vec{x}_b[t], t) + iJ_a(x_a, \vec{x}_b[t], t) \right) \psi_a(x_a, t), \quad (\text{A.42})$$

where we have defined

$$G_a(\vec{x}, t) = U_b(\vec{x}_b, t) + \sum_{k=1; k \neq a}^N \left(K_a(\vec{x}, t) + Q_a(\vec{x}, t) - \frac{\partial S(\vec{x}, t)}{\partial x_k} v_k(\vec{x}[t], t) \right), \quad (\text{A.43})$$

and

$$J_a(\vec{x}, t) = \sum_{k=1; k \neq a}^N \frac{\hbar}{2R^2(\vec{x}, t)} \left(\frac{\partial R^2(\vec{x}, t)}{\partial x_k} v_k(\vec{x}[t], t) - \frac{\partial}{\partial x_k} \left(\frac{R^2(\vec{x}, t)}{m} \frac{\partial S(\vec{x}, t)}{\partial x_k} \right) \right). \quad (\text{A.44})$$

In the previous equations we have defined $\vec{x} = \{x_a, \vec{x}_b\}$. In order to obtain these expressions, one has to carefully evaluate:

$$\frac{\partial S(x_a, \vec{x}_b[t], t)}{\partial t} = \left(\frac{\partial S(x_a, \vec{x}_b, t)}{\partial t} \right)_{\vec{x}_b = \vec{x}_b[t]} + \sum_{k=1}^N \frac{\partial S(x_a, \vec{x}_b[t], t)}{\partial x_k} v_k(\vec{x}[t], t), \quad (\text{A.45})$$

and use expression (A.35) evaluated at $\{x_a, \vec{x}_b[t]\}$. Identically for $\partial R^2(x_a, \vec{x}_b[t], t)/\partial t$ with expression (A.34).

It is interesting to understand what will be the solution $\psi_a(x_a, t)$ when the wavefunction is separable. Then, equation (A.5) is valid for each summand of the term of $G_a(x_a, \vec{x}_b[t], t)$, so that it can be written as:

$$G_a(x_a, \vec{x}_b[t], t) = - \sum_{k=1; k \neq a}^N \frac{dS_k(x_k[t], t)}{dt}. \quad (\text{A.46})$$

Then, a (real) time-dependent term (without any spatial dependence) appears in the potential energy of expression (A.42). It can be easily demonstrated that such term introduces a time-dependent term $\beta_a(t)$ into the phase of $\psi_a(x_a, t)$:

$$\beta_a(t) = - \sum_{k=1; k \neq a}^N \int_{t_0}^t \frac{dS_k(x_k[t'], t')}{dt} dt' = - \sum_{k=1; k \neq a}^N S_k(x_k[t'], t'). \quad (\text{A.47})$$

Identically, equation (A.4) is valid for each term of $J_a(x_a, \vec{x}_b[t], t)$, so that it can be written as:

$$J_a(x_a, \vec{x}_b[t], t) = - \sum_{k=1; k \neq a}^N \frac{\hbar}{2} \frac{d}{dt} \ln(R_k^2(x_k[t])). \quad (\text{A.48})$$

Using that $\ln(ab) = \ln(a) + \ln(b)$, then, we can obtain an $\alpha_a(t)$ term multiplying the wave function:

$$\alpha_a(t) = -\hbar \int_{t_0}^t \frac{d}{dt} \ln \left(\prod_{k=1; k \neq a}^N R_k(x_k[t'], t') \right) dt' = -\hbar \ln \left(\prod_{k=1; k \neq a}^N R_k(x_k[t'], t') \right). \quad (\text{A.49})$$

Finally, we obtain:

$$\psi_a(x_a, t) = \psi_1(x_1[t], t) \dots \psi_a(x_a, t) \dots \psi_N(x_N[t], t), \quad (\text{A.50})$$

certainly, the expected result.

In the rest of this section, I explain how the previous formulation of the many-particle Schrödinger equation is used in combination with our quantum approach to electron transport. The procedure that I will explain here have similarities with the original work of Kohn and Sham on the DFT [22]: the formidable simplification on the many-particle computations comes at the price that some terms of the potential energy of the corresponding single-particle Schrödinger equations are unknown [the exchange-correlation functional in the DFT and, here, the terms (A.43) and (A.44)].

I consider a system of N electrons with Coulomb interaction but without exchange interaction. As mentioned, the solution of Eq. (A.42) needs educated guesses for the terms (A.43) and (A.44). Since no exchange interaction is considered, the correlation between the x_a electron and the rest is mainly contained in the term $U_a(x_a, \vec{x}_b[t], t)$. Thus, we can assume a zero-order Taylor expansion of the terms (A.43) and (A.44) in the variable x_a around $x_a[t]$ to obtain $G_a(x_a, \vec{x}_b[t], t) \approx G_a(x_a[t], \vec{x}_b[t], t)$ and $J_a(x_a, \vec{x}_b[t], t) \approx J_a(x_a[t], \vec{x}_b[t], t)$ [67]. Then, the wave-function solution of (A.42) can be written as

$\psi_a(x_a, t) \approx \tilde{\psi}_a(x_a, t) \cdot \exp[\frac{\alpha_a(t)}{\hbar} - \frac{i\beta_a(t)}{\hbar}]$ where $\alpha_a(t) = \int_{t_0}^t J_a(x_a[t'], x_b[t'], t') \cdot dt' + \alpha_a(t_0)$ and $\beta_a(t) = \int_{t_0}^t G_a(x_a[t'], x_b[t'], t') \cdot dt' + \beta_a(t_0)$. The wave function $\tilde{\psi}_a(x_a, t)$ is the solution of Eq. (A.42) with $U_a(x_a, \vec{x}_b[t], t) = u_a(x_a, t)$. Since the velocity in (A.35) does not depend on the terms $\alpha_a(t)$ and $\beta_a(t)$, we do not have to compute them explicitly. Finally, if we fix the initial many-particle wave function $\psi(x_a, \vec{x}_b, t_0) = \chi_1(x_1, t_0) \cdots \chi_N(x_N, t_0)$ as a product of single-particle wave functions. Then, the initial boundary condition for solving $\tilde{\psi}_a(x_a, t_0)$ is just $\chi_a(x_a, t_0)$.

APPENDIX B

Electron injection model for non zero-external impedance systems

A time-dependent degenerate (i.e. taking into account Pauli the exclusion principle) injection model for electron devices is presented here under the assumption that the sample is part of a circuit with non zero external impedance (see figure B.0.1). In this appendix, I will present a brief summary of such an injection model and its ability to determine either the average value of the current or its time-dependent fluctuations for non-zero external impedance systems and also its limit for zero external impedance systems. There are well-know analytical expressions for the average current and its fluctuations at zero frequency in either equilibrium or far from equilibrium situations, when the zero-external impedance assumption is considered. We will reproduce those expressions here as a particular case.

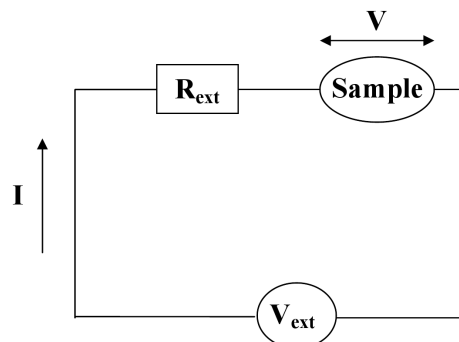


Figure B.0.1: Schematic description of a circuit with non-zero external impedance

Electron injection probability

The rate and randomness of the injection of electrons into the sample can be modeled through the following binomial probability $P(E, N, \tau)$ defined in Ref. [140]:

$$P(E, N, \tau) = \frac{M_\tau!}{N! \cdot (M_\tau - N)!} f_{S/D}(E)^N (1 - f_{S/D}(E))^{M_\tau - N} \quad (\text{B.1})$$

This expression defines the probability that N electrons with wave-vectors in the range $k_x \in [k_{ox}, k_{ox} + \Delta k_x)$ are injected into the sample during the time interval τ . The parameter M_τ is the number of attempts of injecting electrons during the previous time interval τ , defined as a number that rounds the quotient τ/t_0 to the nearest natural number towards zero. The number of injected electrons can be $N = 1, 2, \dots \leq M_\tau$. The time t_0 is the minimum temporal separation between the injection of two electrons into the particular cell phase-space cell $k_x \in [k_{ox}, k_{ox} + \Delta k_x)$ and $x \in [x_o, x_o + \Delta x)$. For a 1D system, the value of t_0 can be easily estimated. The number of electrons n_{1D} in the particular phase space cell $\Delta k_x \cdot \Delta x$ is $n_{1D} = 2 \cdot \Delta k_x \cdot \Delta x / (2\pi)$ where we consider a factor 2 for spin degeneracy [140]. These electrons have been injected into Δx during the time interval Δt defined as the time needed for electrons with velocity $v_x = \Delta x / \Delta t = \hbar k_x / m_t$ to travel a distance Δx . Therefore, the minimum temporal separation, t_0 , between the injection of two electrons into the previous particular cell is Δt divided by the maximum number n_{1D} of electrons:

$$t_0(k_x)|_{1D} = \frac{\Delta t}{n_{1D}} = \left(\frac{1}{\pi} \frac{\hbar k_x}{m_t} \Delta k_x \right)^{-1} \quad (\text{B.2})$$

The practical application of such definition of t_0 requires a mesh with a small step Δk_x on all possible values of k_x . Identically, for a 2D and 3D system, we obtain:

$$t_0(y, k_x, k_y)|_{2D} = \frac{\Delta t}{n_{2D}} = \left(\frac{1}{2\pi^2} \frac{\hbar k_x}{m_t} \Delta y \Delta k_x \Delta k_y \right)^{-1} \quad (\text{B.3})$$

and

$$t_0(y, z, k_x, k_y, k_z)|_{3D} = \frac{\Delta t}{n_{3D}} = \left(\frac{1}{4\pi^3} \frac{\hbar k_x}{m_t} \Delta y \Delta z \Delta k_x \Delta k_y \Delta k_z \right)^{-1} \quad (\text{B.4})$$

On the other hand, the function $f_s(E)$ that appears in (B.1) determines the probability that a state with kinetic energy E measured from the bottom of the conduction band $-q \cdot V_S(t)$ is occupied by an electron that will effectively enter into the simulation box. In particular, we assume that such probabilities is determined by half of the Fermi distribution:

$$f_S(E) = \frac{1}{1 + \exp\left(\frac{E - F_S^{inj}(t) + q \cdot V_S(t)}{k_B \cdot \Theta}\right)} \quad \text{for } E = E(\vec{k}) \text{ with } k_x > 0 \quad (\text{B.5})$$

where the electron wave-vector \vec{k} is related with the "kinetic" energy by the appropriate energy dispersion relationship $E(\vec{k})$. The term $F_S^{inj}(t)$ is defined here as the source injecting energy level and it determines how to increase the rate of injection of electrons, while respecting the Pauli restriction. This restriction implies that injecting two electrons with identical velocity have to be injected with a temporal separations equal or larger than the t_0 . In order to avoid confusion, we avoid the name electrochemical-potential for such energy $F_S^{inj}(t)$ because (B.5) does not refer to all electrons, but only to those with $k_x > 0$. In addition, close to the active region the electron distribution for $k_x < 0$ will be quite unpredictable (see insets of figure 18 in ref. [65]). We reserve the name electrochemical-potential to the energy levels of the "thermalized" energy distribution deep inside the reservoirs, at $x = \mp L_C$. In other words, the parameter $F_S^{inj}(t)$ is a parameter that control the rate of injection of electrons in the border of the simulation box. Equivalently, the electrons injected from the drain have an energy distribution determined by:

$$f_D(E) = \frac{1}{1 + \exp\left(\frac{E - F_D^{inj}(t) + q \cdot V_D(t)}{k_B \cdot \Theta}\right)} \quad \text{for } E = E(\vec{k}) \text{ with } k_x < 0 \quad (\text{B.6})$$

with $F_D^{inj}(t)$ the drain injecting energy level.

It is very instructive to understand the Binomial distribution of the injection process, expression (B.1), as a consequence of the discreteness of the electron charge. For a particular cell, at zero temperature, we inject an electron every interval of time t_0 . The average current per cell is e/t_0 . At room temperature, the average current is lower, $e \cdot f(E)/t_0$, because of the uncertainty in the occupation. However, it is not possible to inject a fractional charge $e \cdot f(E)$ into the system at each interval of time t_0 (i.e. the electron charge is indivisible). Therefore, at each interval of time t_0 , either we inject the full charge, e (if the state is occupied), or we do not inject charge (if the state is empty) according to the probability $f(E)$.

Test for zero external impedance

As a simple test of our injection model in the zero-external impedance limit, we compute analytically the current and its fluctuations (i.e. the noise) for a one-subband ballistic 1D system. According to the zero external impedance, we assume that $F_{S/D}^{inj}(t) \rightarrow E_F$ (where E_F is the Fermi level) and that $V_{S/D}(t) \rightarrow V_{S/D}^{ext}$, where $V_{S/D}^{ext}$ are the external applied voltages in (B.5) and (B.6). We assume a transmittance equal to unity. For such

conditions, the injection probability and the transmitting probability are identical and there are well-known analytical results in the literature for both, average current and noise [8, 11].

The average current $\langle I \rangle$ is an experimental measure of the charged transmitted through the system during a long time interval. For our ballistic system, the charge transmitted through the source is just the charge injected over the barrier. Therefore:

$$\langle I \rangle = \lim_{\tau \rightarrow \infty} e \sum_E \frac{E_N[\tau, E]}{\tau} \quad (\text{B.7})$$

An irrelevant negative sign (the current and the electron flow have opposite direction) is omitted in (B.7). The average number $E_N[\tau, E]$ of injected particles during the time interval τ is computed from the probability $P(E, N, \tau)$:

$$E_N[\tau, E] = \sum_{N=0}^{N=\infty} P(E, N, \tau) \cdot N \quad (\text{B.8})$$

As we mentioned before, we divide the whole phase-space into cells with a small Δk_x , so that all electrons in the cell have roughly the same energy. The average number of injected particles with wave vector k_x during the time τ can be computed from (B.8) as $E_N[\tau, E] = f_S(E) \cdot \tau/t_o(k_x)$ for each cell of the source injection. Previous expression is just the mean value of the Binomial distribution (B.1) where $f_S(E)$ is defined by expressions (B.5). From (B.7), the average current of each k_x -phase-space cell can be computed as $\langle I \rangle^{k_x} = e \cdot f_S(E)/t_o(k_x)$. The sum over all phase-space cells with $k_x > 0$, $\langle I \rangle = \sum_{k_x} \langle I \rangle^{k_x}$, does exactly reproduce the Landauer average current. The drain current is computed equivalently. The total current is the source component minus the drain component:

$$\langle I \rangle = 2e/h \int_0^\infty (f_S(E) - f_D(E)) \cdot dE \quad (\text{B.9})$$

where we have used $dE \approx \hbar^2 k_x \cdot \Delta k_x / m_t$ and $1/t_o(k_x) = \hbar k_x \cdot dk_x / (\pi \cdot m_t)$. This is just expressions [49] and [47] in ref. [11] for a transmission coefficient equal to one. For low temperature (i.e. $f(E) = 1$ for all injected electrons), we obtain the well-known Landauer conductance $G = 2e^2/h$.

For the ballistic devices, the one-side power spectral density of the current fluctuations at zero (low) frequency can be also obtained from probability (B.1) as:

$$S_I(0) = \lim_{\tau \rightarrow \infty} 2 \cdot e^2 \sum_E \frac{E_{N^2}[\tau, E] - (E_N[\tau, E])^2}{\tau}, \quad (\text{B.10})$$

where we defined $E_{N^2}[\tau, E]$ as:

$$E_{N^2}[\tau, E] = \sum_{N=0}^{N=\infty} P(E, N, \tau) \cdot N^2. \quad (\text{B.11})$$

For the binomial distribution of expression (B.1), we obtain $E_{N^2}[\tau, E] - (E_N[\tau, E])^2 = f_S(E) \cdot (1 - f_S(E)) \cdot \tau/t_o(k_x)$. Then, using (B.10), we found $S_I^{k_x}(0) = 2 e^2 \cdot f_S(E) \cdot (1 - f_S(E)) / t_o(k_x)$ for the source injection. Identical results are obtained for the drain injection. Since there is no drain-source correlation in our simple ballistic model, the total power is the sum of both. After integration over all energies, we obtain:

$$S_I(0) = (4 e^2/h) \int_0^\infty (f_S(E) \cdot (1 - f_S(E)) + f_D(E) \cdot (1 - f_D(E))) \cdot dE \quad (\text{B.12})$$

This expression does exactly reproduce Büttiker results for a system with transmission coefficient equal to one. See expression (61) in Ref. [8]. Expression (B.12) includes the thermal and the shot noise (i.e. it is valid at equilibrium and far from equilibrium). Under equilibrium conditions, the previous result reproduces the Nyquist-Johnson thermal noise, as can be shown by introducing the identity $-k_B T \cdot \partial f(E)/\partial E = f(E) \cdot (1 - f(E))$ into the previous result.

In conclusion, the (time-dependent) injection model discussed here correctly accounts for the Pauli correlations amount electrons under the assumption that the active region is part of a circuit with zero external impedance. In this case, the voltages applied to the sample can be viewed as a fixed non-fluctuating quantity and the noise properties are determined only by the Pauli correlations discussed above. In general, the sample is a part of a larger circuit (with non-zero external impedances). Then, the current fluctuations in the sample, implies voltage fluctuations in the leads [through the time-dependence of $V_S(t)$ and $V_D(t)$ in (B.5) and (B.6)] that, in turn, implies fluctuations on the injecting probabilities into the sample [through expression (B.1)] and the current in the sample. The complicated correlations that appears between sample and leads shows the importance of such time-dependent correlations to correctly achieve the “current conservation” requirement.

APPENDIX C

Classical and quantum expectation values for mixed open systems

In this section I provide a formal (in contraposition to the practical discussion of sections 3.2.2 and 3.2.3) discussion of the expectation value of an observable $A(t)$ for classical and quantum mixed open systems.

Classical expectation values of mixed states in open systems

Let me first reintroduce the concept of the *many-particle distribution function* (already defined in expression (1.2)). That is $f(\vec{r}_{1,k}, \dots, \vec{r}_{W',k}, t)$, i.e. the probability of finding a carrier distribution with locations centered at $(\vec{r}_{1,k}, \dots, \vec{r}_{W',k}, t)$ and time t , where the subindex W' refers to the total number of variables conforming a whole closed circuit plus the variables conforming the measuring apparatus.

Now, we know that, the many-particle distribution function, f , fulfills, by construction, the normalization relation

$$1 = \sum_{k=1}^{\infty} f(\vec{r}_{1,k}, \dots, \vec{r}_{p1}, \dots, \vec{r}_{pN}, \dots, \vec{r}_{W',k}, t). \quad (\text{C.1})$$

We can extend the previous expression to the case of an open system subject to an stochastic injection of electrons as

$$1 = \sum_{k=1}^{\infty} \sum_{N(t)=1}^{\infty} f(\vec{r}_{1,k}, \dots, \vec{r}_{N(t),k}, t), \quad (\text{C.2})$$

where now $f(\vec{r}_{1,k}, \dots, \vec{r}_{N(t),k}, t)$ is defined as the probability of finding $N(t)$ electrons within the opened region with positions $\{\vec{r}_{1,k}, \dots, \vec{r}_{N(t),k}\}$ at time t . Equation (C.2) emphasizes

the fact that, since our knowledge on how the electrons are distributed outside the open system is certainly statistical, our knowledge on how are distributed those inside becomes also unprecise. As I have already mentioned in chapter 3, such a transference of uncertainty from the environment into the active region of an electron device is partially introduced by the stochastic injection of electrons (see figure 3.1.1).

As discussed at the beginning of chapter 3, we can now relate an outcome a_i of the observable A at time t to the position of the pointer of the measuring apparatus $\{\vec{r}_{p1,i}[t], \dots, \vec{r}_{pN,i}[t]\}$. Such a particular microstate of the pointer, however, can be identified, in general, to more than one microstate of the open system. For any particular number of electrons conforming the open system, $N(t)$, the s microstates $\{\vec{r}_{1,k}[t], \dots, \vec{r}_{N(t),k}[t]\}$, with $k = k_{1,i,N(t)}, \dots, k_{s,i,N(t)}$ (where the value of s depends, at the same time, on the subindexes i and $N(t)$) are all giving rise exactly to the same outcome a_i . Expression (3.2) can then be written in terms of the many-particle distribution function of the open system as

$$\langle A(t) \rangle = \sum_{i=1}^{\infty} \sum_{N(t)=1}^{\infty} \sum_{k=k_{1,i,N(t)}}^{k_{s,i,N(t)}} f'_A(\vec{r}_{1,k}[t], \dots, \vec{r}_{N(t),k}[t]) \cdot f(\vec{r}_{1,k}[t], \dots, \vec{r}_{N(t),k}[t]). \quad (\text{C.3})$$

Comparing expressions (C.3) and (3.2), we realize that

$$P(a_i, t) = P(\vec{r}_{p,i}[t]) = \sum_{N(t)=1}^{\infty} \sum_{k=k_{1,i,N(t)}}^{k_{s,i,N(t)}} f(\vec{r}_{1,k}[t], \dots, \vec{r}_{N(t),k}[t]) \quad (\text{C.4})$$

is the probability of finding the outcome a_i , when measuring A at time t , in terms of the classical trajectories simulated within our open system.

In expression (C.3), it is implicit that, in principle, we can compute the expectation value of an observable without explicitly simulating the degrees of freedom of the “pointer” of the measuring apparatus. Such an affirmation could seem a little bit tricky. Indeed, although we can easily find an expression for the function of the pointer positions f_A (given directly by the functionality of the measuring apparatus), it is not obvious how to find the function f'_A .

Quantum expectation values of mixed states in open systems

Here, I will first discuss the quantum expectation of an observable by means of orthodox quantum mechanics. Later, in contraposition, I will introduce the same concept in terms of bohmian trajectories.

The quantum expectation value of an observable result in orthodox quantum mechanics

We can establish an analogy between the classical many-particle distribution function introduced in (C.1) and the quantum many-particle density matrix, already introduced in section 1.3, i.e.

$$\hat{\rho} = \sum_{k=1}^{\infty} P(\varphi_k, t) |\varphi_k(t)\rangle \langle \varphi_k(t)|. \quad (\text{C.5})$$

In particular, expression (C.5) tells us that in orthodox quantum mechanics the definition of a particular microstate of the system is no longer defined by the distribution of particles in the phase-space configuration but by the wave functions $\varphi_k(t)$, (i.e. $\{\vec{r}_{1,k}, \dots, \vec{r}_{W',k}, t\} \rightarrow \varphi_k(t)$).

Now, the expectation value of the operator $\hat{Q}(\vec{r}_1, \dots, \vec{r}_{W'}) = |\vec{r}_1, \dots, \vec{r}_{W'}\rangle \langle \vec{r}_1, \dots, \vec{r}_{W'}|$ (where, again, the subindex W' refers to the total number of particles conforming the whole closed circuit plus those of the measuring apparatus) can be defined in terms of the density matrix as:

$$1 = \text{tr} \left(\hat{\rho} \cdot \hat{Q}(\vec{r}_1, \dots, \vec{r}_{W'}) \right) = \sum_{k=1}^{\infty} P(\varphi_k, t) \int_{-\infty}^{+\infty} d^3 r_1 \cdots d^3 r_{W'} |\varphi_k(\vec{r}_1, \dots, \vec{r}_{W'}, t)|^2, \quad (\text{C.6})$$

where I have used the cyclic property of the trace [139]. Expression (C.6) can be understood as the quantum counterpart of the classical equality (C.1). However, while we can establish a direct analogy between $f(\vec{r}_{1,k}, \dots, \vec{r}_{W',k}, t)$ and $P(\varphi_k, t)$, we have an additional uncertainty with a pure quantum origin, $|\varphi_k(\vec{r}_1, \dots, \vec{r}_{W'}, t)|^2$, that has not any classical counterpart. Even if we could have total confidence on the definition of the microstate occupied by the system, let me say φ_k ($P(\varphi_j, t)$ is 0 for all unoccupied states and 1 for the single occupied state k), then, contrarily to the classical case, we would be still dealing with some amount of uncertainty coming from the wave nature of the carriers, $|\varphi_k(\vec{r}_1, \dots, \vec{r}_{W'}, t)|^2$. In other words, a *pure density matrix* contains an intrinsic uncertainty described by the square modulus of the wave function, i.e.

$$1 = \left(\hat{\rho}_{\text{pure}} \hat{Q}(\vec{r}_1, \dots, \vec{r}_{W'}) \right) = \int_{-\infty}^{+\infty} d^3 r_1 \cdots d^3 r_{W'} |\varphi(\vec{r}_1, \dots, \vec{r}_{W'}, t)|^2 \quad (\text{C.7})$$

We can now extend expression (C.6) to the case of an open system subject to an

stochastic injection of electrons as

$$1 = \text{tr} \left(\hat{\rho} \cdot \hat{Q}(\vec{r}, t) \right) = \sum_{k=1}^{\infty} \sum_{N(t)=1}^{\infty} P(\varphi_{N(t),k}, t) \int_{-\infty}^{+\infty} d^3 r_1 \cdots d^3 r_{N(t)} \left| \varphi_{N(t),k}(\vec{r}_1, \dots, \vec{r}_{N(t)}, t) \right|^2, \quad (\text{C.8})$$

where $\varphi_{N(t),k}(t)$ is now the k -th many-particle wave function describing $N(t)$ electrons at time t ¹. Although $P(\varphi_{N(t),k}, t)$ has a clear analogy in classical systems $f(\vec{r}_{1,k}, \dots, \vec{r}_{N(t),k}, t) \rightarrow P(\varphi_{N(t),k}, t)$, again we cannot find a classical counterpart for the quantum probability distribution $|\varphi_{N(t),k}(\vec{r}_1, \dots, \vec{r}_{N(t)}, t)|^2$. Therefore, contrarily to the classical case, due to the uncertainty related to the wave nature of electrons, we cannot associate the outcome a_i of an observable A to a particular microstate of the system anymore (the outcome of the quantum measurement of a pure state is still uncertain). Instead, according to the orthodox quantum theory, an observable A is associated to an hermitian operator \hat{A} which describes the measurement process². Such an operator determines the possible outcomes a_i and the eigenstates, u_i , with $\hat{A}|u_i\rangle = a_i|u_i\rangle$. Therefore, the expectation value of \hat{A} , i.e.

$$\langle \hat{A}(t) \rangle = \text{tr} \left(\hat{\rho} \hat{A}(t) \right) = \sum_{k=1}^{\infty} \sum_{N(t)=1}^{\infty} P(\varphi_{N(t),k}, t) \langle \varphi_{N(t),k} | \hat{A}(t) | \varphi_{N(t),k} \rangle, \quad (\text{C.9})$$

can be written as

$$\langle \hat{A}(t) \rangle = \sum_{i=1}^{\infty} a_i \sum_{k=1}^{\infty} \sum_{N(t)=1}^{\infty} P(\varphi_{N(t),k}, t) \left| \langle u_i | \varphi_{N(t),k} \rangle \right|^2, \quad (\text{C.10})$$

where I have used the identity relation $\mathbb{I} = \sum_{i=1}^{\infty} |u_i\rangle \langle u_i|$ defining the orthonormality of the eigenstates u_i . Now, comparing equation (C.10) with expression (3.2) we can state the next equality

$$P(a_i, t) = \sum_{k=1}^{\infty} \sum_{N(t)=1}^{\infty} P(\varphi_{N(t),k}, t) \left| \langle u_i | \varphi_{N(t),k} \rangle \right|^2, \quad (\text{C.11})$$

As in (C.3), equation (C.10) expresses the probability of measuring a particular observable result a_i as a function of the uncertainties involved in our quantum open system, one

¹For a quantum system, the number of particles inside the volume $N(t)$ has not only a dependence on time, but a dependence on all particle positions. In any case, since our quantum solution will deal with quantum (Bohm) trajectories (rather than wave-functions), the simple notation mentioned here is appropriate for the classical and quantum algorithms.

²Recall that the ‘‘orthodox’’ time-evolution of a wavefunction is governed by two different dynamical laws. First, there is a dynamical (deterministic) evolution according to the Schrödinger equation. Second, there is an (stochastic) evolution known as ‘‘collapse’’ of the wavefunction when it interacts with a measurement apparatus

with a classical counterpart and another with a pure quantum origin. However, expression (C.10) does not say anything about any “pointer” position or a measuring apparatus. The measurement process explained by orthodox quantum mechanics states that we measure directly an observable instead of the position of a “pointer”, and furthermore, it is done by a rather strange process called wavefunction collapse.

The quantum expectation value of an observable result in Bohmian mechanics

Whenever we can express the operator \hat{A} as a function of the position operator \hat{X} , i.e. $\hat{A} = f'_A(\hat{X})$, then we can assure that the eigenstates of \hat{A} are also eigenstates of the position operator, i.e. $f'_A(\hat{X}) |\vec{r}_{1,k}, \dots, \vec{r}_{N(t),k}\rangle = f'_A(\vec{r}_{1,k}, \dots, \vec{r}_{N(t),k}) |\vec{r}_{1,k}, \dots, \vec{r}_{N(t),k}\rangle$. Therefore, from (C.9) we can write the expectation value of \hat{A} in (C.9) as

$$\langle f'_A(\hat{X}) \rangle = \sum_{k=1}^{\infty} P(\varphi_k, t) \int_{-\infty}^{+\infty} d^3\vec{r}_1 \cdots d^3\vec{r}_{N(t)} f'_A(\vec{r}_{1,k}, \dots, \vec{r}_{N(t),k}) \cdot |\varphi_k(\vec{r}_{1,k}, \dots, \vec{r}_{N(t),k}, t)|^2, \quad (\text{C.12})$$

where I have used the identity operator $\mathbb{I} = \int_{-\infty}^{+\infty} |\vec{r}_1, \dots, \vec{r}_{N(t)}\rangle \langle \vec{r}_1, \dots, \vec{r}_{N(t)}| d^3r_1 \cdots d^3r_{N(t)}$.

In the predictions of Bohmian mechanics concerning the result of a quantum experiment, it is assumed that, prior to the experiment, the positions of the particles of the system involved are randomly distributed according to Born’s statistical law. Then, according to the quantum equilibrium hypothesis (also called the second postulate of Bohmian mechanics, i.e. expression (A.14) in Appendix A), the relation between the quantum trajectories and the modulus of the wave function in the position representation is:

$$R_k^2(\vec{r}_1, \dots, \vec{r}_{N(t)}, t) = |\varphi_k(\vec{r}_{1,k}, \dots, \vec{r}_{N(t),k}, t)|^2 = \lim_{G \rightarrow \infty} \frac{1}{G} \sum_{g=1}^G \prod_{j=1}^{N(t)} \delta(\vec{r}_{j,k} - \vec{r}_{j,k,g}[t]), \quad (\text{C.13})$$

where the summation over trajectories (referred with the subindex g) implicitly accounts for the shape of the initial wave function. Indeed, expression (C.13) can be alternatively written as

$$R_k^2(\vec{r}_1, \dots, \vec{r}_{N(t)}, t) = \sum_{l=1}^{\infty} \prod_{j=1}^{N(t)} |\varphi(\vec{r}_{1,k}, \dots, \vec{r}_{N(t),k}, t_0)|^2 \delta(\vec{r}_{j,k} - \vec{r}_{j,k,l}[t]). \quad (\text{C.14})$$

Now, if we introduce expression (C.14) into (C.12) we obtain

$$\langle f'_A(\hat{X}) \rangle = \sum_{k=1}^{\infty} \sum_{l=1}^{\infty} f'_A(\vec{r}_{1,k,l}[t], \dots, \vec{r}_{N(t),k,l}[t]) \cdot P(\varphi_k, t) \cdot |\varphi_k(\vec{r}_{1,k,l}, \dots, \vec{r}_{N(t),k,l}, t_0)|^2. \quad (\text{C.15})$$

In expression (C.15), each value of $f'_A(\vec{r}_{1,k,l}[t], \dots, \vec{r}_{N(t),k,l}[t])$ corresponds to a particular outcome a_i corresponding to a particular position of the pointer of the measuring apparatus $\{\vec{r}_{p1,i}[t], \dots, \vec{r}_{pN,i}[t]\}$. Indeed, such a particular microstate of the pointer can correspond, again, to more than one microstate of the open system $\{\vec{r}_{1,k,l}[t], \dots, \vec{r}_{N(t),k,l}[t]\}$. For each initial wave function, $\varphi_{k,N(t)}$, all the above microstates with $l = l_{1,i,N(t),k}, \dots, l_{s,i,N(t),k}$ (where the value of s depends, at the same time, on the subindexes i , $N(t)$, and k), give rise to the same outcome a_i . Expression (3.2) can then be written for quantum open systems in terms of bohmian trajectories as

$$\langle A(t) \rangle = \sum_{i=1}^{\infty} \sum_{N(t)=1}^{\infty} \sum_{k=1}^{\infty} \sum_{l=l_{1,i,N(t),k}}^{l_{s,i,N(t),k}} f'_A(\vec{r}_{1,k,l}[t], \dots, \vec{r}_{N(t),k,l}[t]) \cdot P(\varphi_{N(t),k}, t) \cdot |\varphi_{N(t),k}(\vec{r}_{1,k,l}, \dots, \vec{r}_{N(t),k,l}, t_0)|^2. \quad (\text{C.16})$$

Now, comparing from (C.16) and (3.2), we can identify

$$P(a_i, t) = P(\vec{r}_{p,i}[t]) = \sum_{N(t)=1}^{\infty} \sum_{k=1}^{\infty} \sum_{l=l_{1,i,N(t),k}}^{l_{s,i,N(t),k}} P(\varphi_{N(t),k}, t) \cdot |\varphi_{N(t),k}(\vec{r}_1, \dots, \vec{r}_{N(t)}, t_0)|^2, \quad (\text{C.17})$$

as the probability of finding the outcome a_i when measuring the observable A at time t in terms of the bohmian trajectories explicitly simulated in our open system.

Let me now compare expression (C.16) with its classical counterpart, expression (C.3). It can be seen that they are very similar in structure. Indeed, the only difference between them is the additional summation over quantum trajectories in (C.16) (referred with the subindex l) weighted by the square modulus of the initial wave function $|\varphi_{N(t),k}(\vec{r}_{1,k,l}, \dots, \vec{r}_{N(t),k,l}, t_0)|^2$.

APPENDIX D

Publications, Conferences and Book chapters

Publications

- A*:** G. Albareda, H. López, X. Cartoixà, J. Suñé, and X. Oriols, “*Time-dependent boundary conditions with lead-sample Coulomb correlations: Application to classical and quantum nanoscale electron device simulators*”, Phys. Rev. B (Accepted).
- B*:** G. Albareda, X. Saura, X. Oriols, and J. Suñé, “*Many-particle Transport in the Channel of Quantum Wire Double-Gate MOSFETs with Charged Atomistic Impurities*”, J. Appl. Phys. (Accepted).
- C:** G. Albareda, A. Alarcón, and X. Oriols, “*Electric Power in Nanoscale Devices with Full Coulomb Interaction*”, Int. J. Numer. Model. DOI: 10.1002/jnm.748 (2010).
- D:** G. Albareda, J. Suñé, and X. Oriols, “*Many-particle Hamiltonian for Open Systems with Full Coulomb Interaction: Application to Classical and Quantum Time-dependent Simulations of Nanoscale Electron Devices*”, Phys. Rev. B 79, 075315 (2009).
- E:** G. Albareda, D. Jiménez, and X. Oriols, “*Intrinsic Noise in Aggressively Scaled Field-effect Transistors*”, J. Stat. Mech. (2009) P01044.
- F:** G. Albareda, J. Suñé, and X. Oriols, “*Monte Carlo simulations of nanometric devices beyond the mean-field approximation*”, J. Comput. Electron. 7, 197 (2008).
- G*:** H. López, G. Albareda, X. Cartoixà, J. Sué, and X. Oriols, “*Boundary conditions with Pauli Exclusion and Charge Neutrality: Application to the Monte Carlo Simulation of Ballistic Nanoscale Devices*”, J. Comput. Electron. 7, 213 (2008).

* **NOTE:** The articles marked with an asterisk will not be considered as fundamental part of the thesis due to regulation reasons. Furthermore, since some of them are not already in press, due to their extension, they will be included in the attached CD.

Conferences

- C1:** X. Oriols, F. Traversa, A. Alarcón and G. Albareda, “*Quantum many-particle computations with Bohmian trajectories: Application to electron transport in nanoelectronic devices*”. Workshop on Quantum Trajectories, Bangor, Wales (UK) Jul/2010.
- C2:** G. Albareda, H. López, X. Cartoixà, J. Suñé, and X. Oriols, “*Boundary conditions for nanoscale electron devices with realistic lead-sample Coulomb correlations in small simulation boxes*”. Nanospain 2010, Malaga (Spain). Mar/2010.
- C3:** E. Buccafurri, F.L. Traversa, X. Oriols, A. Alarcón, G. Albareda, R. Clerc, F. Calmon and A. Poncet, “*High frequency resonant tunneling behavior: Testing an analytical small signal equivalent circuit with time dependent many-particle quantum simulations*”. Nanospain 2010, Malaga (Spain). Mar/2010.
- C4:** G. Albareda and X. Oriols, “*Many-particle effects in the electric power of nanoscale open systems*”. Trends in Nanotechnology 2009, Barcelona (Spain). Sep/2009.
- C5:** A. Benali, G. Albareda, A. Alarcón, M. Aghoutane and X. Oriols, “*High frequency modeling of classical and quantum nanoscale electron devices*”. Trends in Nanotechnology 2009, Barcelona (Spain) 2009. Sep/2009
- C6:** G. Albareda, X. Saura, X. Oriols and J. Suñé, “*Monte Carlo modelling of electron transport in Si nanowires in presence of atomistic impurities*”. Trends in Nanotechnology 2009, Barcelona (Spain) 2009. Sep/2009
- C7:** G. Albareda and X. Oriols, “*A Novel Approach for Many-electron transport in Nanoelectronic Devices with full Coulomb Interaction*”. Nanospain 2009, Zaragoza (Espaa). Mar/2009.
- C8:** G. Albareda, A. Alarcón and X. Oriols, “*Electric power in ballistic devices: A reformulation with full Coulomb interaction*”. 7th Conferencia de dispositivos electrónicos, Santiago de Compostela (Espaa). Feb/2009.

- C9:** A. Alarcón, A. Benali, G. Albareda and X. Oriols, “*On the computation of high frequency current in nanoelectronic ballistic devices*”. 7th Conferencia de dispositivos electronicos, Santiago de Compostela (Espaa). Feb/2009.
- C10:** G. Albareda, D. Jiménez and X. Oriols, “*Can analog and digital applications tolerate the intrinsic noise of aggressively-scaled field-effect transistors?*”. 5th International Conference on Unsolved Problems on Noise and Fluctuations in Physics, Biology and High Technology, Lyon (France). Jun/2008.
- C11:** H. López, G. Albareda, X. Cartoixà, J. Suñé and X. Oriols, “*Boundary conditions with Pauli exclusion and charge neutrality: application to the Monte Carlo simulation of ballistic nanoscale devices*”, 12th International Workshop on Computational Electronics, Boston (USA). October/2007.
- C12:** G. Albareda, J. Suñé and X. Oriols, “*Monte Carlo simulations of nanometric devices beyond the mean-field approximation*”. 12th International Workshop on Computational Electronics, Boston (USA). Oct/2007.
- C13:** X. Oriols, D. Jiménez, G. Albareda and H. López, “*Smaller are noisier: Signal-to-noise ratio and bit-error degradation in bulk-, quantum well- and quantum wire-nanoscale FETs*”. 19th International Conference on Noise and Fluctuations, Tokyo (Japan). Sep/2007.
- C14:** G. Albareda, J. Suñé and X. Oriols, “*Semi-classical study of the limitations of the mean-field approximation*”. 6th Conferencia de dispositivos electronicos, S. Lorenzo del Escorial. Madrid (Spain). Jan/2007.

Book chapters

- B1:** Book Title: “Applied Bohmian Mechanics: From Nanoscale Systems to Cosmology”. Chapter: “Nanoelectronics Physics: Quantum Electron Transport”. Editorial: Pan Stanford Estimated Date of Publication: at the end of 2010. Authors: A. Alarcón, G. Albareda, F. L. Traversa, and X. Oriols
- B2:** Book Title: “Theory and Applications of Monte Carlo Simulations”. Chapter: “Monte Carlo simulations beyond the mean-field approximation: Application to Electron transport at the nanoscale”. Editorial: InTech Estimated Date of Publication: January 2011. Authors: G. Albareda, F. L. Traversa, A. Benali, and X. Oriols

Time-dependent boundary conditions with lead-sample Coulomb correlations: Application to classical and quantum nanoscale electron device simulators

G. Albareda, H. López, X. Cartoixà, J. Suñé, and X. Oriols*

Departament d'Enginyeria Electrònica, Universitat Autònoma de Barcelona, 08193 Bellaterra, Spain

(Received 28 March 2010; revised manuscript received 1 June 2010)

Standard boundary conditions (BCs) for electron-transport simulators are based on specifying the value of the scalar potential (or the electric field) and the charge density at the borders of the simulation box. Due to the computational burden associated to quantum or atomistic descriptions, the use of small simulation boxes that exclude the leads is a mandatory requirement in modern nanoscale simulators. However, if the leads (where screening takes place) are excluded, standard BCs become inaccurate. In this work, we develop analytical expressions for the charge density, the electric field, and the scalar potential along the leads and reservoirs. From these expressions, we present a (time-dependent) BCs algorithm that transfers the specification of the BCs at the boundaries of the simulation box to a deeper position inside the reservoirs. Numerical solutions of the time-dependent Boltzmann equation with our algorithm using a large (reservoir, leads, and sample) and a small (sample alone) simulation boxes are compared, showing an excellent agreement even at (far from equilibrium) high bias conditions. Numerical results demonstrating the limitations of standard BCs for small simulation boxes are presented. Finally, time-dependent simulations of a resonant tunneling diode (using a quantum trajectory-based simulator) are presented, emphasizing the ability of this BCs algorithm to ensure overall charge neutrality in simulation boxes much smaller than the total lead-sample-lead length. This BCs algorithm requires a minimum computational effort and it can be applied to study dc, ac, and current or voltage fluctuations in nanoscale devices.

DOI: XXXX

PACS number(s): 85.30.-z, 41.20.Cv, 02.70.-c, 73.40.-c

I. INTRODUCTION

In order to correctly model the dc and/or ac conductance of nanoscale systems, one has to ensure “overall charge neutrality” and “current conservation.”^{1,2} The implementation of such requirements into modern nanoscale electron simulators demands some kind of reasonable approximation for the Coulomb interaction.

On one hand, the importance of overall charge neutrality (i.e., that the total charge in the whole device is zero) in nanoscale ballistic devices was clarified by the work of Landauer, Büttiker, and co-workers³ on the “two-terminal” and the “four-terminal” conductance of ballistic devices. The well-known standard textbook expression of the dc (zero-temperature) conductance through a tunneling obstacle is known as the two-terminal equation because it is defined as the current divided by the voltage drop sufficiently far from the obstacle. However, the original formulation of the conductance proposed by Landauer^{4,5} in 1957 was known as the four-terminal conductance because its experimental validation needs two additional voltage probes to measure the voltage drop close to the tunneling obstacle. The presence of resistances in the leads⁶ explains the difference between both expressions. The ultimate origin of such resistances is the requirement of overall charge neutrality that transforms unbalanced charges in the leads into a voltage drop there, via the Poisson (Gauss) equation. See Appendix A for a qualitative discussion of such lead resistances.

On the other hand, the “current conservation” (i.e., the total current computed on a surface in the simulation box is equal to the total current measured on a surface of an ammeter located far from the sample) is a necessary requirement for the prediction of ac conductances. The displacement cur-

rent, i.e., the time-dependent variations in the electric field, assures that the total (conduction plus displacement) current density is a divergenceless vector. Important theoretical contributions were done by Büttiker and co-workers for predicting ac properties of mesoscopic systems within a frequency-dependent scattering matrix formalism, in weakly nonlinear regimes taking into account overall charge neutrality and current conservation.^{1,7-12}

In general, modern electron-transport simulators do include reasonable approximations for the Coulomb interactions that can guarantee the accomplishment of the overall-charge-neutrality requirement. In addition, those simulators that are developed within a time-dependent or frequency-dependent framework can also assure the current conservation requirement. However, the powerful treatment of quantum and atomistic effects can only be applied to a very limited number of degrees of freedom.¹³ In fact, due to computational restrictions, a small simulation box is a mandatory requirement in many modern simulators. Here, the adjective small means that the leads are directly excluded from the simulation box. Neglecting the leads implies serious difficulties for the achievement of overall charge neutrality in the simulation box because the unbalanced charge in the leads is not considered. In addition, a possible inaccuracy in the computation of the overall charge neutrality affects our ability to treat the time-dependent Coulomb correlation among electrons and, therefore, the requirement of current conservation. In conclusion, due to computational difficulties, modern electron-transport simulators have to be implemented in small simulation boxes that imply important difficulties for providing dc or ac conductances of nanoscale devices because they neglect the lead-sample Coulomb correlation. An exception to this conclusion appears in nanoscale devices

89 with metallic leads that imply screening lengths of few
90 Angstroms.^{14,15} However, many other scenarios with highly
91 doped polysilicon leads or modern junctionless devices¹⁶
92 have screening length on the order of few nanometers. In
93 addition, in all scenarios with far-from equilibrium condi-
94 tions (with high bias), the screening length in the leads have
95 to be complemented by the presence of a depletion length
96 there.

97 In principle, the problem of excluding the leads from the
98 simulation box, while retaining the lead-sample Coulomb
99 correlation, could be solvable by providing adequate bound-
100 ary conditions (BCs) on each of the “open” borders of the
101 simulation box.¹⁷ In the literature, there are many different
102 and successful BCs (Refs. 18–39) for describing nanoscale
103 electron devices with simulation boxes large enough to in-
104 clude the leads. However, BCs found in the literature are not
105 directly applicable for small simulation boxes. This is the
106 main motivation of this work. Before presenting our BCs
107 proposal, let us describe the standard BCs found in the lit-
108 erature for nanoscale electron device simulators. They are
109 based on specifying two conditions at each of the borders of
110 the simulation box:

111 (i) “*Border_charge_BC*s.” The charge density inside the
112 simulation box depends on the electrons injected from its
113 borders. Therefore, any BCs algorithm for electron devices
114 has to include information on the charge density at the bor-
115 ders as an additional BCs assumption.

116 (ii) “*Border_potential_BC*s.” The value of the scalar po-
117 tential (or electric field) on the borders of the simulation box
118 has to be specified. This condition is a direct consequence of
119 the uniqueness theorem for the Poisson equation¹⁷ which en-
120 sures that these values are enough to completely determine
121 the solution of Poisson equation, when the charge inside the
122 simulation domain is perfectly determined.

123 In many cases, the electrons injected through the bound-
124 aries depend, somehow, on the scalar potential determined by
125 the “*border_potential_BC*s” (and a fixed electrochemical
126 potential). Therefore, a coupled system of the two BCs ap-
127 pears.

128 Elaborated semiclassical electron-transport simulators
129 solve the time-dependent Boltzmann equation by means
130 of the Monte Carlo (MC) technique. In particular, most of
131 them fix the potential at the borders of the box equal to the
132 external bias an assume *ad hoc* modification of the injection
133 rate to achieve local charge neutrality.^{18–26} Some works do
134 also include analytically the series resistances of a large
135 reservoir²⁷ which can be considered an improvement over
136 the previous “*border_potential_BC*s.” Other MC simulators
137 consider Neumann BCs (i.e., a fixed zero electric field for
138 “*border_potential_BC*s”).²⁸ In principle, there are no com-
139 putational difficulties in applying the semiclassical MC tech-
140 nique in large (≈ 50 – 100 nm) simulation boxes. Neverthe-
141 less, the possibility of using smaller boxes will be very
142 welcomed for some intensive time-consuming simulations.
143 For example, to repeat multiple ($\sim 100\,000$) simulations to
144 obtain statistical information about the macroscopic role of
145 some uncertain microscopic parameter (such as impurity
146 positions);²⁹ to simulate real three-dimensional (3D) solu-
147 tions of the Poisson equation (involving matrix inversions of
148 ~ 2 – 3000 nodes),³⁰ to compute (not only average values,

but) current or voltage fluctuations that need very large simu- 149
150 lation times (with $\sim 10^5$ and 10^6 time steps) to obtain reason-
151 able estimators,^{21–23} to go beyond mean-field
152 approximations,³⁰ etc.

153 The development of electron-transport simulators with the
154 explicit consideration of the wave nature of electrons implies
155 an important increase in the computational burden. The use
156 of the external bias as the Dirichlet BCs (“*border_potential-
157 BC*s”) was quite usual^{31,32} in the simulation of ballistic
158 electron devices such as the resonant tunneling diode (RTD).
159 The “*border_charge_BC*s” was directly specified from the
160 energy difference between the fixed scalar potential and the
161 fixed electrochemical potential. In 1989, Pötz³³ was one of
162 the first in emphasizing the importance of flexible BCs at the
163 borders of the simulation boxes of RTD to ensure local
164 charge neutrality. Recently, more elaborated quantum-
165 mechanical simulators are being used based on the self-
166 consistent solution of the nonequilibrium Green’s functions
167 and Poisson equation pioneered by Datta.^{34–39} They use ei-
168 ther Dirichlet-type BCs (Refs. 34 and 35) or Neumann BCs
169 (Refs. 36–39) for the “*border_potential_BC*s.” Again, the
170 “*border_charge_BC*s” condition was indirectly determined
171 from a fixed electrochemical potential and a fixed or floating
172 scalar potential. All these BCs algorithms are very successful
173 because they are implemented into simulation boxes large
174 enough to explicitly include the leads. However, such algo-
175 rithms are basically developed for static scenarios within a
176 mean-field treatment of the Coulomb interaction. Its exten-
177 sion to time-dependent scenarios or the inclusion of correla-
178 tions beyond the mean-field approximation has many com-
179 putational difficulties that will certainly benefit from the
180 possibility of using smaller simulation boxes.

181 As mentioned in the initial paragraphs, the extension of
182 such quantum-transport to time-dependent scenarios is a
183 complicated issue that requires not only overall charge neu-
184 trality but also current conservation. Büttiker and co-workers
185 were the first to study quantum ac conductances with both
186 requirements. They applied different many-body approxima-
187 tions (a simple one potential per conductor,⁷ a Thomas-Fermi
188 screening potential,⁸ Hartree-type approximations,⁹ a treat-
189 ment of the electron-electron interactions on the level of a
190 Hartree-Fock approach,¹⁰ and also a generalization of the
191 scattering matrix to deal with a Coulomb blockade system¹¹)
192 to provide self-consistent theories for the ac conductance of
193 mesoscopic systems. As a relevant example of their deep
194 understanding of time-dependent mesoscopic scenarios, they
195 predicted the value of the resistance in a quantum RC (single
196 electronic mode) circuit,¹² which has been recently experi-
197 mentally confirmed.⁴⁰ However, the practical implementation
198 of the Büttiker theory for ac conductance in real RTD [with
199 two-dimensional (2D) or 3D treatments] has many computa-
200 tional difficulties because of the use of large simulation
201 boxes that have to include the leads explicitly (see Refs. 41
202 and 42).

203 Finally, there are even more computational difficulties in
204 using large simulation boxes to include the leads in the so-
205 called “first-principles” electron-transport simulators because
206 of its huge demand of computational resources for their ato-
207 mistic description. One strategy of such first-principles
208 simulators^{14,15} is based on dividing the whole system in three

209 regions (left lead, sample,⁶ and right lead) and solving them
 210 separately. Once the (Hartree) potentials at the leads are
 211 known, the solution of the potentials in the sample is ob-
 212 tained by imposing that the Hartree potential in the simula-
 213 tion box matches those in the leads at equilibrium. If an
 214 external bias is applied, they shift the scalar (Hartree) poten-
 215 tial between each lead exactly equal to this applied bias con-
 216 sidering a negligible voltage drop in the leads. This specifies
 217 “*border_potential_BCs*” assuming that the screening effects
 218 are shorter than few tens of Angstroms. However, as dis-
 219 cussed in the introduction, such small screening lengths are
 220 only applicable for metallic leads close to equilibrium but
 221 invalid in most practical scenarios of electron devices. In
 222 addition, although it is not explicitly explained, the “*border-*
 223 *_charge_BCs*” is determined from standard Fermi (zero-
 224 temperature) statistics that depend on the energetic separa-
 225 tion between a fixed electrochemical potential and the
 226 bottom of the conduction band. Whether or not such condi-
 227 tion implies local or overall charge neutrality in the whole
 228 structure is not considered. Another approach is the one de-
 229 veloped by Di Ventra, Lang, and co-workers^{43–47} where a
 230 specific discussion of the “*border_charge_BCs*” to ensure
 231 overall charge neutrality inside the simulation box is consid-
 232 ered. Assuming a jellium model for the leads and letting the
 233 bottom of the conduction band to move relative to the elec-
 234 trochemical potential, they are able to assure overall charge
 235 neutrality in their lead-sample-lead simulation box. Their al-
 236 gorithm imposes an energy separation between a fixed elec-
 237 trochemical potential and a floating bottom of the conduction
 238 band (i.e., “*border_potential_BCs*”) that provides local
 239 charge neutrality deep inside the leads. In addition, an *ad hoc*
 240 (δ) charge density has to be included into the sample-lead
 241 interface (without any clear physical justification), in order to
 242 make compatible their local and global charge-neutrality re-
 243 quirements. Once more, the algorithm is numerically applied
 244 to systems with leads and small screening length. The modi-
 245 fication of the previous BCs toward explicit time-dependent
 246 density-functional models, where the requirement of current
 247 conservation will be necessary, is starting to be
 248 developed.^{46–49}

249 In summary, the strategies mentioned above for specify-
 250 ing the BCs at the borders of the simulation box are similar
 251 for classical or quantum simulators. However, as we will
 252 show numerically in Sec. IV B, none of these BCs can be
 253 applied in simulation boxes that explicitly exclude the leads.
 254 The successful educated guesses applied in large simulation
 255 boxes become inapplicable in small simulation boxes. Nei-
 256 ther the charge density, nor the electric field nor the scalar
 257 potential has easily predictable values at the borders of the
 258 sample. In addition, the energy distribution of electrons close
 259 to the active region can be very different from its thermal
 260 energy distribution deep inside the reservoirs. Therefore, the
 261 value of the electrochemical potential deep inside has no
 262 direct relevance close to the sample. The key point of our
 263 BCs is that we will not impose any of the previous require-
 264 ments at the borders of the sample. We will obtain analytical
 265 expressions for the charge density, electric field, and scalar
 266 potential in the leads. Such analytical expression will allow
 267 us to transfer the BC deep inside the reservoirs into informa-
 268 tion of charge density, electric field, and scalar potential at

the sample borders. This BCs algorithm requires a minimum 269
 computational effort and it can be implemented into either 270
 quantum or classical time-dependent simulators with large or 271
 small simulation boxes, for dc and ac conditions, and even 272
 for the study of current (or voltage) fluctuations. 273

The structure of this paper is as follow. After this intro- 274
 duction, in Sec. II, we discuss some preliminary issues that 275
 will be used for the description of the BCs. In particular, we 276
 first discuss the time-dependent overall charge neutrality re- 277
 quirements, modeled through the dielectric relaxation time. 278
 Later, we present a simple parametric analytical expression 279
 of the impedance of the leads. Finally, we present a time- 280
 dependent degenerate injection model to control the charge 281
 density at the borders of the simulation box. In Sec. III, we 282
 develop our original time-dependent BCs algorithm taking 283
 into account all the ingredients discussed in Sec. II. In Sec. 284
 IV, we test our BCs algorithm with semiclassical MC simu- 285
 lations of a nanoscale silicon resistor with large and small 286
 simulation boxes. The excellent agreement between both sets 287
 of simulations (without any fitting parameter) confirms the 288
 merit and accuracy of our BCs algorithm. We also present a 289
 numerical simulation for a (quantum) double barrier RTD to 290
 show the importance of the BCs discussed here. The conclu- 291
 sions are presented in Sec. V. There are two additional ap- 292
 pendixes. First, we summarize the enlightening work of Lan- 293
 dauer and Büttiker about the role of the lead resistances in 294
 the overall charge neutrality. Second, we discuss the limits of 295
 the quasistatic electromagnetic approximation to justify the 296
 exclusive use of a scalar potential. 297

II. PRELIMINARY ISSUES 298

The original motivation of this work was the development 299
 of a BCs algorithm with an appropriate treatment of the lead- 300
 sample correlation for a general-purpose many-particle 301
 quantum-trajectory electron-transport simulator, previously 302
 developed by one of the authors.⁵⁰ From a computational 303
 point of view, such a quantum-trajectory algorithm (with 304
 Coulomb and exchange interactions) can only be imple- 305
 mented in small simulation boxes. Before presenting our al- 306
 gorithm, we develop some preliminary expressions that will 307
 be later used in Sec. III. 308

A. Time-dependent overall charge neutrality 309 in nanoscale electron devices 310

We are interested in developing our BCs algorithm in a 311
 time-dependent framework because of the following two rea- 312
 sons. First, because it will be applicable not only to obtain dc 313
 (zero-frequency) result, but also to ac (high-frequency) ones. 314
 Second, because it is known that the lead-sample correlations 315
 are better treated with time-dependent BCs conditions that 316
 allow the exchange of energy between the leads and the 317
 sample. 318

In order to impose a time-dependent condition for the 319
 solutions of the charge density $\rho(\vec{r}, t)$, the electric field 320
 $\vec{E}(\vec{r}, t)$, and the scalar potential $V(\vec{r}, t)$, we start by integrating 321
 the local continuity equation [i.e., the charge conservation 322
 implicit in Maxwell’s Eq. (B2)] in a large volume Ω , that 323

324 includes the sample, the leads and the reservoirs

$$\frac{\partial}{\partial t} \int_{\Omega} \rho(\vec{r}, t) \cdot dv + \int_S \vec{J}_C(\vec{r}, t) \cdot d\vec{s} = 0. \quad (1)$$

326 The volume Ω is limited by the surface S . We assume that
 327 the particle current $\vec{J}_C(\vec{r}, t)$ in Eq. (1) is parallel to all the
 328 subsurfaces of S , except in those open surfaces¹⁷ ($\vec{r}_S \in A_S$ in
 329 the source and $\vec{r}_D \in A_D$ in the drain reservoirs), which are
 330 perpendicular to the transport direction

$$\frac{\partial}{\partial t} \int_{\Omega} \rho(\vec{r}, t) \cdot dv + \int_{A_S} \vec{J}_C(\vec{r}_S, t) \cdot d\vec{s}_S + \int_{A_D} \vec{J}_C(\vec{r}_D, t) \cdot d\vec{s}_D = 0. \quad (2)$$

332 Next, we assume that the current density and the electric
 333 field at the surfaces $\vec{r}_S \in A_S$ and $\vec{r}_D \in A_D$, deep inside the res-
 334 ervoires, are related by the Ohm law⁵¹ (no Ohmic assumption
 335 is imposed in this volume Ω). Thus

$$\int_{A_{S/D}} \vec{J}_C(\vec{r}, t) \cdot d\vec{s} = \sigma \int_{A_{S/D}} \vec{E}(\vec{r}, t) \cdot d\vec{s} \quad (3)$$

337 being σ the reservoir (frequency-independent) conductivity.
 338 The use of expression (3) imposes an important limitation on
 339 the frequency validity of our BCs algorithm. For example,
 340 the Drude's deduction of Ohm's law requires times which are
 341 larger than the inelastic scattering time. We can rewrite Eqs.
 342 (2) and (3) as

$$\frac{\partial}{\partial t} \int_{\Omega} \rho(\vec{r}, t) \cdot dv + \sigma [E_S^C(t) + E_D^C(t)] = 0, \quad (4)$$

344 where we have defined $E_S^C(t) = -\int_{A_S} \vec{E}(\vec{r}_S, t) \cdot d\vec{s}_S$ and $E_D^C(t)$
 345 $= \int_{A_D} \vec{E}(\vec{r}_D, t) \cdot d\vec{s}_D$. See Fig. 1 for the explicit location of $E_S^C(t)$
 346 and $E_D^C(t)$, deep inside the reservoir. The next step is the
 347 integration of the Gauss equation [Eq. (B4) in Appendix B]
 348 in the same volume

$$\int_{\Omega} \rho(\vec{r}, t) \cdot dv - \int_S \vec{D}(\vec{r}, t) \cdot d\vec{s} = 0, \quad (5)$$

350 where $\vec{D}(\vec{r}, t) = \varepsilon(\vec{r}) \cdot \vec{E}(\vec{r}, t)$ is the electric displacement field
 351 and $\varepsilon(\vec{r})$ the (frequency-independent) dielectric constant.
 352 Again, we assume that $\vec{D}(\vec{r}, t)$ is very small at all surfaces
 353 except at those at the source and drain. Therefore

$$\int_{\Omega} \rho(\vec{r}, t) \cdot dv - \varepsilon [E_S^C(t) + E_D^C(t)] = 0 \quad (6)$$

355 with $\varepsilon = \varepsilon(\vec{r}_d) = \varepsilon(\vec{r}_s)$. Combining expressions (4) and (6), we
 356 obtain

$$\frac{\partial}{\partial t} \int_{\Omega} \rho(\vec{r}, t) \cdot dv = -\frac{\sigma}{\varepsilon} \int_{\Omega} \rho(\vec{r}, t) \cdot dv. \quad (7)$$

358 Expression (7) provides the time evolution of the total charge
 359 $Q(t) = \int_{\Omega} \rho(\vec{r}, t) \cdot dv$ in the whole system. Its solution is

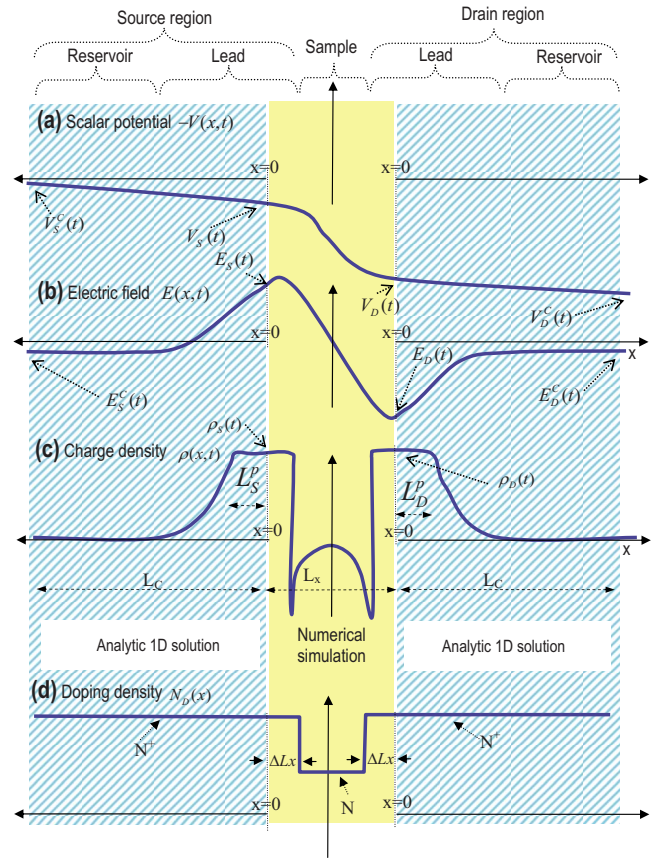


FIG. 1. (Color online) Definition of the variables used in the BCs algorithm and schematic representation of the (a) scalar potential, (b) electric field, (c) total charge density, and (d) doping density. An analytical parametric 1D solution is deduced in the (blue) dashed region while a numerical 3D solution is obtained in the (yellow) solid central region that we define as the simulation box. A part ΔL_x of the highly doping leads is included into the simulation box in order to account for complex phenomena that can appear at the interface.

$$Q(t) = Q(t_0) \cdot \exp\left(-\frac{t-t_0}{\tau_c}\right) \quad (8) \quad 360$$

with the dielectric relaxation time (sometimes called Maxwell relaxation time) being defined as

$$\tau_c = \varepsilon / \sigma. \quad (9) \quad 363$$

As expected, the meaning of expression (8) is that the total charge inside the system tends to zero in periods of time related to the dielectric relaxation time. Identically, from Eqs. (4) and (6), we see that

$$E_S^C(t) - E_D^C(t) = [E_S^C(t_0) - E_D^C(t_0)] \cdot \exp\left(-\frac{t-t_0}{\tau_c}\right) \quad (10) \quad 368$$

this meaning that the electric field tends to be the same deep inside both reservoirs. Finally, we know that the time-averaged electric field deep inside the reservoir tends to the Drude value $E_{S/D}^{drift}(t)$. Therefore, one possible solution of Eq. (10) with the additional requirement $E_{S/D}^C(t) \rightarrow E_{S/D}^{drift}(t)$ when $t \gg \tau_c$ is

$$E_S^C(t) - E_S^{drift}(t) = [E_S^C(t_0) - E_S^{drift}(t_0)] \cdot \exp\left(-\frac{t-t_0}{\tau_c}\right) \quad (11)$$

375

376 and

$$E_D^{drift}(t) - E_D^C(t) = [E_D^{drift}(t)(t_0) - E_D^C(t_0)] \cdot \exp\left(-\frac{t-t_0}{\tau_c}\right). \quad (12)$$

377

378 When imposing $E_S^{drift}(t) = E_D^{drift}(t)$, we recover Eq. (10) by
 379 summing Eqs. (11) and (12). The frequency limitation of
 380 expressions (11) and (12) is ultimately determined by the
 381 assumption that the parameters σ and ε are constant (time
 382 independent and frequency independent). Therefore, the di-
 383 electric relaxation time used in expressions (11) and (12)
 384 cannot be shorter than the interval of time needed for making
 385 reasonable the assumption that σ and ε are constants.

386 B. Analytical spatial-dependent charge density, electric field, 387 and scalar potential in the leads

388 In order to evaluate the total charge in expression (8) or to
 389 apply expressions (11) and (12), we need to know the charge
 390 densities or the electric fields deep inside the leads. Since we
 391 are interested in not simulation explicitly the leads, we look
 392 for analytical expressions. Nonlinear screening theory is im-
 393 portant but a general analytical solution to the Poisson equa-
 394 tion does not exist. Therefore, we will have to make some
 395 simplifying assumptions. We will use the schemes depicted
 396 in Fig. 1 to explain our analytical solution in the leads and
 397 the assumed simplifications. Throughout this paper, we will
 398 assume a two-terminal device, source and drain, to explain
 399 our BCs algorithm. In any case, it can be straightforwardly
 400 adapted to multiterminal systems with an arbitrary number of
 401 open boundaries.⁵²

402 First, we assume that all expressions in the leads depend
 403 only on the variable x along the transport direction but are
 404 independent on the lateral directions y and z so that a one-
 405 dimensional (1D) scheme in the leads and reservoirs is ap-
 406 propriate. In order to develop simpler analytical expressions
 407 we consider one specific negative x axis, $(-\infty, 0]$, for the
 408 source and another positive, $[0, +\infty)$, for the drain with dif-
 409 ferent origins. The point $x=0$ is located at the interface be-
 410 tween the numerical solution in the simulation box and the
 411 analytical solution in the lead (see Fig. 1). Let us notice that
 412 a small part of the lead is explicitly included into the simu-
 413 lation box (see the length ΔLx in Fig. 1). The exact length
 414 ΔLx depends on a trade-off between computational limita-
 415 tions and accuracy to treat complex effects in the interfaces
 416 (such as the presence of quasibound states in the accumula-
 417 tion well⁵³ or the Friedel oscillations⁵⁴).

418 Second, we assume that the electron charge distribution in
 419 the leads can be reasonably described by standard textbook⁵¹
 420 expressions and that charge density due to ionized impurities
 421 is uniformly distributed in the leads and reservoirs. There-
 422 fore, we write the Poisson equation as

$$\frac{\varepsilon}{q} \frac{\partial^2 \Delta Ec(x,t)}{\partial x^2} = \rho(x,t) = qN_D \left\{ 1 - \exp\left[\frac{\Delta Ec(x,t)}{k_B \cdot \Theta}\right] \right\}, \quad (13)$$

423

where N_D is the uniform doping density, $\Delta Ec(x,t) = Ec(x,t)$
 $- Ec$ is the offset of the bottom of the conduction band mea-
 sured from its average value deep inside the reservoir Ec
 $= Ec(x_{S/D}, t)$, Θ the absolute temperature, and k_B the Boltz-
 mann constant. The bottom of the conduction band $Ec(x,t)$
 and the scalar potential are related by $Ec(x,t) = -qV(x,t)$
 (more complex screening theories can also be adapted to our
 BCs algorithm as far as they provide analytical solutions
 in the leads^{54,55}). We assume the standard Debye
 approximation⁵¹ $|\Delta Ec(x,t)| \leq k_B \cdot \Theta$ to solve the Poisson Eq.
 (13). Then, under a first-order Taylor expansions, we obtain
 $\rho(x,t) \approx \frac{qN_D \cdot \Delta Ec(x,t)}{k_B \cdot \Theta}$. Then, the solution of Eq. (13) in the
 source lead $-L_C \leq x \leq 0$ is

$$\rho(x,t) = \rho_S(t) \exp\left(\frac{x + L_S^p}{l}\right), \quad (14)$$

437

where we have assumed $\rho(x,t) = 0$ when $x \rightarrow -\infty$ because of
 the screening. We have defined $\rho_S(t) = \rho(-L_S^p, t)$ as the
 (surface-averaged) electron density at $x = -L_S^p$ (see Fig. 1).
 We can identify the parameter l as the Debye length⁵¹

$$l = \sqrt{\frac{\varepsilon \cdot k_B \cdot \Theta}{q^2 N_D}}. \quad (15)$$

442

Identically, the solution in the drain lead $0 \leq x \leq L_C$ is

$$\rho(x,t) = \rho_D(t) \exp\left(-\frac{x - L_D^p}{l}\right). \quad (16)$$

444

For simplicity, we assume equal doping densities and
 screening lengths in the drain and source leads. Expressions
 (14) and (16) are only valid for small applied bias, i.e., close
 to equilibrium conditions. However, large bias can drive the
 device far from equilibrium. For such conditions, it is quite
 usual that one lead suffers accumulation of electrons while
 the other suffers depletion. In the depleted regions, there are
 no electrons that can participate on the screening of positive
 charge, therefore, the screening length has to be comple-
 mented with an additional depletion length. See a schematic
 plot in Fig. 1(c). Then, a reasonable expression for the charge
 density at the source is

$$\rho(x,t) = \begin{cases} \rho_S(t) \exp\left(\frac{x + L_S^p}{l}\right) & -L_C \leq x \leq -L_S^p \\ \rho_S(t) & -L_S^p \leq x \leq 0, \end{cases} \quad (17)$$

457

where L_S^p is the depletion length of the source lead indicated
 in Fig. 1. Identically, the charge density in the drain lead is

$$\rho(x,t) = \begin{cases} \rho_D(t) \exp\left(-\frac{x - L_D^p}{l}\right) & L_D^p \leq x \leq L_C \\ \rho_D(t) & 0 \leq x \leq L_D^p. \end{cases} \quad (18)$$

460

By applying the Gauss Eq. (B4), from Eq. (17) we can deter-
 mine the electric field along the source lead and the source
 reservoir

463

$$E(x,t) = \begin{cases} E_S^C(t) + \frac{\rho_S(t)l}{\varepsilon} \exp\left(\frac{x+L_S^p}{l}\right) & -L_C \leq x \leq -L_S^p \\ E_S^C(t) + \frac{\rho_S(t)(l+L_S^p)}{\varepsilon} + \frac{\rho_S(t)x}{\varepsilon} & -L_S^p \leq x \leq 0. \end{cases} \quad (19)$$

the lead-sample region. Identically, in the drain lead, we obtain

$$E(x,t) = \begin{cases} E_D^C(t) - \frac{\rho_D(t)l}{\varepsilon} \exp\left(\frac{-x+L_D^p}{l}\right) & L_D^p \leq x \leq L_C \\ E_D^C(t) - \frac{\rho_D(t)(l+L_D^p)}{\varepsilon} + \frac{\rho_D(t)x}{\varepsilon} & 0 \leq x \leq L_D^p. \end{cases} \quad (20)$$

Finally, the definition of the scalar potential in the source leads is given by the spatial integration of expression (19) as

$$V(x,t) = \begin{cases} V_S^C(t) - E_S^C(t)(x+L_C) - \frac{\rho_S(t)l^2}{\varepsilon} \exp\left(\frac{x+L_S^p}{l}\right) & -L_C \leq x \leq -L_S^p \\ V_S^C(t) - E_S^C(t)(x+L_C) - \frac{\rho_S(t)(x+L_S^p)^2}{2 \cdot \varepsilon} - \frac{\rho_S(t)l(l+L_S^p+x)}{\varepsilon} & -L_S^p \leq x \leq 0 \end{cases} \quad (21)$$

and integration of Eq. (20) in the drain

$$V(x,t) = \begin{cases} V_D^C(t) + E_D^C(t)(-x+L_C) - \frac{\rho_D(t)l^2}{\varepsilon} \exp\left(\frac{-x+L_D^p}{l}\right) & L_D^p \leq x \leq L_C \\ V_D^C(t) + E_D^C(t)(-x+L_C) - \frac{\rho_D(t)(-x+L_S^p)^2}{2 \cdot \varepsilon} - \frac{\rho_D(t)l(l+L_S^p-x)}{\varepsilon} & 0 \leq x \leq L_D^p. \end{cases} \quad (22)$$

Apart from the frequency restrictions mentioned in Sec. II A, the validity of expressions (17)–(22) is limited to frequencies lower than the plasma frequency in the leads. In addition, when large bias conditions are considered, the presence of hot carriers (with high velocities) in the leads will modify the (quasiequilibrium) screening length found in Eq. (15). This effect will provide a limitation of our BCs model for very high bias.

Then, in Sec. III, we will discuss how this injection model can be adapted to situations with arbitrary external impedance.

The rate and randomness of the injection of electrons into the sample can be modeled through the following binomial probability $P(k_x, N, \tau)$ defined in Ref. 56

$$P(k_x, N, \tau) = \frac{M_\tau!}{N! \cdot (M_\tau - N)!} f_{S/D}(E)^N [1 - f_{S/D}(E)]^{M_\tau - N}. \quad (23)$$

This expression defines the probability that N electrons with wave vectors in the range $k_x \in [k_{ox}, k_{ox} + \Delta k_x)$ are injected into the sample during the time interval τ . The parameter M_τ is the number of attempts of injecting electrons during the previous time interval τ , defined as a number that rounds the quotient τ/t_0 to the nearest natural number toward zero. The number of injected electrons can be $N=1, 2, \dots, \leq M_\tau$. The time t_0 is the minimum temporal separation between the injection of two electrons into the particular cell phase-space cell $k_x \in [k_{ox}, k_{ox} + \Delta k_x)$ and $x \in [x_o, x_o + \Delta x)$. For a 1D system, the value of t_0 can be easily estimated. The number of electrons n_{1D} in the particular phase space cell $\Delta k_x \cdot \Delta x$ is $n_{1D} = 2 \cdot \Delta k_x \cdot \Delta x / (2\pi)$ where we consider a factor 2 for spin degeneracy.⁵⁷ These electrons have been injected into Δx during the time interval Δt defined as the time needed for electrons with velocity $v_x = \Delta x / \Delta t = \hbar k_x / m_t$ to travel a distance Δx . Therefore, the minimum temporal separation, t_0 ,

532 between the injection of two electrons into the previous par-
533 ticular cell is Δt divided by the maximum number n_{1D} of
534 electrons

$$535 \quad t_0(k_x)|_{1D} = \frac{\Delta t}{n_{1D}} = \left(\frac{1}{\pi} \frac{\hbar k_x}{m_t} \Delta k_x \right)^{-1}. \quad (24A)$$

536 The practical application of such definition of t_0 requires a
537 mesh with a small step Δk_x on all possible values of k_x .
538 Identically, for a 2D and 3D system, we obtain

$$539 \quad t_0(y, k_x, k_y)|_{2D} = \frac{\Delta t}{n_{2D}} = \left(\frac{1}{2\pi^2} \frac{\hbar k_x}{m_t} \Delta y \Delta k_x \Delta k_y \right)^{-1}, \quad (24B)$$

$$540 \quad t_0(y, z, k_x, k_y, k_z)|_{3D} = \frac{\Delta t}{n_{3D}} = \left(\frac{1}{4\pi^3} \frac{\hbar k_x}{m_t} \Delta y \Delta z \Delta k_x \Delta k_y \Delta k_z \right)^{-1}. \quad (24C)$$

541 On the other hand, the function $f_S(E)$ that appears in Eq. (23)
542 determines the probability that a state with kinetic energy E
543 measured from the bottom of the conduction band $-qV_S(t)$ is
544 occupied by an electron that will effectively enter into the
545 simulation box. In particular, we assume that such probabil-
546 ity is determined by half of the Fermi distribution [E
547 $= E(\vec{k})$ with $k_x > 0$], as:

$$548 \quad f_S(E) = \frac{1}{1 + \exp \left[\frac{E - F_S^{inj}(t) + qV_S(t)}{k_B \cdot \Theta} \right]} \quad (25)$$

549 where the electron wave vector \vec{k} is related to the kinetic
550 energy by the appropriate energy-dispersion relationship
551 $E(\vec{k})$. The term $F_S^{inj}(t)$ is defined here as the source injecting
552 energy level and it determines how to increase the rate of
553 injection of electrons while respecting the Pauli restriction.
554 This restriction implies that two electrons with identical ve-
555 locity have to be injected with a temporal separation equal or
556 larger than t_0 . We avoid the name electrochemical potential
557 for such energy $F_S^{inj}(t)$ because Eq. (25) does not refer to all
558 (source) electrons but only to those with $k_x > 0$. In addition,
559 close to the active region, the electron distribution for k_x
560 < 0 will be quite unpredictable (see insets in Fig. 18 in Ap-
561 pendix A). We reserve the name electrochemical potential to
562 the thermalized energy distribution deep inside the reser-
563 voirs, at $x = \mp L_C$. Here, $F_S^{inj}(t)$ is just a parameter that con-
564 trols the rate of injection of electrons at the border of the
565 simulation box to ensure overall charge neutrality. Equiva-
566 lently, the electrons injected from the drain have an energy
567 distribution determined by [$E = E(\vec{k})$ with $k_x < 0$] as:

$$568 \quad f_0(E) = \frac{1}{1 + \exp \left[\frac{E - F_D^{inj}(t) + qV_D(t)}{k_B \cdot \Theta} \right]} \quad (26)$$

with $F_D^{inj}(t)$ the drain injecting energy level. We will later use 569
the parameters $F_S^{inj}(t)$ and $F_D^{inj}(t)$ to indirectly increase/ 570
decrease the charge density $\rho_{S/D}(t)$ at the lead-sample inter- 571
face, at each time step of the simulation. 572

It is very instructive to understand the Binomial distribu- 573
tion of the injection process, expression (23), as a conse- 574
quence of the discreteness of the electron charge. For a par- 575
ticular cell, at zero temperature, we inject an electron every 576
interval of time t_0 . The average current per cell is $-q/t_0$. At 577
room temperature, the average current is lower, $-q \cdot f(E)/t_0$, 578
because of the uncertainty in the occupation. However, it is 579
not possible to inject a fractional charge $-qf(E)$ into the 580
system at each interval of time t_0 (i.e., the electron charge is 581
indivisible). Therefore, at each interval of time t_0 , either we 582
inject the full charge, $-q$ (if the state is occupied), or we do 583
not inject charge (if the state is empty) according to the prob- 584
ability $f(E)$. 585

As a simple test of our injection model in zero-external 586
impedance circuits, we compute analytically the current and 587
its fluctuations (i.e., the noise) for a one-subband ballistic 1D 588
system. According to the zero-external impedance, we as- 589
sume that $V_S(t)$ and $V_D(t)$ in Eqs. (25) and (26) are fixed by 590
the time-independent external bias. We assume a transmit- 591
tance equal to unity. For such conditions, all injected elec- 592
trons are finally transmitted (i.e., injection probability and 593
the transmitting probability are identical) and there are well- 594
known analytical results in the literature for both, average 595
current and noise.^{1,58,59} 596

The average current $\langle I \rangle$ is an experimental measure of the 597
charged transmitted through the system during a long time 598
interval. For our ballistic system, the charge transmitted 599
through the source is just the charge injected. Therefore 600

$$\langle I \rangle = - \lim_{\tau \rightarrow \infty} q \sum_{k_x} \frac{E_N[\tau, k_x]}{\tau}. \quad (27) \quad 601$$

The average number $E_N[\tau, k_x]$ of injected particles during 602
the time interval τ is computed from the probability 603
 $P(k_x, N, \tau)$ 604

$$E_N[\tau, k_x] = \sum_{N=0}^{N=\infty} P(k_x, N, \tau) N. \quad (28) \quad 605$$

As we mentioned before, we divide the whole phase space 606
into cells with a small Δk_x so that all electrons in the cell 607
have roughly the same energy. The average number of in- 608
jected particles with wave vector k_x during the time τ can be 609
computed from Eq. (28) as $E_N[\tau, k_x] = f_S(E) \cdot \tau / t_0(k_x)$ for each 610
cell of the source injection. Previous expression is just the 611
mean value of the Binomial distribution in Eq. (23), where 612
 $f_S(E)$ is defined by expression (25). From Eq. (27), the aver- 613
age current of each k_x -phase space cell can be computed as 614
 $\langle I \rangle^{k_x} = -q f_S(E) / t_0(k_x)$. The sum over all phase-space cells 615
with $k_x > 0$, $\langle I \rangle = \sum_{k_x} \langle I \rangle^{k_x}$, does exactly reproduce the Land- 616
auer average current. The drain current is computed equiva- 617
lently. The total current is the source component minus the 618
drain component 619

$$\langle I \rangle = -\frac{2q}{h} \int_0^\infty [f_S(E) - f_D(E)] dE, \quad (29)$$

620 where we have used $dE \approx \hbar^2 k_x \cdot \Delta k_x / m_t$ and $1/t_0(k_x)$
 621 $= \hbar k_x \cdot dk_x / (\pi \cdot m_t)$. This is just expressions (39) and (40) of
 622 Ref. 1 for a transmission coefficient equal to one. For low
 623 temperature [i.e., $f(E)=1$ for all injected electrons], we ob-
 624 tain the well-known Landauer conductance $G=2q^2/h$.
 625 For ballistic devices, the one-side power spectral density
 626 of the current fluctuations at zero (low) frequency can be also
 627 obtained from probability in Eq. (23) as

$$S_I(0) = \lim_{\tau \rightarrow \infty} 2q^2 \sum_{k_x} \frac{E_{N^2}[\tau, k_x] - (E_N[\tau, k_x])^2}{\tau}, \quad (30)$$

629 where we defined $E_{N^2}[\tau, k_x]$ as

$$E_{N^2}[\tau, k_x] = \sum_{N=0}^{N=\infty} P(k_x, N, \tau) N^2. \quad (31)$$

631 For the binomial distribution of expression (23), we obtain
 632 $E_{N^2}[\tau, k_x] - [E_N(\tau, k_x)]^2 = f_S(E)[1 - f_S(E)] \cdot \tau / t_0(k_x)$. Then, us-
 633 ing Eq. (30), we found $S_I^{k_x}(0) = 2q^2 f_S(E)[1 - f_S(E)] / t_0(k_x)$ for
 634 the source injection. Identical results are obtained for the
 635 drain injection. Since there is no drain-source correlation in
 636 our simple ballistic model, the total power is the sum of both.
 637 After integration over all energies, we obtain

$$S_I(0) = \frac{4q^2}{h} \int_0^\infty \{f_S(E)[1 - f_S(E)] + f_D(E)[1 - f_D(E)]\} dE. \quad (32)$$

639 This expression does exactly reproduce Büttiker results for a
 640 system with transmission coefficient equal to one [see ex-
 641 pression (61) in Ref. 58]. Expression (32) includes the ther-
 642 mal and the shot noise (i.e., it is valid both at equilibrium and
 643 far from equilibrium). Under equilibrium conditions, the
 644 previous result reproduces the Nyquist-Johnson thermal
 645 noise, as can be shown by introducing the identity
 646 $-k_B \Theta \cdot \partial f(E) / \partial E = f(E)[1 - f(E)]$ into the previous result.
 647 In conclusion, the (time-dependent) injection model dis-
 648 cussed here correctly accounts for the Pauli correlations
 649 among electrons under the assumption that the active region
 650 is part of a circuit with zero-external impedance. In this case,
 651 the voltages applied to the sample can be viewed as a fixed
 652 nonfluctuating quantity and the noise properties are deter-
 653 mined only by the Pauli correlations discussed above. In
 654 general, the sample is a part of a larger circuit (with nonzero-
 655 external impedances). Then, the current fluctuations in the
 656 sample imply voltage fluctuations in the leads [through the
 657 time dependence of $V_S(t)$ and $V_D(t)$ in Eqs. (25) and (26)]
 658 that, in turn, imply fluctuations on the injecting probabilities
 659 into the sample [through expression (23)] and the current in
 660 the sample [see expression (63) in Ref. 1]. These compli-
 661 cated correlations between sample and leads highlight the
 662 importance of the BCs algorithm mentioned here.

III. TIME-DEPENDENT BOUNDARY-CONDITIONS AT THE BORDERS OF THE SAMPLE FOR OVERALL CHARGE NEUTRALITY

A. General consideration

664 According to Fig. 1, we have to specify the values $V_S(t)$
 665 and $V_D(t)$ for the “border_potential_BCs,” and $\rho_S(t)$ and
 666 $\rho_D(t)$ for the “border_charge_BCs.” In addition, in Sec. II B,
 667 we have derived analytical relationships between scalar po-
 668 tentials, electric fields, and charge densities at the borders of
 669 the simulation box, at $x=0$, and those values deep inside the
 670 reservoirs, at $x = \mp L_C$. We have to add the four additional
 671 unknowns $V_S^C(t)$, $V_D^C(t)$, $E_D^C(t)$, and $E_S^C(t)$. In total, for two-
 672 terminal models, we have eight unknowns. Hence, we need
 673 eight conditions to specify the BCs.

674 As we have explained in the introduction, and it will be
 675 numerically confirmed in Sec. IV, it is very difficult to pro-
 676 vide an educated guess of the scalar potential, the electric
 677 field or the charge density at the borders of a small simula-
 678 tion box where leads are excluded. In addition, the electro-
 679 chemical potential for thermal distributions becomes an ill-
 680 defined parameter for small simulation boxes. One can
 681 assume a well-known value of the electrochemical potential
 682 deep inside the reservoir. However, close to the active re-
 683 gion, where the (far from equilibrium) momentum distribu-
 684 tion can be quite arbitrary, the prediction of any value of the
 685 electrochemical potential for injected and reflected electrons
 686 is quite inappropriate.

687 Fortunately, the analytical results of Sec. II for the leads
 688 and reservoirs can be used to transfer the unknown “border-
 689 potential_BCs” and “border_charge_BCs” at the borders
 690 of the simulation box into simpler BCs deep inside the res-
 691 ervoirs. This is the key point of our BCs algorithm.
 692 In particular, the two new BCs that we will impose at
 693 $x = \mp L_C$ are:

(i) “Deep_drift_BCs.” We assume that the inelastic scatter-
 694 ing mechanisms at, both, the source $x \leq -L_C$ and the drain
 695 $x \geq L_C$ reservoirs provides a quasiequilibrium position-
 696 independent thermal distribution of electrons (it is implicitly
 697 assumed that the contact length L_C is large enough so that
 698 inelastic scattering is relevant there). Such position-
 699 independent electron distribution is consistent with charge
 700 neutrality deduced in expressions (17) and (18), deep inside
 701 the reservoir, that implies a uniform electric field there. Then,
 702 according to the Ohm’s law mentioned in expression (3), we
 703 know that the electric fields tend to $E_{S/D}^C(t) \rightarrow E_{S/D}^{drift}(t)$ at the
 704 source and drain reservoir.

(ii) “Deep_potential_BCs.” We assume that electrochemi-
 705 cal potentials can be defined for the position-independent
 706 thermal distribution deep inside both reservoirs. We know
 707 that the applied bias coincides with the energy separation of
 708 the electrochemical potentials between the source and drain
 709 reservoirs. In addition, due to the position-independent elec-
 710 tron distribution deep inside the reservoirs, we assume that
 711 the energy separation between the electrochemical potential
 712 and the bottom of the conduction band is perfectly known in
 713 the drain and source reservoirs. When equal doping is used
 714 in both contacts (as done in the numerical examples of this
 715 work), the energy separation between the bottoms of the

722 conduction bands at both reservoirs is equal to the difference
723 of the external voltages. Hence, $V_S^C(t)=0$ and $V_D^C(t)$
724 $= V_{external}(t)$.

725 These two conditions, “*deep_drift_BCs*” and “*deep_po-*
726 *tential_BCs*” are quite reasonable for any electron device
727 deep inside the reservoirs. In fact, we will show in Sec. III B
728 that the numerical MC solution of the nonequilibrium Bolt-
729 zmann equation in a large simulation box confirms the ad-
730 equacy of these conditions in the reservoirs. Therefore, from
731 the initial eight unknowns, we have the “*deep_drift_BCs*”
732 and “*deep_potential_BCs*” considerations that provide four
733 conditions (two for each border). However, we do still need
734 four additional conditions in order to completely specify our
735 BCs unknowns. Such conditions come from imposing, at the
736 borders of the simulation box, the continuity between the
737 analytical expression of the electric field (and the scalar po-
738 tential) in the leads and the numerical values obtained inside
739 the simulation box. Therefore, we will be able to determine
740 the initial unknowns $V_S(t)$, $V_D(t)$, $\rho_S(t)$, and $\rho_D(t)$ in the bor-
741 ders of the simulation box, by imposing four conditions deep
742 inside the reservoir and imposing continuous profiles. The
743 value of the $E_{S/D}^{drift}(t)$ is not a parameter because it is imposed
744 by the conduction current, via the Ohm’s law. As discussed
745 in Sec. II A, imposing equal electric fields deep inside the
746 reservoirs guaranties the overall-charge-neutrality require-
747 ment.

748 Finally, we have to comment on the time dependence of
749 our algorithm. On one hand, most of the expressions devel-
750 oped in Sec. II have some frequency restrictions. In Appen-
751 dix B, we have also discussed the frequency limitations re-
752 lated to assuming that only the scalar potential is necessary
753 to describe time-dependent nanoscale scenarios. Our BCs al-
754 gorithm is valid for frequencies lower or equal than the
755 lowest-frequency restriction mentioned above. We will refer
756 to such frequency limit as the, f^{qs} , which will be considered
757 in next section.

758 B. Practical implementation of the boundary conditions 759 in classical or quantum time-dependent simulators

760 In Fig. 2, we represent schematically the flux diagram of
761 the BCs algorithm presented in this paper. After initializing
762 all variables and functions to predetermined values and mov-
763 ing particles (or solving wave-equation time evolution), we
764 arrive at the specific BCs algorithm. We know the old values
765 of $V_S(t)$, $V_D(t)$, $\rho_S(t)$, and $\rho_D(t)$ at time t . The BCs algorithm
766 will provide their new values at time $t=t+\Delta t$. We have di-
767 vided the algorithm into five different steps that we will de-
768 scribe in detail below:

769 *Step-(1) evaluation of the charge density at the sample*
770 *(inside) boundary.* The first step is the evaluation of the
771 charge density at the boundaries of the sample at time t . This
772 will be computed in the spatial cell closer to the border but
773 still inside the simulation box (see ΔLx in Fig. 1). Since we
774 describe a one-dimensional version of the BCs algorithm, we
775 will need a surface integration of such magnitudes that we
776 refer to as the instantaneous charge densities $\rho_{S/D}^{ins}(t')$. As
777 mentioned before, due to frequency restrictions of the algo-
778 rithm, what we will finally compute is a running average

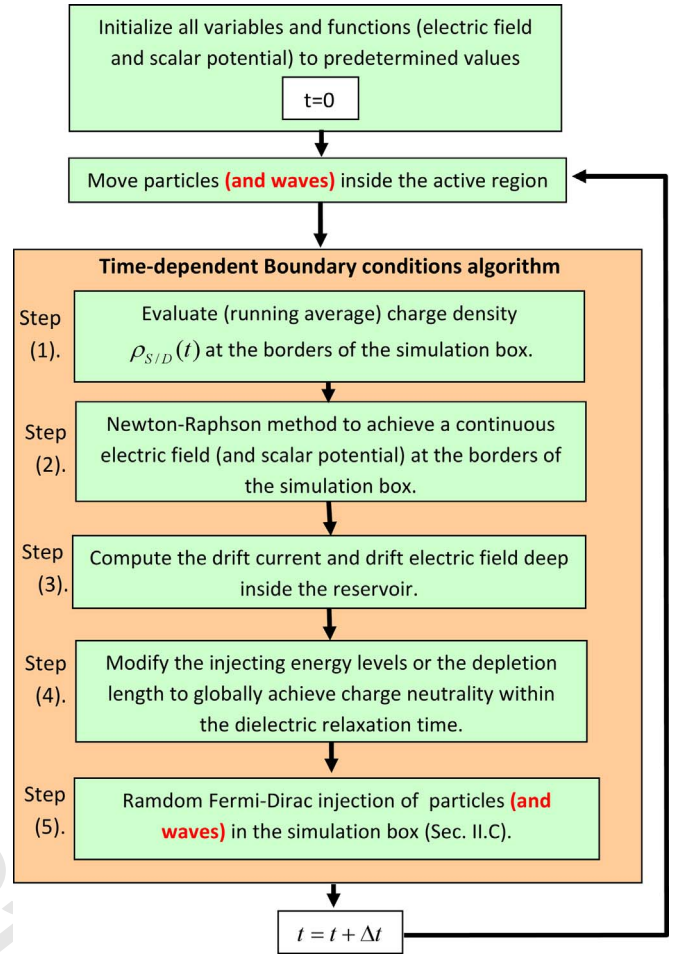


FIG. 2. (Color online) Schematic representation of our (time-dependent) BCs algorithm coupled to a particle-based electron (classic and quantum) transport simulator.

$$\rho_{S/D}(t) = \frac{1}{T^{qs}} \cdot \int_{t-T^{qs}}^t \rho_{S/D}^{ins}(t') \cdot dt' \quad (33) \quad 779$$

with the temporal interval T^{qs} equal to the integer N^{qs} multiplied by the simulation time step, $T^{qs} = N^{qs} \cdot \Delta t \approx 1/f^{qs}$. Let us notice that we just calculate the charge density at time t , not at time $t+\Delta t$.

Step (2)—imposing continuity of the electric field and the scalar potential at the sample-lead interface by means of a Newton-Raphson method. As mentioned in the previous section, the electric field and the scalar potential have to be continuous at both lead-sample interfaces. In one hand, the electric field, at the $x=0$ and the electric field at $x=-L_C$, of the source lead, are related from expression (19) as

$$E_S^C(t+\Delta t) = E_S(t+\Delta t) - \frac{\rho_S(t)[l + L_S^p(t)]}{\epsilon}, \quad (34) \quad 791$$

where we have defined $E_S(t+\Delta t) = E(0, t+\Delta t)$. Here, we assume $\rho_{S/D}(t+\Delta t) \approx \rho_{S/D}(t)$ and $L_{S/D}^p(t+\Delta t) \approx L_{S/D}^p(t)$. We will later relax these assumptions. Identically, from Eq. (20), we define in the drain

$$E_D^C(t + \Delta t) = E_D(t + \Delta t) + \frac{\rho_D(t)[l + L_D^p(t)]}{\varepsilon}. \quad (35)$$

In addition, from Eq. (21), we obtain

$$V_S(t + \Delta t) = V_S^C(t + \Delta t) - E_S^C(t + \Delta t)L_C - \frac{\rho_S(t)[l + L_S^p(t)]^2}{2\varepsilon} - \frac{\rho_S(t)l^2}{2\varepsilon} \quad (36)$$

and from Eq. (22)

$$V_D(t + \Delta t) = V_D^C(t + \Delta t) + E_D^C(t + \Delta t)L_C - \frac{\rho_D(t)[l + L_D^p(t)]^2}{2\varepsilon} - \frac{\rho_D(t)l^2}{2\varepsilon}. \quad (37)$$

As mentioned before, we fix the value $V_S^C(t + \Delta t) = 0$ and $V_D^C(t + \Delta t) = V_{external}(t + \Delta t)$. We also know the charge density $\rho_S(t)$ and $\rho_D(t)$ from “step 1.” We will use $E_S^C(t + \Delta t)$ and $E_D^C(t + \Delta t)$ to find the continuous solution of the electric field according to the procedure explained in the next paragraph. Later, in “step 4,” we will relate the new parameters of $E_S^C(t + \Delta t)$ and $E_D^C(t + \Delta t)$ to new values of $\rho_S(t + \Delta t)$ and $\rho_D(t + \Delta t)$.

We will follow a Newton-Raphson method to find the best parameters $E_S^C(t + \Delta t)$ and $E_D^C(t + \Delta t)$ that provide continuity of the electric field at the borders of the simulation box. We use expressions (34) and (35) to determine $E_S(t + \Delta t)$ and $E_D(t + \Delta t)$, and Eqs. (36) and (37) for $V_S(t + \Delta t)$ and $V_D(t + \Delta t)$. Then, we apply these new voltages on the source and drain surfaces of the 3D simulation box and solve the 3D Poisson equation there. Next, we compute the electric field at the spatial step closer to the borders but still inside the 3D simulation box. We made a surface integral to transform the electric field in the surface of the simulation box into a 1D parameter. In order to obtain a continuous shape of the electric field in the whole system we repeat the previous sequence by slightly modifying the values of $E_S^C(t + \Delta t) \pm \delta E$ and/or $E_D^C(t + \Delta t) \pm \delta E$ until we find new values $V_S(t + \Delta t)$ in Eq. (36) and $V_D(t + \Delta t)$ in Eq. (37) so that the analytical and numerical electric fields at the borders of the simulation boxes coincide. Such a loop will provide a continuous analytical-numerical coupling for the electric field and, as a consequence, will also assure the continuity of the scalar potential. In summary, in this step 2, we determine the new values $V_S(t + \Delta t)$ and $V_D(t + \Delta t)$.

Step-(3) calculation of the drift electric field at $x = \mp L_C$. The $J_{SID}^{drift}(t)$ is computed inside the sample from the number of electrons crossing the source (or drain) surfaces. In addition, the value $J_{drift}(t)$ is time averaged as described in expression (33).

$$J_{SID}^{drift}(t) = \frac{1}{T^{bc}} \cdot \int_{t-T^{bc}}^t J_{SID}^{drift-ins}(t') dt', \quad (38)$$

where $J_{SID}^{drift-ins}(t')$ is the value computed at each time step. Finally, from the Ohm’s law of expression (3) we will compute the average drift electric fields deep inside the reservoirs at $x = \mp L_C$. Let us notice that we just calculate the drift electric field at time t , not at $t + \Delta t$.

Step 4—modification of the injecting energy levels and the depletion lengths. In step 2 we have already computed $E_S^C(t + \Delta t)$ and $E_D^C(t + \Delta t)$ as fitting parameters instead of $\rho_S(t + \Delta t)$ and $\rho_D(t + \Delta t)$. In this step, we will relate the modification of the electric fields deep inside the reservoir to the charge density at the borders of the simulation box. This two-step procedure is justified because we deal with a very small time step, which implies very small variations of all these parameters. From Eqs. (11) and (19), we can state a direct relationship that gives the value of the charge density required at the borders of the active region in the next time step

$$\rho_S(t + \Delta t) = \rho_S(t) + [E_S^C(t) - E_S^{drift}(t)] \frac{\varepsilon \cdot \Delta T}{[l + L_S^p(t)] \cdot \tau_c} \quad (39)$$

and from Eqs. (12) and (20)

$$\rho_D(t + \Delta t) = \rho_D(t) - [E_D^C(t) - E_S^{drift}(t)] \frac{\varepsilon \cdot \Delta T}{[l + L_D^p(t)] \cdot \tau_c}. \quad (40)$$

We have assumed the following simplification, $\exp[-(t - t_0)/\tau_c] \approx 1 - \Delta t/\tau_c$ with $\Delta t = t - t_0$ which is much smaller than τ_c , in expressions (11) and (12). Since we are only interested on relating $E_{SID}^C(t)$ with $\rho_{SID}(t + \Delta t)$, we have assumed that $E_{SID}(t)$ and $L_{SID}^p(t)$ in expressions (19) and (20) does not change with time.

Although Eqs. (39) and (40) together with the values $\rho_S(t)$ and $\rho_D(t)$ clearly define $\rho_S(t + \Delta t)$ and $\rho_D(t + \Delta t)$, we do not have a complete control on how to increase/decrease these values in our simulator. On the contrary, we only have the possibility of increasing/decreasing the injecting probability in Eq. (23) through the parameters $F_S^{inj}(t + \Delta t)$ and $F_D^{inj}(t + \Delta t)$ that appear in Eqs. (25) and (26). The exact relationship between the displacement of the injecting energy levels and the variation in the injected charge density in the simulation box boundaries is not trivial. We perform a pre-processing computation of the function $\rho^{inj}(F_{S,D}^{inj} + qV_{S,D})$ according to the injection model described in Sec. II C. Once such a relation has been established, we can determine exactly in which way the injecting energy levels have to be displaced.

As mentioned several times along this paper, there is a particular scenario that cannot be managed just by modifying the injecting energy levels. Far from equilibrium, at high applied bias, we can accumulate electrons as much as needed to decrease $\rho_S(t)$ in order to achieve overall charge neutrality. However, we cannot deplete electrons as much as possible in the sample-lead interface. Once we arrive at zero injected electrons, we cannot decrease this number any more. In such situations, the only way to decrease the negative charge is to enlarge the depleted (positive charge) region in the drain [see Fig. 1(c)]. The same depletion procedure could be needed in the source for a negative bias. From Eqs. (11) and (19), if we consider $\rho_S(t)$ fixed but $L_S^p(t)$ variable, we obtain in the source

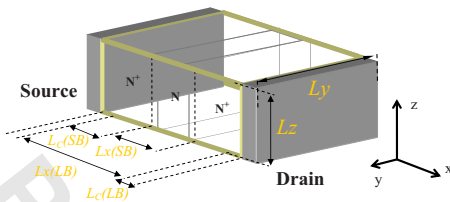


FIG. 3. (Color online) Schematic representation of the N^+NN^+ structure.

TABLE I. Parameters for the N^+NN^+ structure depicted on Fig. 3.

	Units	Symbol	Value
Lengths	(nm)	$L_x(\text{LB})$	42
		$L_x(\text{SB})$	8
		L_y	60
		L_z	60
		$L_C(\text{LB})$	3
		$L_C(\text{SB})$	20
Spatial step	(nm)	Δx	1
		Δy	60
		Δz	60
Relative permittivity		Air	1.0005
		Silicon	11.7514
Dielectric relaxation time	(sec.)	τ_c	1×10^{-13}
Silicon conductivity	$(\Omega \text{ m})^{-1}$	σ	2.5×10^5
Screening length	(nm)	l	0.95
Doping	(cm^{-3})	Channel N	Intrinsic
		Contact N^+	2×10^{19}
Simulation time	(sec.)	T	2×10^{-10}
Temporal step	(sec.)	Δt	2×10^{-16}

point in our computing tools because of the large number of particles simulated, its simulation with the SB decreases down to only 3 h.

Before comparing the SB and LB results, let us mention some details commons to both sets of MC simulations. We assume an effective-mass approximation. Electron transport in the “ x ” direction (from source to drain) takes place along a silicon (100) orientation channel, at room temperature. In particular, the electron mass is taken according to the six equivalent ellipsoidal constant energy valleys of the silicon band structure. The effective masses of the ellipsoids are $m_l^* = 0.9163m_0$ and $m_t^* = 0.1905m_0$ with m_0 the free electron mass. Finally, all simulations use a 3D finite-difference Poisson solver. Hence, the volumes Ω_{SB} (for the small box simulations) and Ω_{LB} (for the large box simulations) are divided into cells of spatial dimensions $\Delta X = 1$ nm, $\Delta Y = 60$ nm, and $\Delta Z = 60$ nm. See Table I for more details.

In Fig. 4, we have plotted (in dashed lines) the (time-averaged) self-consistent scalar potential for the LB. The results are obtained by applying our BCs algorithm explained in Sec. III for the large simulation box. In particular, we have used $L_C(\text{LB}) = 3$ nm so that, according to Fig. 1, the total length of the resistor is $2L_C(\text{LB}) + L_x(\text{LB}) = 48$ nm. Interestingly, the simulations reproduce a net charge equal to zero deep inside the reservoirs (see dashed line in Fig. 5) and a small uniform electric field proportional to the current, i.e., the drift value. The deep region of the reservoir can be modeled by a simpler series resistance confirming that our BCs algorithm can be perfectly used in large simulation boxes that include the leads. Then, our model provides the voltage drop due to a simpler (reservoir) series resistance. Another relevant issue of these LB results is that they provide a numerical justification of our “*deep_drift_BC*s” that

$$L_S^p(t + \Delta t) = L_S^p(t) + [E_S^C(t) - E_S^{\text{drift}}(t)] \frac{\varepsilon \cdot \Delta t}{\rho_S(t) \cdot \tau_c} \quad (41)$$

and, identically from Eqs. (12) and (20), we obtain in the drain

$$L_D^p(t + \Delta t) = L_D^p(t) - [E_D^C(t) - E_D^{\text{drift}}(t)] \frac{\varepsilon \cdot \Delta t}{\rho_D(t) \cdot \tau_c}. \quad (42)$$

At this point, we have determined the evolution of the injection energy levels $F_{S/D}^{\text{inj}}(t + \Delta t)$ and the depletion lengths $L_{S/D}^p(t + \Delta t)$.

Step 5-electron injection. Finally, according to the new values of the scalar potential $V_{S/D}(t + \Delta t)$ (step 2) and the injecting energy levels $F_{S/D}^{\text{inj}}(t + \Delta t)$ (step 4) at the boundaries of the simulation box, a new injecting process is performed according to expressions developed in Sec. II C. This is the last step of the BCs algorithm before the simulator can go back to moving the particles (and waves) as shown in the flux diagram of Fig. 2.

These five steps of the BCs algorithm are repeated for each time step. The time step is so small, $\Delta t \sim fs$, so that very small variations in all magnitudes are obtained. In turn, these very small variations justify the approximations developed in the procedure explained above.

IV. NUMERICAL RESULTS

Now, we report the numerical results obtained by applying the previous BCs to classical and quantum (time-dependent) electron-transport simulators. All simulations are carried out at room temperature.

A. Testing of our boundary condition algorithm: Comparison between large and small simulation boxes

In this section, we consider the N^+NN^+ resistor depicted in Fig. 3 with two different simulation boxes. First, a large simulation box (LB), $L_x(\text{LB}) = 42$ nm, that includes the leads and reservoirs (N^+ region) plus the sample (N region). Second, a smaller simulation box (SB), $L_x(\text{SB}) = 8$ nm, that only includes the sample (N region) plus a small part, $\Delta L_x(\text{SB})$, of the leads. See Fig. 3 and Table I. We will use the semiclassical MC simulator⁶⁰ of Ref. 30 that provides a detailed treatment of the Coulomb correlations among electrons inside the device. The use of the smaller simulation box certainly implies a considerable reduction in the computational burden. In particular, while the computational times related with the LB simulations imply approximately 1 day per bias

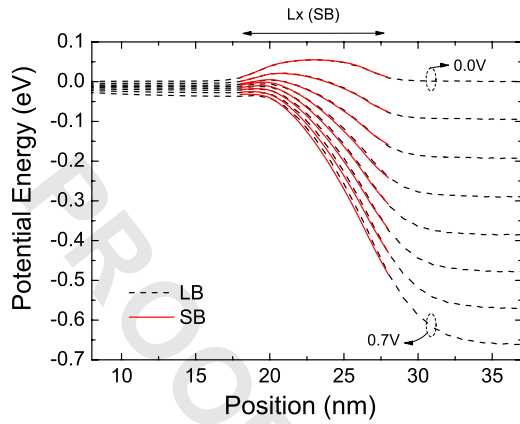


FIG. 4. (Color online) Potential-energy profile computed with our BCs algorithm for a large simulation box (dashed line) and for a small simulation box (solid lines).

967 we impose on our BCs algorithm deep inside the reservoir,
968 i.e., $E_{SID}^C(t) \rightarrow E_{SID}^{drift}(t)$.

969 In Fig. 4, we have also plotted (in solid line) the (time-
970 averaged) self-consistent scalar potential profiles obtained
971 for the SB. In particular, we have used $L_c(SB)=20$ nm so
972 that, according to Fig. 1, the total length of the resistor in this
973 second set of simulations, $2L_c(SB)+L_x(SB)=48$ nm, is
974 identical to the first ones. The agreement between both sets
975 of simulations is excellent, even for large external bias. This
976 highlights the accuracy of our BCs algorithm for simulation
977 boxes of few nanometers and its ability for incorporating the
978 Coulomb correlations among the electrons inside the sample
979 (N region) and those located in the leads (N^+ region).

980 Figure 5 shows the charge density distribution along the
981 N^+NN^+ structure for both sets of simulations. The agreement
982 among the LB and SB curves is quite acceptable. Let us
983 notice that charge density is the second derivative of the
984 scalar potential distribution, and hence, the imperceptible
985 discrepancies encountered in Fig. 4 are now magnified. The
986 depletion region in the drain for large bias merits some spe-
987 cial attention. An exponential shape describes reasonably
988 well the charge density in the source lead, however, due to

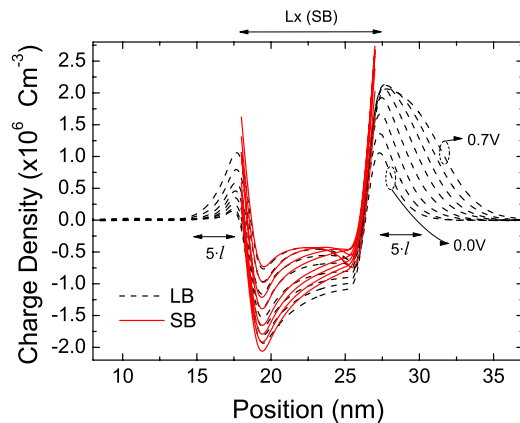


FIG. 5. (Color online) Charge-density profile computed with our BCs algorithm from a large simulation box (dashed line) and from a small simulation box (solid lines).

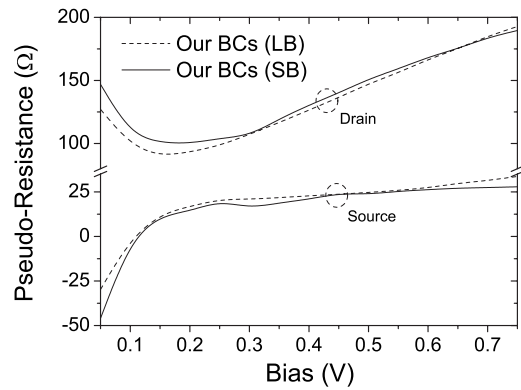


FIG. 6. Pseudoresistance of the reservoir plus lead computed from our BCs algorithm with a large simulation box (dashed lines) and with a small simulation box (solid lines).

the formation of a depletion region in the drain side, the
989 charge there does not tend to zero within the five Debye
990 lengths ($\sim 5l$). Due to the important voltage drop there, elec-
991 trons coming from the drain reservoir are not able to reach
992 the sample-lead interface and, therefore, they cannot screen
993 the positive doping charge and a depletion region appears.
994 The ability of dealing with depletion regions appearing in far
995 from equilibrium scenarios represents an important landmark
996 of our model.
997

998 There is an interesting explanation for the slight differ-
999 ences between the charge density in the LB and SB results.
1000 The semiclassical MC method⁶⁰ used in both sets of simula-
1001 tions only takes into account the Pauli exclusion principle in
1002 the electron injection process as described in Sec. II C. For
1003 example, in the source, it will not be possible to inject two
1004 electrons with identical positive velocity (wave vector) sim-
1005 ultaneously. Our injecting process waits, at least, an inter-
1006 val of time t_0 before sending the second identical electron.
1007 However, once the electrons are inside the simulation box,
1008 the semiclassical MC technique does not impose any Pauli
1009 restriction on their dynamics so that, after a large enough
1010 time from their injection, two electrons can occupy the same
1011 position with the same velocity. In this sense, the momentum
1012 distribution at the boundaries (close to the active region) will
1013 be different when large or small simulation boxes are consid-
1014 ered. When using small simulation boxes, the addition of
1015 electrons into the active region implies an increase in its
1016 energy because lower states are already occupied (i.e., the
1017 quantum capacitance). On the contrary, when using a large
1018 simulation box, the addition of electrons into the active re-
1019 gion can come from identical energies. Interestingly, we can
1020 argue that (in the MC simulations) the small simulation box
1021 provides a better electron momentum close to the sample
1022 than that obtained with a large simulation box. The slight
1023 differences appearing in Fig. 5 might partially be explained
1024 by this effect.
1025

1026 Finally, Fig. 6 shows the contact plus lead pseudoresis-
1027 tances as a function of bias. They are defined directly as the
1028 voltage drop in the lead region divided by the (average) cur-
1029 rent flowing through the whole structure. From our defini-
1030 tion, a negative value of the source resistance means that the
1031 potential energy deep inside the reservoir is lower than that

1031 at the lead-sample interface (see, for example, the 0.0 V
 1032 potential profile in Fig. 4). Obviously, the total (reservoir,
 1033 leads plus sample) resistance in the whole electron device
 1034 will be positive. We use the word “pseudo” to emphasize that
 1035 such resistances cannot be directly associated to energy dis-
 1036 sipation. As it can be observed, although the contact series
 1037 resistances (related to the drift electric field deep inside the
 1038 reservoir) are constant, the bias dependence of the resistance
 1039 in the lead is far from trivial because it takes into account the
 1040 complex electrostatic coupling of the leads and the sample
 1041 described by expressions (36) and (37). This result shows
 1042 that a constant resistance cannot account accurately for the
 1043 Coulomb correlations between electrons in the active region
 1044 and those in the leads.

1045 In conclusion, in this section we have shown that our BCs
 1046 provides an excellent description of the coulomb coupling
 1047 between the sample and the leads. The (reservoir plus lead)
 1048 resistance obtained from a LB simulation box is practically
 1049 identical to that obtained from a SB simulation. The com-
 1050 parison of the current-voltage characteristic will be discussed
 1051 in next section. Let us emphasize that our BCs algorithm is a
 1052 parameter free algorithm. Only the external bias is necessary.
 1053 Even the electric drift field is obtained from the numerical
 1054 computation of the average conduction current. In next sec-
 1055 tion, we show numerically the enormous difficulties that the
 1056 standard BCs, applied to small simulation boxes that exclude
 1057 the leads, have when trying to reproduce the previous set of
 1058 results obtained with our algorithm.

1059 **B. Limitations of standard boundary condition algorithms**
 1060 **for (small) simulation boxes that exclude the leads**

1061 In the present section, we simulate the same N^+NN^+ struc-
 1062 ture with the same MC technique and the same small simu-
 1063 lation box (that excludes the leads) considered in the previ-
 1064 ous section. The only difference will be the consideration of
 1065 two different BCs algorithms.

1066 The first type of BCs, that we named *Dirichlet external*
 1067 *bias*, uses the external bias as the BCs for the Poisson equa-
 1068 tion (“border_potential_BCs”) and the injection model de-

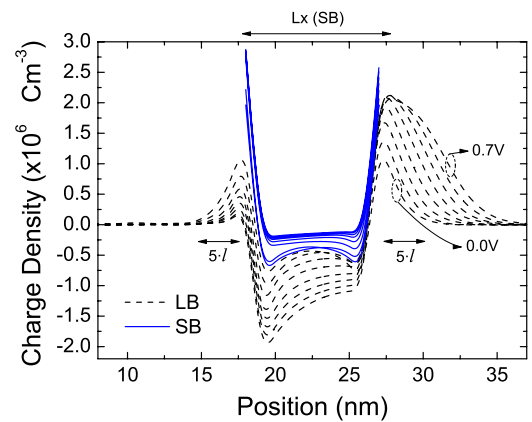


FIG. 8. (Color online) Charge-density profile computed in the large simulation box with our BCs algorithm (dashed lines) and that corresponding to the implementation of the Dirichlet external bias BCs in the small simulation box (solid lines).

scribed in Sec. II C with a fixed $F_{SD}^{inj}(t)$ equal to the equilibrium electrochemical value (“border_charge_BCs”). Since such Dirichlet BCs consider zero-external impedance so that it can only be acceptable for large simulation boxes. Here, we explicitly demonstrate its limitations for small simulation boxes.

The second type of BCs, that we named *local charge neutrality*, is based on ensuring that the total charge is zero at the borders (“border_charge_BCs”). The *local charge neutrality* is achieved by moving the bottom of the conduction (border_scalar_BCs), while fixing $F_{SD}^{inj}(t)$ equal to the equilibrium electrochemical value, to increase/decrease the charge at the border. This second type can be used in simulation boxes slightly smaller than the ones required by the previous BCs algorithm. In any case, although the assumption of local charge neutrality inside the leads (i.e., a few Debye lengths away from the lead-sample interface) is correct, it is not valid close to the active region as shown below.

The LB results depicted in Figs. 7–10 are the ones obtained in the previous subsection. The first type of BCs, the Dirichlet external bias implies a very restrictive constriction

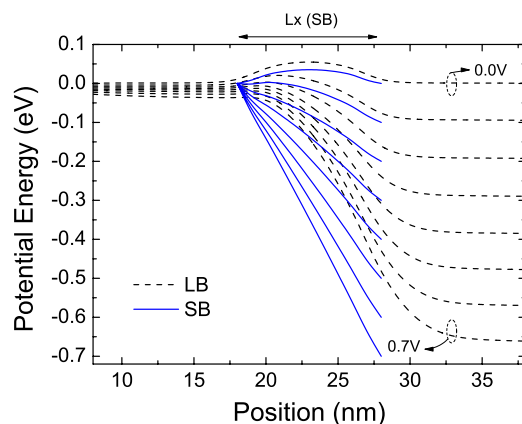


FIG. 7. (Color online) Scalar potential-energy profile computed in the large simulation box with our BCs algorithm (dashed lines) and that corresponding to the implementation of the Dirichlet external bias BCs in the small simulation box (solid lines).

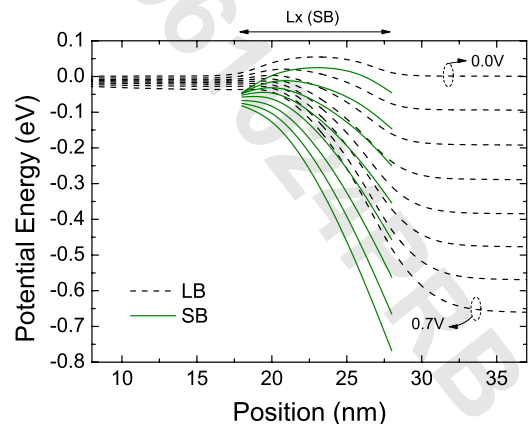


FIG. 9. (Color online) Scalar potential-energy profile computed in the large simulation box with our BCs algorithm (dashed lines) and that corresponding to the implementation of the local charge neutrality BCs model in the small simulation box (solid lines).

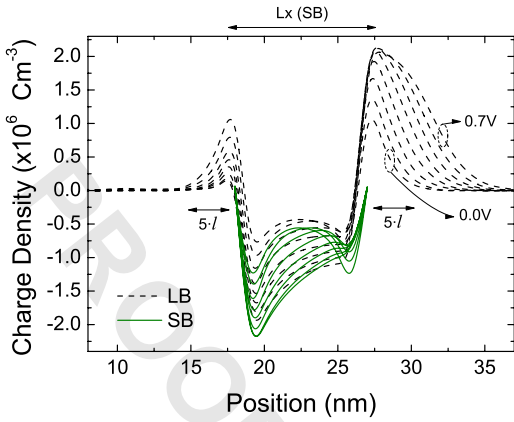


FIG. 10. (Color online) Charge-density profile computed in the large simulation box with our BCs algorithm (dashed lines) and with the local charge neutrality BCs model in the small simulation box (solid lines).

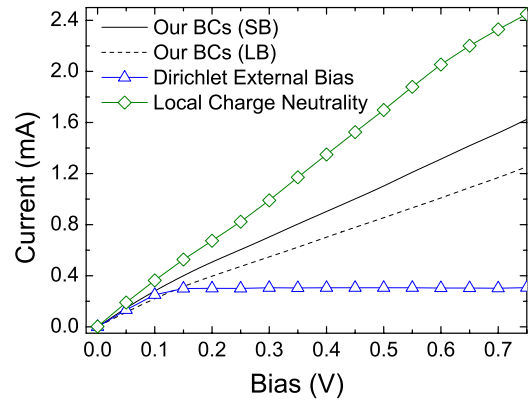


FIG. 12. (Color online) Current-voltage characteristics for the N^+NN^+ structure. The solid line corresponds to our BCs algorithm applied in the small box region. Open triangles correspond to Dirichlet external bias and open diamonds to local charge neutrality BCs. In dotted line we have plotted the I - V characteristic correspondent to our BCs applied in the large box including the leads.

1090 that neglects any correlation among the electrons inside and
 1091 outside the active region. The scalar potential at the borders
 1092 does not depend on the charge (accumulated or depleted) in
 1093 the leads. As seen in Figs. 7 and 8, these limitations are
 1094 obviously translated into a bad description of the conduction
 1095 band and the charge density.

1096 The second type of BCs in small simulation boxes, local
 1097 charge neutrality, is plotted in Figs. 9 and 10. It cannot prop-
 1098 erly describe the (accumulated or depleted) charge at the
 1099 N^+-N and $N-N^+$ interfaces. The charge density at those inter-
 1100 faces is always zero with these BCs (see Fig. 10). The con-
 1101 dition of charge neutrality is reasonable deep inside the
 1102 leads, but not close to the sample, where the excess/deficit of
 1103 charge has not yet been screened. This second type of BCs is
 1104 unable to properly describe the bottom of the conduction
 1105 band depicted in Fig. 9.

1106 The ultimate reason why none of the two previous BCs
 1107 types are able to produce reasonable results is because they
 1108 do not achieve the overall-charge-neutrality requirement dis-
 1109 cussed in the introduction. In Fig. 11, we demonstrate that a
 1110 nonaccurate description of the lead-sample Coulomb corre-

lations cannot provides an accurate description of the (lead
 plus reservoir) pseudoresistance. The first type of BCs, Dir-
 ichlet external bias, gives a trivial and incorrect zero resis-
 tance. The second type, local charge neutrality, accounts for
 a nonlinear dependence of the resistances on the applied
 voltage that assumes some kind of electrostatic correlations
 between sample and leads. However, Fig. 11 shows that such
 correlations are clearly unphysical when small simulation
 boxes are considered.

1120 Finally, in Fig. 12, we plot the characteristic current-
 voltage curves for the large and small simulation boxes com-
 puted by means of our BCs algorithm and those computed
 through the Dirichlet external bias and the local charge neu-
 trality algorithms with small boxes. For very small voltages
 (close to equilibrium), all BCs gives similar results. How-
 ever, for large voltages (far from equilibrium), the discrep-
 ancies among the different models are more than notable.

1128 The Dirichlet external bias (open triangles) fixes not only
 the potential at the borders of the simulation box but also the
 electrochemical potentials there. This means that the injec-
 tion of electrons in each side is independent of the rest of the
 system (and neglects the Coulomb correlations between elec-
 trons in the sample and the leads). Therefore, when the ap-
 plied bias is enough to avoid that electrons coming from the
 drain contact reach the source, the current saturates. The local
 charge neutrality (open diamonds) wants to preserve
 charge neutrality, locally, in the lead border. As we increase
 the voltage, in the source border, the number of electrons
 reflected by the sample (with negative momentum) tends to
 decrease because most of source electrons are finally trans-
 mitted. In addition, the mean velocity of the carriers tends to
 increase in the active region implying a reduction in negative
 charge in the sample (while the positive charge remains con-
 stant). Therefore, when we increase the voltage, the source
 electron density at the source border tends to decrease and,
 consequently, the injection rate must increase to ensure local
 charge neutrality in the source border. This explains why the
 current saturates at a much larger voltage (not plotted in Fig.
 12) than that obtained for the Dirichlet external voltage. A

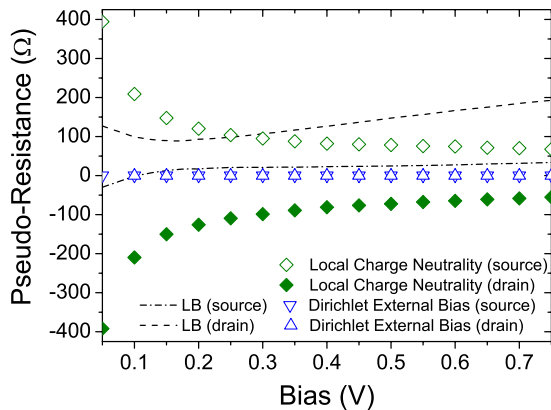


FIG. 11. (Color online) Pseudoresistance of the reservoir plus lead computed from our BCs model for the large simulation box (dashed lines) and from the Dirichlet external bias and local charge neutrality for the small simulation box (symbols).

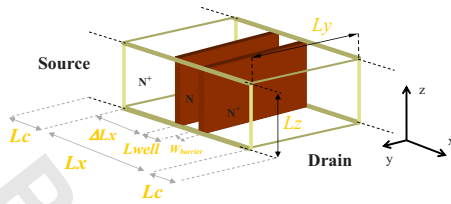


FIG. 13. (Color online) Schematic representation of the RTD.

1150 similar explanation can be applied to understand the current-
 1151 voltage obtained with our BCs model for a SB (solid lines).
 1152 Again, the solution to obtain overall charge neutrality is to
 1153 incorporate more and more electrons from the source but at
 1154 slower rate. Certainly, our BCs model with a small box (solid
 1155 line) is the one that provides currents closer to the LB results
 1156 (dashed lines).

1157 The small differences between the two curves obtained
 1158 with our BCs for small and large boxes can be explained
 1159 with the same arguments used to explain the differences in
 1160 the charge density of Fig. 5. The MC method⁶⁰ used in both
 1161 sets of simulations only takes into account the Pauli exclu-
 1162 sion principle in the electron injection process at the bound-
 1163 aries of the simulation box, as described in Sec. II C. How-
 1164 ever, once the electrons are inside the simulation box, the
 1165 semiclassical MC technique does not impose any (Pauli) re-
 1166 striction on their dynamics. When using small simulation
 1167 boxes, the addition of electrons at the borders of the active
 1168 region implies an increase in their (kinetic) energy because
 1169 lower states are already occupied (this is not true for the LB
 1170 because the injection is far from the borders of the active
 1171 region). This means that the average velocity in the borders
 1172 is slightly higher with the small simulation box than with the
 1173 large one. Hence, as depicted in Fig. 12, the current com-
 1174 puted with the SB is slightly higher than the LB current.

1175 C. Application of our boundary condition algorithm for 1176 (time-dependent) quantum electron transport simulators

1177 In this section, we provide an example of the implemen-
 1178 tation of our BCs algorithm into a time-dependent quantum
 1179 simulator, where the need for small simulation boxes is still a
 1180 more relevant computational requirement. In fact, it is not
 1181 strange to find in the literature, atomistic structures with
 1182 simulation boxes of few tens of Angstrom.^{14,15,45} In order to
 1183 emphasize the relevance of taking into account the Coulomb
 1184 correlations among the active region and the leads, we will
 1185 compare the results obtained with our BCs model and those
 1186 obtained through standard Dirichlet external bias at the bor-
 1187 ders of the simulation box. Contrarily to Sec. IV A, no com-
 1188 parison with a large simulation box (including the leads and
 1189 reservoirs) is done because such simulation would be com-
 1190 putationally inaccessible. This computational difficulty was,
 1191 precisely, the initial motivation for this work.

1192 As described in Fig. 13 and Table II, we consider an RTD
 1193 consisting on two highly doped drain-source GaAs regions
 1194 (the leads), two AlGaAs barriers, and a quantum well (the
 1195 active region). Such structure is simulated with a quantum
 1196 electron-transport simulator based on the algorithm dis-

TABLE II. Parameters for the RTD depicted on Fig. 13.

	Units	Symbol	Value
Lengths	(nm)	L_x	17.1
		L_y	48.6
		L_z	48.6
		ΔL_x	4.5
		L_C	6
		Equilibrium screening lengths	(nm)
Barrier dimensions	(eV)	High	0.6
Relative permittivity	(nm)	L_{well}	5.7
	(nm)	$W_{barrier}$	1.2
Spatial step (Poisson equation)		Air	1.0005
		GaAs	13.1800
Spatial step (Schrödinger equation)		AlGaAs	11.7760
	(nm)	Δx	0.30
	(nm)	Δy	8.1
		Δz	8.1
Doping	(cm^{-3})	Channel N	Intrinsic
		Contact N^+	4.8×10^{18}
GaAs conductivity	$(\Omega \text{ m})^{-1}$	σ	1.5×10^5
Dielectric relaxation time	(sec.)	τ_c	5×10^{-14}
Simulation time	(sec.)	T	4×10^{-11}
Temporal step (Poisson equation)	(sec.)	Δt	8×10^{-16}
Temporal step (Schrödinger equation)	(sec.)	Δt_S	2×10^{-17}

1197 cussed in Ref. 50, where it is demonstrated that the many-
 1198 particle Schrödinger equation can be efficiently solved using
 1199 quantum (Bohmian) trajectories computed from (time-
 1200 dependent) single-particle Schrödinger equations. In this pa-
 1201 per, we assume a constant effective mass $m=0.067m_o$, with
 1202 m_o the electron free mass, along the whole structure that
 1203 accounts for the interaction of free electrons with the peri-
 1204 odic atomic structure under the Born-Oppenheimer
 1205 approximation.⁶² In any case, the BCs algorithm presented in
 1206 this paper can be straightforwardly adapted to a discrete de-
 1207 scription of the atom structure. Then, the analytical expres-
 1208 sions of Sec. II B have to be matched to the Hartree potential
 1209 of the simulation box. Transport takes place from source to
 1210 drain direction. The lateral dimensions are $L_y=L_z=48.6$ nm.
 1211 The practical quantum algorithm for the RTD implies solving
 1212 numerically $N(t)$ time-dependent single-particle 1D
 1213 Schrödinger equations⁵⁰ for the transport direction x . All
 1214 Schrödinger equations are coupled to the Poisson equations
 1215 with the BCs given by our algorithm. The number of elec-
 1216 trons, $N(t)$, around 20–30, implies a computational time on
 1217 the order of 1–2 days per bias point. In order to take into
 1218 account the Friedel oscillations⁵⁴ and the formation of qua-
 1219 sibound states⁵³ in the leads, we extend the simulation box
 1220 inside the leads a distance ΔL_x . More technical details about
 1221 the computation of Bohmian trajectories can be found in
 1222 Refs. 30 and 50 and Table II.

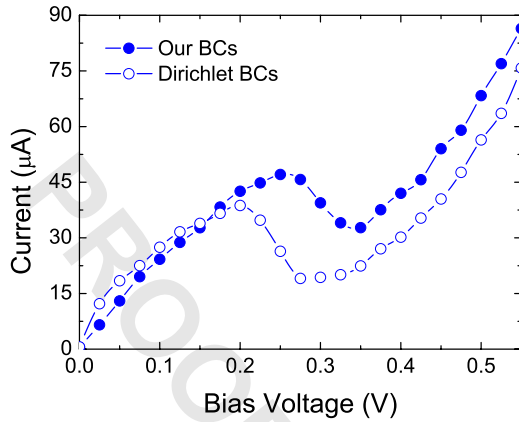


FIG. 14. (Color online) RTD Current-voltage characteristic taking according to our BCs algorithm (solid circles) and to a Dirichlet external bias BCs (open circles).

1223 In Fig. 14, we present the current-voltage curves of the
 1224 simulated RTD using our BCs algorithm (solid circles) and
 1225 standard Dirichlet external bias BCs (open circles). As it can
 1226 be observed, the differences between these two approaches
 1227 appear not only in the magnitude of the current but also in
 1228 the position of the resonant voltage. These differences are
 1229 fully compatible with previous current-voltage simulations
 1230 done with/without explicitly including the leads in the self-
 1231 consistent simulation scheme.³³ The differences in Fig. 14
 1232 can be easily explained from the information depicted in Fig.
 1233 15.

1234 In Fig. 15, we represent the (time-averaged) voltage drop
 1235 $\Delta V_{S/D}$ of the scalar potential outside the simulation box de-
 1236 fined as, $\Delta V_S = V_S^C - V_S$ in the source and $\Delta V_D = V_D - V_D^C$ in the
 1237 drain regions. While Dirichlet BCs assume a zero-voltage
 1238 drop outside the simulation box, our BCs algorithm predicts
 1239 a nonlinear drop of the bottom of the conduction band at the
 1240 borders of the simulation box. In particular, ΔV_D is higher
 1241 than ΔV_S in magnitude and it is the main responsible of the
 1242 displacement of the resonant voltage. As seen in the insets
 1243 (a) and (b) of Fig. 15, our model predicts a drop of the scalar
 1244 potential in the drain lead that maintains the resonant energy

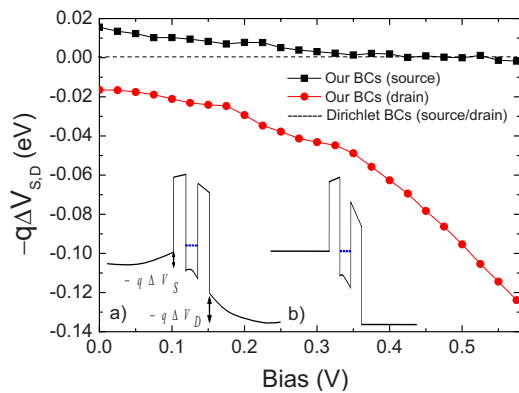


FIG. 15. (Color online) Potential-energy drop in the highly doped drain lead, $-q\Delta V_D$ (red circles), and in the source lead, $-q\Delta V_S$ (black squares). The insets represent a schematic representation of the potential energy profile at $V=0.2$ V using (a) our BCs algorithm and (b) the Dirichlet external bias approach.

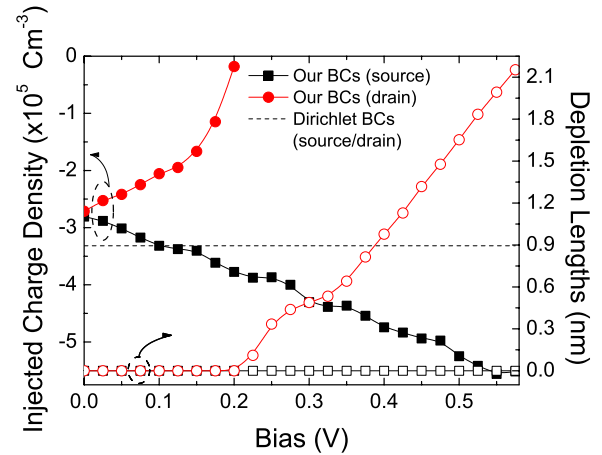


FIG. 16. (Color online) On the left axis: injecting charge density at the borders of the simulation box as a function of the applied bias. On the right axis: depletion lengths as a function of the applied bias. The dashed line represents the constant injected charge density obtained with external bias Dirichlet BCs.

level significantly above the bottom of the source conduction
 band at that particular 0.2 V bias (i.e., the resonant voltage
 for the Dirichlet external bias). As explained in Sec. III, the
 behavior of ΔV_D and ΔV_S is also coupled to the value of ρ_D
 and ρ_S . The latter, in turn, are the responsible of a higher
 source injection that explains the higher current when our
 BCs algorithm is used.

In Fig. 16, we discuss in detail the coupling between
 $\Delta V_{S/D}$ and $\rho_{S/D}$. First, let us notice that the BCs with a stan-
 dard Dirichlet conditions equal to the external bias always
 injects electrons at the same rate because it does not allow
 neither a displacement of the bottom of the conduction band
 $V_{S/D}$ nor a movement of the injecting energy levels $F_{S,D}^{inj}$.
 Thus, the injecting probabilities of Eqs. (25) and (26) remain
 bias independent. On the contrary, our BCs algorithm does
 not fix any of the two parameters. We have only an indirect
 control on the values of $\rho_{S/D}$ because we can only increase/
 decrease the rate of injection into the simulation box by modi-
 fying the values $F_{S/D}^{inj}$ and $V_{S/D}$ [see expressions (25) and
 (26)]. As seen in Fig. 16, for bias below 0.15 V, the charge
 injected from the source border decreases while the charge
 injected from the drain increases with the bias. These in-
 jected charges and the potential profiles are consistent with
 the requirement of overall charge neutrality. In particular, the
 increase of the electrons injected from the source is the main
 reason why our algorithm predicts a larger current than the
 results obtained from a Dirichlet external bias. The situations
 changes when the external bias approaches 0.2 V. The prob-
 ability of injecting electrons from the drain is very low so
 that any further decrease in the injecting energy level does
 not cause any variation in the charge density there. There-
 fore, the only way to decrease an excess of negative charge
 in the whole system, in order to achieve overall charge neu-
 trality, is creating a depletion region at the drain side [see
 expression (42)]. For larger values of ΔV_D , the most relevant
 effect in the drain lead is not the screening of positive charge
 by electrons but the appearance of a depletion region. As
 discussed in Sec. IV A, this is an important contribution of

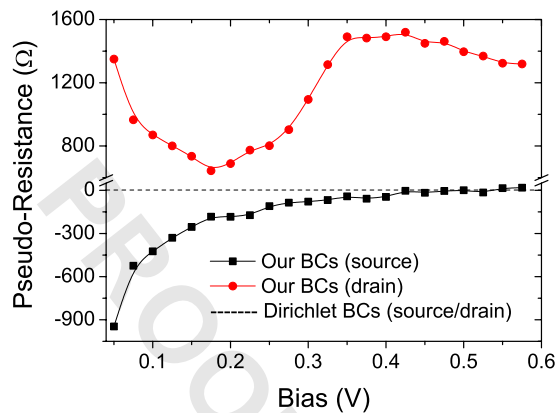


FIG. 17. (Color online) Pseudo-resistance of the RTD in the drain and source regions.

our BCs algorithm that allows us to satisfactorily simulate far from equilibrium conditions in small simulation boxes of electron devices.

Finally, in Fig. 17, we discuss the resulting pseudo-reservoir plus lead) resistances. The external bias Dirichlet BCs predicts a zero effective resistance and our BCs algorithm describes a highly asymmetric and nonlinear behavior. Even more, the source pseudo-resistance takes negative values up to very high applied bias (the negative sign in the pseudo-resistance means a positive spatial derivative of the potential energy). In any case, obviously, the total (source, sample plus drain) resistance is positive. Importantly, the practical results of such lead resistances are quite different from the expressions (A1) and (A2) deduced in Appendix A, where a constant value of both resistances is predicted. In Appendix A, zero temperature is assumed while, here, we consider a room temperature and an energy-dependent density of states. In addition, in Appendix A, Poisson equation is substituted by some kind of linear “capacitor” that can be justified for small variations around equilibrium. However, here, we solve explicitly the Poisson equation and the charge is related not only to the number of electrons but also to its dynamics (fast electrons provide less charge than slow electrons).

In conclusion, in the results of the RTD with our BCs algorithm, we can guarantee that the profile of the charge density along the whole device (the reservoirs, the leads, and the sample) is compatible with the requirement of overall charge neutrality discussed in the introduction. In addition, we can also guarantee that the profiles of the electric field and scalar potential are self-consistent with the previous profile of the charge density. Even more, the requirement of overall charge neutrality is achieved in time intervals related with the relaxation dielectric time.

V. CONCLUSIONS

The Coulomb interaction among electrons introduces two fundamental requirements for the accurate simulation of electron devices. First, the screening of electrons implies that the total charge in the whole (reservoirs, leads plus sample⁶) device region is zero, i.e., overall charge neutrality. Second,

the total time-dependent current computed in a surface of the simulation box is equal to that measured by an ammeter far from the sample, i.e., current conservation.

Due to the computational burden associated to quantum and atomistic description of nanoscale structures, the explicit and accurate simulation of the lead-sample-lead region⁶ is not always possible. Therefore, quite often, a small simulation box that excludes the leads⁶ is a mandatory requirement in modern electron-transport simulators. This restriction on the box length is a serious problem for the requirement of overall charge neutrality because the total charge has to include the (accumulated/depleted) charge in the leads. In addition, the inaccuracy in achieving the overall-charge-neutrality requirement affects the computation of the time-dependent variations in the scalar potential (i.e., the electric field) and, thus, the requirement of current conservation.

As explained in the introduction, all BCs used in electron transport simulators are based on specifying the value of the scalar potential, or the electric field, at the borders of the simulation box (“border_potential_BCs”) and the charge density there (“border_charge_BCs”). However, it is very difficult to anticipate an educated guess for these magnitudes at the boundaries of a small simulation box that excludes the leads (see Sec. IV B). Alternatively, in Sec. II, we have developed analytical and time-dependent expressions for the charge density, the electric field, and the scalar potential along the leads and reservoirs. These analytical expressions take into account electron screening leading to accumulation and depletion regions in the leads. From these analytical expressions, we can transfer the assumptions about the BCs at the borders of a small simulation box into the simpler specifications of the BCs deep inside the reservoirs. This is the key point of our BCs algorithm. In particular, the two new BCs that we impose deep inside the reservoirs are, first, the electric field tends to a drift value $E_{S/D}^C(t) \rightarrow E_{S/D}^{drift}(t)$ (that we refer as “deep_drift_BCs”) and, second, the scalar potentials deep inside the reservoir is fixed by the external bias $V_S^C(t) = 0$ and $V_D^C(t) = V_{external}(t)$. In Sec. IV A, we have shown that these two new BCs conditions are perfectly supported from a numerical MC solution of the nonequilibrium Boltzmann equation in a large simulation box that includes the leads and reservoirs.

Our BCs algorithm requires a minimum computational effort and it can be implemented into either quantum or classical time-dependent simulators, for dc, ac, and current (or voltage) fluctuations. We have tested our BCs algorithm with semiclassical MC simulations of a nanoscale silicon resistor with large and small simulation boxes. As seen in Fig. 4, the excellent agreement between both sets of simulations confirms the accuracy of our BCs algorithm. Let us emphasize that no fitting parameter is used and that our BCs algorithm includes the trivial series resistance plus the complicated lead resistance (see Appendix A). We have also presented a numerical simulation for a (quantum) double barrier RTD to show the importance of the BCs discussed here. In particular, we have highlighted that our BCs algorithm is able to discuss far from equilibrium situations where depletion lengths in the leads have to be added to standard screening. Our BCs algorithm guarantees that the profile of the charge density along the whole device (not only along the simulation box

1383 but the reservoirs, the leads, and the sample) is compatible
 1384 with the requirement of overall charge neutrality and that the
 1385 profiles of the electric field and scalar potential are self-
 1386 consistent with the charge density along the whole device.
 1387 The numerical results presented in this paper deal with
 1388 classical and quantum dc scenarios. However, our BCs algo-
 1389 rithm can be equivalently applied to ac (time-dependent)
 1390 scenarios up to a frequency f^{qs} (defined from the lowest-
 1391 frequency restriction for the validity of expressions devel-
 1392 oped in Sec. II). The requirement of overall charge neutrality
 1393 is achieved in time intervals related with the relaxation di-
 1394 electric time of the device. Therefore, for time intervals
 1395 lower than the inverse of f^{qs} , the temporal variations in the
 1396 scalar potential (and the electric field) at the borders of the
 1397 simulation box are physically meaningful because they are
 1398 the reaction of the Coulomb interaction in the whole electron
 1399 device system to temporal perturbation that deviates the de-
 1400 vice from its “state” compatible with overall charge neutral-
 1401 ity. Such frequency-dependent correlations allows us to con-
 1402 fidently compute the displacement current (i.e., time-
 1403 dependent variations in the electric field inside) in the
 1404 simulation box and assume that the total current computed
 1405 there is equal to the value measured in an ammeter far from
 1406 the simulation box, i.e., current conservation.
 1407 Identically, the frequency-dependent correlations included
 1408 into our BCs algorithm, due to sample-lead Coulomb inter-
 1409 action, allow us to investigate the computation of (zero-
 1410 frequency or high-frequency) current fluctuations beyond the
 1411 standard external zero impedance assumption (i.e., most of
 1412 the computations of current fluctuations in electron devices
 1413 assume that the voltage applied in the simulation box is a
 1414 nonfluctuating quantity). As discussed at the end of Sec.
 1415 IV C, the intrinsic charge fluctuations are coupled to voltages
 1416 fluctuations at the borders of the simulation boxes that, in
 1417 turn, induce additional fluctuations of the injected charge
 1418 (i.e., current) in a quite complicated self-consistent loop.
 1419 Studies of these two directions are in progress.

1420 **ACKNOWLEDGMENTS**

1421 This work has been partially supported by the Ministerio
 1422 de Ciencia e Innovación under Project No. TEC2009-06986
 1423 and by the DURSI of the Generalitat de Catalunya under
 1424 Contract No. 2009SGR783. J. Suñé acknowledges support
 1425 from ICREA ACADEMIA.

1426 **APPENDIX A: QUALITATIVE ESTIMATION OF LEAD**
 1427 **RESISTANCE IN PURE BALLISTIC DEVICES**

1428 As mentioned in the introduction, the importance of the
 1429 resistance in the leads when dealing with electric transport
 1430 through ballistic devices was well understood some time ago
 1431 due to the enlightening work of Landauer, Büttiker, and
 1432 co-workers¹⁻⁵ on the “two-terminal” G^{2t} and “four-terminal”
 1433 G^{4t} conductances. We will use here an argument to obtain the
 1434 same lead resistances but emphasizing the role of the overall-
 1435 charge-neutrality requirement mentioned along this paper.
 1436 The effect of these lead resistances on the measured charac-
 1437 teristics of the electron device is, somehow, rediscovered for

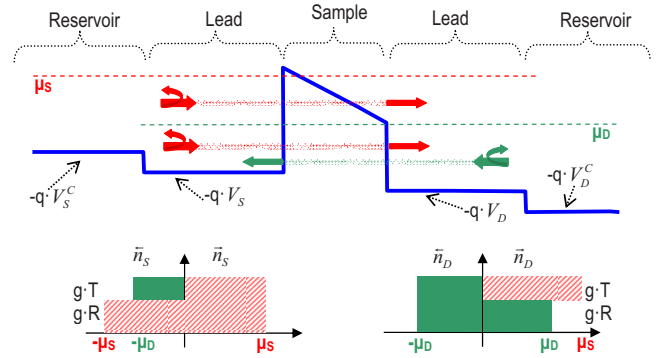


FIG. 18. (Color online) Schematic representation of the bottom of the conduction band and the electrochemical potential as a function of position for a tunneling obstacle with transmission T and reflection R coefficients. Left/right insets: particle density on the source/drain lead as a function of the kinetic energy (with sign defined by their velocity direction) of electrons. The total particle density $\tilde{n}_{S/D}$ ($\tilde{n}_{S/D}$) of electrons in the source/drain lead is equal to the area above of the negative (positive) axis. Solid green (dashed red) indicates electrons initially injected from the drain (source) reservoir.

each new generation of electron-transport simulator (see, for
 example, Ref. 33 for a discussion of this issue on the self-
 consistent scattering-states algorithm for a RTD or Ref. 45
 for a DFT electron-transport simulator).

As depicted in Fig. 18, we define the sample (or the active
 region⁶) as an obstacle that is tunneled by electrons. We do
 also consider two ideal reservoirs acting as a perfect
 (absorbing/emitting) black bodies with a source μ_S and drain
 μ_D well-defined electrochemical potentials. We defined the
 leads as the region that connects the obstacle (i.e., sample)
 with the ideal reservoirs. Electrons leaving the sample, either
 by transmission or reflection, are effectively screened and
 they suffer inelastic scattering, so that their energy distribu-
 tion becomes a (quasi-) equilibrium distribution at the reser-
 voir. The “two terminals” conductance $G^{2t} = I/V^{2t} = 2q^2 T/h$ is
 defined as the total average (dc) current I divided by the
 voltage drop $V^{2t} = V_D^C - V_S^C$ between the reservoirs.¹⁻³ The pa-
 rameter T is the transmission coefficient of a tunneling ob-
 stacle, h the Plank constant. The original formulation of the
 “four terminals” conductance proposed by Landauer^{4,5} was
 $G^{4t} = I/V^{4t} = 2q^2/h(T/R)$, when $V^{4t} = V_D - V_S$. The difference
 between both expressions is due to the resistance (i.e., volt-
 age drop) in the leads.

Now, we deduce the value of such lead resistances in
 the source and drain by imposing (a simplified version of)
 the overall-charge-neutrality requirement mentioned in the
 paper. As seen in Fig. 18, we apply a bias $V^{2t} = V_D^C - V_S^C$
 $= (\mu_S - \mu_D)/q$ with net flux of electrons from source to drain.
 The energies $-qV_S^C$ and $-qV_D^C$ are the conduction band bot-
 tom at the source and drain reservoir, respectively. Deep in-
 side the source reservoirs, the total particle density is equal
 to the doping density N_D . Thus, $n_S^C = \tilde{n}_S^C + \tilde{n}_S^C = N_D$, where
 \tilde{n}_S^C and \tilde{n}_S^C refer to the particle density of electrons with positive
 (from left to right) and negative velocities, respectively. If
 the series resistances of the reservoirs are negligible, we can
 assume $\tilde{n}_S^C = g(\mu_S + qV_S^C) = N_D/2$ and $\tilde{n}_S^C = g(\mu_S + qV_S^C) = N_D/2$

1474 where g is the density of states that we assume constant in
1475 order to avoid irrelevant energy integrals in our *qualitative*
1476 argumentation. In addition, zero temperature is assumed to
1477 simplify arguments. Identical charge distribution can be de-
1478 fined in the drain reservoir.

1479 However, close to the barrier, in the leads, the electron
1480 charge density depends on the barrier transmittance. The
1481 number of electrons arriving at one lead depends on the
1482 number of electrons injected from the reservoir of the other
1483 side and the transmission of the barrier. For example, elec-
1484 trons with negative velocity in the source lead are those in-
1485 cident from the drain region and effectively transmitted, plus
1486 those incident from the source that have been reflected by the
1487 barrier, $\tilde{n}_S = Tg(\mu_D + qV_S) + Rg(\mu_S + qV_S)$. On the other hand,
1488 electrons with positive velocity in the source lead are \tilde{n}_S
1489 $= g(\mu_S + qV_S)$. In particular, in a simple treatment of the Cou-
1490 lomb interaction, we define $-qV_S$ and $-qV_D$ as the energies
1491 of the conduction band bottom at the source and drain leads,
1492 respectively. See left inset in source region of Fig. 18.

1493 In order to accomplish the overall-charge-neutrality con-
1494 dition, assuming that the reservoirs are already neutral and
1495 that the charge in the barrier regions is negligible, then, the
1496 total charge in each lead must be neutral (i.e., electron charge
1497 equal to the doping) to assure overall charge neutrality in the
1498 whole device. This is the crucial point of our argumentation
1499 in this appendix. Therefore, for the degenerate system con-
1500 sidered here (where the Pauli principle implies that any in-
1501 crease in charge must come from higher energies) the voltage
1502 close to the barrier must vary to accommodate the previous
1503 charge-neutrality restriction. Thus, the charge neutrality at
1504 the leads, $\tilde{n}_S + \tilde{n}_D = N_D$ with $\tilde{n}_S = Tg(\mu_D + qV_S) + Rg(\mu_S + qV_S)$
1505 and $\tilde{n}_D = g(\mu_D + qV_D)$, implies the following relationship
1506 between the reservoir and lead voltages, $V_S = V_S^C + T(\mu_S$
1507 $- \mu_D)/(2q)$, with a source lead “pseudoresistance” equal to

$$R_{SL} = \frac{V_S - V_S^C}{I} = \frac{T(\mu_S - \mu_D)/(2q)}{2q^2 T/hV^{2t}} = \frac{1}{2} \frac{h}{2q^2 T}. \quad (\text{A1})$$

1508
1509 The bottom of the conduction band decreases in the source
1510 lead because the number of electrons with negative velocity
1511 is less than expected in the energy range $\mu_S - \mu_D$ (i.e., only
1512 electrons reflected by the barrier in the source will contribute
1513 to \tilde{n}_S). Identically, electrons with positive velocity in the
1514 drain lead are transmitted electrons from the source or re-
1515 flected electrons from the drain, $\tilde{n}_D = Tg(\mu_S + qV_D) + Rg(\mu_D$
1516 $+ qV_D)$ and $\tilde{n}_D = g(\mu_D + qV_D)$. Then, from the charge neutrality
1517 condition, $\tilde{n}_D + \tilde{n}_S = N_D$, we obtain the relation $V_D = V_D^C$
1518 $- T(\mu_S - \mu_D)/(2 \cdot q)$ that implies the drain lead pseudoresis-
1519 tance

$$R_{DL} = \frac{V_D^C - V_D}{I} = \frac{T(\mu_S - \mu_D)/(2q)}{2q^2 T/hV^{2t}} = \frac{1}{2} \frac{h}{2q^2 T}. \quad (\text{A2})$$

1520
1521 Again, we realize that the bottom of the conduction band in
1522 the drain lead have to be a bit higher than that deep in the
1523 reservoir because the number of electrons with positive ve-
1524 locity is more than expected in the energy range $\mu_S - \mu_D$.

1525 In many textbooks,⁶⁵ there is an even simpler develop-
1526 ment of the expression of the source in Eq. (A1) and drain in
1527 Eq. (A2) lead expressions of the pseudoresistances. If we

assume a zero-series resistance in the reservoir, the total con- 1528
ductance $G^{2t} = I/V^{2t} = 2q^2 T/h$ can be decomposed as follows: 1529

$$\frac{1}{G^{2t}} = \frac{h}{2q^2 T} = \frac{h}{2q^2} \left(1 + \frac{1-T}{T} \right) = \frac{h}{2q^2} + \frac{h}{2q^2} \frac{R}{T} \quad (\text{A3})$$

$$= R_{SL} + R_{DL} + \frac{h}{2q^2} \frac{R}{T}, \quad (\text{A3})$$

where $R_{SL} = h/4q^2$ is the source lead resistance, $R_{DL} = h/4q^2$ 1532
is the drain lead resistance and $hR/(2q^2 T)$ the intrinsic 1533
sample resistance deduced by Landauer, originally. 1534

This simple example does show the inevitable presence of 1535
lead resistances in ballistic systems. The accurate computa- 1536
tion of such resistances needs a more appropriate treatment 1537
of the Coulomb interaction among electrons than the capaci- 1538
tive linear relation between charge and voltage that we have 1539
assumed above. Therefore, a better treatment of coulomb in- 1540
teraction in the leads needs a self-consistent solution of the 1541
charge density and scalar potential, as we did in the paper. 1542

Finally, let us emphasize the different origins of the 1543
standard-series resistance present in any electron device and 1544
the lead resistances discussed here. The former is due to the 1545
presence of a small and homogenous electric field deep in- 1546
side the reservoir, which provides a net current. The voltage 1547
drop in the reservoir is only due to this homogenous electric 1548
field deep inside the reservoir where local charge neutrality 1549
is guaranteed. However, the voltage drop in the leads is im- 1550
posed by the Poisson (Gauss) equation that relates the shape 1551
of the charge density to the voltage drop in the conduction 1552
band close to the tunneling obstacle with a complicated non- 1553
homogenous electric field. As seen in Sec. II B, the first term 1554
of the right-hand side of expressions (21) and (22) account 1555
for the reservoir series resistance while the rest account for 1556
the complicated lead resistance. 1557

APPENDIX B: THE QUASISTATIC ELECTROMAGNETIC 1558 APPROXIMATION FOR THE TIME-DEPENDENT 1559 SIMULATION OF NANOSCALE ELECTRON DEVICES 1560

Along this paper, we have assumed that the dynamics of 1561
electrons is controlled only by the scalar potential. We have 1562
argued that our algorithm is valid even for terahertz frequen- 1563
cies. However, in principle, any time-dependent variation in 1564
the scalar potential must imply a time-dependent vector po- 1565
tential. We discuss here the validity of our assumption of 1566
neglecting the vector potential. 1567

In principle, electron dynamics in nanoscale electron de- 1568
vices are determined by, both, the (time-dependent) electric 1569
field intensity, $\vec{E}(\vec{r}, t)$, and the magnetic flux density, $\vec{B}(\vec{r}, t)$. 1570
The electric field intensity is computed from the scalar po- 1571
tential, $V(\vec{r}, t)$, and the vector potential, $\vec{A}(\vec{r}, t)$ 1572

$$\vec{E}(\vec{r}, t) = -\vec{\nabla}V(\vec{r}, t) - \frac{\partial \vec{A}(\vec{r}, t)}{\partial t} \quad (\text{B1})$$

while $\vec{B}(\vec{r}, t)$ depends only on the vector potential $\vec{B}(\vec{r}, t)$ 1574
 $= \vec{\nabla} \times \vec{A}(\vec{r}, t)$. These electromagnetic fields can be computed 1575
from the four well-known Maxwell¹⁷ equations 1576

1577 $\vec{\nabla} \cdot \vec{D}(\vec{r}, t) = \rho(\vec{r}, t),$ (B2a)

1578 $\vec{\nabla} \cdot \vec{B}(\vec{r}, t) = 0,$ (B2b)

1579 $\vec{\nabla} \wedge \vec{E}(\vec{r}, t) = -\frac{\partial \vec{B}(\vec{r}, t)}{\partial t},$ (B2c)

1580 $\vec{\nabla} \wedge \vec{H}(\vec{r}, t) = \vec{J}(\vec{r}, t) + \frac{\partial \vec{D}(\vec{r}, t)}{\partial t},$ (B2d)

1581 where $\vec{H}(\vec{r}, t) = \vec{B}(\vec{r}, t) / \mu$ and $\vec{D}(\vec{r}, t) = \epsilon \vec{E}(\vec{r}, t)$ are the mag-
 1582 netic and electric flux intensities, and $\vec{J}_c(\vec{r}, t)$ and $\rho(\vec{r}, t)$ are
 1583 the (particle) current and charge densities, respectively.

1584 However, when no external magnetic field is applied to a
 1585 nanoscale electron device, the electron dynamic in nanoscale
 1586 systems can be computed only from the scalar potential. This
 1587 quasistatic electromagnetic approximation assumes that the
 1588 time-dependent magnetic induction in the definition of the
 1589 electric field in Eq. (B2c) can be neglected. Then, the electric
 1590 field is essentially an irrotational vector, $\vec{\nabla} \wedge \vec{E}(\vec{r}, t) = 0$ There-
 1591 fore, the electric field, decoupled from the magnetic counter-
 1592 part, can be computed from

1593 $\vec{E}(\vec{r}, t) \approx -\vec{\nabla} V(\vec{r}, t).$ (B3)

1594 Equations (B3) leads to the time-dependent Poisson equation
 1595 used in our paper

1596 $\vec{\nabla} [\epsilon \vec{\nabla} V(\vec{r}, t)] = -\rho(\vec{r}, t).$ (B4)

1597 The (time-dependent) boundaries conditions of the scalar po-
 1598 tential imposed on the open⁵² borders of the simulation box
 1599 are the central issue of this paper.

1600 Let us discuss the limits of applicability of the quasistatic
 1601 approximation in nanoscale electron devices. For a simple
 1602 estimations, we assume only one typical length scale L so
 1603 that we can approximate spatial derivatives that make up the
 1604 curl and divergence operators by $\partial / \partial x \sim 1 / L$. Identically, we
 1605 assume that time derivatives are roughly equal to a multiply-
 1606 ing factor f related to the frequency of the signal, $\partial / \partial t \sim f$.
 1607 Then, from the gauss law in Eq. (B1) we obtain for the

charge density $\rho(\vec{r}, t) \approx \epsilon \cdot E / L$ with $E \equiv \max |\vec{E}(\vec{r}, t)|$. Identically, from the continuity equation

$\frac{\partial \rho(\vec{r}, t)}{\partial t} + \vec{\nabla} \cdot \vec{J}(\vec{r}, t) = 0,$ (B5) 1610

we obtain for the current density $\vec{J}(\vec{r}, t) \approx \epsilon \cdot E \cdot f$. From the
 knowledge of the current and charge density, we can estimate
 the magnetic flux, using Eq. (B1), as $\vec{B}(\vec{r}, t) \approx \mu \cdot \epsilon \cdot f L E$ (we
 neglect numerical factors such as 2). Then, the vector poten-
 tial is $\vec{A}(\vec{r}, t) \approx \mu \cdot \epsilon \cdot f L^2 E$ and its time derivative is
 $\partial \vec{A}(\vec{r}, t) / \partial t \approx \mu \cdot \epsilon \cdot f^2 L^2 E$. On the other hand, the gradient of
 the scalar potential can be written as $\vec{\nabla} V(\vec{r}, t) \approx E$. Finally, we
 obtain that the electric field in Eq. (B1) can be written as
 expression (B3) under the quasistatic assumption $\mu \cdot \epsilon |f^2 L^2$
 $\ll 1$. This inequality can be interpreted as the condition that
 the length L of the system is much smaller than the wave-
 length $\lambda = c / f$ of the electromagnetic signal of frequency
 f (with $c = 1 / \sqrt{\mu \epsilon}$ the speed of the electromagnetic signal).
 For the dimensions used in this work, never longer than few
 hundreds of nanometers, the contribution of the electromag-
 netic vector potential can be reasonably neglected at frequen-
 cies lower than about 10 THz.^{66,67} If one is interested in
 using larger reservoirs (with L on the order of microns) this
 approximation is not valid and a whole electromagnetic solu-
 tion is needed to treat electromagnetic transport, as dis-
 cussed in Ref. 68.

Let us clarify that one can arrive to the time-dependent
 Poisson Eq. (B4) directly from the Coulomb gauge. We have
 not followed this path here because we are not only inter-
 ested in arriving to Eq. (B4) but also in showing that the
 electric field is much more important than the magnetic field
 when describing electron dynamics. In particular, with the
 approximations discussed above we realize that the Lorentz
 force $\vec{F}(\vec{r}, t) = q \cdot \vec{E}(\vec{r}, t) + q \cdot \vec{v}(\vec{r}, t) \times \vec{B}(\vec{r}, t)$ can be written as
 $|\vec{F}(\vec{r}, t)| \approx q \cdot E + q \mu \cdot \epsilon \cdot f^2 L^2 E$, where we have assumed that
 the electron velocity $|\vec{v}(\vec{r}, t)| \leq L f$. Then, from the previous
 scenarios that satisfy the quasistatic condition $\mu \cdot \epsilon \cdot f^2 L^2 \ll 1$,
 we realize identically that the magnetic field can be ne-
 glected in front of the electric field when describing electron
 dynamics.

1646
 1647
 1648

1649 *xavier.oriols@uab.es

1650 ¹Y. M. Blanter and M. Büttiker, *Phys. Rep. Rev.* **336**, 2 (2000).

1651 ²R. Landauer, *Phys. Scr.* **T42**, 110 (1992).

1652 ³M. Büttiker, Y. Imry, R. Landauer, and S. Pinhas, *Phys. Rev. B*
 1653 **31**, 6207 (1985).

1654 ⁴R. Landauer, *Philos. Mag.* **21**, 863 (1970).

1655 ⁵R. Landauer, *IBM J. Res. Dev.* **1**, 223 (1957).

1656 ⁶In this paper, we refer to the “sample” as the device active region
 1657 and the “leads” as the regions connecting the sample and the
 1658 ideal (black-body) reservoirs. The reservoirs are usually called
 1659 “contacts” in mesoscopic devices. We avoid this last name here
 1660 because, in those papers related with the simulation of atomistic

structures, the word contacts are usually understood as what we
 call here the sample.

⁷M. Büttiker, H. Thomas, and A. Prêtre, *Phys. Lett. A* **180**, 364
 (1993).

⁸M. Büttiker, A. Prêtre, and H. Thomas, *Phys. Rev. Lett.* **70**, 4114
 (1993).

⁹M. Büttiker, H. Thomas and A. Prêtre, *Z. Phys. B* **94**, 133
 (1994).

¹⁰M. Büttiker, *J. Phys.: Condens. Matter* **5**, 9361 (1993).

¹¹M. Büttiker and S. E. Nigg, *Nanotechnology* **18**, 044029 (2007).

¹²M. C. Goorden and M. Büttiker, *Phys. Rev. Lett.* **99**, 146801
 (2007).

- 13 In principle, a formal quantum treatment of the openness of the sample requires quite elaborate formalisms to “trace out” the degrees of freedom not explicitly simulated (Ref. 68). In this sense, the Lindblad (Ref. 69) or quantum master equations are the accurate substitutes of the Schrödinger or Liouville equations which are applicable for closed systems. This formal treatment of an open system is far from the scope of this work and we follow the standard way of dealing with open systems by specifying educated guesses for the BCs on the borders of the simulation box.
- 14 J. Taylor, H. Guo, and J. Wang, *Phys. Rev. B* **63**, 245407 (2001).
- 15 M. Brandbyge, J. L. Mozos, P. Ordejón, J. Taylor, and K. Stokbro, *Phys. Rev. B* **65**, 165401 (2002).
- 16 J. P. Colinge, C.-W. Lee, A. Afzaljan, N. D. Akhavan, R. Yan, I. Ferain, P. Razavi, B. O’Neill, A. Blake, M. White, A.-M. Kelleher, B. McCarthy, and R. Murphy, *Nat. Nanotechnol.* **5**, 225 (2010).
- 17 M. Javid and P. M. Brown, *Field Analysis and Electromagnetics* (McGraw-Hill, New York, USA, 1963).
- 18 T. Gonzalez and D. Pardo, *Solid-State Electron.* **39**, 555 (1996).
- 19 G. Gomila, I. R. Cantalapiedra, T. Gonzalez, and L. Reggiani, *Phys. Rev. B* **66**, 075302 (2002).
- 20 C. Jacoboni and P. Lugli, *The Monte Carlo Method for Semiconductor Device Simulation* (Springer-Verlag, Wien, New York, 1989).
- 21 R. Ugajin, A. Ishibashi, K. Funato, and Y. Mori, *J. Appl. Phys.* **73**, 1 (1993).
- 22 A. Reklaitis and L. Reggiani, *Phys. Rev. B* **60**, 11683 (1999).
- 23 T. González, O. M. Bulashenko, J. Mateos, D. Pardo, and L. Reggiani, *Phys. Rev. B* **56**, 6424 (1997).
- 24 O. M. Bulashenko, J. Mateos, D. Pardo, T. Gonzalez, L. Reggiani, and J. M. Rubí, *Phys. Rev. B* **57**, 1366 (1998).
- 25 M. V. Fischetti and S. E. Laux, *J. Appl. Phys.* **89**, 1205 (2001).
- 26 C. J. Wordelman and U. Ravaioli, *IEEE Trans. Electron Devices* **47**, 410 (2000).
- 27 S. Babiker, A. Asenov, N. Cameron, and S. P. Beaumont, *IEEE Trans. Electron Devices* **43**, 2032 (1996).
- 28 C. Riddet, A. R. Brown, S. Roy, and A. Asenov, *J. Comput. Electron.* **7**, 231 (2008).
- 29 D. Reid, C. Millar, G. Roy, S. Roy, and A. Asenov, *IEEE Trans. Electron Devices* **56**, 2255 (2009).
- 30 G. Albareda, J. Suñé, and X. Oriols, *Phys. Rev. B* **79**, 075315 (2009).
- 31 B. Ricco and M. Y. Azbel, *Phys. Rev. B* **29**, 1970 (1984).
- 32 M. O. Vassell, J. Lee, and H. F. Lockwood, *J. Appl. Phys.* **54**, 5206 (1983).
- 33 W. Pötz, *J. Appl. Phys.* **66**, 2458 (1989).
- 34 M. J. McLennan, Y. Lee, and S. Datta, *Phys. Rev. B* **43**, 13846 (1991).
- 35 A. Rahman, J. Guo, S. Datta, and M. S. Lundstrom, *IEEE Trans. Electron Devices* **50**, 1853 (2003).
- 36 R. Venugopal, Z. Ren, and M. S. Lundstrom, *IEEE Trans. Nanotechnol.* **2**, 135 (2003).
- 37 Z. Ren, R. Venugopal, S. Goasguen, S. Datta, and M. S. Lundstrom, *IEEE Trans. Electron Devices* **50**, 1914 (2003).
- 38 R. Venugopal, S. Goasguen, S. Datta, and M. S. Lundstrom, *J. Appl. Phys.* **95**, 292 (2004).
- 39 G. C. Liang, A. W. Ghosh, M. Paulsson, and S. Datta, *Phys. Rev. B* **69**, 115302 (2004).
- 40 J. Gabelli, G. Fève, J.-M. Berroir, B. Plaçais, A. Cavanna, B. Etienne, Y. Jin, and D. C. Glattli, *Science* **313**, 499 (2006).
- 41 T. C. Au Yeung, Y. Yu, W. Z. Shangguan, and W. K. Chow, *Phys. Rev. B* **68**, 075316 (2003).
- 42 J. Quan, Y. Yu, and Y. H. Tang, *Phys. Rev. B* **73**, 195314 (2006).
- 43 N. D. Lang, *Phys. Rev. B* **52**, 5335 (1995).
- 44 M. Di Ventra, S. T. Pantelides, and N. D. Lang, *Phys. Rev. Lett.* **84**, 979 (2000).
- 45 M. Di Ventra and N. D. Lang, *Phys. Rev. B* **65**, 045402 (2001).
- 46 R. Baer, T. Seideman, S. Llani, and D. Neuhauser, *J. Chem. Phys.* **120**, 3387 (2004).
- 47 X. Q. Li and Y. J. Yan, *Phys. Rev. B* **75**, 075114 (2007).
- 48 S. Kurth, G. Stefanucci, C. O. Almbladh, A. Rubio, and E. K. U. Gross, *Phys. Rev. B* **72**, 035308 (2005).
- 49 R. Baer and D. Neuhauser, *Int. J. Quantum Chem.* **91**, 524 (2003).
- 50 X. Oriols, *Phys. Rev. Lett.* **98**, 066803 (2007).
- 51 Thomas Ihn, *Semiconductor Nanostructures: Quantum States and Electronic Transport* (Oxford University Press, New York, 2010).
- 52 Due to the openness of the system, we can distinguish between open borders that allow the flux of particles and “close” borders that do not. In this work, we discuss only the modeling of the BCs of such open borders.
- 53 X. Oriols, J. Suñé, F. Martín, and X. Aymerich, *J. Appl. Phys.* **78**, 2135 (1995).
- 54 G. F. Giuliani and G. E. Simion, *Solid State Commun.* **127**, 789 (2003).
- 55 V. A. Sablikov, S. V. Polyakov, and M. Büttiker, *Phys. Rev. B* **61**, 13763 (2000).
- 56 X. Oriols, E. Fernandez-Diaz, A. Alvarez, and A. Alarcon, *Solid-State Electron.* **51**, 306 (2007).
- 57 See an alternative demonstration to the periodic (Born-Von-Karman) Boundary conditions in reference: X. Oriols, *Nanotechnology* **15**, 167(S) (2004).
- 58 M. Büttiker, *Phys. Rev. Lett.* **65**, 2901 (1990).
- 59 L. S. Levitov and G. B. Lesovik, *JETP Lett.* **58**, 230 (1993).
- 60 Strictly speaking, our many-electron method applied to semiclassical devices cannot be considered as a direct solution of the Boltzmann equation because the latter is developed within a classical mean-field approximation. In the approach explained in Ref. 30, each particle “sees” its own electrostatic potential (or electric field), which is different from that of others. This is the fundamental difference between our many-electron method applied to classical transport and the standard MC method for electron transport. See Ref. 30 for a detailed explanation.
- 61 J. Wang, A. Rahman, A. Ghosh, G. Klimeck, and M. Lundstrom, *IEEE Trans. Electron Devices* **52**, 1589 (2005).
- 62 M. Born and R. Oppenheimer, *Ann. Phys.* **84**, 0457 (1927).
- 63 V. Sverdlov, X. Oriols, and K. Likharev, *IEEE Trans. Nanotechnol.* **2**, 59 (2003).
- 64 C. Jacoboni and L. Reggiani, *Rev. Mod. Phys.* **55**, 645 (1983).
- 65 S. Datta, *Electronic Transport in Mesoscopic Systems* (Cambridge University Press, Cambridge, 1995).
- 66 B. Pellegrini, *Phys. Rev. B* **34**, 5921 (1986).
- 67 B. Pellegrini, *Nuovo Cimento D* **15**, 855 (1993).
- 68 M. Di Ventra, *Electric Transport in Nanoscale Systems* (Cambridge University Press, Cambridge, 2008).
- 69 G. Lindblad, *Commun. Math. Phys.* **48**, 119 (1976).

1 Many-particle transport in the channel of quantum wire double-gate metal- 2 oxide-semiconductor field-effect transistors with charged atomistic 3 impurities

4 G. Albareda, X. Saura, X. Oriols, and J. Suñé

5 *Departament d'Enginyeria Electrònica, Universitat Autònoma de Barcelona, 08193 Bellaterra, Spain*

6 (Received 3 April 2010; accepted 19 May 2010; published online xx xx xxxx)

AQ: #1 7 One of the most reported causes of variations in electron devices characteristics (coming from the
8 atomistic nature of matter) are discrete doping induced fluctuations. In this work we highlight the
9 importance of accurately accounting for (time-dependent) coulomb correlations among (transport)
10 electrons in the analysis of such fluctuations. In particular, we study the effect of single ionized
11 dopants on the performance of a quantum wire double-gate metal-oxide-semiconductor field-effect
12 transistor, mainly when its lateral dimensions approach the effective cross section of the charged
13 impurities. In this regard, we use a recently developed many-particle semiclassical simulation
14 approach by Albareda *et al.* [Phys. Rev. B **79**, 075315 (2009)] which provides an accurate treatment
15 of electron–electron and electron–impurity interactions (avoiding the mean-field approximation).
16 We reveal the significant impact of the sign and position of the impurity along the transistor channel
17 on the on-current, the threshold voltage, the distribution of the current in the channel cross-section,
18 the transmission probabilities, and the distribution of transit times. We find that neglecting the
19 (time-dependent) coulomb correlations among (transport) electrons can lead to misleading
20 predictions of the previous results. © 2010 American Institute of Physics. [doi:10.1063/1.3455878]
21

22 I. INTRODUCTION

AQ: #2 23 At deep nanometer scale, the number of dopants con-
24 tained in sub-10 nm channel devices will decrease to a few
25 tens.¹ In addition, this number and the position of dopant
26 atoms, introduced either deliberately to improve device
27 characteristics or accidentally from contamination sources,
28 will vary among electron devices. Such differences will pro-
29 duce important variations on the devices' microscopic
30 behavior,^{2–10} and consequently, the variability of macro-
31 scopic parameters such as drive current or threshold voltage
32 will increase.^{11–28} This particular phenomenon, known as
33 discrete dopant induced fluctuation (DDIF), represents a
34 little fraction of the whole set of undesirable effects arising
35 from the atomistic nature of matter, but is considered as one
36 of the main drawbacks in downscaling complementary
37 metal-oxide semiconductor (CMOS) technology. In order
38 to predict the impact of such phenomena in future
39 decananotransistors, during the last decade, several works,
40 both experimental and theoretical, have been carried
41 out.^{2–31} In particular, many simulations have been done using
42 drift-diffusion approaches,^{2,11–25} Monte Carlo (MC) solu-
43 tion of the Boltzmann equation,^{3–6,25–28} and quantum
44 approaches.^{7–10,25}

45 The aim of the drift-diffusion simulations of DDIF, in-
46 stead of predicting the characteristics of a single device, is
47 focused on obtaining quantitative estimations of the variance
48 of basic design parameters, such as threshold voltage, sub-
49 threshold slope, or drive current for a whole ensemble of
50 microscopically different devices. Since such a statistical job
51 has to manage with a large ensemble of electron devices, a
52 fast simulation technique is required. Drift-diffusion simula-
53 tions have limitations due to their inability of capturing non-

equilibrium quasiballistic transport effects.^{12–14,23} They uti- 54
lize bulk mobilities that are not able to describe the complex 55
effects associated with the variations in the discrete configu- 56
ration of ionized dopants within the channel. Therefore, the 57
variation in the drive current obtained from drift-diffusion 58
simulations underestimate the real magnitude of the intrinsic 59
parameter variations.^{4,25,26} On the other hand, the “atomistic” 60
resolution of individual charges in drift-diffusion simulations 61
using fine meshes generate some problems.^{15,19,32} Due to the 62
classical time-independent nature of the drift-diffusion ap- 63
proach, a significant amount of mobile charge can become 64
trapped in the sharply resolved coulomb potential wells cre- 65
ated by discrete dopant (donors) charges assigned to a very 66
fine mesh.³² Such an artificial charge trapping in drift- 67
diffusion simulations give rise to several detrimental effects. 68
Attempts to correct these problems in “atomistic” simula- 69
tions have been made by charge smearing,³³ incorporating 70
density gradient corrections^{15,19} or by splitting of the cou- 71
lomb potential into short- and long-range components.³² 72

Due to its particle-based nature, the MC technique for 73
solving the Boltzmann equation can easily account for time- 74
dependent nonequilibrium phenomena. However, this advant- 75
age over the drift-diffusion approach entails an increment of 76
the computational time required to perform numerical simu- 77
lations. In this regard, although the MC method cannot man- 78
age with large statistical analysis, it is an excellent tool for 79
accurately studying electron transport phenomena related 80
with time-dependent coulomb correlations. In the last de- 81
cade, several works have remarked the electrostatic origin of 82
the DDIF phenomena and thus the necessity of paying maxi- 83
mum attention to electron–electron (e–e) and the electron– 84
impurity (e–i) coulomb interactions.^{34–38} Historically, e–i 85
(and also part of the e–e) interactions have been introduced 86

B 87 perturbatively as an “instantaneous” and “local” transitions
 88 of electrons between different regions of the k -space. How-
 89 ever, such approach is clearly inappropriate^{34–38} for studying
 90 DDIF because it assumes a homogenous distribution of im-
 91 purities, so that the effects of “scattering” of electrons with
 92 impurities become independent of the position of the impu-
 93 rity. In addition, the expressions for the e - i scattering rates in
 94 k -space are based on a two-body model which accounts for
 95 many-particle (MP) contributions only through an assumed
 96 screening function for the effective potentials,³⁵ and it does
 97 not take into account the electrostatic effects of the gate,
 98 drain, and source terminals on the interaction. The standard
 99 solution to avoid such important limitations, without signifi-
 100 cantly increasing the computational cost of the simulations,
 101 is defining an *ad hoc* division of the spatial range of the e - e
 102 and e - i interactions into two parts. The long-range part is
 103 enclosed in the solution of the scalar potential from the
 104 mesh-dependent mean-field Poisson equation, and the short-
 105 range part is introduced, either as an analytical expression of
 106 the scalar potential^{4,34,36} (the so-called MC molecular dy-
 107 namics approach, MCMD), or sometimes perturbatively.³⁸
 108 The MCMD approach, however, shows up several inconve-
 109 nient. The first reported limitation was the so-called “double
 110 counting” of the electrostatic force in the short-range inter-
 111 action term.^{6,36} Since the e - e and e - i interactions is already
 112 included, in a smoothed way, in the self-consistent potential
 113 computed through the Poisson equation, the addition of a
 114 separate analytical force (the molecular dynamics term) in
 115 the MC transport kernel leads to the overestimation of both
 116 the e - e and the e - i interactions.³⁶ Such a problem can be
 117 avoided by properly identifying the spatial region where
 118 short-range coulomb interactions have to be included. Then,
 119 the Molecular dynamics routine^{6,36,37} uses a “corrected”
 120 short-range coulomb interaction there, that excludes the
 121 long-range contribution from the Poisson equation. However,
 122 then, the problem is the analytical nature of the corrections
 123 incorporated in the short-range region that can lead to un-
 124 physically large forces that cause artificial heating and cool-
 125 ing (for acceptors and donors, respectively) of the
 126 carriers.^{37,39} This problem can be corrected by introducing
 127 modifications for the analytical expressions of the coulomb
 128 interaction inside the short-range zones^{4,26} or by introducing
 129 density gradient quantum corrections that accounts for the
 130 formation of bound states in the donor induced wells.^{25,28}
 131 Nevertheless, the MCMD continues suffering from its intrin-
 132 sic analytical description of the short-range interaction. Stan-
 133 dard analytic short-range coulomb corrections cannot ac-
 134 count for the electrostatic influence of the (gate, source, and
 135 drain) boundaries.

136 During the last years, also some works have been de-
 137 voted to study electron transport in presence of atomistic
 138 impurities with full-scale quantum transport simulators.^{7–9,25}
 139 A common limitation of quantum simulations dealing with
 140 such systems is the high time-consumption related with the
 141 self-consistent solution of the Schrödinger and Poisson equa-
 142 tions. In order to reduce the degrees of freedom of the sys-
 143 tem, a common practice consists on assuming an effective
 144 mass approximation for the description of the electronic
 145 band structure and on suppressing the time-dependence of

the transport problem.^{7–9,25} Such approximations neglect an
 important part of the coulomb correlations among electrons
 and dopants. Finally, more sophisticated quantum approaches
 can avoid the effective mass approximation by describing the
 whole atomic structure from first-principles.¹⁰ Then, those
 simulators provide a rigorous treatment of the effect of elec-
 tron correlation on the description of the band structure, but
 fail in providing a reasonable description of the correlation
 among transport electrons. The reason is that electron de-
 vices work under nonequilibrium conditions, while band-
 structure improvements are generally computed from
 (ground-state) equilibrium conditions.¹⁰ In other words, elec-
 tron dynamic properties (such as charge distribution or cor-
 relations among electrons) far from equilibrium can be quite
 different from that computed at equilibrium.

Finally, let us notice that, when device dimensions are
 drastically reduced to a few nanometers in both the lateral
 and the longitudinal directions, the separation between long-
 (screened) and short-(unscreened) range contributions of the
 coulomb interaction becomes quite misleading. Then, the
 fact that all electrons share the same solution of the Poisson
 equation, at least for the long-range of the scalar potential
 profile, implies important drawbacks for the correct treat-
 ment of the e - e and e - i interactions. The charge of the whole
 system is included in the kernel of the Poisson equation (in a
 mean-field approximation) that provides an unphysical
 self-interaction,⁴⁰ i.e., an electron interacts with itself. This
 effect becomes more relevant in small than in large meshed.
 In particular, it can become quite dramatic when the reso-
 lution of the mesh is increased up to cell spacing below
 ~ 2 nm.⁴⁰

In the present work we describe the coulomb correla-
 tions by means of a semiclassical particle-based electron
 transport formalism (MC like) that goes beyond the standard
 mean-field approximation^{40,41} by considering a particular
 scalar potential profile for each electron on the device active
 region (computed as a solution of a Poisson equation where
 the own charge of electron is excluded). This procedure al-
 lows us to include, semiclassically, the effect of the e - e and
 the e - i coulomb interactions with an exact procedure, i.e.,
 without setting any arbitrary division between long- and
 short-range,⁴⁰ even in far from equilibrium conditions. On
 the contrary, the effect of the e - e and electron-atom correla-
 tions in the description of the band structure is considered
 within the simple effective-mass approximation. Although
 our approach fails to capture the energy levels and density of
 states close to the impurity, it is sufficient for our purpose
 and allows us to capture the effects of e - e and e - i correla-
 tions among (transport) electrons in far from equilibrium (re-
 alistic) scenarios.

Here we will employ the approach mentioned above⁴⁰ to
 study DDIF effects within a particular example of deep
 nanoscale few-electron device, i.e., the silicon quantum wire
 double-gate metal-oxide-semiconductor field-effect transistor
 (MOSFET) (Refs. 2, 22, 24, and 42) (QWDG-FET). Such
 device is now-a-days accepted as one of the most promising
 candidates to fulfil near future CMOS technology scaling
 requirements. The addition of multiple-gate structures to the
 near vicinity of the extremely thin nanowire channels, offers

205 an exceptional electrostatic robustness that prevents from the
 206 jeopardizing short-channel effects and makes their operation
 207 without channel doping feasible. In one hand, the undoped
 208 nature of the channel region dictates that the threshold volt-
 209 age is determined by the work function difference between
 210 the gate material and the intrinsic silicon body. On the other
 211 hand, it makes such devices inherently more resistant to ran-
 212 dom dopant fluctuation effects than conventional single-gate
 213 MOSFETs. Nevertheless, with regard to this second point,
 214 even “undoped” channels can contain ionized doping atoms
 215 arising from contamination or from source/drain implanta-
 216 tion processes. Due to the random nature of such processes,
 217 the number, sign, and position of doping atoms are subject to
 218 stochastic variations. Furthermore, at deep nanometer scale,
 219 the effective cross section of such impurities dangerously
 220 approaches the lateral dimensions of the channel, thus having
 221 a much more stronger impact on carrier transport.

222 This paper is organized as follows: after this introduc-
 223 tion, in Sec. II, we discuss the details of our MP approach. In
 224 Sec. III we describe how DDIF affect the main characteris-
 225 tics of the QWDG-FET and we highlight the importance of
 226 accurately account for the dynamic MP effects. Finally, in
 227 Sec. IV we summarize the main results of the work.

228 II. COMPUTATION OF MANY-ELECTRON COULOMB 229 CORRELATIONS IN OPEN SYSTEMS INCLUDING 230 E-I INTERACTION

231 This section is devoted to describe the semiclassical
 232 many-electron MC used to simulate DDIF. We discuss the
 233 expression of the MP Hamiltonian, under standard effective
 234 mass approximation,^{43,44} that describes a system of spinless
 235 electrons in a solid-state semiconductor open system⁴⁰ in-
 236 cluding charged impurities. As discussed in the introduction,
 237 due to the fundamental electrostatic origin of DDIF effects,
 238 this approach is focused in accurately describing the e-e and
 239 e-i coulomb interactions.

AQ: #3
 240 We start the discussion with the description of a system
 241 consisting of M (valence) electrons and P ionized atoms.^{45,46}
 242 Because we are interested only on electron dynamics (with a
 243 Born-Oppenheimer approximation), the corresponding
 244 Hamiltonian contains only the e-e and e-i coulomb interac-
 245 tion terms and the kinetic energies of the M electron system,
 246 i.e.,

$$247 \quad H(\vec{r}_1, \dots, \vec{r}_M, \vec{p}_1, \dots, \vec{p}_M) = \sum_{k=1}^M \left\{ K(\vec{p}_k) + \frac{1}{2} \sum_{\substack{j=1 \\ j \neq k}}^M q \cdot V(\vec{r}_k, \vec{r}_j) \right. \\ 248 \quad \left. + \sum_{j=1}^P q \cdot V(\vec{r}_k, \vec{R}_j) \right\}, \quad (1)$$

249 where q represents the charge of the k -th electron and the
 250 condition $j \neq k$ takes into account the obvious restriction that
 251 a particle cannot interact with itself. We refer to \vec{r}_k or \vec{p}_k as
 252 the k -th electron position and momentum, respectively. No-
 253 tice that the right hand side of Eq. (1) contains also the
 254 positions of the charged impurities, \vec{R}_j . The kinetic energy
 255 term $K(\vec{p}_k)$ is defined as

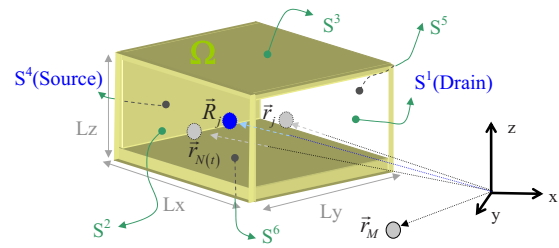


FIG. 1. (Color online) Schematic representation of the volume $\Omega = L_x \cdot L_y \cdot L_z$ and its limiting surface $S = \{S^1, S^2, \dots, S^6\}$. There are $N(t)$ electrons inside and $M - N(t)$ outside this volume.

$$K(\vec{p}_k) = \frac{1}{2m_k} (\vec{p}_k)^2, \quad (2) \quad 256$$

where m_k is the particle effective mass. On the other hand,²⁵⁷
 the coulomb interaction potentials in Eq. (1) are defined as²⁵⁸

$$V(\vec{r}_k, \vec{r}_j) = \frac{q}{4\pi\epsilon |\vec{r}_k - \vec{r}_j|}, \quad (3) \quad 259$$

for e-e interaction and²⁶⁰

$$V(\vec{r}_k, \vec{R}_j) = \frac{q_j}{4\pi\epsilon |\vec{r}_k - \vec{R}_j|}, \quad (4) \quad 261$$

for e-i interaction. The parameter q_j is the charge of the j -th²⁶²
 ionized atom and ϵ is the electric permittivity. As mentioned²⁶³
 above, the contribution of the atomic structure is accounted²⁶⁴
 for by considering a dielectric medium and using an effective²⁶⁵
 mass.²⁶⁶

A complete electronic circuit (including the devices, the²⁶⁷
 wires and the batteries) behaves as a closed system with a²⁶⁸
 large number ($M, P \rightarrow \infty$) of electrons and dopants. However,²⁶⁹
 since we can only deal with a finite number of degrees of²⁷⁰
 freedom, we restrict our system to a small part of the circuit,²⁷¹
 for example, the channel of a transistor. Therefore, we divide²⁷²
 the previous ensemble of M electrons and P dopants into a²⁷³
 subensemble of electrons, $\{1, 2, 3, \dots, N(t)\}$, and dopants²⁷⁴
 $\{1, 2, 3, \dots, D\}$, with positions inside the volume Ω and a²⁷⁵
 second subensemble, $\{N(t)+1, \dots, M\}$ and $\{D+1, \dots, P\}$,²⁷⁶
 which are outside it. As drawn in Fig. 1, we assume a paral-²⁷⁷
 lelepiped with six rectangular surfaces $S = \{S^1, S^2, \dots, S^6\}$ ²⁷⁸
 which are the boundaries of Ω . Since we are only interested²⁷⁹
 in the dynamics of the $N(t)$ particles, the kinetic energy and²⁸⁰
 the coulomb interaction between the carriers of the second²⁸¹
 subensemble does not appear in the new Hamiltonian of the²⁸²
 open system. Thus, according to the detailed procedure de-²⁸³
 scribed in Ref. 40, the MP Hamiltonian describing the dy-²⁸⁴
 namics of the $N(t)$ particles can be written as²⁸⁵

$$H(\vec{r}_1, \dots, \vec{r}_{N(t)}, \vec{p}_1, \dots, \vec{p}_{N(t)}, t) = \sum_{k=1}^{N(t)} \{K(\vec{p}_k) + q \cdot \bar{W}_k(\vec{r}_k, t)\}. \quad (5) \quad 286$$

Each i -term of the electrostatic potential, $\bar{W}_k(\vec{r}_k, t)$, is a solu-²⁸⁷
 tion of one particular three-dimensional (3D) Poisson equa-²⁸⁸
 tion²⁸⁹

$$\nabla_{\vec{r}_i}^2[\varepsilon(\vec{r}_i) \cdot \vec{W}_i(\vec{r}_i, t)] = \bar{\rho}_i(\vec{r}_i, t), \quad (6)$$

Notice that the use of the Poisson Eq. (6) for the scalar potential, instead of expressions (3) and (4), has the additional advantage of using position dependent electric permittivity $\varepsilon(\vec{r}_i)$. The charge density depends on the position of the $N(t)$ electrons and the D ions

$$\bar{\rho}_i(\vec{r}_i, t) = \sum_{j=1}^{N(t)} q \cdot \delta(\vec{r}_i - \vec{r}_j[t]) + \sum_{j=1}^D q_j \cdot \delta(\vec{r}_i - \vec{R}_j), \quad (7)$$

where $\vec{r}_j[t]$ is the classical trajectory of the j -th electron.

Now Eq. (5) is independent of the position of the external particles because they only affect the boundary conditions of Eq. (6) in the six rectangular surfaces S .

The classical description of the electron dynamics subjected to the MP Hamiltonian of Eq. (5) will be computed using the well-known Hamilton equations. In particular, we can obtain the (Newton-type) description of the classical trajectory $\vec{r}_i[t]$ in the real space through

$$\frac{d\vec{p}_i[t]}{dt} = [-\nabla_{\vec{r}_i} H(\vec{r}_1, \dots, \vec{r}_{N(t)}, \vec{p}_1, \dots, \vec{p}_{N(t)}, t)]_{\vec{r}_1=\vec{r}_1[t], \dots, \vec{p}_{N(t)}=\vec{p}_{N(t)}[t]} \quad (8)$$

and

$$\frac{d\vec{r}_i[t]}{dt} = [\nabla_{\vec{p}_i} H(\vec{r}_1, \dots, \vec{r}_{N(t)}, \vec{p}_1, \dots, \vec{p}_{N(t)}, t)]_{\vec{r}_1=\vec{r}_1[t], \dots, \vec{p}_{N(t)}=\vec{p}_{N(t)}[t]}. \quad (9)$$

For the MP Hamiltonian of Eq. (5), Eq. (9) gives the trivial result

$$m \cdot \vec{v}_i[t] = \vec{p}_i[t], \quad (10)$$

while Eq. (8) can be expressed as

$$\frac{d\vec{p}_i[t]}{dt} = \nabla_{\vec{r}_i} \bar{W}_i(\vec{r}_i, t). \quad (11)$$

Let us therefore keep the important idea that expressions (5)–(7), together with a set of appropriate boundary conditions, provide an exact treatment of the MP coulomb correlations in semiclassical scenarios. Let us emphasize that the subindex “ k ” in $\bar{W}_k(\vec{r}_k, t)$ implies that there are $N(t)$ scalar potential, one for each electron. This implies a coupled system of Newton equations that will be used to describe DDIF effects in Sec. III.

III. NUMERICAL SIMULATION OF ELECTRON TRANSPORT WITH SINGLE DOPANTS IN THE CHANNEL OF A NANOWIRE DOUBLE-GATE MOSFET

As mentioned in the introduction, although silicon nanowire multiple-gate MOSFETs are semiconductor devices with a great acceptance due to its relevant electrostatic improvement with respect to other structures, DDIF effects can significantly degrade their expected performance. In order to qualitatively evaluate the importance of such limitation, in this work we study the effects of DDIF in a silicon QWDG-FET. We are especially interested in analyzing the impact of

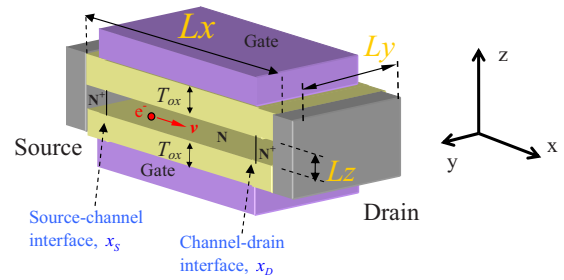


FIG. 2. (Color online) Schematic representation of the QWDG-FET.

the sign of the dopant charge and its position along the channel. After exposing some relevant details of the simulated device and some technical remarks, we will evaluate the importance of random doping fluctuation effects on the main characteristics of the QWDG-FET.

A. Device characteristics and simulation details

1. Description of the simulated device: QWDG-FET

The structure of the simulated QWDG-FET (see Fig. 2) is described in Table I. Two highly N doped Si contacts ($N^+ = 2 \times 10^{19} \text{ cm}^{-3}$) are connected to an intrinsic Si channel with lateral dimensions $L_y = 5 \text{ nm}$ and $L_z = 2 \text{ nm}$. Such dimensions originate quantum confinement in the lateral directions (a quantum wire), not only reducing the degrees of freedom of the system but also inducing volume inversion within the channel⁴⁷ (see Sec. III A 2 for a detailed explanation on how is quantum confinement taken into account in our semiclassical approach). In this sense, the electrostatic blockade generated by the ionized dopants is expected to be favored when impurities are distributed mainly in the center of the channel cross section. At the same time, the length of the quantum wire is 10 nm. This results in a volume of only 100 nm^3 , so that the number of interacting channel electrons is of the order of 10. Under such special conditions, the importance of the interaction among electrons is particularly relevant.

TABLE I. Simulation parameters for the DG-FET depicted on Fig. 9.

	Units	Symbol	Value
Lengths	(nm)	L_x	10
		L_y	5
		L_z	2
		T_{ox}	2
Spatial step	(nm)	DX	0.85
		DY	0.5
		DZ	0.2
Relative permittivity	...	Air	1.0005
		Oxide	3.8000
		Silicon	11.7514
Doping	(cm^{-3})	Channel N	Intrinsic
		Contact N^+	2×10^{19}
Simulation time	(s)	T	1×10^{-9}
Temporal step	(s)	Dt	2×10^{-16}

358 2. Simulation details

359 We use the classical solution of the MP system described
 360 in Eq. (5) to simulate the electron transport in the quantum
 361 wire DG-FET depicted in Fig. 2. Electron transport in the
 362 “*x*” direction (from source to drain) takes place along a Sili-
 363 con (100) oriented channel, at room temperature. In particu-
 364 lar, the electron mass is taken according to the six equivalent
 365 ellipsoidal constant energy valleys of the silicon band
 366 structure.^{48,49} The effective masses of the ellipsoids are m_l^*
 367 $=0.9163m_0$ and $m_t^*=0.1905m_0$ with m_0 being the free elec-
 368 tron mass.⁴⁸ As commented above, the lateral dimensions of
 369 the Si channel L_z and L_y are both small enough (see Table I),
 370 so that the active region behaves as a one-dimensional (1D)
 371 system and the energy of an electron in one particular
 372 valley is $E = \hbar^2 k_x^2 / (2m_l) + E_{1D}^q$, where $E_{1D}^q = \hbar^2 \pi^2 / (2m_l L_y^2)$
 373 $+ \hbar^2 \pi^2 / (2m_l L_z^2)$ represents the minimum energy of the first
 374 subband, whose value is $E_{1D}^q = 0.182$ eV for $L_z = 2$ nm and
 375 $L_y = 5$ nm. The energies of the next lowest subbands (E_{1D}^q
 376 $= 0.418$ eV or $E_{1D}^q = 0.489$ eV) are assumed to be high
 377 enough to keep a single band simulation. Therefore, we use a
 378 3D Poisson solver to deal with the device electrostatics, but a
 379 1D algorithm to describe the velocity of each electron in the
 380 “*x*” direction. Due to the lateral electron confinement, the
 381 velocities in the “*y*” and “*z*” directions are zero.^{50,51} This is
 382 an exact result for describing electron confinement in the
 383 rectangular structure of Fig. 2 when the e–e and e–i are not
 384 considered. The explicit consideration of the effect of e–e
 385 and e–i correlations on the electron confinement (energy lev-
 386 els) is an extremely complicated issue within the MP strategy
 387 developed here (which considers one different scalar poten-
 388 tial for each electron) and it is far from the scope of this
 389 work.

390 All the simulations carried out in the present work use a
 391 3D finite-difference Poisson solver scheme. The whole vol-
 392 ume Ω of the active region drawn in Fig. 1 is divided
 393 into $N_x \cdot N_y \cdot N_z$ cells. Each 3D cell has spatial dimensions
 394 DX , DY , and DZ (see Table I). Thus, the active region
 395 of our simulated device has a volume equal to
 396 $(N_x \cdot DX) \cdot (N_y \cdot DY) \cdot (N_z \cdot DZ) = L_x \cdot L_y \cdot L_z$. The boundary con-
 397 ditions of the Poisson equation on the six rectangular sur-
 398 faces of Fig. 1 are defined using either Dirichlet or Neumann
 399 criteria. On the closed “nonmetallic” surfaces, Neumann
 400 boundary conditions are used with the educated guess that
 401 the component of the electric field normal to that surfaces is
 402 zero. The continuity of the displacement vector normal to
 403 surfaces justifies this assumption at the boundaries when the
 404 relative permittivity inside Ω is much higher than the corre-
 405 sponding value outside. On the other hand, in the contact
 406 surfaces of Fig. 1 we use the Dirichlet boundary conditions
 407 reported in Ref. 40.

408 B. Effects of single ionized impurities in a QWDG-ET

409 In this section we evaluate the impact of single ionized
 410 impurities on the previously defined QWDG-FET, consider-
 411 ing three different positions along the transistor channel.
 412 Since the lateral confinement induces volume inversion in
 413 the channel of the QWDG-FET, in order to maximise the
 414 DDIF effects, we place the impurities centered in the lateral

directions. Most of the carriers are hence forced to cross the
 channel in the very vicinity of the impurity positions. We
 will analyze three different scenarios corresponding to three
 different positions of the impurities along the channel, i.e.,
 the source–channel interface, the center of the channel, and
 the channel–drain interface (see Fig. 2).

We will start by discussing a series of microscopic char-
 acteristics of the QWDG-FET. First we will consider the
 spatial distribution of the current density, J_x . After that we
 will discuss the transmission characteristics of the device.
 We will also study the variations in the transit time, the pa-
 rameter that ultimately defines the intrinsic switching speed
 of the technology. Finally, we will compute the macroscopic
 current-voltage characteristics and the threshold voltage
 variations.

The importance of accurately treating the coulomb cor-
 relations in the study of DDIF in such nanoscale devices has
 been advanced in the introduction. Here, in order to highlight
 the importance of taking into account the time-dependent e–e
 and e–i correlations, we compare some results with those
 obtained with a single-particle (SP) mean-field approach dis-
 cussed in Appendix A. In this regard, we will refer to MP
 results to describe the simulation performed with the algo-
 rithms that require solving $N(t)$ Poisson equations with $N(t)$
 charge densities [expressions (5)–(7)] at each time step. Al-
 ternatively, we refer to the time-independent SP approxima-
 tion to the more simplistic (though usual) approach that con-
 sists in solving a single time-independent Poisson equation
 [expressions (A1) and (A2) in Appendix A] for all electrons
 at each time step of the simulation.

415 1. Spatial distribution of the current density

416 In this section we analyze how dopants placed in the
 417 channel of a QWDG-FET induce significant changes in the
 418 spatial distribution of the current density across the channel
 419 section. We consider the steady state current corresponding
 420 to a fixed bias point ($V_{\text{Gate}} = 0$ V; $V_{\text{Drain}} = 0.5$ V) and ana-
 421 lyze the spatial distribution of the current in the channel
 422 cross section. Since we deal with a confined electron system
 423 under stationary conditions, the continuity equation reduces
 424 to $\vec{\nabla} \cdot J_x = 0$ and consequently the spatial distribution of J_x is
 425 the same in any section along the transistor channel. Before
 426 discussing some interesting results, it is important to recall
 427 that, due to the lateral confinement, the injection of carriers
 428 obeys a sinusoidal spatial distribution centered on the *y* and *z*
 429 directions that causes volume inversion along the channel. In
 430 Fig. 3 we present the current density distribution when a
 431 negative impurity is located at the source–channel interface.
 432 As it can be observed, for zero applied gate voltage [Fig.
 433 3(a)], its presence produces an important deformation of its
 434 spatial distribution, pushing carriers away from its location.
 435 As shown in Fig. 6 such a result can be justified through the
 436 potential barrier induced by the presence of the negative im-
 437 purity. Figure 4(a) represents the same information but now
 438 placing the dopant in the center of the channel. Even though
 439 the height of the potential barriers corresponding to these
 440 two previous cases are quite similar (see Fig. 6), the magni-
 441 tude of the current density is importantly reduced in the sec-

B

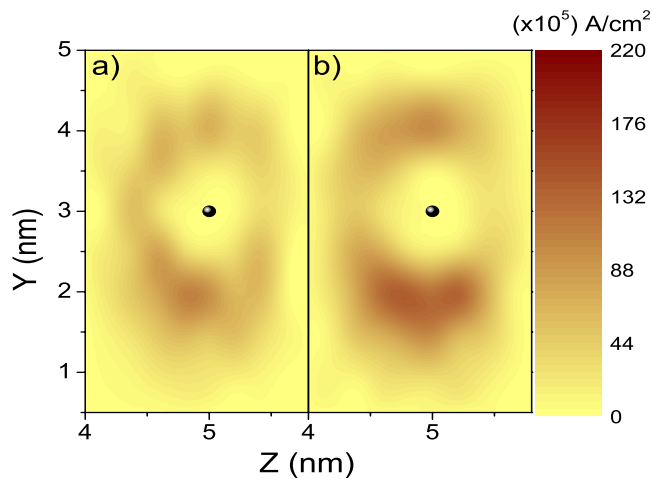


FIG. 3. (Color online) Current density across the channel section when the negative impurity is placed at the source–channel interface. In (a) the results correspond to a MP treatment of the system (see Sec. II). In (b) the results have been computed within a SP mean-field approach discussed in Appendix A.

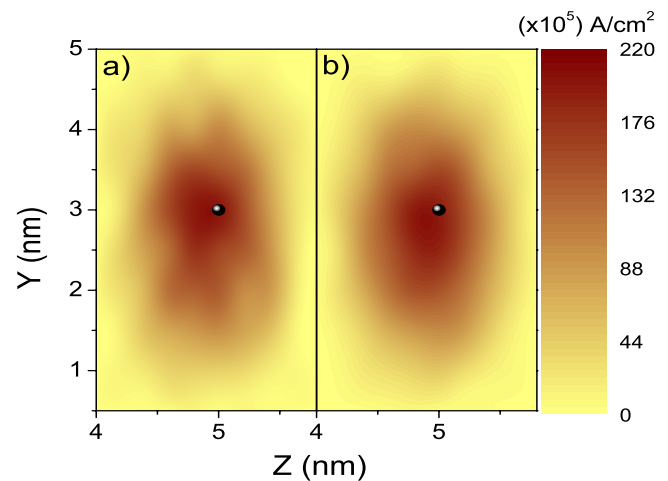


FIG. 5. (Color online) Current density across the channel section when the negative impurity is placed at the channel–drain interface. In (a) the results correspond to a MP treatment of the system (see Sec. II). In (b) the results have been computed within a SP mean-field approach discussed in Appendix A.

472 and case with respect to the former. Notice that from a SP
473 point of view (see Appendix A) such a situation cannot be
474 accepted. Due to the one-by-one electron energy conserva-
475 tion, two identical potential barriers (despite its position
476 along the channel) would result in an identical current distri-
477 bution. From a MP point of view, the time-dependent e–e
478 interaction implies a much looser restriction on the energy of
479 the carriers. This result will be discussed later. On the con-
480 trary, as shown in Figs. 3(b) and 4(b), a SP treatment of the
481 electron transport gives quite similar current density distri-
482 butions for these two cases. Finally, in Fig. 5, the impurity
483 has been placed at the channel–drain interface. In this a case,
484 the applied bias reduces drastically the influence of the po-
485 tential deformation induced by the ionized dopant atom (see
486 Fig. 6). Under such conditions, the electron transport is
487 roughly ballistic, the e–e interaction effects are masked, and

the predictions of the current density distribution arising 488
from a MP simulation are practically equivalent to those cor- 489
responding to a SP simulation. 490

2. Fluctuations of the transmission coefficient 491

Another important magnitude that can contribute to the 492
understanding of the influence of single charged impurities 493
within the channel of a QWDG-FET is the transmission co- 494
efficient. The probability of an electron injected from the 495
source contact to reach the drain contact (i.e., transmission 496
probability) is presented in Fig. 7 as a function of the inject- 497
ing energy (i.e., the kinetic energy of the carrier when it 498
enters the channel through the source–channel interface), 499
again for $V_{\text{Gate}}=0$ V and $V_{\text{Drain}}=0.5$ V. The transmission is 500
computed in the presence of an ionized acceptor at the three 501
predefined positions along the channel. Once more, in order 502
to highlight the relevance of the coulomb correlations among 503
the electrons, we also present the same type of results though 504
obtained with a SP treatment (see Appendix A). 505

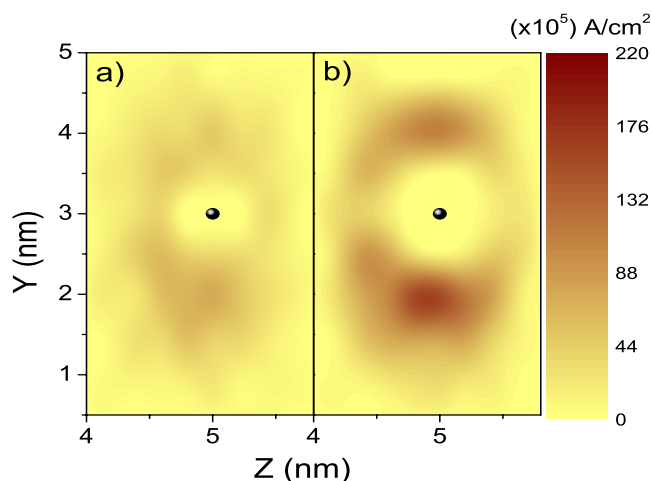


FIG. 4. (Color online) Current density across the channel section when the negative impurity is placed at the center of the channel length. In (a) the results correspond to a MP treatment of the system (see Sec. II). In (b) the results have been computed within a SP mean-field approach discussed in Appendix A.

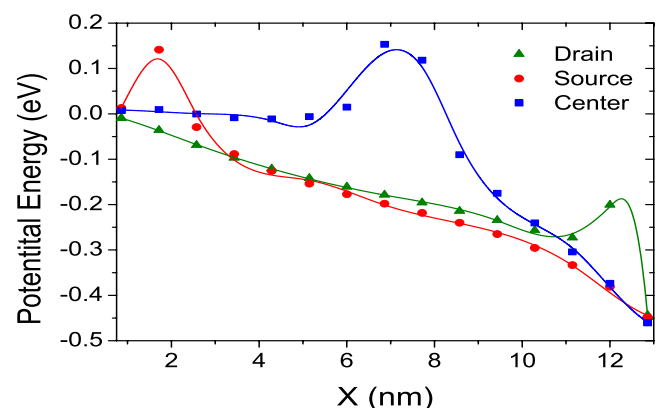


FIG. 6. (Color online) Mean potential energy profiles along the channel (centered in lateral directions) for the three different positions of the negatively charged impurity. These curves are identical independently of the used treatment (SP or MP).

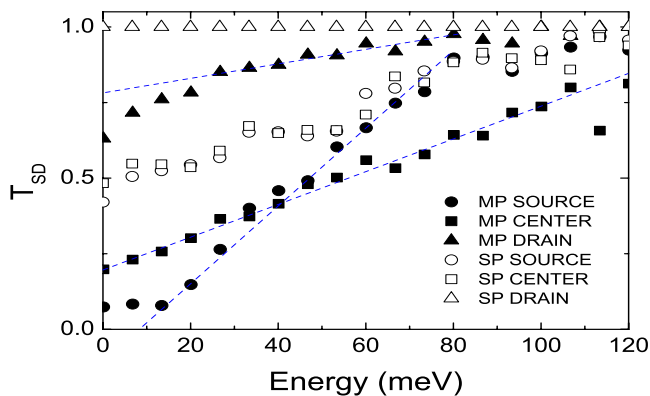


FIG. 7. (Color online) Transmission coefficients as a function of the injection energy for three different positions of a negatively charged impurity. Results are presented for the MP framework presented in Sec. II and for the SP one developed in the Appendix A. MP refers to the MP (solid symbols) and SP to SP (empty symbols).

nanowire with a diameter of approximately 2 nm. Under these particular conditions, the results showed transmission coefficients of the order of 1×10^{-3} for minority carriers (electrons). The origin of the divergence between these drastically reduced transmission values and those presented in Fig. 7 can be ascribed to several differences related to both the simulated device and to the underlying assumptions of both simulation procedures. First of all, the nanowire considered in Ref. 10 is quite thinner than the one considered in this paper. This means that the impact of an impurity on the electron transmission is expected to be stronger because the nanowire cross-section is similar to the effective cross-section of the impurity. On the other hand, the 1D description of the channel of the nanowire reported in Ref. 10 certainly overestimates the electrostatic blockade induced by the impurities even if tunnelling is naturally included in the calculations. In the semiclassical 3D approach considered in our work, the current density is found to flow (as shown in Figs. 3 and 5) far from the ionized dopants, where the potential barrier is substantially lower. Such a spatial distribution cannot be reproduced by a 1D approach as that of Ref. 10, which would only allow the current to flow above a potential barrier which is homogeneous in the nanowire cross-section.

3. Fluctuations of the transit time

Let us discuss how single ionized impurities influence the transit time, τ , of the carriers traversing the QWDG-FET. The relevance of studying this particular characteristic comes from the fact that the switching speed of any FET technology depends ultimately on the transit time. As far as we know, this is the first time that the effects of single ionized dopants on the carrier transit time are analyzed. Within the (frozen) time-independent SP approach, the time spent by the k -th electron (injected in a particular y_{0k} and z_{0k} positions at the source contact with an injecting energy E_{k0}) to achieve the drain contact, can be analytically calculated as

$$\tau_k(E_{k0}, y_{k0}, z_{k0}) = \int_{x_S}^{x_D} \frac{dx_k}{\sqrt{E_{k0} + q\bar{W}(x_k, y_{k0}, z_{k0})}}, \quad (12)$$

where x_S and x_D refer to the position of the source-channel and channel-drain interfaces in the transport direction, and $\bar{W}(x_k, y_{k0}, z_{k0})$ is the mean-field potential profile [see expression (A2) in Appendix A].

When using the time-dependent MP approach described in Sec. II, E_{k0} in Eq. (12) is no longer a constant because the total energy of each carrier is no longer a constant of movement. Moreover, each electron is affected by its own potential profile, which is different from that affecting the other carriers. The transit time corresponding to the k -th electron is hence,

$$\tau_k(E_{k0}, y_{k0}, z_{k0}) = \int_{x_S}^{x_D} \frac{dx_k[t]}{\sqrt{E_k(x_k[t]) + q\bar{W}_k(x_k[t], y_{k0}, z_{k0}, t)}}, \quad (13)$$

where $\bar{W}_k(x_k, y_{k0}, z_{k0})$ is the MP potential profile described in Sec. II, the injecting energy is now $E_{k0} = E_k(x_S)$, and $x_k[t]$ is the classical trajectory of the k -th electron.

As evidenced in Fig. 7, the transmission probabilities for low-energy electrons decrease as the impurity is moved from the channel-drain to the source-channel interface. While the important difference between the channel-drain case and the other two can be easily understood through the potential energy profiles depicted in Fig. 6, the differences between the centered and the source-channel cases at low energy require a more detailed explanation. Since the height of the potential barriers is very similar in both cases, a SP treatment of the electron transport gives identical results (see Fig. 7). Hence, as already discussed for the spatial distribution of J_x , major differences can only be attributed to coulomb correlations. Even more, when the impurity is located at the channel-drain interface, the SP approach results in a constant transmission value equal to the unity. Therefore, the e-e interaction also explains why, even in the absence of a potential barrier, there is no total transmission. At higher energies (from 0.05 eV and above), the order of the transmission curves at low energies (higher transmission when the dopant is moved from source to drain) is lost as a consequence of a different slope of the transmission curves in their linear region (dotted lines in Fig. 7). This effect is a particular feature of the MP system. As the ionized impurity is moved from source to drain, the time required for any electron to reach the position of the impurity increases. Thus, when the ionized impurity is placed toward the drain, the electrons will have more time to interact with the rest of the carriers before reaching the position of the ion and hence, the probability of conserving their initial energy decreases. From Figs. 6 and 7, it can be inferred that, despite the similarity of the potential profiles corresponding to the impurities located at the source and the channel center, a displacement of the ionized dopant toward the drain induces a reduction in the slope of the transmission curve in its linear region. Let us remark that such a particular behavior cannot be described by a SP approach of electron transport, which forces every electron to conserve its total energy (see the empty squares and circles in Fig. 7).

Recently, a study of the transmission coefficient in ultra-thin Si nanowires in the presence of charged impurities has been addressed with a density functional theory approach.¹⁰ In that work, a boron ionized atom was placed in a $\langle 100 \rangle$ Si

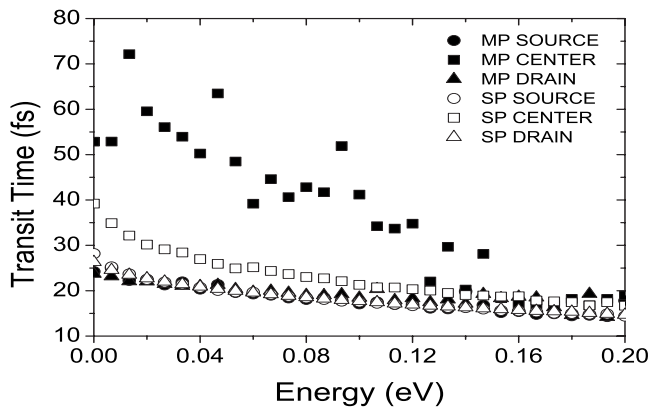


FIG. 8. Transit times as a function of the injection energy for the three different positions of the negatively charged impurity. Results are presented for the MP approach (solid symbols) presented in Sec. II and for the SP treatment of Appendix A (empty symbols). Here, MP refers to the MP and SP to SP.

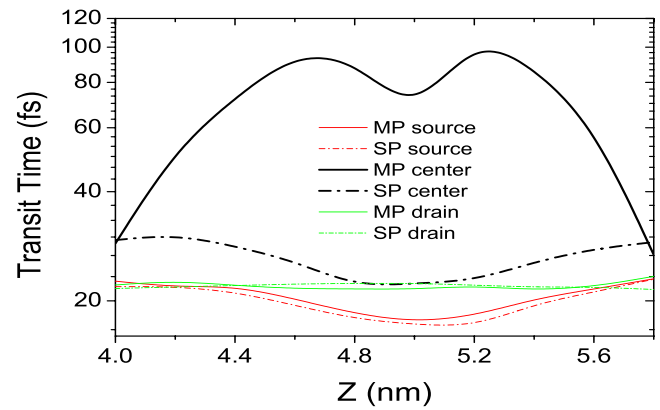


FIG. 10. (Color online) Spatial distribution of the transit times along the z direction (centered in y) when a negatively charged impurity is placed at different places of the channel.

598 In Fig. 8 we present the transit time, averaged over y and
 599 z directions, for the carriers traversing the QWDG-FET from
 600 source to drain as a function of the injecting energy, E_{k0} . The
 601 symmetry of the potential profiles $\bar{W}(x_k, y_{k0}, z_{k0})$ when the
 602 ionized dopant is placed at source and drain contact-channel
 603 interfaces lead to identical transit times for the SP treatment
 604 [see Eq. (12) and open symbols in Fig. 8]. Moreover, since
 605 the variations in the potential profiles introduced by the MP
 606 interaction effects are minimized when the dopant is placed
 607 at the borders of the active region, we find a roughly identi-
 608 cal result for these two situations in the MP approach (solid
 609 symbols). The highest transit times correspond to the cen-
 610 tered impurity, which largely exceed those corresponding to
 611 the previous two cases. The differences between the SP re-
 612 sults and those coming from the MP approach are maximized
 613 in this case, and thus, the switching speed predictions from
 614 these methods would notably differ in this particular case.
 615 While the differences among the SP results come exclusively
 616 from the differences in the shape of the potential profiles, in
 617 the MP approach such differences are added to those coming
 618 from the MP correlations. In this regard, as we will further
 619 discuss below (in relation to Figs. 9 and 10), the physical
 620 origin of the differences between the SP and the MP results

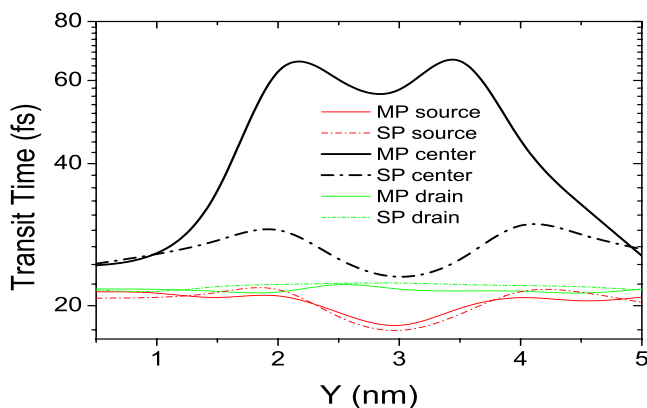


FIG. 9. (Color online) Spatial distribution of the transit times along the y direction (centered in z) when a negatively charged impurity is placed at different places of the channel.

621 corresponding to the centered impurity are found to be re-
 622 lated to a transfer of energy between the electrons crossing
 623 the channel and those that are reflected back to the source.
 624 From Fig. 8 two important results can be extracted. First,
 625 that the transit time variations related to random impurity
 626 fluctuations are not negligible in QWDG-FETs. Second, that
 627 considering e-e coulomb interactions is crucial to correctly
 628 simulate the time-dependent response of such nanoscale de-
 629 vices in the presence of atomistic impurities.

630 Finally, let us discuss the spatial distribution of transit
 631 times in the cross-section of the device averaged over the
 632 injecting energies. Figures 9 and 10 represent the distribution
 633 of the transit times along the y (centered in z) and z (centered
 634 in y) directions, respectively. If all the traversing carriers had
 635 the same total energy, according to Eq. (12) one would ex-
 636 pect to find the largest times concentrated around the impu-
 637 rity location, where the potential barrier is higher (see Fig.
 638 6). Nevertheless, since the injected carriers are energetically
 639 spread according to Fermi statistics, only the fastest electrons
 640 (the most energetic ones) are able to achieve the drain con-
 641 tact across the top of the barrier. Consequently, a minimum
 642 of the transit time is found at the location of the impurity
 643 atom. When the dopant is placed at the source-channel in-
 644 terface, the largest transit times appear away from the impu-
 645 rity and the minimum above the dopant becomes absolute.
 646 Although both, SP and MP simulations give similar overall
 647 results in this case, some discrepancies can be appreciated
 648 due to an energy exchange among the different regions of the
 649 channel. On the other hand, when the impurity is placed in
 650 the center of the channel, the transit times increase drasti-
 651 cally up to 60 fs. Although the shape of the scalar potential
 652 has to do with the important increment both in the SP and the
 653 MP results, e-e interactions play a crucial role in the varia-
 654 tion in transit times. While the SP and the MP results show
 655 again a very similar pattern in this particular case, the mag-
 656 nitude of the transit time differs enormously between these
 657 two approaches. Since the spatial integral of the MP aver-
 658 aged transit times along the y and z directions diverges sig-
 659 nificantly from its SP counterpart, it can be inferred that the
 660 exchange of energy is produced not only among the electrons
 661 crossing the channel but also between them and those being
 662 backscattered. If the energy transfer would only involve elec-

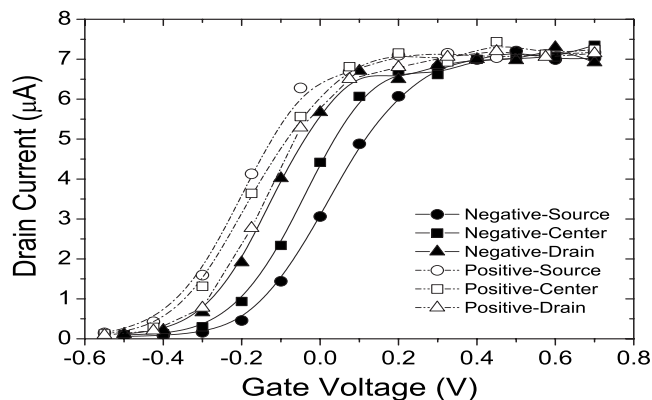


FIG. 11. Average drain current at $V_{\text{Drain}}=1$ V as a function of the gate voltage for positive/negative impurities located at different places along the channel.

such a behavior is quite simple. Since the majority carriers are electrons, positive charged impurities introduce a potential well that favors the flow of the current, while negative impurities appear as potential barriers which tend to block the transmission of electrons. A dependence of the saturation threshold voltage on the position of the impurities along the channel can also be observed (see Fig. 12). As a negative (positive) dopant is displaced from drain to source, the threshold voltage is increased (decreased) in a nonlinear way due to an increment of the height (depth) of the induced potential deformation that is less and less masked by the applied drain voltage. As shown in Fig. 12, positive impurities generate less variation in the threshold voltage than negative ones in NFET devices (the opposite is expected to occur in PFETs).

IV. CONCLUSIONS

The atomistic nature of matter is an important source of random variations on the performance of electron devices scaled to the nanometer scale. In this work, we have focused on one of the most promising device structures to reach the limit of CMOS with sufficient electrostatic control, the quantum wire DG-FET. This device is very robust from the point of view of the control of short-channel effects. Nevertheless, since its dimensions are very small, its performance is strongly influenced by fluctuations in the number, sign, and position of impurities. To avoid the use of the mean-field approximation and the arbitrary separation of the e-i interaction into short-range and long-range terms, we have studied the impact of single impurities using an exact treatment of the e-e and e-i interactions in the framework of MP MC simulation. We have revealed the significant impact of the sign and position of the impurity along the transistor channel not only on the threshold voltage but also on hidden aspects of electron transport such as the distribution of the current in the channel cross-section, the transmission probabilities and the distribution of transit times, which finally determine the intrinsic speed of the device. Comparison with more standard simulations which assume a time-independent mean-field approximation has allowed us to reveal the importance of an accurate treatment of the e-e interactions in the study of DDIF in nanometer scale devices. The correlations between electrons in these ultrascaled systems are very strong and have significant impact on the electron transport, in general, and on the DDIF, in particular. Finally, let us emphasize that many efforts are being done in the literature to improve the treatment of electron (and electron-atom) correlations on the description of the band structure for electron devices in (ground-state) equilibrium conditions. On the contrary, in this work we open a new path to study the effects of e-e (and e-i) correlations in the current measured in nanoscale electron device under (applied bias) far from equilibrium conditions. Future work will improve the treatment of confinement and exchange interactions⁵¹ in the many particle strategy presented here.

trons crossing the device, their total energy would remain unchanged, and thus their averaged transit time would be identical to that found for the SP approach. On the contrary, the mixture of energy exchange among the traversing electrons and among traversing and backscattered electrons give rise to a nonconserving averaged transit time. In fact such an energy transfer is at the origin of the big transit times differences found in Fig. 7. Finally, when the impurity is placed at the channel-drain position, the system becomes basically ballistic, and divergences between expressions (12) and (13) become negligible.

674 4. Fluctuations of the threshold voltage

In order to avoid an excessive increase in the length of this paper, these results will be presented only for our novel algorithm that includes e-e and e-i coulomb correlations. Threshold voltage (V_T) fluctuations are a well known effect related to DDIF in MOSFETs.¹¹⁻²⁸ In this section we analyze this phenomenon in the QWDG-FET from both positive and negative impurities. Figure 11 shows the value of the mean current as a function of the applied gate voltage (transfer characteristic) in the saturation region ($V_{\text{Drain}}=1$ V). As shown in Fig. 12, while negative ions induce a shift of the threshold voltage toward higher values, positively charged impurities shift it down to lower values. The explanation of

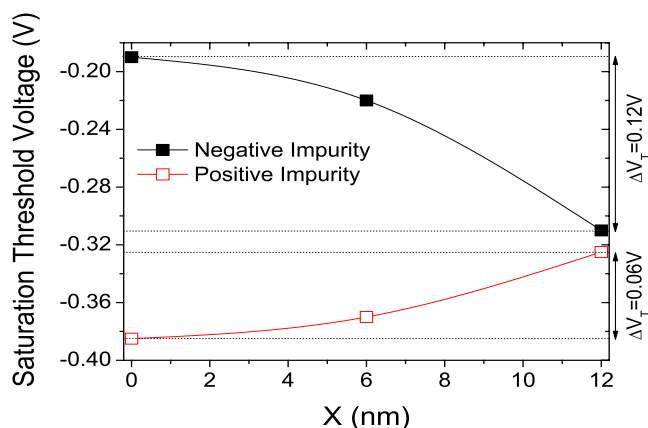


FIG. 12. (Color online) Saturation threshold voltage, V_T , as a function of the position of the p- and n-type impurities along the channel.

741 APPENDIX A

742 1. SP HAMILTONIAN FOR AN OPEN SYSTEM

743 In order to highlight the importance of accurately ac-
744 count for the e–e time-dependent coulomb correlations,
745 throughout the discussion of the results we compare our MP
746 approach with a particular mean-field approach. In this ap-
747 pendix we want to describe such a mean-field approach.

748 The SP approach consists on a mean-field treatment of
749 the e–e interaction described by the next Hamiltonian

$$H(\vec{r}_1, \dots, \vec{r}_{N(t)}, \vec{p}_1, \dots, \vec{p}_{N(t)}, t) = \sum_{k=1}^{N(t)} \{K(\vec{p}_k) + q_k \cdot \bar{W}(\vec{r}_k)\}. \quad (\text{A1})$$

750

751 Comparing Eqs. (5) and (A1), let us notice that the potential
752 $\bar{W}(\vec{r}_k)$ has no longer a subscript k , neither a time dependence.

753 The potential profile, $\bar{W}(\vec{r}_k)$, describing the electrostatics of
754 the problem is now time-independent and equal to the aver-
755 age (over time and particles) value of the MP potential pro-
756 file, i.e.,

$$\bar{W}(\vec{r}_k) = \frac{1}{T \cdot N_T(T)} \int_0^T \sum_{k=1}^{N(t)} \bar{W}_k(\vec{r}_k, t) \cdot dt, \quad (\text{A2})$$

757

758 where $T \rightarrow \infty$ and $N_T(T)$ is the total number of electrons that
759 have been involved in the QWDG-FET during T . $\bar{W}_k(\vec{r}_k, t)$ is
760 defined as in Eqs. (6) and (7). The static potential profile
761 appearing in Eq. (A2) is only capable of capturing the mean
762 behavior of the system electrostatics.

763 Once the electrostatic potential is defined, the time-
764 dependent 3D electron dynamics are computed using the
765 Hamilton equations in Eqs. (8) and (9). In particular, we can
766 obtain the (Newton-type) description of the SP classical tra-
767 jectory $\vec{r}_i[t]$ in the real space through

$$m \cdot \vec{v}_i[t] = \vec{p}_i[t] \quad (\text{A3})$$

769 and

$$\frac{d\vec{p}_i[t]}{dt} = \nabla_{\vec{r}_i} \bar{W}(\vec{r}_i), \quad (\text{A4})$$

770

771 exactly in the same way as in the MP case (see Sec. II).

772 ¹S. Roy and A. Asenov, *Science* **309**, 388 (2005).

AQ: #6 773 ²R. Yan, D. Lynch, T. Cayron, D. Lederer, A. Afzalilian, C. Lee, N. Dehdashtii, and J. P. Colinge, *Solid-State Electron.* **52**, 1872 (2008).

775 ³P. Dollfus, A. Bournel, S. Galdin, S. Barraud, and P. Hesto, *IEEE Trans. Electron Devices* **51**, 749 (2004).

AQ: #7 777 ⁴C. Alexander, A. R. Brown, J. R. Watling, and A. Asenov, *IEEE Trans. Nanotechnol.* **4**, 339 (2005).

779 ⁵P. Dollfus, A. Bournel, and J. E. Velázquez, *J. Comput. Electron.* **5**, 119 (2006).

781 ⁶W. J. Gross, D. Vasileska, and D. K. Ferry, *VLSI Des.* **10**, 437 (2000).

782 ⁷M. Bescond, C. Li, and M. Lannoo, *J. Comput. Electron.* **8**, 382 (2009).

783 ⁸A. Martinez, M. Bescond, J. R. Baker, A. Sivzhenko, M. P. Anantram, C. Millar, and A. Asenov, *IEEE Trans. Electron Devices* **54**, 2213 (2007).

AQ: #8 785 ⁹A. Martinez, J. R. Barker, A. Zvizhenko, M. P. Anantram, A. R. Brown, B. Biegel, and A. Asenov, *J. Phys.: Conf. Ser.* **38**, 192 (2006).

787 ¹⁰R. Rurali, T. Markussen, J. Suñé, M. Brandbyge, and A. Jahuo, *Nano Lett.* **8**, 2825 (2008).

789 ¹¹H. Wong and Y. Taur, *Tech. Dig. - Int. Electron Devices Meet.* **1993**, #9

¹²A. Asenov, A. R. Brown, J. H. Davies, S. Kaya, and G. Slavcheva, *IEEE Trans. Electron Devices* **50**, 1837 (2003). **791**

¹³D. Reid, C. Millar, G. Roy, S. Roy, and A. Asenov, *IEEE Trans. Electron Devices* **56**, 2255 (2009). **792**

¹⁴C. Millar, D. Reid, G. Roy, S. Roy, and A. Asenov, *IEEE Electron Device Lett.* **29**, 946 (2008). **793**

¹⁵G. Roy, A. R. Brown, F. Adamu-Lema, S. Roy, and A. Asenov, *IEEE Trans. Electron Devices* **53**, 3063 (2006). **794**

¹⁶A. Asenov, *IEEE Trans. Electron Devices* **45**, 2505 (1998). **795**

¹⁷A. Asenov and S. Saini, *IEEE Trans. Electron Devices* **46**, 1718 (1999). **796**

¹⁸A. Asenov, R. Balasubramaniam, A. R. Brown, and H. Davies, *IEEE Trans. Electron Devices* **50**, 839 (2003). **797**

¹⁹A. Asenov, G. Slavcheva, A. R. Brown, J. H. Davies, and S. Saini, *IEEE Trans. Electron Devices* **48**, 722 (2001). **798**

²⁰U. Kovac, D. Reid, C. Millar, G. Roy, S. Roy, and A. Asenov, *Micro. Rel.* **48**, 1572 (2008). **799**

²¹Y. Li, C. Hwang, and H. Huang, *Phys. Status Solidi A* **205**, 1505 (2008). **800**

²²A. R. Brown, A. Asenov, and J. R. Watling, *IEEE Trans. Nanotechnol.* **1**, 195 (2002). **801**

²³A. Asenov, *Nanotechnology* **10**, 153 (1999). **802**

²⁴K. Samsudin, F. Adamu-Lema, A. R. Brown, S. Roy, and A. Asenov, *Solid-State Electron.* **51**, 611 (2007). **803**

²⁵A. Asenov, A. R. Brown, G. Roy, B. Cheng, C. Alexander, C. Riddet, U. Kovac, A. Martinez, N. Seoane, and S. Roy, *J. Comput. Electron.* **8**, 349 (2009). **804**

²⁶C. Alexander, G. Roy, and A. Asenov, *IEEE Trans. Electron Devices* **55**, 3251 (2008). **805**

²⁷W. J. Gross, D. Vasileska, and D. K. Ferry, *J. Appl. Phys.* **91**, 3737 (2002). **806**

²⁸D. Vasileska and S. S. Ahmed, *IEEE Trans. Electron Devices* **52**, 227 (2005). **807**

²⁹M. Hori, T. Shinada, K. Taira, N. Shimamoto, T. Tani, T. Endo, and I. Ohdomari, *Nanotechnology* **20**, 365205 (2009). **808**

³⁰T. Shinada, S. Okamoto, T. Kobayashi, and I. Ohdomari, *Nano Lett.* **437**, 1128 (2005). **809**

³¹T. Shinada, T. Kurosawa, H. Nakayama, Y. Zhu, M. Hori, and I. Ohdomari, *Nanotechnology* **19**, 345202 (2008). **810**

³²N. Sano, K. Matsuzawa, M. Mukai, and N. Nakayama, *Microelectron. Reliab.* **42**, 189 (2002). **811**

³³A. Asenov *et al.*, Proceedings of SISPAD 2002, p. 87. **812**

³⁴C. J. Wordelman and U. Ravaioli, *IEEE Trans. Electron Devices* **47**, 410 (2000). **813**

³⁵R. P. Joshi and D. K. Ferry, *Phys. Rev. B* **43**, 9734 (1991). **814**

³⁶W. J. Gross, D. Vasileska, and D. K. Ferry, *IEEE Electron Device Lett.* **20**, 463 (1999). **815**

³⁷W. J. Gross, D. Vasileska, and D. K. Ferry, *IEEE Trans. Electron Devices* **47**, 1831 (2000). **816**

³⁸S. Barraud, P. Dollfus, S. Galdin, and P. Hesto, *Solid-State Electron.* **46**, 1061 (2002). **817**

³⁹S. M. Ramey and D. K. Ferry, *IEEE Trans. Nanotechnol.* **2**, 193 (2003). **818**

⁴⁰G. Albareda, J. Suñé, and X. Oriols, *Phys. Rev. B* **79**, 075315 (2009). **819**

⁴¹Strictly speaking, our many-electron method applied to semiclassical devices cannot be considered as a direct solution of the Boltzmann equation because the latter is developed within a classical mean-field approximation. The term $\bar{W}_k(\vec{r}_k, t)$ in the Hamiltonian of expression (5) means that each particle “sees” its own electrostatic potential (or electric field), which is different from that of others. This is the fundamental difference between our many-electron method applied to classical transport and the standard MC method for electron devices. **820**

⁴²J. P. Colinge, *Solid-State Electron.* **48**, 897 (2004). **821**

⁴³M. Born and R. Oppenheimer, *Ann. Phys.* **389**, 457 (1927). **822**

⁴⁴S. Datta, *Transport in Mesoscopic Systems* (Cambridge University Press, Cambridge, 1995). **823**

⁴⁵Only the interaction of the free electrons with the charges associated to the core of ionized atoms is explicitly treated in the Hamiltonian. The interaction with the core charges associated to neutral atoms is indirectly considered via average polarization charges within a spatially-dependent permittivity (Ref. 46). **824**

⁴⁶J. Wang, A. Rahman, A. Ghosh, G. Klimeck, and M. Lundstrom, *IEEE Trans. Electron Devices* **52**, 1589 (2005). **825**

⁴⁷F. Balestra, S. Cristoloveanu, M. Benachir, J. Brini, and T. Elewa, *IEEE Electron Device Lett.* **8**, 410 (1987). **826**

⁴⁸C. Jacoboni and L. Reggiani, *Rev. Mod. Phys.* **55**, 645 (1983). **827**

⁴⁹X. Oriols, E. Fernandez-Diaz, A. Alvarez, and A. Alarcon, *Solid-State Electron.* **51**, 306 (2007). **828**

865 ⁵⁰We assume that the electron velocity is equal to zero in the lateral direc-
866 tions where there is energy confinement. This is a reasonable assumption
867 that can be formally justified for Ref. [51](#) when the probability presence in
868 that direction does not change with time. The main approximation here is

assuming that the time dependence of the wave function involves only one **869**
quantized energy in the mentioned direction. We define the geometry of **870**
the QWDG-FET to support these approximations. **871**
⁵¹X. Oriols, [Phys. Rev. Lett.](#) **98**, 066803 (2007). **872**

Electric power in nanoscale devices with full Coulomb interaction

G. Albareda^{*,†}, A. Alarcón and X. Oriols

Departament d'Enginyeria Electrònica, Universitat Autònoma de Barcelona, 08193 Bellaterra, Spain

SUMMARY

An accurate reformulation of the electric power in quasi-ballistic (classical or quantum) scenarios is deduced within an explicit many-particle treatment of the Coulomb interaction. The traditional definition of the electric power is compared with the new formulation presented here for classical bulk, quantum well and quantum wire double-gate MOSFETs by means of 3D many-electron Monte Carlo simulations. The accurate results with the many-electron approach show not-negligible discrepancies when compared with the conventional definition. Such small discrepancies become very important when the single-transistor power is multiplied by the huge number of transistors present in the state-of-the-art integrated circuits. Copyright © 2010 John Wiley & Sons, Ltd.

Received 12 June 2009; Revised 19 October 2009; Accepted 2 November 2009

KEY WORDS: electric power; many-particle; double-gate FET; ballistic transport; Coulomb correlations

1. INTRODUCTION

Power consumption is one of the main drawbacks when scaling down any new technology [1, 2]. In the last few years, the electronic development is being driven not only by the desire of improving circuit density and speed but also of reducing power consumption. The ITRS has identified this last constraint as one of the top three overall challenges for the next 15 years [3]. In this sense, accuracy is a mandatory requirement when predicting electric power in the active region of a MOS transistor because the results of the single transistor are then extrapolated to the large number of transistors in present-day CPUs.

For any set of electrons (for example, a nanotransistor), the dynamic of one particular electron is coupled to all other electrons because of their mutual Coulomb interactions. This

*Correspondence to: G. Albareda, Departament d'Enginyeria Electrònica, Universitat Autònoma de Barcelona, 08193 Bellaterra, Spain.

†E-mail: guillem.albareda@uab.cat

Contract/grant sponsor: Ministerio de Ciencia e Innovación; contract/grant number: N. MICINN TEC2009-06986

indicates that the electrostatic force made over each particular electron depends on the instantaneous position of the rest of charges. In other words, and hence that the trajectory followed by a particular electron depends on the trajectories followed by the rest of the electrons.

From a computational point of view, the direct solution of such a many-electron Coulomb-interacting system is usually inaccessible. In most electron transport models, the standard solution to overcome this computational barrier is based on assuming that electrons move according to a unique ‘average’ potential profile (the so-called mean field approximation). This is the strategy used in the traditional Monte Carlo method applied to study electron transport in semiconductor electron devices, where the Coulomb interaction is separated into two parts [4–7]. The first part is the long-range Coulomb interaction that is included in a mean-field solution of Poisson equation in the real space. The second part is the short-range Coulomb interaction that is usually taken into account perturbatively (i.e. approximately) in the reciprocal space via the consideration of electron-electron scattering rates.

Nowadays, in state-of-the-art nanometric electron devices, the output current is carried by very few electrons inside very small (nanometric) regions. One can expect that the simulation of electron devices using the mean-field approximation is not accurate enough for power estimations. Many works are being devoted to deeply understand the energy consumption in both, *on/off* and *switching* states. However, to our knowledge, the energy consumption problem from a perspective beyond the mean-field approach has not been addressed in the literature. This is the goal of this seminal manuscript.

After this introduction, in the second section of this work, we present an accurate reformulation of the electric power in ballistic (classical or quantum) nanoscale devices based on a direct solution of the many-particle equation of motion of the system by solving a particular Poisson equation for each electron. A third section is devoted to a numerical comparison between the standard expression for the electric power and the new reformulation. In particular, we use a numerical simulation of a double-gate quantum-wire FET (1D DG-FET), a double-gate quantum-well FET (2D DG-FET), and a double-gate bulk FET (3D DG-FET). The final part is dedicated to summarize the most important conclusions of this work.

2. ELECTRIC POWER IN CLASSICAL AND QUANTUM ELECTRON DEVICES

We consider a system of $N(t)$ electrons inside a volume Ω . Here we are especially interested on the application of our results to nanoscale electron devices and, hence, we consider the volume Ω as the active region of a DG-FET (see Figure 1). Each electron is defined by a particular trajectory $\vec{r}_i[t]$ and velocity $\vec{v}_i(t) = \dot{\vec{r}}_i[t]$. When dealing with pure quantum systems, the previous definitions are ascribed to a quantum (Bohm) trajectory [8, 9].

In order to treat Coulomb interaction among electrons exactly, we have to avoid the electron self-interaction that arises from the resolution of a common Poisson equation for all electrons. Hence, we solve a particular Poisson equation for each electron:

$$\nabla^2(\epsilon V_i(\vec{r}, t)) = \rho_i(\vec{r}, t) \quad (1)$$

where $V_i(\vec{r}, t)$ represents the electrostatic potential ‘seen’ by the i -th electron and $\rho_i(\vec{r}, t)$ accounts for all charges except the i -th electron [10] (in the present work the assignation of charge will follow a cloud-in-cell scheme) The parameter ϵ is the permittivity. From expression (1), it can be

ELECTRIC POWER IN NANOSCALE DEVICES

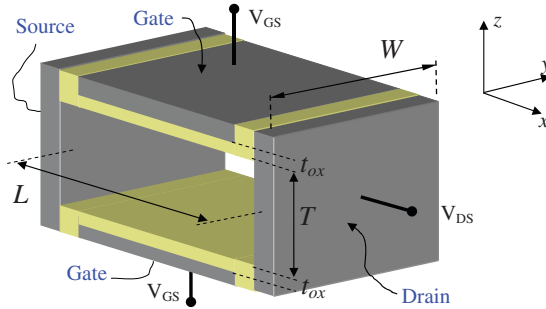


Figure 1. Schematic representation of the DG-FET geometry from source to drain.

easily inferred that the force over each electron is $q_i \cdot \vec{E}_i(\vec{r}, t)$, which does not account for the self-interaction because each electron has its own electric field.

Now, the work done to ‘move’ the i -th electron from the initial position, $\vec{r}_i[0]$, to a final position, $\vec{r}_i[t]$, is

$$W_i(t) = \int_0^t q_i \cdot \vec{v}_i(\vec{r}_i[t']) \cdot \vec{E}_i(\vec{r}_i[t'], t') \cdot dt' \quad (2)$$

Then, our original reformulation of the many-electron electric power, computed as the time-derivative of this work, can be written as

$$P_{m-e,i}(t) = q_i \cdot \vec{v}_i(\vec{r}_i[t]) \cdot \vec{E}_i(\vec{r}_i[t], t) \quad (3)$$

where $j_i(t) = q_i \cdot \vec{v}_i(t)$ can be understood as the current density associated to the i -th charge. Note the subindex m-e indicating that we are using a many-electron formulation. A simple integration over the whole volume Ω gives the total electric power for this particular region of space

$$P_{m-e}(t) = \sum_{i=1}^{N(t)} q_i \cdot \vec{v}_i(\vec{r}_i[t]) \cdot \vec{E}_i(\vec{r}_i[t], t) \quad (4)$$

where $N(t)$ is the number of electrons in the volume Ω at time t . Let us notice the use of $N(t)$ different electric fields in (4). On the contrary, the standard definition of electric power assumes the following mean-field approximation, $\vec{E}_i(\vec{r}, t) \approx \vec{E}(\vec{r}, t)$; a common electric field for all electrons. For the particular mean-field model we are considering, $\vec{E}(\vec{r}, t)$ is defined from the solution of a single Poisson equation,

$$\nabla^2(\epsilon V(\vec{r}, t)) = \rho(\vec{r}, t) \quad (5)$$

where $\rho(\vec{r}, t)$ accounts for all charges (the charge assignment follows a cloud-in-cell scheme in the same way as in the exact treatment).

Using (4) and the previous approximation, (5), one obtains the standard definition of the power

$$P_{m-f}(t) = \int_{\Omega} \vec{E}(\vec{r}, t) \cdot \vec{j}(\vec{r}, t) \cdot d\vec{r} = \sum_{i=1}^{N(t)} q_i \cdot \vec{v}_i(t) \cdot \vec{E}(\vec{r}_i[t], t), \quad (6)$$

where $\vec{j}(\vec{r}, t) = \sum_{i=1}^{N(t)} q_i \cdot \vec{v}_i(\vec{r}, t) \cdot \delta(\vec{r} - \vec{r}_i(t))$ is the total conduction current density in the volume Ω . To compare these different expressions (4) and (6) for the electric power it is convenient to define the error between the mean-field approximation and the exact many-electron i -th electric field as:

$$\Delta \vec{E}_i(\vec{r}, t) = \vec{E}_i(\vec{r}, t) - \vec{E}(\vec{r}, t) \quad (7)$$

Hence, the error $\Delta P(t) = P_{m-e} - P_{m-f}$ when defining (6) as the time-derivative of the work done over a set of $N(t)$ charges in Ω is:

$$\Delta P(t) = \sum_{i=1}^{N(t)} q_i \cdot \vec{v}_i(t) \cdot \Delta \vec{E}_i(\vec{r}_i[t], t) \quad (8)$$

Notice the dependence of the error on the number of electrons, $N(t)$, the electron velocity, $\vec{v}_i(t)$, and the value of $\Delta \vec{E}_i(\vec{r}_i[t], t)$.

3. NUMERICAL COMPUTATION OF THE ELECTRIC POWER

In this section, we evaluate the differences on the electric DC power obtained from the accurate many-electrons (m-e) method, (4), and the approximate mean-field (m-f) method, (6), within an electron device Monte Carlo simulation of a 1D DG-FET, a 2D DG-FET and a 3D DG-FET.

3.1. Device description

We consider a Monte Carlo simulation for a DG-FET electron device (see Figure 1), where electron transport (from source to drain) takes place along a Silicon (100) orientation channel, at room temperature. In particular, the electron mass is taken according to the six equivalent ellipsoidal constant energy valleys of the silicon band structure [11, 12]. The effective masses of the ellipsoid are $m_l^* = 0.9163 m_0$ and $m_t^* = 0.1905 m_0$ with m_0 the free electron mass. For details on the particular effective mass taken by the electrons in each direction and valley, see reference [13, 14]. The dimension of the channel of the device depicted in Figure 1 are L , W , and T .

We consider three different geometries with different degrees of electron confinement in order to be able to deal with a bulk device (3D), a quantum well (2D), and a quantum wire (1D). When W and T are much larger than the electron de Broglie wave length, the active region is a three-dimensional (3D) system (bulk) and there is no restriction in the possible values of the energies of an electron in each of the six valley. The total electron energy for a particular valley is $E = E_x + E_\perp$, where the energies E_x and E_\perp are defined in the parabolic approach as $E_x = \hbar^2 k_x / (2m_t)$ and $E_\perp = \hbar^2 k_y / (2m_t) + \hbar^2 k_z / (2m_t)$. On the other hand, for a small enough value of T , the system becomes a two-dimensional 2D (quantum well) and the total electron energy for one particular valley of the first sub-band is $E = \hbar^2 k_x / (2m_t) + E_\perp$, where $E_\perp = \hbar^2 k_y / (2m_t) + E_{2D}^q$. The energy $E_{2D}^q = \hbar^2 \pi^2 / (2m_t T^2)$ is the minimum quantized energy level of the first sub-band, whose value is $E_{2D}^q = 0.103$ eV for $T = 2$ nm. The energy of the second sub-band is $E_{2D}^q = 0.410$ eV. Under this conditions only two identical valleys become relevant, and although energies above the first level can be reached at high drain bias, in this particular work we assume that only the first energy sub-band is available. In this sense, our numerical results would be slightly modified for supplied drain voltages beyond 0.5 eV. We assume, in addition, that the electron velocity in the z -direction is zero due to the electron confinement. This last statement can be formally justified, for example using Bohm trajectories, when the

probability presence in the z -direction does not change with time. The main approximation here is assuming that the single-particle wave-function is separable in the 3D space and that only one subband is relevant for electron transport. Finally, when T and W are both small enough, the active region becomes a 1D system (a quantum wire) and the energy of an electron in one particular valley is $E = \hbar^2 k_x^2 / (2m_l) + E_{1D}^q$, where $E_{1D}^q = \hbar^2 \pi^2 / (2m_l W^2) + \hbar^2 \pi^2 / (2m_l T^2)$ represents the minimum energy of the first sub-band, whose value is $E_{1D}^q = 0.182$ eV for $T = 2$ nm and $W = 5$ nm. The energies of the next lowest sub-bands are $E_{1D}^q = 0.418$ eV or $E_{1D}^q = 0.489$ eV. As in the previous case (2D system), although energies above the first level can be reached at high drain bias, we assume that only this first energy sub-band is available. Again only two valleys become relevant.

The details of the geometries, doping, and simulating parameters of the three simulated devices can be found in Table I.

3.2. Numerical simulation algorithm

All simulations use a 3D finite-difference Poisson solver scheme. The whole volume Ω mentioned in Section 2 is now understood as the active region drawn in Figure 1 and is divided into $N_x \cdot N_y \cdot N_z$ cells. Each 3D cell has spatial dimensions DX , DY , and DZ . Thus, the active region of our simulating device has a volume equal to $(N_x \cdot DX) \cdot (N_y \cdot DY) \cdot (N_z \cdot DZ) = L \cdot W \cdot T$. A total number of cells, $N_x \cdot N_y \cdot N_z$, in the order of 100 and a number of electrons, $N(t)$, about 20–50, implies a simulation time on the order of 3–4 h for each bias point within our many-electron algorithm, while it takes 20–30 min within the mean field approximation.

The boundary conditions of the Poisson equation on the six rectangular surfaces of the volume Ω of Figure 1 are defined using either Dirichlet or Neumann arguments. In general, on the interfaces air-silicon, Neumann boundary conditions are used with the educated guess that the component of the electric field normal to the surface is zero there. The continuity of the displacement vector normal to the surfaces justifies this assumption at the boundaries when the relative permittivity inside Ω is much higher than the corresponding value outside. On the other hand, at the four metal interfaces (drain, source, and two gates) we use Dirichlet boundary conditions. In order to avoid charge imbalance on the source and drain contacts, at each simulation time, we slightly modify the value of the conduction band in order to increase/decrease the electron injecting probability [15].

Table I. Main parameters of the Monte Carlo simulation for the 1D, 2D, and 3D DG-MOSFET.

	Magnitude	3D bulk	2D quantum well	1D quantum wire
Channel dimensions (nm)	L	15	15	15
	W	10	10	5
	T	8	2	2
Spatial step (nm)	DX	1.5	1.5	1.5
	DY	2.5	2.5	1.6
	DZ	2	1	1
Doping (cm^{-3})	Channel	2×10^{19}	2×10^{19}	2×10^{19}
	Contact	2×10^{19}	2×10^{19}	2×10^{19}
Simulation time (s)	T	3×10^{-10}	4×10^{-10}	5×10^{-10}
Temporal step (s)	Dt	2×10^{-16}	2×10^{-16}	2×10^{-16}

When dealing with our many-particle model, the numerical algorithm for solving the dynamics of an ensemble of interacting electrons is quite close, but not identical, to the standard Monte Carlo method applied to semiconductor electron devices. In the later, a unique Poisson equation is solved at each time step of the simulation, while in our many-electron method we solve $N(t)$ Poisson equations with $N(t)$ different boundary conditions and charge densities [10]. In addition, our numerical algorithm includes electron confinement. We also use an injection model applicable to systems with arbitrary electron confinement, valid for degenerate and non-degenerate systems [13].

3.3. Main results

Our reformulation of the electric power can be applied to switching or maintenance logic states in a CMOS circuit. In this work we deal with a simple *ON* state of a DG-FET, focusing on the computation of the DC electric power consumption.

Figure 2 shows this characteristic curves computed by means of the exact many-electron method, for the 1D, 2D, and 3D DG-FETs mentioned in the Section 3.2 (schematically represented in Figure 1). The computation of the electric power has been carried out within the saturation region of this I–V characteristic. Power results are presented in Figures 3 and 4.

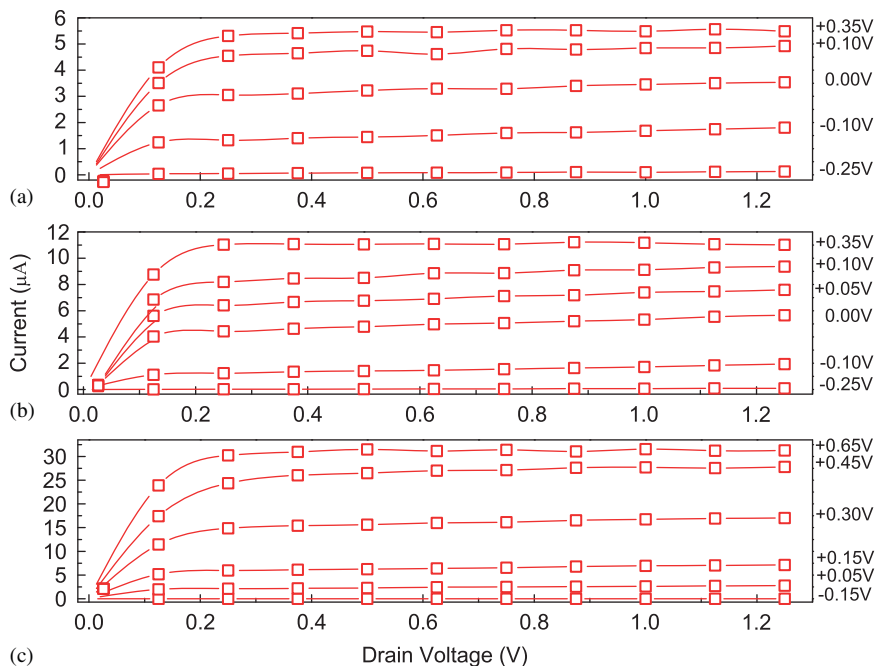


Figure 2. Current–voltage characteristic for the simulated 1D DG-FET (a), 2D DG-FET (b), and 3D DG-FET (c), computed by means of the exact method (m-e). For a fixed drain voltage (1 V), five different gate voltages have been considered in (a) and (b) (-0.25 , -0.10 , 0.05 , 0.20 , and 0.35 V), and other five different gate voltages have been considered in (c) (0.0 , 0.15 , 0.30 , 0.45 , and 0.60 V).

ELECTRIC POWER IN NANOSCALE DEVICES

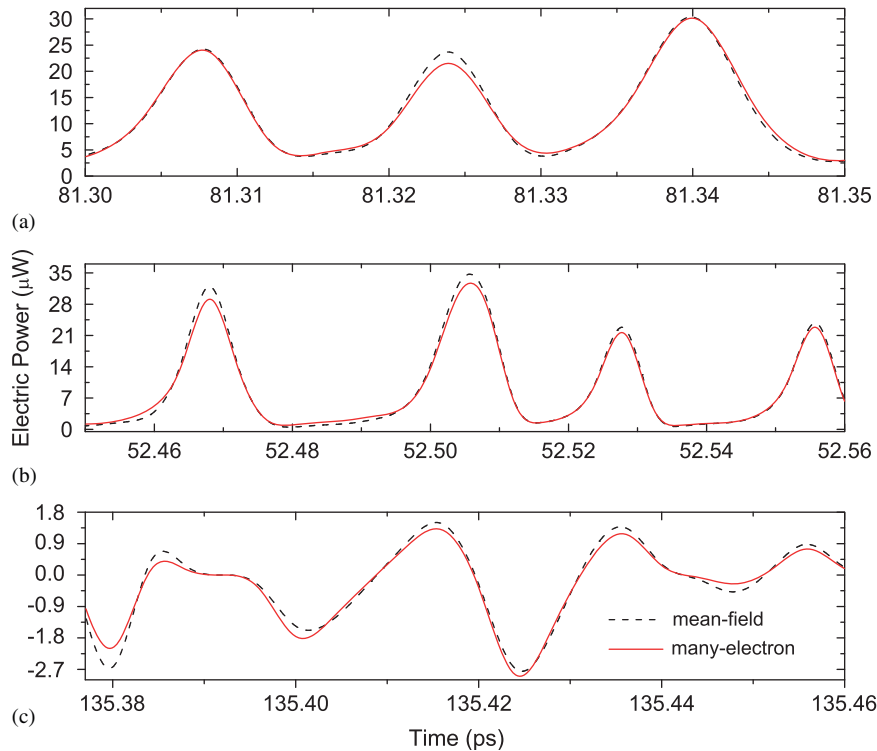


Figure 3. Time evolution of the power consumption in the 1D DG-FET (a), 2D DG-FET (b), and 3D DG-FET (c), for the two computational methods at $V_{\text{drain}} = 1 \text{ V}$ and $V_{\text{gate}} = 0.05 \text{ V}$ in (a) and (b), and $V_{\text{gate}} = 0 \text{ V}$ in (c). Dashed line refers to the many-electrons method and solid line refers to the mean-field method.

Figure 3 presents a zoom of the instantaneous time-dependent electric power defined as (4) and (6) for the three geometries mentioned in Table I at low-gate voltages. Even when decreasing the supplied voltage at the gates, differences between both methods remain instantaneously appreciable. The disagreement between the many-particle and the mean-field method become larger when the lateral area of the DG-FET is increased. The explanation of this divergence lies on the presence of a higher number of electron in the active region (see expression 8).

Figure 4 presents time averaged DC values of the power consumption per transistor on the saturation region ($V_{\text{drain}} = 1 \text{ V}$) as a function of the gate voltage. At the same time, we represent the differences between the exact (m-e) method and the approximated (m-f) method defined in (8). Roughly speaking, for higher gate voltages we find higher longitudinal electric fields and, consequently, electron velocities rise. This is why differences become larger in magnitude (there is an irrelevant negative sign in Figure 4) when the applied gate voltage is increased. Again, the increment on the number of electrons in the channel region due to an enlargement of the lateral area makes the upper limit of the sum in (8) grow. Hence, we find the largest discrepancies for the 3D system.

Differences on a single transistor are in the order of 0.12, 0.24, and 0.55 μW for the 1D, 2D, and 3D systems respectively. Nevertheless, when we multiply these errors per transistor by the number of transistors present in a CPU (approximately 10^9 transistors), the global error in the estimation of the consumption is dramatic. In particular, the computation of the electric power

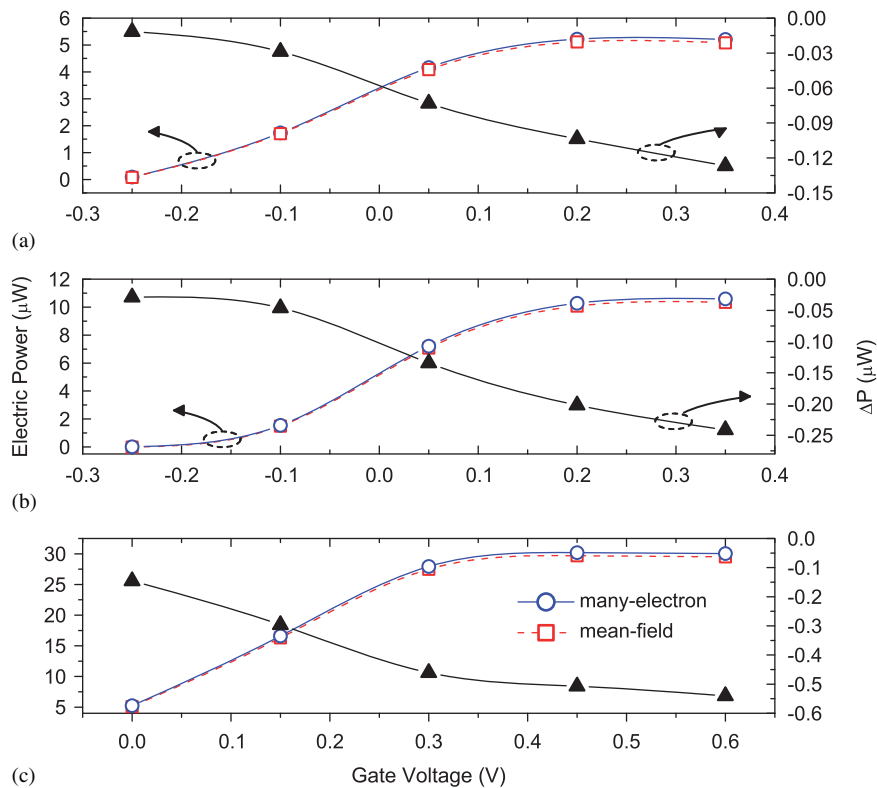


Figure 4. Time averaged (DC) values for the electric power computed from the many-electron method and the mean-field approach in a single 1D DG-FET (a), 2D DG-FET (b), and 3D DG-FET (c). Differences between time averaged powers, $\langle P \rangle_{\text{mean-field}}$ and $\langle P \rangle_{\text{many-electrons}}$, are also presented in absolute values.

consumption by means of the mean-field approach leads an erroneous prediction per CPU around 150, 240, and 550 W for 1D DG-FETs, 2D DG-FETs, and 3D DG-FETs respectively. At the same time, not only the prediction of the electric power grows (in magnitude) as the gate voltage rises, but also the difference between both methods. This non-linearity of the error is quite relevant because it implies that extrapolations carried out with mean-field approximations can lead to erroneous predictions.

4. CONCLUSIONS

Although power consumption is an extremely important parameter in scaling down electronic technology, its standard predictions are based on approximate expressions that can become inaccurate in some scenarios. A reformulation of the electric power is presented for (classical or quantum) electron devices within a many-particle formulation of the Coulomb interaction [10]. When many-electron and mean-field simulations are carried out, results show subtle differences per transistor for the simulated 1D, 2D, and 3D DG-FET. Nevertheless, the multiplication of the error-per-transistor by the huge number of them present in a CPU makes estimation of power consumption within a mean-field framework quite inaccurate.

ACKNOWLEDGEMENTS

This work has been partially supported by the Ministerio de Ciencia e Innovación through project N. MICINN TEC2009-06986.

5. REFERENCES

1. Frank DJ. Power-constrained CMOS scaling limits. *IBM Journal of Research and Development* 2002; **46**(2/3):235.
2. Horowitz M *et al.* Scaling, power, and the future of CMOS. In *Electron Devices Meeting, 2005. IEDM Technical Digest*. IEEE International, Washington, DC, December 2005.
3. International Technology Roadmap for Semiconductors, 2008 Update.
4. Jacoboni C, Reggiani L. The Monte Carlo method for the solution of charge transport in semiconductors with applications to covalent materials. *Reviews of Modern Physics* 1983; **55**:645–700.
5. Anil KG, Mahapatra S, Esiele I. Electron-electron interaction signature peak in the substrate current versus gate characteristic of n-channel silicon MOSFETs. *IEEE Transactions on Electron Devices* 2003; **49**(7):1283–1288.
6. Gross WJ, Vasileska D, Ferry DK. A novel approach for introducing the electron-electron and electron-impurity interaction in particle-based simulations. *IEEE Electron Device Letters* 1999; **20**(9):463–465.
7. Wordelman CJ, Ravaioli U. Integration of a particle- particle-mesh algorithm with the ensemble Monte Carlo method for the simulation of ultra-small semiconductor devices. *IEEE Transactions on Electron Devices* 2000; **47**(2):410–416.
8. Oriols X. Quantum-trajectory approach to time-dependent transport in mesoscopic systems with electron-electron interactions. *Physical Review Letters* 2007; **98**:066803.
9. Kobe DH. Quantum power in de Broglie-Bohm theory. *Journal of Physics A: Mathematical and General* 2007; **40**:5155.
10. Albareda G, Suñe J, Oriols X. Many-particle Hamiltonian for open systems with full Coulomb interaction: application to classical and quantum time-dependent simulations of nanoscale electron devices. *Physical Review B* 2009; **79**:075315.
11. Jacoboni C, Reggiani L. The Monte Carlo method for the solution of charge transport in semiconductors with applications to covalent materials. *Reviews of Modern Physics* 1983; **55**:645.
12. Sverdlov V, Oriols X, Likharev K. Effective boundary conditions for carriers in ultrathin SOI channels. *IEEE Transactions on Nanotechnology* 2003; **2**:59.
13. Oriols X, Fernandez-Diaz E, Alvarez A, Alarcón A. An electron injection model for time-dependent simulators of nanoscale devices with electron confinement: application to the comparison of the intrinsic noise of 3D-, 2D- and 1D-ballistic transistors. *Solid State Electronics* 2007; **51**:306.
14. Büttiker M. Scattering-theory of thermal and excess noise in open conductors. *Physical Review Letters* 1990; **65**:2901.
15. López H, Albareda G, Cartoixà X, Suñe J, Oriols X. Boundary conditions with Pauli exclusion and charge neutrality: application to the Monte Carlo simulation of ballistic nanoscale devices. *Journal of Computational Electronics* 2008; **7**(3).

AUTHORS' BIOGRAPHIES



Guillem Albareda Piquer received his Bachelor Degree in Physics from the *Universidad Autónoma de Barcelona (Spain)* in 2006 and a Master in Micro and NanoElectronics from the *Universidad Autónoma de Barcelona* in 2007. He is currently elaborating his PhD thesis at the Computational Nanoelectronics group at the Department d'Enginyeria Electrònica at *Universidad Autónoma de Barcelona*. His present research activity is focused on the numerical simulation of classical/quantum transport in nanoelectronic devices.



Alfonso Alarcón Pardo received his Bachelor Degree in Physics from the *Universidad Autónoma de Barcelona (Spain)* in 2007 and a Master in Nanotechnology from *Universidad Autónoma de Barcelona* in 2009. He is currently elaborating his PhD thesis at the Computational Nanoelectronics group at the Department d'Enginyeria Electrònica at *Universidad Autónoma de Barcelona*. His present research activity is focused on the numerical simulation of quantum transport in nanoelectronic devices.



Dr. Xavier Oriols received his BS, MS degree in Physics from the *Universitat Autònoma de Barcelona (Spain)* in 1993 and 1994 respectively. During 1997, he worked at the *Institute d'Electronique, Microelectronique and Nanotechnology (France)* on the simulation of resonant tunneling devices. He received his PhD degree in Enginyeria Electrònica from the *Universitat Autònoma de Barcelona (Spain)* in 1999 and the *Diploma d'Estudis Avançats* in Signal Theory and Communications from *Universitat Politècnica de Catalunya* in 2001. During 2001 and 2002 he was a visiting professor at the *State University of New York (USA)* working on the simulation of nanomofets. He is currently an associate professor at the Department d'Enginyeria Electrònica in the *Universitat Autònoma de Barcelona*. He is the author or co-author of over 100 contributions for scientific journals and conferences in the field of semiconductor device physics. In 2008, he received the prize for young investigators in the framework of the Spanish I3 Program. His present research is focused on the time-dependent simulation of electron correlations (high-frequency and noise) in nanoelectronic devices and the inclusion of 'first principles' band-structure techniques in the modelling of electron transport for nanoelectronic applications.

Many-particle Hamiltonian for open systems with full Coulomb interaction: Application to classical and quantum time-dependent simulations of nanoscale electron devices

G. Albareda, J. Suñé, and X. Oriols*

Departament d'Enginyeria Electrònica, Universitat Autònoma de Barcelona, 08193 Bellaterra, Spain

(Received 12 July 2008; published 17 February 2009)

A many-particle Hamiltonian for a set of particles with Coulomb interaction inside an open system is described without any perturbative or mean-field approximation. The boundary conditions of the Hamiltonian on the borders of the open system [in the real three-dimensional (3D) space representation] are discussed in detail to include the Coulomb interaction between particles inside and outside of the open system. The many-particle Hamiltonian provides the same electrostatic description obtained from the image-charge method, but it has the fundamental advantage that it can be directly implemented into realistic (classical or quantum) electron device simulators via a 3D Poisson solver. Classically, the solution of this many-particle Hamiltonian is obtained via a coupled system of Newton-type equations with a different electric field for each particle. The quantum-mechanical solution of this many-particle Hamiltonian is achieved using the quantum (Bohm) trajectory algorithm [X. Oriols, *Phys. Rev. Lett.* **98**, 066803 (2007)]. The computational viability of the many-particle algorithms to build powerful nanoscale device simulators is explicitly demonstrated for a (classical) double-gate field-effect transistor and a (quantum) resonant tunneling diode. The numerical results are compared with those computed from time-dependent mean-field algorithms showing important quantitative differences.

DOI: [10.1103/PhysRevB.79.075315](https://doi.org/10.1103/PhysRevB.79.075315)

PACS number(s): 73.23.-b, 71.10.-w, 02.70.-c, 41.20.Cv

I. INTRODUCTION

The exact computation of a system of interacting electrons is extremely complicated^{1,2} because the motion of one electron depends on the positions of all others (i.e., electrons are correlated³). Thus, the prediction of the collective behavior of many electrons is still a very active field of research in nanoelectronics, quantum chemistry, nanobiology, quantum computing, materials science, etc. Several theoretical approximations have been proposed to improve the treatment of electron-electron correlations.

In quantum systems in equilibrium, the time-independent mean-field approximation appears as a successful solution to treat a set of interacting electrons. It simplifies the exact many-particle potential by an average or mean potential² that transforms the many-body Schrödinger equation into a much more simple set of time-independent single-particle Schrödinger equations. The Hartree-Fock method^{4,5} is a successful example of such approximation. However, by construction, the correlations among electrons can only be treated approximately. In principle, the density-functional theory^{6,7} provides an exact path to deal with full electron correlations using single-particle potentials. However, since the exact form of the single-particle potentials⁶⁻⁹ is unknown, an educated guess for these average single-particle potentials is needed in all practical algorithms. Therefore, again, the electron-electron correlations are treated approximately.^{9,10}

The accurate treatment of the electron-electron correlations in electric circuits is even a more difficult issue¹¹⁻²⁶ because we deal with nonequilibrium open systems¹¹⁻¹³ (where the system interchanges energy and particles with its environment). In fact, the Coulomb interaction among electrons is directly not considered in many quantum transport formalisms^{11,12} under the assumption that the open system

behaves as a Fermi liquid.¹⁴ The well-known Landauer approach^{15,16} is a very successful example of the applicability of this assumption. Nevertheless, the Fermi-liquid paradigm has difficulties dealing with high-frequency,^{11,17} low-dimensionality,^{1,2} or Coulomb blockade regimes.^{11,18} On the other hand, the nonequilibrium Green's-function formalism (also referred to as the Keldysh formalism) provides an interesting path to solve the Schrödinger equation with the Coulomb interaction introduced perturbatively.¹⁹ Alternatively, under the assumption that the system behaves like a capacitor, one can use a simple linear relationship between the number of electrons and the electrostatic potential in a particular region to introduce partially Coulomb effects.^{12,18} The mean-field approximation appears again as a solution for electron transport. For example, an average single-particle time-independent potential profile can be computed, self-consistently, from the set of wave-function solutions of a single-particle time-independent Schrödinger equation.^{2,12} This represents a zero-order approximation (sometimes called the Hartree⁴ approximation) to the complex problem of electron-electron correlations. Additionally, remarkable efforts have been done by Büttiker and co-workers²⁰⁻²² to include Coulomb interaction in their scattering matrix approach by applying different many-body approximations to provide self-consistent electron-transport theories with overall charge neutrality and total current conservation. Finally, extensions of the equilibrium density-functional theory to deal with electron transport, by means of a time-independent formalism,²³ or with a powerful time-dependent version²⁴⁻²⁶ can also be found in the literature. The exact exchange-correlation functionals needed in both formalisms are unknown and they have to be approximated. Therefore, in all the descriptions of nonequilibrium quantum systems mentioned here, the electron-electron correlations are approximated to some extent.

D For classical electron devices, the electrostatic interaction among electrons is commonly obtained from an explicit solution of the Poisson (Coulomb) equation. However, again, this does not provide an exact treatment of the classical electron-electron correlations but only an average estimation.^{27,28} It is well known that the solution of a classical many-particle system can always be written as a coupled system of single-particle Newton-type equations. However, a classical mean-field approximation is explicitly assumed in semiclassical transport simulators in order to deal with a unique average electrostatic potential for all electrons.²⁷ A successful application of the classical mean-field approximation appears, for example, in the semiclassical Boltzmann equation that describes the time evolution of the electron distribution function in a one-electron phase space.²⁷ The use of a unique electric field (i.e., a unique average electrostatic potential) in the Boltzmann equation neglects the correct electron-electron correlations because each electron “feels” its own charge.^{28–32} A powerful time-dependent technique to solve the Boltzmann equation is the semiconductor Monte Carlo method applied to electron devices.²⁷

In this work, we are interested in revisiting the computation of an ensemble of Coulomb-interacting particles in an open system without any of the approximations mentioned in the previous paragraphs. With this goal, we have developed an exact many-particle Hamiltonian for Coulomb-interacting electrons in an open system in terms of the solutions of the Poisson equation. To our knowledge, the type of development of the many-particle Hamiltonian proposed in this paper has not been previously considered in the literature because, up to now, it was impossible to handle the computational burden associated with a direct solution of a many-particle Hamiltonian. Here, we present a classical and also a quantum solution of the many-particle Hamiltonian, both of which are applicable to realistic three-dimensional (3D) electron devices. The classical solution is obtained by solving a coupled system of Newton-type equations with a different electric field for each particle. The quantum solution of the many-particle Hamiltonian is obtained from the use of quantum trajectories.³³ The merit of the quantum solution is certainly remarkable because, nowadays, the computational burden associated with the direct (i.e., without any approximation) solution of the many-particle wave function is only accessible for very few (2,3,...) electrons.^{1,2} Our quantum algorithm is able to treat electron dynamics without any (mean-field or perturbative) approximation in the description of the electrostatic interaction among a larger number (~ 50) of electrons. In this paper, we present the classical and quantum algorithms together because they solve exactly the same many-particle Hamiltonian and both share many technical details (such a 3D Poisson solver to treat spatial-dependent permittivity scenarios) in their implementation into realistic 3D electron devices.

After this introduction, the rest of the paper is divided as follows. In Sec. II, we write the many-particle Hamiltonian for an ensemble of electrons in an open system. We discuss the role of the boundary conditions on the borders of the open system to include the Coulomb interaction between particles inside and outside of the open system in Sec. III. In Sec. IV, we discuss the solution of the many-particle Hamil-

tonian in classical scenarios. The path for the quantum solution is provided in Sec. V using quantum (Bohm) trajectories. In Sec. VI, we show the numerical results for the classical and quantum solutions of the many-particle Hamiltonian for nanoscale electron devices and we compare the results with time-dependent mean-field approximation. We conclude in Sec. VII. Appendixes A and B discuss the technical details of the image-charge method and mean-field approximation.

II. MANY-PARTICLE HAMILTONIAN IN OPEN SYSTEM

In this section, we develop an exact expression for the many-particle Hamiltonian that describes a set of electrons in an open system. Throughout this paper, we will assume that the magnetic field is negligible and that the particle velocity is small enough to assume a nonrelativistic behavior. In addition, in order to provide a discussion valid for either classical or quantum systems, we will assume spinless particles. Let us clarify that the exchange interaction is always present in a system of identical particles (electrons), but it will not be mentioned in this section because it does not affect explicitly the expression of the (first-quantization) many-particle Hamiltonians discussed here. The exchange interaction is introduced into the symmetry (when electron positions are interchanged) of the many-body wave function. We will briefly revisit this issue in Sec. V when dealing with the quantum solution.

A. Many-particle Hamiltonian for a closed system

First, we start our discussion with a set of M particles in a closed system. The many-particle Hamiltonian contains kinetic plus Coulomb energies,

$$H(\vec{r}_1, \dots, \vec{r}_M, \vec{p}_1, \dots, \vec{p}_M) = \sum_{k=1}^M \left\{ K(\vec{p}_k) + \frac{1}{2} \sum_{\substack{j=1 \\ j \neq k}}^M q_k \cdot V(\vec{r}_k, \vec{r}_j) \right\}. \quad (1)$$

The factor $\frac{1}{2}$ that appears in the second term of the right-hand side is due to the fact that each two-particle interaction is counted twice [i.e., $V(\vec{r}_k, \vec{r}_j)$ is identical to $V(\vec{r}_j, \vec{r}_k)$]. The condition $j \neq k$ takes into account the obvious restriction that a particle cannot interact with itself. The kinetic energy $K(\vec{p}_k)$ that appears in Eq. (1) is defined, for a classical system, as

$$K(\vec{p}_k) = \frac{1}{2 \cdot m_k} (\vec{p}_k)^2, \quad (2a)$$

while for a quantum system

$$K(\vec{p}_k) = -\frac{\hbar^2}{2 \cdot m_k} \nabla_{\vec{r}_k}^2. \quad (2b)$$

Let us notice that the position and momentum in Hamiltonian (1) can be either classical variables, \vec{r}_k and \vec{p}_k in Eq. (2a), or quantum (real-space representation) operators, \vec{r}_k and $-i\hbar \nabla_{\vec{r}_k}$ in Eq. (2b). In particular, it is important to emphasize that when we refer to \vec{r}_k as the electron position, we are not referring to a fixed position but a variable vector. On the

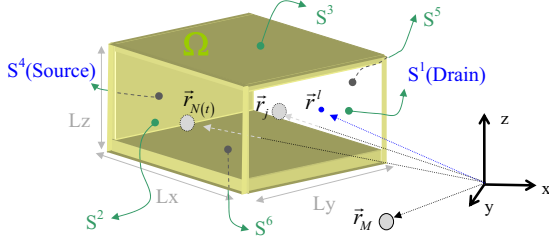


FIG. 1. (Color online) Schematic representation of the volume $\Omega = L_x \cdot L_y \cdot L_z$ and its limiting surface $S = \{S^1, S^2, \dots, S^6\}$. There are $N(t)$ particles inside and $M - N(t)$ outside this volume. The vector \vec{r}^l points an arbitrary position at the boundary surface S^l .

contrary, when we are interested in specifying a fixed electron position, we will write $\vec{r}_k[t]$. The parameter m_k is the particle mass that, in Sec. VI, will be understood as the particle effective mass. Identically, we define the Coulomb potential in Eq. (1) as

$$V(\vec{r}_k, \vec{r}_j) = \frac{q_j}{4\pi\epsilon|\vec{r}_k - \vec{r}_j|}, \quad (3)$$

where q_j is the particle charge and ϵ is the permittivity. Although we are always thinking about electrons in semiconductors, the development of this section is valid for arbitrary particles with different masses and charges.

A complete electronic circuit (including the devices, the wires, and the batteries) behaves as a closed system with a large ($M \rightarrow \infty$) number of electrons. However, since we can only deal with a finite number of electrons, we restrict our system to a small part of the circuit, for example, the channel of a transistor. Thus, we need to develop the Hamiltonian that describes the dynamics of a subensemble of the whole set of M particles in an open system inside a limited volume Ω (see Fig. 1).

B. Many-particle Hamiltonian for an open system

We divide the previous ensemble of M particles into a subensemble $\{1, 2, 3, \dots, N(t)\}$ of particles whose positions are inside the volume Ω and a second subensemble $\{N(t) + 1, \dots, M\}$ which are outside it (see Ref. 34). We assume that the number of particles inside, $N(t)$, is a time-dependent function that provides an explicit time dependence in the many-particle (open-system) Hamiltonian. As drawn in Fig. 1, we assume a parallelepiped where the six rectangular surfaces $S = \{S^1, S^2, \dots, S^6\}$ are the boundaries of Ω . Along this paper, we use \vec{r}^l as the ‘‘boundary’’ vector representing an arbitrary position on the surfaces S^l .

Since we are only interested in the dynamics of the first $N(t)$ particles, the kinetic energy and the Coulomb interaction between the particles of the second subensemble do not appear in the new Hamiltonian of the open system. Nevertheless, the Coulomb interaction between particles of the first and second subensembles must explicitly appear. Thus, the many-particle Hamiltonian for the first $N(t)$ particles can be written as

$$H(\vec{r}_1, \dots, \vec{r}_{N(t)}, \vec{p}_1, \dots, \vec{p}_{N(t)}, t) = \sum_{k=1}^{N(t)} \left\{ K(\vec{p}_k) + \frac{1}{2} \sum_{\substack{j=1 \\ j \neq k}}^{N(t)} q_k \cdot V(\vec{r}_k, \vec{r}_j) + \sum_{j=N(t)+1}^M q_k \cdot V(\vec{r}_k, \vec{r}_j) \right\}. \quad (4)$$

Let us notice also that the factor $\frac{1}{2}$ disappears in the last term of Eq. (4) because there is no double counting of interactions between electrons inside and outside Ω . For convenience, we rewrite Eq. (4) as

$$H(\vec{r}_1, \dots, \vec{r}_{N(t)}, \vec{p}_1, \dots, \vec{p}_{N(t)}, t) = \sum_{k=1}^{N(t)} \left\{ K(\vec{p}_k) + \sum_{\substack{j=1 \\ j \neq k}}^{N(t)} q_k \cdot V(\vec{r}_k, \vec{r}_j) + \sum_{j=N(t)+1}^M q_k \cdot V(\vec{r}_k, \vec{r}_j) - \frac{1}{2} \sum_{\substack{j=1 \\ j \neq k}}^{N(t)} q_k \cdot V(\vec{r}_k, \vec{r}_j) \right\}. \quad (5)$$

Although up to this point we have discussed the many-particle Hamiltonian in terms of the Coulomb force, this approach is inconvenient to deal with solid-state scenarios with a spatial-dependent permittivity.^{35,36} For this reason, we rewrite our many-particle Hamiltonian in terms of the more generic Poisson (or Laplace) equation, which can be applied to systems with (or without) a spatial-dependent permittivity [by substituting $\epsilon \rightarrow \epsilon(\vec{r})$ in the Poisson equation].

Each term $V(\vec{r}_k, \vec{r}_j)$ that appears in Eq. (5) can be explicitly obtained from a Poisson (or Laplace) equation inside the volume Ω . Then, using the superposition property of the Poisson (or Laplace) equations, we can rewrite Eq. (5) as

$$H(\vec{r}_1, \dots, \vec{r}_{N(t)}, \vec{p}_1, \dots, \vec{p}_{N(t)}, t) = \sum_{k=1}^{N(t)} \left\{ K(\vec{p}_k) + q_k \cdot W_k(\vec{r}_1, \dots, \vec{r}_{N(t)}, t) - \frac{1}{2} \sum_{\substack{j=1 \\ j \neq k}}^{N(t)} q_k \cdot V(\vec{r}_k, \vec{r}_j) \right\}, \quad (6)$$

where the term $W_k(\vec{r}_1, \dots, \vec{r}_k, \dots, \vec{r}_{N(t)})$ is a particular solution of the following Poisson equation:

$$\nabla_{\vec{r}_k}^2 \{ \epsilon \cdot W_k(\vec{r}_1, \dots, \vec{r}_{N(t)}) \} = \rho_k(\vec{r}_1, \dots, \vec{r}_{N(t)}). \quad (7)$$

The term $\rho_k(\vec{r}_1, \dots, \vec{r}_{N(t)})$ in Eq. (7) depends on the position of the first $N(t)$ electrons,³⁴

$$\rho_k(\vec{r}_1, \dots, \vec{r}_k, \dots, \vec{r}_{N(t)}) = \sum_{\substack{j=1 \\ j \neq k}}^{N(t)} q_j \cdot \delta(\vec{r}_k - \vec{r}_j), \quad (8)$$

but Eq. (8) is independent of the position of the external particles because they only affect the boundary conditions of Eq. (7). Let us notice that there are still terms, $V(\vec{r}_k, \vec{r}_j)$, in

Eq. (6) that are not computed from Poisson equation but from Eq. (3). However, we will show that these terms $V(\vec{r}_k, \vec{r}_j)$ have no role in the classical (i.e., Sec. IV) or quantum (i.e., Sec. V) solutions of Eq. (6).

By construction, comparing Eqs. (5) and (6), the term $W_k(\vec{r}_1, \dots, \vec{r}_{N(t)}, t)$ can be rewritten as

$$W_k(\vec{r}_1, \dots, \vec{r}_{N(t)}, t) = \sum_{j=1}^{N(t)} V(\vec{r}_k, \vec{r}_j) + \sum_{i=N(t)+1}^M V(\vec{r}_k, \vec{r}_i). \quad (9)$$

The dependence of $W_k(\vec{r}_1, \dots, \vec{r}_{N(t)}, t)$ on the positions of the external particles is explicitly written in the last sum in Eq. (9), while in Eq. (7) this dependence is hidden in the boundary conditions of $W_k(\vec{r}_1, \dots, \vec{r}_k, \dots, \vec{r}_{N(t)})$ on the surface $S = \{S^1, S^2, \dots, S^6\}$. In fact, the boundary conditions are a delicate issue that we will discuss in Sec. III. Finally, we want to remark that this discussion is valid for either classical or quantum Hamiltonians because the expression (9) [or its equivalent definition in (7) and (8)] of $W_k(\vec{r}_1, \dots, \vec{r}_{N(t)}, t)$ at $\vec{r}_1, \dots, \vec{r}_k, \dots, \vec{r}_{N(t)}$ is identical for a classical or a quantum system.

III. BOUNDARY CONDITIONS FOR THE ELECTROSTATIC POTENTIAL $W_k(\vec{r}_1, \dots, \vec{r}_{k-1}, \vec{r}, \vec{r}_{k+1}, \vec{r}_{N(t)}, t)$ ON THE BORDERS OF THE OPEN SYSTEM

Since we want to deal with solutions of the Poisson equation [Eq. (7)], the boundary conditions for the $N(t)$ terms $W_k(\vec{r}_1, \dots, \vec{r}_k, \dots, \vec{r}_{N(t)})$ have to be specified on the border surface $S = \{S^1, S^2, \dots, S^6\}$. Such boundary conditions will provide, somehow, information on the electrostatic effect that outside electrons [i.e., $N(t) + 1, \dots, M$] have on the electrons inside Ω . In order to provide a clear notation for discussing the boundary conditions of $W_k(\vec{r}_1, \dots, \vec{r}_k, \dots, \vec{r}_{N(t)})$, we distinguish between the “source” vectors $\vec{r}_1, \dots, \vec{r}_{k-1}, \vec{r}_{k+1}, \vec{r}_{N(t)}$ and the additional “observation” vector \vec{r} that runs over all space.³⁶ In particular, the electrostatic potential that appears in Hamiltonian (6) is defined as the value of the potential $W_k(\vec{r}_1, \dots, \vec{r}_{k-1}, \vec{r}, \vec{r}_{k+1}, \vec{r}_{N(t)}, t)$ at the particular position $\vec{r} = \vec{r}_k$,

$$W_k(\vec{r}_1, \dots, \vec{r}_{k-1}, \vec{r}_k, \vec{r}_{k+1}, \vec{r}_{N(t)}, t) = W_k(\vec{r}_1, \dots, \vec{r}_{k-1}, \vec{r}, \vec{r}_{k+1}, \vec{r}_{N(t)}, t)|_{\vec{r}=\vec{r}_k}. \quad (10)$$

Our goal is to find an educated guess for all the $N(t)$ terms $W_k(\vec{r}_1, \dots, \vec{r}_{k-1}, \vec{r}, \vec{r}_{k+1}, \vec{r}_{N(t)}, t)$ at all observation points $\vec{r} = \vec{r}^l$ on all surfaces $l = 1, \dots, 6$. For example, the information of such boundary conditions can come from the value of the total voltage (due to internal and external electrons) at position \vec{r}^l and time t . We define the total voltage $B(\vec{r}_1, \dots, \vec{r}_{N(t)}, \dots, \vec{r}_M, \vec{r}^l, t)$ as the electrostatic potential associated to an additional probe charge q_{M+1} situated on that boundary, $\vec{r}^l \equiv \vec{r}_{M+1} \in S^l$ (see Fig. 2). The electrostatic potential “seen” by this extra charge due to the presence of the rest of the particles is just

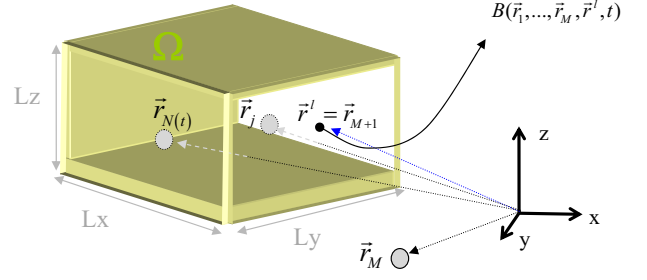


FIG. 2. (Color online) The electrostatic potential $B(\vec{r}_1, \dots, \vec{r}_{N(t)}, \dots, \vec{r}_M, \vec{r}^l, t)$ measured on a surface S^l at position \vec{r}^l and time t (due to internal and external electrons) by an additional probe charge q_{M+1} situated on the boundary $\vec{r}^l \equiv \vec{r}_{M+1} \in S^l$.

$$B(\vec{r}_1, \dots, \vec{r}_{N(t)}, \dots, \vec{r}_M, \vec{r}^l, t) \equiv \sum_{j=1}^M V(\vec{r}_{M+1}, \vec{r}_j)|_{\vec{r}_{M+1}=\vec{r}^l}, \quad (11)$$

where the expected restriction $j \neq M+1$ is hidden in the limit of the sum.

Once relationship (11) is established, we can easily define the boundary conditions of any of the $N(t)$ electrostatic potential $W_k(\vec{r}_1, \dots, \vec{r}, \dots, \vec{r}_{N(t)})$ from the function $B(\vec{r}_1, \dots, \vec{r}_{N(t)}, \dots, \vec{r}_M, \vec{r}^l, t)$. In particular, from Eq. (9), we know that

$$W_k(\vec{r}_1, \dots, \vec{r}_{k-1}, \vec{r}, \vec{r}_{k+1}, \vec{r}_{N(t)}, t)|_{\vec{r}=\vec{r}^l} = \sum_{j=1}^M V(\vec{r}^l, \vec{r}_j) = B(\vec{r}_1, \dots, \vec{r}_M, \vec{r}^l, t) - V(\vec{r}^l, \vec{r}_k), \quad l = 1, \dots, 6. \quad (12)$$

The discussion done here is valid for either classical or quantum systems (see Ref. 37). In the previous discussion we have assumed Dirichlet boundary conditions; however it is a straightforward procedure to develop the same argumentations for Neumann boundary conditions.

The reader can be surprised by the fact that the right-hand side of expression (12) tends to infinite, $V(\vec{r}^l, \vec{r}_k) \rightarrow \infty$, when $\vec{r}_k \rightarrow \vec{r}^l$. However, when $\vec{r}_k \rightarrow \vec{r}^l$, the extra particle at $\vec{r}^l \equiv \vec{r}_{M+1} \in S_l$ will also provide an infinite value of the electrostatic potential, i.e., $B(\vec{r}_1, \dots, \vec{r}_{N(t)}, \dots, \vec{r}_M, \vec{r}^l, t) \rightarrow \infty$, due to the presence of the k particle on the surface. Therefore, the first infinite, $V(\vec{r}^l, \vec{r}_k) \rightarrow \infty$, is canceled by the second infinite, $B(\vec{r}_1, \dots, \vec{r}_{N(t)}, \dots, \vec{r}_M, \vec{r}^l, t) \rightarrow \infty$. This discussion will be relevant in Sec. VI when we discuss the numerical implementation of these boundary conditions.

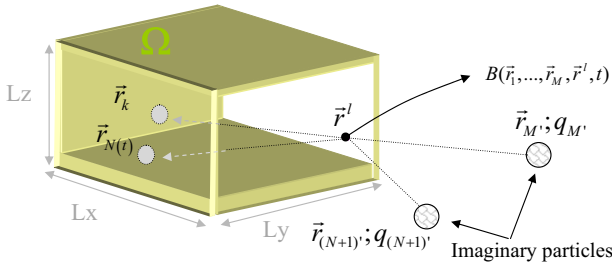


FIG. 3. (Color online) The imaginary charges $q_{(N+1)'}$ and $q_{M'}$, located outside the volume Ω at $\vec{r}_{(N+1)'}$ and $\vec{r}_{M'}$, together with the real particles inside Ω reproduce the electrostatic potential $B(\vec{r}_1, \dots, \vec{r}_{N(t)}, \dots, \vec{r}_M, \vec{r}^l, t)$ on all l surfaces.

Up to here, our argumentation might seem somehow tricky. We have defined the value of $W_k(\vec{r}_1, \dots, \vec{r}, \dots, \vec{r}_M)|_{\vec{r}=\vec{r}^l}$ on the volume boundaries without mentioning the position of the external particles but using the function $B(\vec{r}_1, \dots, \vec{r}_{N(t)}, \dots, \vec{r}_M, \vec{r}^l, t)$ which is unknown. This strategy transforms the complexity of finding the boundary conditions of $N(t)$ electrostatic potential $W_k(\vec{r}_1, \dots, \vec{r}, \dots, \vec{r}_{N(t)})$ into providing an educated guess for a unique function $B(\vec{r}_1, \dots, \vec{r}_{N(t)}, \dots, \vec{r}_M, \vec{r}^l, t)$. In our numerical results in Sec. VI, we will fix $B(\vec{r}_1, \dots, \vec{r}_{N(t)}, \dots, \vec{r}_M, \vec{r}^l, t)$ based on standard arguments for electron devices. We will assume a uniform value of the voltage on the l surface independent of the external electrons, $B(\vec{r}_1, \dots, \vec{r}_{N(t)}, \dots, \vec{r}_M, \vec{r}^l, t) \approx B^l(\vec{r}_1, \dots, \vec{r}_{N(t)}, t)$. Such value can be obtained taken into account the voltage fixed by the external battery and the requirement of charge neutrality at the contacts.^{35,38}

Finally, we want to enlighten the physical interpretation of the many-particle Hamiltonian (6) and boundary conditions of Eq. (12) developed here. To do this, we compare our approach with the image-charge method applied to electron transport. The image-charge method is a basic solving tool in electrostatics³⁶ that has been successfully applied, for example, in the calculation of the electric field in field-emission devices³⁹ or the barrier-reduction in the metal-semiconductor Schottky contacts.⁴⁰ The name of the method originates from the replacement of certain “real” charges by a set of few “imaginary” charges that replicate the real boundary conditions at the surface (see Fig. 3). From the uniqueness theorem of electrostatics,³⁶ once the charge of the $1, \dots, N(t)$ particles inside a volume is fixed and the correct electrostatic potential (or electric field) is specified at the boundaries of that volume, $B(\vec{r}_1, \dots, \vec{r}_{N(t)}, \dots, \vec{r}_M, \vec{r}^l, t)$, the solution of the Poisson equation inside the volume is unique and does not depend on whether the external charges are real or imaginary. Then, according to the image-charge method, the electrostatic potential seen by the k particle is equal to the electrostatic potential generated by the sum of the imaginary plus the real particles except the k particle. Thus, identically to our many-particle Hamiltonian, the image-charge method goes beyond the mean-field approximation (discussed in Appendix B) because each particle feels its own potential profile that excludes the Coulomb interaction with itself. In Appendix A, we show in detail that the boundary conditions in

Eq. (12) are identical to the boundary conditions found with the image-charge method.

However, although the outcome of the image-charge method and our many-particle Hamiltonian are identical, the Hamiltonian presented in this paper has an unquestionable advantage over the image-charge method: the former can be directly implemented into practical 3D electron device simulators as we will see in Sec. VI while the latter cannot. For example, let us consider the numerical simulation of the transistor done in Sec. VI. The system consists in a large number (~ 20) of electrons inside a volume Ω limited by surfaces $\{S^1, S^2, \dots, S^6\}$ with Dirichlet and Neumann boundary conditions. Then, the exact application of the image-charge method faces up to the following serious difficulties. The computation of the imaginary charges in an arbitrary surface (different from the standard infinite plane whose imaginary charges are found in textbooks⁴¹) is not at all obvious.⁴² Let us notice that each imaginary charge that provides the correct value of the Neumann boundary condition on S^i does also affect the Neumann (or Dirichlet) boundary condition on all other surfaces $\{S^1, S^2, \dots, S^6\}$. Finally, even after assuming that we would be able to find somehow the density distribution of imaginary charges that reproduces simultaneously the boundary conditions on all six surfaces, the practical application of this method in a time-dependent simulator with a 3D Poisson solver (to be able to deal with spatial-dependent permittivity scenarios) would require simulating much more particles (the real plus the imaginary) in a larger simulation box (to include the location of those imaginary particles outside of Ω). In summary, the image-charge method is an excellent approach to obtain analytical expression for the many-body description of electron transport in simple systems (such as one electron crossing an infinite ideal⁴¹ metallic surface), but it is not practically possible to implement it in simulators for actual 3D electron devices.⁴² On the contrary, as we will show in our numerical result in Sec. VI, the many-particle Hamiltonian (6) and the boundary conditions of Eq. (12) can be implemented in an extremely simple and transparent way in, either classical or quantum, realistic electron device simulators using a 3D Poisson solver for arbitrary surfaces.

IV. EXACT MANY-PARTICLE HAMILTONIAN FOR CLASSICAL OPEN SYSTEMS

In this section, we discuss the classical solution of the many-particle open-system Hamiltonian of expression (6). Interestingly, the results obtained here can partially be used for the quantum solution of the many-particle Hamiltonian developed in Sec. V.

The classical description of the particle dynamics subjected to the many-particle Hamiltonian (6) can be computed by using the well-known Hamilton’s equations. In particular, we can obtain the (Newton-type) description of the classical trajectory $\vec{r}_i[t]$ in the real space through

$$\frac{d\vec{p}_i[t]}{dt} = [-\nabla_{\vec{r}_i} H(\vec{r}_1, \dots, \vec{r}_{N(t)}, \vec{p}_1, \dots, \vec{p}_{N(t)}, t)]_{\vec{r}_1=\vec{r}_1[t], \dots, \vec{p}_{N(t)}=\vec{p}_{N(t)}[t]}, \quad (13a)$$

$$\frac{d\vec{r}_i[t]}{dt} = [\nabla_{\vec{p}_i} H(\vec{r}_1, \dots, \vec{r}_{N(t)}, \vec{p}_1, \dots, \vec{p}_{N(t)}, t)]_{\vec{r}_1=\vec{r}_1[t], \dots, \vec{p}_{N(t)}=\vec{p}_{N(t)}[t]}. \quad (13b)$$

For the many-particle Hamiltonian studied in this work, expression (13b) gives the trivial result $m \cdot \vec{v}_i[t] = \vec{p}_i[t]$, while the evaluation of expression (13a) requires a detailed development. We know that the \vec{r}_i gradient of the exact many-particle Hamiltonian (6) can be written as

$$[\nabla_{\vec{r}_i} H]_{\vec{R}=\vec{R}[t]} = \left[\nabla_{\vec{r}_i} \sum_{k=1}^{N(t)} \left\{ q_k \cdot W_k(\vec{r}_1, \dots, \vec{r}_{N(t)}, t) - \frac{1}{2} \sum_{\substack{j=1 \\ j \neq k}}^{N(t)} q_k \cdot V(\vec{r}_k, \vec{r}_j) \right\} \right]_{\vec{R}=\vec{R}[t]}. \quad (14)$$

We define the multidimensional vector $\vec{R} = (\vec{r}_1, \dots, \vec{r}_{N(t)})$ to account, in a compact way, for the classical trajectories of $N(t)$ electrons, $\vec{R}[t] = (\vec{r}_1[t], \dots, \vec{r}_{N(t)}[t])$. Substituting the definition of $W_k(\vec{r}_1, \dots, \vec{r}_{N(t)}, t)$ done in expression (9) into Eq. (14), we find

$$[\nabla_{\vec{r}_i} H]_{\vec{R}=\vec{R}[t]} = \left[\nabla_{\vec{r}_i} \left\{ 2 \sum_{\substack{j=1 \\ j \neq i}}^{N(t)} q_j V(\vec{r}_j, \vec{r}_i) + \sum_{j=N(t)+1}^M q_j V(\vec{r}_j, \vec{r}_i) \right\} - \nabla_{\vec{r}_i} \sum_{\substack{j=1 \\ j \neq i}}^{N(t)} q_j \cdot V(\vec{r}_j, \vec{r}_i) \right]_{\vec{R}=\vec{R}[t]}. \quad (15)$$

Note the elimination of the factor $\frac{1}{2}$ in the last term of the right-hand part of Eq. (15) that accounts for those terms $q_k \cdot V(\vec{r}_k, \vec{r}_i)$ in Eq. (14), where $\vec{r}_k \neq \vec{r}_i$ and $\vec{r}_j = \vec{r}_i$ that are identical to the term $q_i \cdot V(\vec{r}_i, \vec{r}_i)$ in Eq. (15). For the same reason, we include a factor 2 on the first term of right hand of Eq. (15). From expressions (9) and (15), we realize that

$$[\nabla_{\vec{r}_i} H]_{\vec{R}=\vec{R}[t]} = [\nabla_{\vec{r}_i} W_i(\vec{r}_1, \dots, \vec{r}_{N(t)})]_{\vec{R}=\vec{R}[t]}. \quad (16)$$

Only the term $W_i(\vec{r}_1, \dots, \vec{r}_{N(t)})$ of whole Hamiltonian (6) becomes relevant for a classical description of the i particle. In fact, since we only evaluate a \vec{r}_i gradient, the rest of particle positions can be evaluated at their particular value at time t , i.e., $\vec{r}_k \rightarrow \vec{r}_k[t]$ for all $k \neq i$. Therefore, we define the single-particle potential $\bar{W}_i(\vec{r}_i, t)$ from the many-particle potential as

$$\bar{W}_i(\vec{r}_i, t) = W_i(\vec{r}_1[t], \dots, \vec{r}_{i-1}[t], \vec{r}_i, \vec{r}_{i+1}[t], \dots, \vec{r}_{N(t)}[t]). \quad (17)$$

We use a “hat” to differentiate the (time-dependent) single-particle electrostatic potential from the many-particle poten-

tial. Each i term of the single-particle electrostatic potential, $\bar{W}_i(\vec{r}_i, t)$, is a solution of one particular 3D-Poisson equation,

$$\nabla_{\vec{r}_i}^2 [\varepsilon(\vec{r}_i) \cdot \bar{W}_i(\vec{r}_i, t)] = \bar{\rho}_i(\vec{r}_i, t), \quad (18)$$

where the single-particle charge density is defined as

$$\bar{\rho}_i(\vec{r}_i, t) = \sum_{\substack{j=1 \\ j \neq i}}^{N(t)} q_j \delta(\vec{r}_i - \vec{r}_j[t]), \quad (19)$$

and the boundary conditions [Eq. (12)] are adapted here as

$$\begin{aligned} \bar{W}_i(\vec{r}_i, t)|_{\vec{r}_i=\vec{r}^l} &= B^l(\vec{r}_1[t], \dots, \vec{r}_{N(t)}[t], t) - V(\vec{r}^l, \vec{r}_i[t]), \\ l &= 1, \dots, 6. \end{aligned} \quad (20)$$

where we have included the approximation $B(\vec{r}_1, \dots, \vec{r}_{N(t)}, \dots, \vec{r}_M, \vec{r}', t) \approx B^l(\vec{r}_1, \dots, \vec{r}_{N(t)}, t)$ mentioned in Sec. III. Let us remind that expressions (17)–(20) provide an exact treatment of the many-particle correlations in classical scenarios. They imply a coupled system of Newton equations. The $N(t)$ Newton equations are coupled by $N(t)$ Poisson equations. Therefore, as mentioned in Sec. I, the many-particle Hamiltonian of Eq. (6) can be written exactly (without mean-field approximation) as a sum of single-particle Hamiltonian for classical scenarios,

$$H(\vec{r}_1, \dots, \vec{r}_{N(t)}, \vec{p}_1, \dots, \vec{p}_{N(t)}, t) = \sum_{k=1}^{N(t)} \{K(\vec{p}_k) + q_k \cdot \bar{W}_k(\vec{r}_k, t)\}. \quad (21)$$

The term $\bar{W}_k(\vec{r}_k, t)$ in Eq. (21) means that each particle “sees” its own electrostatic potential (or electric field), which is different from that of others.

V. EXACT MANY-PARTICLE HAMILTONIAN FOR QUANTUM OPEN SYSTEMS

The many-particle open-system Hamiltonian developed in expression (6) is also valid for quantum systems. In this section, we will explain its practical quantum solution using the recent quantum (Bohm) trajectory formalism in Ref. 33. For convenience, we rewrite the many-particle Hamiltonian in Eq. (6) as

$$H(\vec{r}_1, \dots, \vec{r}_{N(t)}, t) = \left\{ \sum_{k=1}^{N(t)} -\frac{\hbar^2}{2 \cdot m_k} \nabla_{\vec{r}_k}^2 + U(\vec{r}_1, \dots, \vec{r}_{N(t)}, t) \right\}, \quad (22)$$

where we explicitly write the electron momentum as $\vec{p}_k = -i\hbar \nabla_{\vec{r}_k}$ in the kinetic energy [as mentioned in Eq. (2b)]. According to Eq. (6), the many-particle electrostatic potential $U(\vec{r}_1, \dots, \vec{r}_{N(t)}, t)$ is defined as

$$U(\vec{r}_1, \dots, \vec{r}_{N(t)}, t) = \sum_{k=1}^{N(t)} \left\{ q_k \cdot W_k(\vec{r}_1, \dots, \vec{r}_{N(t)}, t) - \frac{1}{2} \sum_{\substack{j=1 \\ j \neq k}}^{N(t)} q_k \cdot V(\vec{r}_k, \vec{r}_j) \right\}. \quad (23)$$

Then, the many-particle time-dependent Schrödinger equation that provides the many-particle wave function, $\Phi(\vec{r}_1, \dots, \vec{r}_{N(t)}, t)$, which describes the electron dynamics associated to our many-particle (open-system) Hamiltonian, is

$$i\hbar \frac{\partial \Phi(\vec{r}_1, \dots, \vec{r}_{N(t)}, t)}{\partial t} = \left\{ \sum_{k=1}^{N(t)} -\frac{\hbar^2}{2 \cdot m} \nabla_{\vec{r}_k}^2 + U(\vec{r}_1, \dots, \vec{r}_{N(t)}, t) \right\} \cdot \Phi(\vec{r}_1, \dots, \vec{r}_{N(t)}, t). \quad (24)$$

The practical utility of expression (24) in understanding quantum scenarios can seem quite doubtful because its direct solution becomes computationally inaccessible for more than very few electrons.^{1,2,43} However, one of the authors has recently developed a transport formalism³³ in terms of Bohm trajectories that simplifies the complexity of evaluating Eq. (24).

Some introductory explanations about Bohm trajectories in single-particle and many-body scenarios can be found in Refs. 44–47. Here, we go directly to the main result of Ref. 33 where it is shown that a many-particle electron Bohm trajectory $\vec{r}_a[t]$ computed from the many-particle wave function, $\Phi(\vec{r}_1, \dots, \vec{r}_{N(t)}, t)$, solution of the Eq. (24) can be equivalently computed from the single-particle wavefunction $\Psi_a(\vec{r}_a, t)$ solution of the following single-particle Schrödinger equation:

$$i\hbar \frac{\partial \Psi_a(\vec{r}_a, t)}{\partial t} = \left\{ -\frac{\hbar^2}{2 \cdot m} \nabla_{\vec{r}_a}^2 + U_a(\vec{r}_a, \vec{R}_a[t], t) + G_a(\vec{r}_a, \vec{R}_a[t], t) + i \cdot J_a(\vec{r}_a, \vec{R}_a[t], t) \right\} \Psi_a(\vec{r}_a, t), \quad (25)$$

where we have defined $\vec{R}_a[t] = \{\vec{r}_1[t], \vec{r}_{a-1}[t], \vec{r}_{a+1}[t], \vec{r}_N[t], t\}$ as a vector that contains all Bohm trajectories except $\vec{r}_a[t]$. The exact definition of the other potentials that appear in Eq. (25), $G_a(\vec{r}_a, \vec{R}_a[t], t)$ and $J_a(\vec{r}_a, \vec{R}_a[t], t)$, can be obtained from Ref. 33. The total many-particle electrostatic potential in Eq. (24) has been divided into two parts,

$$U(\vec{r}_a, \vec{R}_a[t], t) = U_a(\vec{r}_a, \vec{R}_a[t], t) + U_b(\vec{R}_a[t], t). \quad (26)$$

From expressions (9) and (23), we realize that $U_a(\vec{r}_a, \vec{R}_a[t], t)$ can be greatly simplified as

$$U_a(\vec{r}_a, \vec{R}_a[t], t) = 2 \sum_{\substack{j=1 \\ j \neq a}}^{N(t)} q_a \cdot V(\vec{r}_a, \vec{r}_j[t]) + \sum_{i=N(t)+1}^M q_a \cdot V(\vec{r}_a, \vec{r}_i[t]) - \sum_{\substack{j=1 \\ j \neq a}}^{N(t)} q_a \cdot V(\vec{r}_a, \vec{r}_j[t]) = \bar{W}_a(\vec{r}_a, \vec{R}_a[t], t). \quad (27)$$

The rest of the terms $V(\vec{r}_j[t], \vec{r}_i[t])$ of expression (26) appear in $U_b(\vec{R}_a[t], t)$ and they are included in the potential $G_a(\vec{r}_a, \vec{R}_a[t], t)$. However, this term $U_b(\vec{R}_a[t], t)$ has no role on the single-particle wave function $\Psi_a(\vec{r}_a, t)$ because it has no dependence on \vec{r}_a and it only introduces an irrelevant global phase on $\Psi_a(\vec{r}_a, t)$.

Let us notice that, in the right-hand side of expression (27), we have used the same definition of the potential profile as in classical expression (17). The only difference here is that $\vec{R}_a[t]$ are not classical trajectories but quantum (Bohm) trajectories. Therefore, the computation of the potential profile $\bar{W}_a(\vec{r}_a, \vec{R}_a[t], t)$ that appears in the single-particle Schrödinger equation [Eq. (25)] just needs 3D Poisson equations [Eqs. (18) and (19)] with the boundary conditions [Eq. (20)]. Interestingly, since the term $\bar{W}_a(\vec{r}_a, \vec{R}_a[t], t)$ is computed from a Poisson equation, our quantum-trajectory algorithm can also be directly extended to spatial-dependent permittivity systems.

In fact, in order to effectively solve the Schrödinger equation [Eq. (25)], we need to know the position of the rest of Bohm particles $\vec{R}_a[t] = \{\vec{r}_1[t], \vec{r}_{a-1}[t], \vec{r}_{a+1}[t], \vec{r}_N[t], t\}$. Therefore, all $N(t)$ Bohm trajectories have to be computed simultaneously within a system of $N(t)$ Schrödinger equations coupled by $N(t)$ Poisson equations. The keystone of our quantum-trajectory algorithm is that, in order to find $\vec{r}_a[t]$, we do not have to evaluate the electrostatic potential, $U(\vec{r}_1, \dots, \vec{r}_{N(t)}, t)$, and the wave function, $\Phi(\vec{r}_1, \dots, \vec{r}_{N(t)}, t)$, everywhere in the N -multidimensional configuration space $\{\vec{r}_1, \dots, \vec{r}_a, \dots, \vec{r}_{N(t)}, t\}$, but only over a smaller number of configuration points where all positions of electrons are fixed, $\vec{R}_a[t]$, except \vec{r}_a , i.e., $\{\vec{r}_1[t], \dots, \vec{r}_a, \dots, \vec{r}_{N(t)}[t], t\}$. We want to remark that the full (short- and long-range) Coulomb interaction present in Eq. (6) is considered explicitly in Eq. (25) without any (mean-field or perturbative) approximation.

Finally, according to the summary done in Sec. I of this work, we want to emphasize the similarities between the (open-system) Bohm-trajectory computational algorithm discussed in Ref. 33 and the (electron-transport version) density-functional theory mentioned in Sec. I. For the latter, the decomposition of the many-particle system into a set of coupled single-particle Schrödinger equations is exact and demonstrated by the Hohenberg-Kohn-Sham theorem.^{6,7} However, from a practical point of view, the exact exchange-correlation functionals that appear in the single-particle

D Schrödinger equations are unknown and, therefore, require some approximation. Identically, in the quantum (Bohm) trajectory algorithm, the use of single-particle Schrödinger equation [Eq. (25)] is exact to treat many-particle system as demonstrated in the theorem considered in Ref. 33. However, the exact values of the terms $G_a(\vec{r}_a, \vec{R}_a[t], t)$ and $J_a(\vec{r}_a, \vec{R}_a[t], t)$ that appear in Hamiltonian (25) are unknown (because they require the partial knowledge of the shape of the many-particle wave function). Thus, from a practical point of view, they need to be approximated by some educated guess as in the density-functional theory.

Finally, the exchange interaction among the (fermions) electrons can also be considered in the present quantum algorithm. A brief explanation of how the exchange interaction can be introduced in the present quantum (Bohm) trajectory algorithm is mentioned in Ref. 33, but the discussion of this issue is far from the goal of the present paper.

VI. NUMERICAL RESULTS FOR THE MANY-PARTICLE HAMILTONIAN IN CLASSICAL AND QUANTUM ELECTRON DEVICES

In Secs. I–V of this paper, a many-particle Hamiltonian has been developed for an arbitrary ensemble of particles with Coulomb interaction among them. In this section, our numerical examples will deal with electrons in solid-state semiconductors. Therefore, first of all, we have to specify under what approximations the theoretical many-particle Hamiltonian developed in the first part can be used to describe solid-state semiconductors. Only the dynamics of the free electrons will be studied in our numerical results. The interaction with the rest of the charges (associated to core electrons and ions) will be considered as average polarization charges via a spatial-dependent permittivity.³⁶ We do also assume an effective mass⁴⁸ for the free electrons that accounts for their interaction with the periodic atomic structure under the standard Born-Oppenheimer approximation⁴⁹ (that neglects the interaction of valence electrons with other kind of particle such as phonons). These are reasonable approximations in most electron-transport models of ballistic devices.^{12,27}

We solve the many-particle (open-system) Hamiltonian from expression (6) to compute the current-voltage characteristic for classical and quantum electron devices. We use the classical algorithm discussed in Sec. IV for the simulation of a double-gate field-effect transistor⁵⁰ (DG-FET), while we use the quantum algorithm discussed in Sec. V for a resonant tunneling diode⁴⁷ (RTD). As mentioned above, no phonon, impurity, or roughness scattering mechanism is included in the simulations and only the full Coulomb interaction is considered explicitly. In order to emphasize the importance of our treatment of the electron-electron correlations in such nanoscale devices, we will compare these current-voltage characteristics with the results obtained with a time-dependent “mean-field” approach that will be discussed in Appendix B. We refer to “many-electron” results to describe the simulation done with either classical (Sec. IV) or quantum (Sec. V) algorithms that requires solving $N(t)$ Poisson equations with $N(t)$ different boundary con-

ditions and charge densities [expressions (17)–(20)] at each time step. Alternatively, we refer to the time-dependent “mean-field” results when a single Poisson equation [expressions (B1)–(B4)] is solved for all electrons at each time step of the simulation.

For all simulations (quantum, classical, mean field, or many electron), the same electron injection model is used. We use an injection model applicable to systems with arbitrary electron confinement, which is a time-dependent version of the Landauer boundary conditions, valid for degenerate and nondegenerate systems. We inject electrons according to the Fermi-Dirac statistics defined by a Fermi level (an electrochemical potential) deep inside the contacts.³⁸ The applied bias provides a difference between the values of the Fermi level at each injecting surface. Our injection model, coupled to the boundary conditions of the Poisson equation, also ensures charge neutrality at the contacts.³⁵

All simulations use a 3D finite-difference Poisson solver scheme. The whole volume Ω of the active region drawn in Fig. 1 is divided into $N_x \cdot N_y \cdot N_z$ cells. Each 3D cell has spatial dimensions of DX , DY , and DZ . Thus, the active region of our simulating device has a volume equal to $(N_x \cdot DX) \cdot (N_y \cdot DY) \cdot (N_z \cdot DZ) = L_x \cdot L_y \cdot L_z$. The boundary conditions of the Poisson equation on the six rectangular surfaces $S = \{S^1, S^2, \dots, S^6\}$ of Fig. 1 are defined using either Dirichlet or Neumann arguments. In general, on the surfaces S_2, S_3, S_5 , and S_6 , Neumann boundary conditions are used with the educated guess that the component of the electric field normal to the surface is zero there, $\vec{E}^j(\vec{r}^j, t) \cdot \vec{n}^j = 0$, where \vec{n}^j is a unit vector normal to the mentioned surfaces and pointing outward. The continuity of the displacement vector normal to surfaces justifies the assumption $\vec{E}^j(\vec{r}^j, t) \cdot \vec{n}^j = 0$ at the boundaries when the relative permittivity inside Ω is much higher than the corresponding value outside. On the other hand, in the surfaces S_1 and S_4 of Fig. 1 we use the Dirichlet boundary conditions discussed in Sec. III, $B^l(\vec{r}_1, \dots, \vec{r}_{N(t)}, t)$, with final expression (20).

Finally, a technical remark about the application of expression (20) in the classical or quantum many-electron simulations is mandatory. Strictly speaking, our assumption that the potential at one particular surface is position independent, $B(\vec{r}_1, \dots, \vec{r}_{N(t)}, \dots, \vec{r}_M, \vec{r}^j, t) \approx B^l(\vec{r}_1, \dots, \vec{r}_{N(t)}, t)$, is not completely accurate because we known from the discussion in Sec. III that the original function $B(\vec{r}_1, \dots, \vec{r}_{N(t)}, \dots, \vec{r}_M, \vec{r}^j, t)$ in expression (11) has to reproduce, somehow, the atomistic charge distribution on the surface.⁴¹ In particular, one can expect $B(\vec{r}_1, \dots, \vec{r}_{N(t)}, \dots, \vec{r}_M, \vec{r}^j, t) \rightarrow \infty$ when the electron is close to the border, $\vec{r}_k \rightarrow \vec{r}^j$. However, due to our ignorance about the atomistic description of the contact interface,⁴¹ we apply the boundary conditions [Eq. (20)] assuming that the distance between \vec{r}_k and \vec{r}^j is always greater than 1 nm (this value is interpreted as a measure of range of the atomistic pseudopotential² in the spatial-dependent permittivity scenarios discussed here).

A. Classical simulation of two-electron system: Many electron versus mean field

In this section we will explain the origin of the important differences that will appear later between the mean-field and

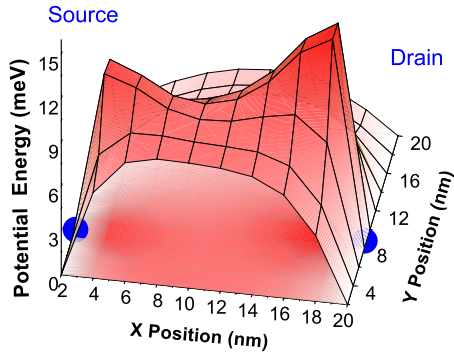


FIG. 4. (Color online) Potential energy profile $\bar{W}_{\text{mean}}(\vec{r}, t)$ computed with a 3D Poisson solver using the classical mean-field approximation on the plane X - Y of the active region $\Omega=(20 \text{ nm})^3$ at $z=6 \text{ nm}$ at 0.4 fs . The solid points are electron positions.

many-electron algorithms using a simple semiclassical two-electron system. We consider one electron (labeled as one electron) injected from the source surface, S_4 , at an arbitrary position. A second electron is injected, arbitrarily, from the drain surface, S_1 . A battery provides an external voltage equal to zero at the drain and source surfaces. A 3D cubic system with a volume of $\Omega=(20 \text{ nm})^3$ is considered as the active device region. We consider silicon parameters for the numerical simulation. Within the mean-field approximation only the potential profile $\bar{W}_{\text{mean}}(\vec{r}, t)$ is calculated for the two-electron system using expressions (B1)–(B4). Then, we realize from Fig. 4 that each electron can be reflected by an artificial alteration of the potential profile related to its own charge. In Figs. 5 and 6 we have plotted the energy potential profile seen by the one electron, $\bar{W}_1(\vec{r}_1, t)$, and by the two electron, $\bar{W}_2(\vec{r}_2, t)$, using the many-electron algorithm described by expressions (17)–(20). Electrons are not affected by their own charge. We clearly see that, within the mean-field approximation, electrons can be unable to overcome the large potential barrier that appears at their own position (due to their own charge). In addition, the simple results confirm that the mean-field error is equal to expression (B7), i.e., the

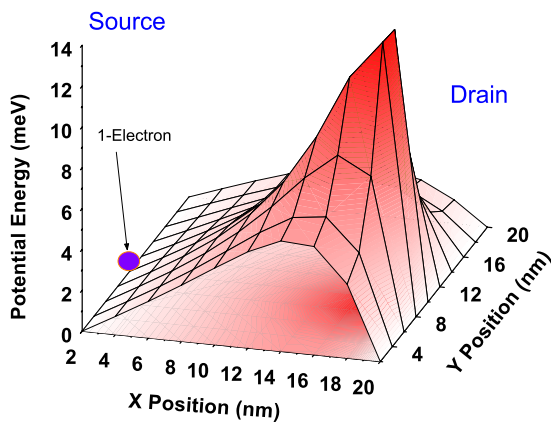


FIG. 5. (Color online) Potential energy profile of the one electron, $\bar{W}_1(\vec{r}_1, t)$, with the many-electron algorithm in the plane X - Y of the active region $\Omega=(20 \text{ nm})^3$ at $z=6 \text{ nm}$ at 0.4 fs . The solid point is the one-electron position.

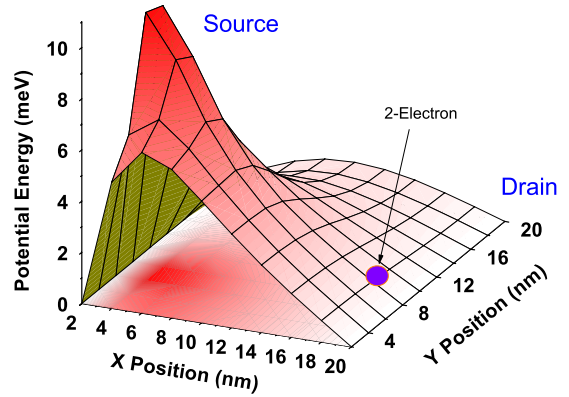


FIG. 6. (Color online) Potential energy profile of the two electron, $\bar{W}_2(\vec{r}_2, t)$, with the many-electron algorithm in the plane X - Y of the active region $\Omega=(20 \text{ nm})^3$ at $z=6 \text{ nm}$ at 0.4 fs . The solid point is the two-electron position.

error of the mean-field potential profile at each position of the active region is $\text{Error}_k(\vec{r}, t) = V(\vec{r}, \vec{r}_k[t])$.

Finally, a discussion about the role of the spatial mesh used for the numerical solution of the Poisson equation is relevant. For an electron device with a length of hundreds of nanometers, we need a mesh of the 3D active region with spatial step $DX \sim DY \sim DZ > 10 \text{ nm}$ to deal with not more than 1000 nodes in the numerical solution of the Poisson equation. This computational limitation in the resolution of the potential is present when solving either the mean-field or the many-electron algorithm. With such spatial resolution, the short-range interaction is missing in both procedures because two electrons inside the same spatial cell will not repel each other. In addition, the error between both procedures, $\text{Error}_k(\vec{r}, t) = V(\vec{r}, \vec{r}_k[t])$, is reduced because the numerical Coulomb potential profile is smoothed due to the low resolution [i.e., the diameter of the region where $V(\vec{r}, \vec{r}_k[t])$ has a strong influence is shorter than the cell dimensions]. Therefore, we obtain roughly identical results with both schemes. In the subplots of Fig. 7, the same electron trajectory is presented for different mesh resolutions. As can be seen, for the best mesh resolution ($DX=DY=DZ=2 \text{ nm}$), the differences between both treatments are maximized due to the important spurious autoreflexion effect found in the mean-field trajectory. On the other hand, as the resolution of our mesh is reduced, differences between both treatments disappear, giving roughly equal trajectories for cell dimensions above 5 nm .

In summary, when the spatial cells are large, the mean-field and the many-electron schemes correctly model the long-range Coulomb interaction, but both neglect the short-range component. On the contrary, with smaller spatial steps $DX \sim DY \sim DZ < 5 \text{ nm}$, the many-electron resolution takes into account long- and short-range Coulomb interactions correctly, whereas the description of the short-range component within the mean-field approximation is completely incorrect (i.e., electrons are repelled by themselves). In other words, when $DX, DY, DZ \rightarrow 0$ the mesh error in our many-electron algorithm reduces to zero, while the error in the mean-field approach tends to infinite, $\text{Error}_k(\vec{r}, t) \rightarrow \infty$ (see a schematic summary of the explanation of this discussion in Fig. 8).

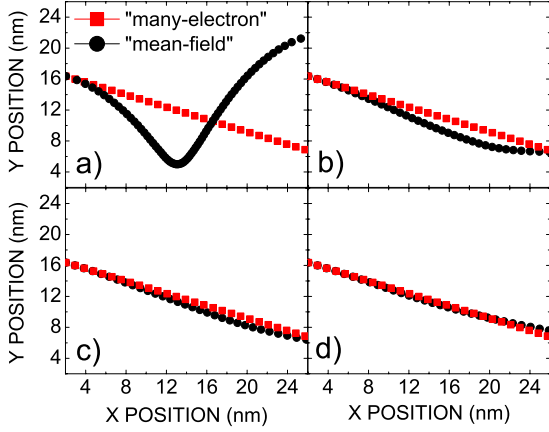


FIG. 7. (Color online) Electron trajectory computed with the mean-field (circles) and the many-electron (squares) algorithms for four different mesh resolutions. (a) $DX=DY=DZ=2$ nm, (b) $DX=DY=DZ=4$ nm, (c) $DX=DY=DZ=6$ nm, and (d) $DX=DY=DZ=8$ nm.

Finally, it is important to remark that the electron trajectories in Fig. 7 are computed using the classical scheme of Sec. IV, but the electrostatic potential profiles are computed from a 3D Poisson solver that is identical for the classical or quantum algorithms. Therefore, the conclusions drawn here for the classical algorithm can be directly extrapolated to our quantum algorithm. In the classical algorithm, the wrong potential profile of Fig. 4 affects the electric field [Eqs. (13a) and (13b)] that modifies the electron dynamics. Identically, the wrong mean-field potential in expression (25) will affect the solution of the Schrödinger equation that will modify Bohm trajectories.

B. Classical simulation of a double-gate field-effect transistor

Now, we use the classical solution of the many-particle Hamiltonian (6) to provide a full simulation⁵¹ for the DG-FET depicted in Fig. 9. Electron transport in the x direction (from source to drain) takes place along a silicon (100) orientation channel at room temperature. In particular, the electron mass is taken according to the six equivalent ellipsoidal constant energy valleys of the silicon band structure.^{27,50} The effective masses of the ellipsoid are $m_l=0.9163m_0$ and $m_t=0.1905m_0$, with m_0 as the free-electron mass. For details on

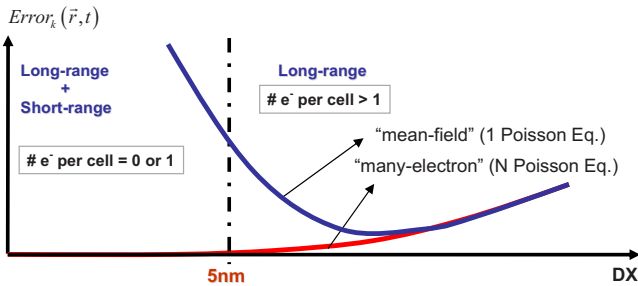


FIG. 8. (Color online) Schematic representation of the errors in the mean-field and the many-electron approaches as a function of the size of the discretization mesh.

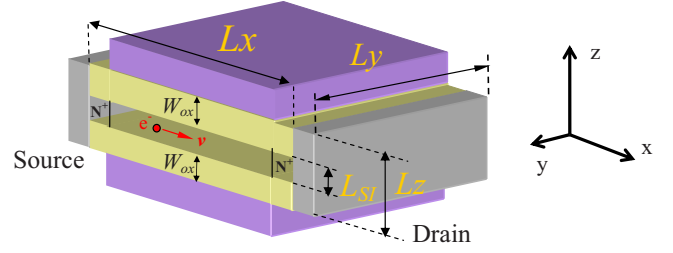


FIG. 9. (Color online) Schematic representation of the DG-FET.

the particular effective mass taken by the electrons in each direction and valley see Ref. 38. The dimensions of the channel of devices L_z and L_y are both small enough, so that the active region becomes an effective one-dimensional (1D) system (a quantum wire) and the energy of an electron in one particular valley is $E=\hbar^2k_x/(2m_l)+E_{1D}^q$, where $E_{1D}^q=\hbar^2\pi^2/(2m_lL_y^2)+\hbar^2\pi^2/(2m_lL_z^2)$ represents the minimum energy of the first subband, whose value is $E_{1D}^q=0.182$ eV for $L_z=2$ nm and $L_y=5$ nm. The energies of the next lowest subbands ($E_{1D}^q=0.418$ eV or $E_{1D}^q=0.489$ eV) are assumed high enough to keep a single band simulation. Therefore, we use a 3D Poisson solver for electrostatic, but a 1D algorithm to describe the velocity of each electron in the x direction. Due to the lateral electron confinement, the velocities in the y and z directions are zero.⁵² We solve $N(t)$ 1D Newton equation [Eq. (13)] coupled by $N(t)$ 3D Poisson equation [Eq. (18)].

We obtain the transistor current-voltage characteristics by computing the time evolution of many interacting electrons inside the 1D DG-FET. The classical many-electron algorithm is compared with the classical mean-field one. The details of the simulation are described in Table I. A total number of cells, $N_x \cdot N_y \cdot N_z$, on the order of 1000 and a number of electrons, $N(t)$, about 20–50, implies a simulation time on the order of 3–4 h for each bias point,⁵³ while it takes 20–30 min within the mean-field approximation.

TABLE I. Parameters for the DG-FET depicted in Fig. 9.

	Units	Symbol	Value
Lengths	(nm)	L_x	15
	(nm)	L_y	5
	(nm)	L_z	6
	(nm)	L_{SI}	2
	(nm)	W_{ox}	2
Spatial step	(nm)	DX	3.0
	(nm)	DY	1.6
	(nm)	DZ	1.0
Relative permittivity		Air	1.0005
		Oxide	3.8000
		Silicon	11.7514
Doping	(cm^{-3})	Channel	Intrinsic
	(cm^{-3})	Contact N^+	2×10^{19}
Simulation time	(sec.)	T	5×10^{-10}
Temporal step	(sec.)	Dt	2×10^{-16}

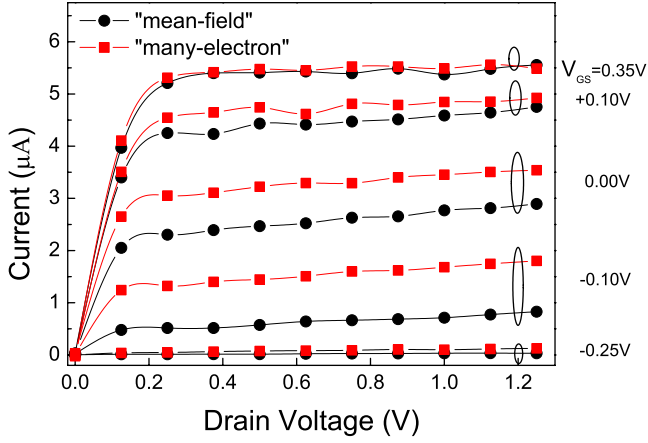


FIG. 10. (Color online) Average current for the 1D DG-FET of Fig. 9 using the many-electron and mean-field algorithms. The open ellipses include results with the same gate voltage indicated on the left.

In Figs. 10 and 11 average values for current and number of particles are presented for different gate and drain voltages. When the FET remains under subthreshold region, the results are quite similar for both methods. However, interestingly, the average current of the FET system in the subthreshold region predicted by the many-electron algorithm is slightly larger than the result obtained by the mean-field approximation. In other words, the mean-field results remain in the subthreshold region, while the many-electron results show a DG-FET channel partially opened. In any case, the most important differences occur for higher gate voltages. In order to understand the results, we have to remind that the DG-FET tends to behave as a capacitor where the charge inside the channel is controlled by the gate voltage. In addition, the charge at the contacts is controlled by the injection process that achieves local charge neutrality there. Therefore, the number of electrons inside the channel tends to be identical within both methods. However, the average current that is sensible to electron dynamics is higher with the many-

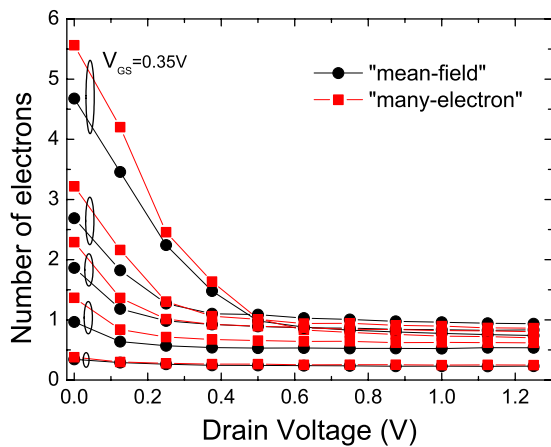


FIG. 11. (Color online) Average number of particles inside the active region of the DG-FET of Fig. 9 using the many-electron and mean-field algorithms. The open ellipses include results with the same gate voltage as indicated on the left of Fig. 10.

TABLE II. Parameters for the RTD depicted in Fig. 12.

	Units	Symbol	Value
Lengths	(nm)	L_x	6.4
	(nm)	L_y	9.0
	(nm)	L_z	9.0
Barrier dimensions	(eV)	High	0.5
	(nm)	L_{well}	2.4
	(nm)	W_{barrier}	1.6
Relative permittivity		Air	1.0005
		GaAs	13.1800
		AlGaAs	11.7760
Spatial step	(nm)	DX	0.20
	(nm)	DY	1.12
	(nm)	DZ	1.12
Doping	(cm^{-3})	Channel	Intrinsic
	(cm^{-3})	Contact N^+	2×10^{19}
Simulation time	(sec.)	T	2×10^{-10}
Temporal step	(sec.)	Dt	1×10^{-17}

electron method than with the mean-field approximation because fewer electrons are reflected in the former (i.e., there are no electrons reflected by its own charge). For the highest gate voltages, equal results for the mean current are obtained for both methods.

C. Quantum simulation of a resonant tunneling diode

In this section, we will provide a numerical example of the solution of the quantum many-particle Hamiltonian (6) for an ensemble of electrons in a RTD of Fig. 12. We again compare our many-electron method with the mean-field approximation. We consider a RTD composed of two highly doped drain-source GaAs regions, two AlGaAs barriers, and a quantum well (see Table II). We assume a constant effective mass $m=0.067m_0$, with m_0 as the electron free mass along the whole structure. Transport takes place from emitter to collector in the x direction. The lateral dimensions are small enough to consider electron confinement in y and z directions.⁵² The energy of an electron in one particular valley is $E=\hbar^2k_x/(2m)+E_{1D}^q$, where $E_{1D}^q=\hbar^2\pi^2/(2mL_y^2)+\hbar^2\pi^2/(2mL_z^2)$ represents the minimum energy of the first subband, whose value is $E_{1D}^q=0.137$ eV for $L_z=9$ nm and $L_y=9$ nm. The energies of the next lowest subbands are inaccessible to electrons ($E_{1D}^q=0.551$ eV or $E_{1D}^q=1.239$ eV). Again, room temperature is assumed.

The practical quantum algorithm for the RTD implies solving numerically $N(t)$ time-dependent single-particle 1D Schrödinger equation [Eq. (25)] for the transport direction x . Due to the confinement in the lateral directions, we assume that the Bohm velocity in y and z directions is negligible.⁵² Since expression (25) deals with time-dependent potential profiles, its solution must be computed with a numerical finite-difference scheme method (see the numerical algorithm presented in Appendix A of Ref. 54). In particular, as discussed in Ref. 33, we assume the zero-order Taylor ap-

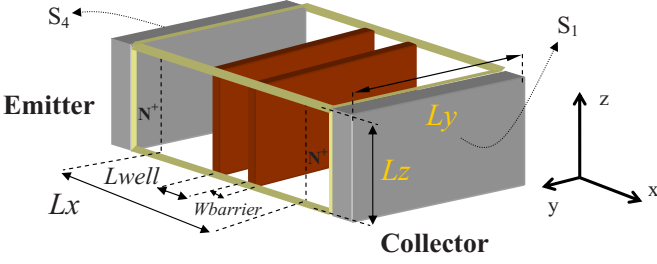


FIG. 12. (Color online) Schematic representation of the RTD.

proximations $G_a(\vec{r}_a, \vec{R}_a[t], t) \approx G_a(\vec{r}_a[t], \vec{R}_a[t], t)$ and $J_a(\vec{r}_a, \vec{R}_a[t], t) \approx J_a(\vec{r}_a[t], \vec{R}_a[t], t)$ in expression (25). We do also emphasize that the term $U_a(\vec{r}_a, \vec{R}_a[t], t)$ that appears in Eq. (25) contains the full (long and short ranges) Coulomb interaction with the particular boundary conditions developed in Sec. III. All Schrödinger equations are coupled by $N(t)$ 3D Poisson equations with $N(t)$ different boundary conditions and charge densities [expressions (17)–(20)]. The total number of cells, $N_x \cdot N_y \cdot N_z$, on the order of 1000, and the number of electrons, $N(t)$, about 10–20, implies a computational time on the order of 2–3 days for each bias point,⁵³ while it takes 10 h within the mean-field approximation. The calculations of the mean-field approximations and our many-electron approach are identical except in the computation of the potential profile. In the former a unique potential profile is computed, while in the later there is one potential profile for each electron. Finally, let us notice that we consider resonant tunneling, electron confinement, and Coulomb interaction in our quantum solution of the many-particle Hamiltonian, but we do not include the exchange interaction among electrons. The algorithm to include such interaction in our quantum (Bohm) trajectory proposal is presented in Ref. 33.

In Fig. 13 average values for current are presented for different biases with the many-electron and mean-field algorithms. We compute the average current at each bias point using a detailed version of the Ramo-Shockley theorem⁵⁴ in surface S4 (emitter) and surface S1 (collector). As expected, identical results are obtained from both surfaces showing the numerical accuracy of our simulator. When the RTD remains far from the resonant voltage, the results are quite similar for both methods, but the many-electron approach provides a bit higher current because it avoids the self-reflected electrons in the contact that are found in the mean-field approach, as mentioned previously in Figs. 4–6. On the contrary, in the resonant region, the correct consideration of the electron-electron interaction is very relevant because the quantum transport is very sensible to the quantum well electrostatics. Now, the potential profile determines the shape of the quantum well and, therefore, the resonant energies [dashed horizontal line in insets (a) and (b) of Fig. 13] of the electrons. When a “mean-field” electron tries to traverse the “empty” double barrier structure, it “feels” a perturbation in the quantum well due to its own charge implying an increase in the resonant energy and the possibility of being finally reflected by its own charge. In other words, the “mean-field” electron can be Coulomb blocked by itself. Our many-electron al-

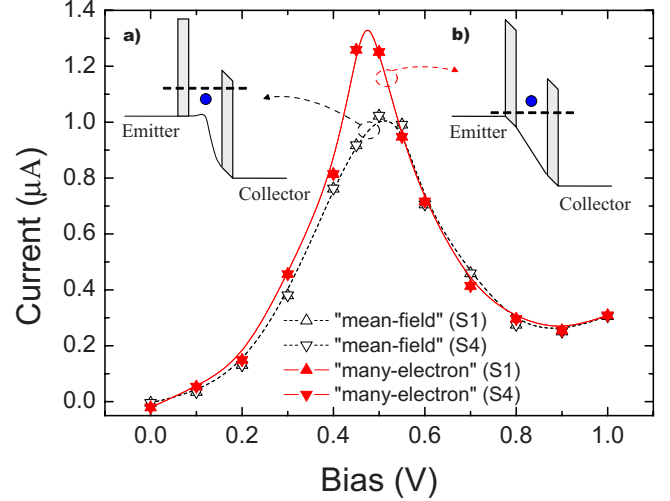


FIG. 13. (Color online) Average current through surfaces S1 and S4 for the RTD of Fig. 12 as a function of bias using the many-electron (solid symbols) and mean-field (open symbols) algorithms (lines are a visual help). Nonuniform voltages steps are used to focus on the resonant region. Insets show schematically the effect of an electron crossing an empty well on its own electrostatic potential using (a) the mean-field or (b) the many-electron approaches.

gorithm is free from this pathological behavior. This important difference explains the spurious reduction in the current with the mean-field method at resonance. It also explains the movement of the position of the resonant voltage (i.e., the voltage at the maximum current) as schematically explained in the insets of Fig. 13. The inset of Fig. 13(a) shows how the electron that traverses an empty quantum well feels its own repulsion when the mean-field approximation is used (increasing the resonant energy in dotted line), while in inset of Fig. 13(b), the electron with a many-electron simulation is free from this pathological effect.

In summary, the relation between the shape of the potential profile and the behavior of the electron can be much more complex in the quantum regime than in its classical counterpart (where the spatial derivative of the potential profile directly defines the electron acceleration). Figure 13 shows the importance of providing the exact many-particle Coulomb description of electrons in the current-voltage characteristic of a RTD. The time-dependent mean-field approach used here provides spurious effects on the correlations of electrons that are evident even in the dc behavior of RTD simulations. To be fair, let us notice that the time-dependent mean-field approach (the same as in Ref. 47) does improve the treatment of the Coulomb correlations when compared with the standard Fermi-liquid approaches^{13,14} because, in spite of providing a pathological “autointeraction” with itself, it captures the Coulomb correlation between one electron and the others.⁴⁷ In any case, the many-electron approach developed here, with the exact description of the electron Coulomb interactions, is greatly preferred.

VII. CONCLUSIONS

The prediction of the collective behavior of many electrons is a very active field of research and several theoretical

approximations have been proposed to improve the treatment of electron-electron correlations. In this work, an exact many-particle Hamiltonian for $N(t)$ electrons inside an open system is developed, without any mean-field or perturbative approximation. The many-particle Hamiltonian (6) is built from a sum of $N(t)$ electrostatic potentials $W_k(\vec{r}_1, \dots, \vec{r}_k, \dots, \vec{r}_{N(t)})$ solutions of $N(t)$ Poisson equation [Eq. (7)] in a 3D volume. We use the Poisson equation to define $W_k(\vec{r}_1, \dots, \vec{r}_k, \dots, \vec{r}_{N(t)})$ instead of the Coulomb law because the former is valid for scenarios with (or without) a spatial-dependent permittivity. In particular, it is shown that the boundary conditions [Eq. (12)] are different for each term $W_k(\vec{r}_1, \dots, \vec{r}_k, \dots, \vec{r}_{N(t)})$. It is shown that these particle-dependent boundary conditions [Eq. (12)] of the electrostatic potentials provide the same electron dynamics than the image-charge method applied to electron transport. However, our many-particle approach has the fundamental advantage that it can be directly implemented into 3D realistic (classical or quantum) electron device simulators, while the image-charge method is an excellent analytical approach applicable only to very simple systems (such as one electron crossing an ideal⁴¹ infinite metallic surface).

A classical solution of the many-particle Hamiltonian is presented for a DG-FET. The results are compared with a time-dependent mean-field approach described in Appendix B. Within the mean-field approximation only one potential profile $\bar{W}_{\text{mean}}(\vec{r}, t)$ is calculated for all electrons. Then, each electron can be reflected by an artificial alteration of the potential profile due to its own charge. On the contrary, in the many-electron algorithm described here, electrons are not affected by their own charge. The average current and the number of particles are computed for the DG-FET showing that the differences between the mean-field approximation and the exact many-electron approach become important when small geometries (that imply stronger electrostatic interaction) are involved.

A quantum solution of the many-particle Schrödinger equation with the exact many-particle (open-system) Hamiltonian developed here is presented in terms of the quantum (Bohm) trajectory algorithm mentioned in Ref. 33. The relevant point of the quantum-trajectory formalism is that Bohm trajectories can be computed without the full knowledge of the many-particle wave function, $\Phi(\vec{r}_1, \dots, \vec{r}_{N(t)}, t)$, but with the knowledge of the single-particle wave function, $\Psi_a(\vec{r}_a, t)$. It is emphasized that the approach presented in Ref. 33 has similarities with the density-functional theory. In both, the decomposition of many-particle system into a coupled set of single-particle Schrödinger equations is exact, but both need an approximation for the single-particle potentials that appear in their equations [i.e., the exchange-correlation functionals in the latter and the terms $G_a(\vec{r}_a, \vec{R}_a[t], t)$ and $J_a(\vec{r}_a, \vec{R}_a[t], t)$ in the former]. We do also emphasize that the electrostatic term $U_a(\vec{r}_a, \vec{R}_a[t], t)$ that appears in the time-dependent Schrödinger equation with time-dependent potentials, expression (25), contains the full (long and short ranges) Coulomb interaction with the particular boundary conditions developed in Sec. III. Numerical results are presented for a RTD and compared with time-dependent mean-field approach developed in Appendix B. The many-

electron approach developed here is greatly preferred because it avoids the “self-interaction” found in the time-dependent mean-field approach discussed in Appendix B.

Finally, since either the classical or the quantum many-electron solutions of the Hamiltonian are time-dependent Coulomb-interacting algorithms, apart from the average (dc) current shown in this work, both many-particle approaches are a really valuable simulation tools to obtain reliable information on the high-frequency and (dc and ac) noise performances of the state-of-the-art nanoscale devices. Future work will follow this direction.

ACKNOWLEDGMENT

This work has been partially supported by the Ministerio de Ciencia y Tecnología through Project No. TEC2006-13731-C02/MIC.

APPENDIX A: THE ELECTRON DYNAMICS OBTAINED BY THE BOUNDARY CONDITIONS [EQ. (12)] AND BY THE IMAGE-CHARGE METHOD

In this appendix, we show that, in principle, the electrostatic potential that guides the dynamics of the i particle obtained by the image-charge method is identical to the one computed with our many-particle Hamiltonian. In fact, we only have to show that the boundary conditions are identical in both approaches.

As seen in Fig. 3 of the paper, we define a subensemble of imaginary particles $\{(N+1)', \dots, M'\}$ located outside Ω . The essential property of these imaginary particles is that, together with the first $N(t)$ particles inside Ω , they reproduce the expected value of the potential $B(\vec{r}_1, \dots, \vec{r}_{M(t)}, \vec{r}^l, t)$ measured at the boundary surface S^l ,

$$\sum_{k=1}^{N(t)} V(\vec{r}^l, \vec{r}_k) + \sum_{j'=N(t)+1}^{M'} \frac{q_{j'}}{4\pi\epsilon|\vec{r}^l - \vec{r}_{j'}|} = B(\vec{r}_1, \dots, \vec{r}_{M(t)}, \vec{r}^l, t), \quad (\text{A1})$$

where the primes M', j' in the second term remind that we deal with imaginary charges (the generalization to a distribution of imaginary charge, rather than point particles, is also available). Then, the electrostatic potential seen by the i particle at the S^l boundary is just

$$\bar{W}_i^{\text{image}}(\vec{r}, t)|_{\vec{r}=\vec{r}^l} = \sum_{\substack{k=1 \\ k \neq i}}^{N(t)} V(\vec{r}^l, \vec{r}_k) + \sum_{j'=N(t)+1}^{M'} \frac{q_{j'}}{4\pi\epsilon|\vec{r}^l - \vec{r}_{j'}|}. \quad (\text{A2})$$

Therefore, from Eqs. (A1) and (A2), the electrostatic potential of the i particle at the boundary can be computed as

$$\bar{W}_i^{\text{image}}(\vec{r}, t)|_{\vec{r}=\vec{r}^l} = B(\vec{r}_1, \dots, \vec{r}_{M(t)}, \vec{r}^l, t) - V(\vec{r}^l, \vec{r}_i). \quad (\text{A3})$$

Expression (A3) is exactly the same result that we obtain from the use of our many-particle boundary conditions [see expression (12)]. Since the charge distribution inside the volume Ω does not change with the image-charge method or

D with our algorithm and both have identical boundary conditions, the uniqueness electrostatic theorem guarantees that the potential distributions obtained by both algorithms are identical not only in the boundaries but in any point inside the volume Ω . Therefore, we obtain the identity $\bar{W}_i^{\text{image}}(\vec{r}, t) = \bar{W}_i(\vec{r}, t); \forall \vec{r} \in \Omega$. An explanation in terms of the electric field, rather than the electrostatic potential, follows identical steps.

Finally, as mentioned in the paper, let us remind that the demonstration of the identity is quite simple, but the relevant point to compare both methods is that finding the imaginary charges, $\sum_{j'=N(t)+1}^{M'} q_{j'}/4\pi\epsilon|\vec{r}^{\vec{z}} - \vec{r}_{j'}|$, which fulfill expression (A1) in 3D realistic scenarios is not at all trivial.^{41,42} On the other hand, the ability of our many-particle Hamiltonian to be included into 3D realistic devices is explicitly demonstrated in Sec. VI.

APPENDIX B: TIME-DEPENDENT MEAN-FIELD APPROXIMATION FOR THE MANY-PARTICLE HAMILTONIAN

As described in Sec. I, the mean-field approximation provides a single average potential for computing the dynamics of all the electrons. This average potential, which we label here by the suffix “mean” $\bar{W}_{\text{mean}}(\vec{r}, t)$, is still capable of preserving most of the collective effects of the Coulomb interaction. Here, we compare this approximation with our exact many-particle Hamiltonian. The term $\bar{W}_{\text{mean}}(\vec{r}, t)$ is computed by taking into account all charges inside the volume Ω . However, since one particle cannot “feel” its own charge, in fact, $\bar{W}_{\text{mean}}(\vec{r}, t)$ can be interpreted as the electrostatic potential seen for an additional probe charge whose position is \vec{r} ,

$$\bar{W}_{\text{mean}}(\vec{r}, t) = \bar{W}_{M+1}(\vec{r}_1[t], \dots, \vec{r}_{N(t)}[t], \vec{r}). \quad (\text{B1})$$

This term $\bar{W}_{\text{mean}}(\vec{r}, t)$ is a solution of a unique 3D Poisson equation,

$$\nabla_{\vec{r}}^2 \bar{W}_{\text{mean}}(\vec{r}, t) = \bar{\rho}_{\text{mean}}(\vec{r}, t), \quad (\text{B2})$$

where the charge density is defined as

$$\bar{\rho}_{\text{mean}}(\vec{r}, t) = \sum_{j=1}^{N(t)} q_j \delta(\vec{r} - \vec{r}_j[t]), \quad (\text{B3})$$

and, according to expression (11) in the paper, the boundary conditions for this additional probe charge must be

$$\bar{W}_{\text{mean}}(\vec{r}, t)|_{\vec{r}=\vec{r}'} = B(\vec{r}_1[t], \dots, \vec{r}_{N(t)}[t], \vec{r}^{\vec{z}}, t), \quad l = 1, \dots, 6. \quad (\text{B4})$$

Let us notice that the time-dependent mean-field approximation discussed here can be applied to either classical or quantum systems. Both approaches share expressions (B2)–(B4) for the computation of the electrostatic potentials (change the classical trajectories by the quantum ones). We also want to remark the time-dependence of expression (B2). This is a common feature for classical (semiconductor Monte

Carlo⁵¹) simulations but less frequent for quantum mean-field approaches.

Now, we estimate the error of our time-dependent mean-field approximation. First, we show that the mean-field potential can be written in terms of the potentials $\bar{W}_i(\vec{r}_i, t)$ mentioned in Eq. (17). In particular, we can write the mean-field potential $\bar{W}_{\text{mean}}(\vec{r}, t)$ as

$$\bar{W}_{\text{mean}}(\vec{r}, t) = \frac{1}{N(t)} \left\{ \sum_{j=1}^{N(t)} \bar{W}_{\text{mean}}(\vec{r}, t) \right\} = \frac{1}{N(t)} \sum_{j=1}^{N(t)} \{ \bar{W}_j(\vec{r}, t) + V(\vec{r}, \vec{r}_j[t]) \}. \quad (\text{B5})$$

Now, we compute the error, $\text{Error}_k(\vec{r}, t)$, as

$$\text{Error}_k(\vec{r}, t) = \bar{W}_{\text{mean}}(\vec{r}, t) - W_k(\vec{r}, t) = \frac{1}{N(t)} \left\{ \sum_{j=1}^{N(t)} \bar{W}_j(\vec{r}, t) + V(\vec{r}, \vec{r}_j[t]) \right\} - \bar{W}_k(\vec{r}, t), \quad (\text{B6})$$

which can be finally rewritten as

$$\begin{aligned} \text{Error}_k(\vec{r}, t) &= \frac{1}{N(t)} \sum_{j=1}^{N(t)} \{ \bar{W}_j(\vec{r}, t) - \bar{W}_k(\vec{r}, t) + V(\vec{r}, \vec{r}_j[t]) \} \\ &= V(\vec{r}, \vec{r}_k[t]), \end{aligned} \quad (\text{B7})$$

where, according to Eq. (9), we have used the identity

$$\begin{aligned} \bar{W}_j(\vec{r}, t) - \bar{W}_k(\vec{r}, t) &= \sum_{\substack{i=1 \\ i \neq j}}^M V(\vec{r}, \vec{r}_i[t]) - \sum_{\substack{i=1 \\ i \neq k}}^M V(\vec{r}, \vec{r}_i[t]) \\ &= V(\vec{r}, \vec{r}_k[t]) - V(\vec{r}, \vec{r}_j[t]). \end{aligned} \quad (\text{B8})$$

Expression (B7) shows that $\text{Error}_k(\vec{r}, t) \rightarrow \infty$ when $\vec{r} \rightarrow \vec{r}_k[t]$. The mean-field approximation implies that the potential “felt” by the k particle at $\vec{r} \rightarrow \vec{r}_k[t]$ is its own potential profile. In fact, from a numerical point of view, the use of the mean-field approximation is not so bad. For example, classical simulators uses 3D meshes with cell sizes of few nanometers, $DX \approx DY \approx DZ \gg 10$ nm. Then, the error of the mean-field approximation is smaller than the technical error (i.e., mesh error) due to the finite size of the cells. The long-range Coulomb interaction is well captured with the mean-field approximation, while this approximation is really bad strategy to capture the short-range Coulomb interaction^{28–32} (see Fig. 8 in the paper).

Finally, let us remark another important point about the mean-field approximation. Looking at final expression (B7), rewritten here as $W_k(\vec{r}, t) = \bar{W}_{\text{mean}}(\vec{r}, t) - V(\vec{r}, \vec{r}_k[t])$, it seems that $W_k(\vec{r}, t)$ can be computed from a unique mean-field solution of the Poisson equation $\bar{W}_{\text{mean}}(\vec{r}, t)$ when subtracting the appropriate two-particle potential $V(\vec{r}, \vec{r}_k[t])$. In fact, this is the strategy used in several recent works^{28–32} to improve the treatments of the short-range Coulomb interaction in electron device Monte Carlo simulators. However, this strategy is not as general as our procedure because these works

need an analytical expression for the two-particle Coulomb interaction $V(\vec{r}, \vec{r}_k[t])$. The analytical expression of $V(\vec{r}, \vec{r}_k[t])$ written in expression (3) is only valid for scenarios with homogenous permittivity. On the contrary, our procedure

with $N(t)$ electrostatic potentials computed from $N(t)$ different Poisson equations in a limited 3D volume Ω can be applied inside general scenario with (or without) spatial-dependent permittivity.

D

*Corresponding author: xavier.oriols@uab.es

- ¹G. F. Giuliani and G. Vignale, *Quantum Theory of Electron Liquid* (Cambridge University Press, Cambridge, 2005).
- ²J. M. Thijssen, *Computational Physics* (Cambridge University Press, Cambridge, 2003).
- ³Strictly speaking, even the many-particle wave function of a system of electrons without Coulomb interaction (described by a Slater determinant of single-particle wave functions) is a correlated wave function due to its antisymmetric structure. However, the word correlation is normally reserved only for those correlations that go beyond the inevitable antisymmetry-related one.
- ⁴D. R. Hartree, Proc. Cambridge Philos. Soc. **24**, 89 (1928).
- ⁵J. C. Slater, Phys. Rev. **81**, 385 (1951).
- ⁶P. Hohenberg and W. Kohn, Phys. Rev. **136**, B864 (1964).
- ⁷W. Kohn and L. J. Sham, Phys. Rev. **140**, A1133 (1965).
- ⁸R. O. Jones and O. Gunnarsson, Rev. Mod. Phys. **61**, 689 (1989).
- ⁹R. O. Jones and O. Gunnarsson, Phys. Rev. Lett. **55**, 107 (1985).
- ¹⁰D. C. Langreth and M. J. Mehl, Phys. Rev. Lett. **47**, 446 (1981).
- ¹¹Y. M. Blanter and M. Büttiker, Phys. Rep. **336**, 1 (2000).
- ¹²S. Datta, *Transport in Mesoscopic Systems* (Cambridge University Press, Cambridge, 1995).
- ¹³W. R. Frensley, Rev. Mod. Phys. **62**, 745 (1990).
- ¹⁴The absence of Coulomb interaction in electron systems was explained, first, by Landau in terms of the Fermi-liquid paradigm, where the real electrons were substituted by “quasielectrons” with a negligible Coulomb interaction among them: L. D. Landau, Sov. Phys. JETP **8**, 70 (1959); L. D. Landau, *ibid.* **3**, 920 (1957).
- ¹⁵R. Landauer, IBM J. Res. Dev. **1**, 223 (1957).
- ¹⁶M. Büttiker, Phys. Rev. Lett. **65**, 2901 (1990).
- ¹⁷R. Landauer, Phys. Scr., T **T42**, 110 (1992).
- ¹⁸I. L. Aleiner, P. W. Brouwer, and L. I. Glazman, Phys. Rep. **358**, 309 (2002).
- ¹⁹E. N. Economou, *Green's Functions in Quantum Physics* (Springer-Verlag, Berlin, 1990).
- ²⁰M. Büttiker, A. Prêtre, and H. Thomas, Phys. Rev. Lett. **70**, 4114 (1993).
- ²¹M. Büttiker, J. Phys.: Condens. Matter **5**, 9361 (1993).
- ²²M. C. Goorden and M. Büttiker, Phys. Rev. Lett. **99**, 146801 (2007).
- ²³M. Brandbyge, J. L. Mozos, P. Ordejon, J. Taylor, and K. Stokbro, Phys. Rev. B **65**, 165401 (2002).
- ²⁴E. Runge and E. K. U. Gross, Phys. Rev. Lett. **52**, 997 (1984).
- ²⁵S. Kurth, G. Stefanucci, C. O. Almbladh, A. Rubio, and E. K. U. Gross, Phys. Rev. B **72**, 035308 (2005).
- ²⁶K. Burke, J. Werschnik, and E. K. U. Gross, J. Chem. Phys. **123**, 062206 (2005).
- ²⁷C. Jacoboni and L. Reggiani, Rev. Mod. Phys. **55**, 645 (1983).
- ²⁸W. J. Gross, D. Vasileska, and D. K. Ferry, IEEE Electron Device Lett. **20**, 463 (1999).

- ²⁹S. M. Ramey and D. K. Ferry, Physica B **314**, 350 (2002).
- ³⁰S. M. Ramey and D. K. Ferry, IEEE Trans. Nanotechnol. **2**, 193 (2003).
- ³¹P. Dollfus, A. Bournel, S. Galdin, S. Barraud, and P. Hesto, IEEE Trans. Electron Devices **51**, 749 (2004).
- ³²W. J. Gross, D. Vasileska, and D. K. Ferry, IEEE Trans. Electron Devices **47**, 1831 (2000).
- ³³X. Oriols, Phys. Rev. Lett. **98**, 066803 (2007).
- ³⁴For a quantum system, the number of particles inside the volume Ω has not only a dependence on time but a dependence on all particle positions $N(\vec{r}_1, \dots, \vec{r}_k, \dots, \vec{r}_M, t)$. Let us assume a wave function whose probability presence occupies regions inside and outside Ω . Then, the limit of the sum in Hamiltonian (6) depends on the exact value of the variable \vec{r}_k . In principle, the k particle has to be included into the first subensemble when the Hamiltonian deals with $\vec{r}_k \in \Omega$ and into the second subensemble when $\vec{r}_k \notin \Omega$. In order to avoid a very complicated notation, we do only write the time dependence of $N(t)$ for either classical or quantum systems. In any case, since our quantum solution will deal with quantum (Bohm) trajectories (rather than wave functions), the simpler notation mentioned here is appropriate for the classical and quantum algorithms.
- ³⁵H. López, G. Albareda, X. Cartoixà, J. Suñé, and X. Oriols (unpublished).
- ³⁶M. Javid and P. M. Brown, *Field Analysis and Electromagnetics* (McGraw-Hill, New York, 1963).
- ³⁷Classically, the definition of $B(\vec{r}_1, \dots, \vec{r}_{N(t)}, \dots, \vec{r}_M, \vec{r}^j, t)$ can be directly associated to the voltage “measured” at \vec{r}^j by an external meter. On the contrary, quantum mechanically, the voltage measured at \vec{r}^j would require evaluating a bracket between the many-particle wave function and $B(\vec{r}_1, \dots, \vec{r}_{N(t)}, \dots, \vec{r}_M, \vec{r}^j, t)$. In Secs. II and III, we are not discussing the many-particle wave function but only an expression of the many-particle Hamiltonian. Therefore, it is important to remark that $B(\vec{r}_1, \dots, \vec{r}_{N(t)}, \dots, \vec{r}_M, \vec{r}^j, t)$ is not defined as the voltage measured at \vec{r}^j but as the electrostatic potential that describes the interaction of the electron at \vec{r}^j with the rest of M electrons. This last definition is identical for classical and quantum cases.
- ³⁸X. Oriols, E. Fernandez-Diaz, A. Alvarez, and A. Alarcon, Solid-State Electron. **51**, 306 (2007).
- ³⁹J. S. Blakemore, *Solid State Physics*, 2nd ed. (Cambridge University Press, Cambridge, 1985).
- ⁴⁰S. M. Sze, *Semiconductor Devices: Physics and Technology*, 2nd ed. (Wiley, New York, 2002).
- ⁴¹The standard image-charge method in metallic interfaces assumes that the electric field is null on the interface. However, this assumption fails at very short distances because it does not correctly account for the atomistic structure of the metal and the band structure of its electrons. See section 3.3 of M. W. Finnis, Acta Metall. Mater. **40**, S25 (1992); F. Ernst, Mater. Sci. Eng. R **14**, 97 (1995).

- D**
- ⁴²Although the image-charge method is an old electrostatics method, its practical application to apparently simple systems has an extraordinary mathematical complexity. See, for example, Z. Jiang, X. Zhang, and J. Han, *J. Electrostat.* **39**, 23 (1997), and references therein for its application to two conducting spheres.
- ⁴³W. Kohn, *Rev. Mod. Phys.* **71**, 1253 (1999).
- ⁴⁴D. Bohm, *Phys. Rev.* **85**, 166 (1952).
- ⁴⁵P. R. Holland, *The Quantum Theory of Motion* (Cambridge University Press, Cambridge, 1993).
- ⁴⁶X. Oriols, *Phys. Rev. A* **71**, 017801 (2005).
- ⁴⁷X. Oriols, A. Trois, and G. Blouin, *Appl. Phys. Lett.* **85**, 3596 (2004).
- ⁴⁸J. Wang, A. Rahman, A. Ghosh, G. Klimeck, and M. Lundstrom, *IEEE Trans. Electron Devices* **52**, 1589 (2005).
- ⁴⁹M. Born and R. Oppenheimer, *Ann. Phys.* **84**, 457 (1927);
- ⁵⁰V. Sverdlov, X. Oriols, and K. Likharev, *IEEE Trans. Nanotechnol.* **2**, 59 (2003).
- ⁵¹Strictly speaking, our many-electron method applied to semiclassical devices cannot be considered as a direct solution of the Boltzmann equation because the latter is developed within a

classical mean-field approximation. The term $\bar{W}_k(\vec{r}_k, t)$ in the Hamiltonian of expression (21) means that each particle “sees” its own electrostatic potential (or electric field), which is different from that of others. Apart from the scattering rates, this is the fundamental difference between our many-electron method applied to classical transport and the standard Monte Carlo method for electron devices.

- ⁵²We assume that the electron velocity is equal to zero in the lateral directions where there is energy confinement. This is a reasonable assumption that can be formally justified for Ref. 33 when the probability presence in that direction does not change with time. The main approximation here is assuming that the time dependence of the wave function involves only one quantized energy in the mentioned direction. We define the geometries of the DG-FET and RTD to support these approximations.
- ⁵³The estimation of the computational time is done for simulation run on a single dual xenon 2×3.06 GHz server.
- ⁵⁴X. Oriols, A. Alarcon, and E. Fernandez-Diaz, *Phys. Rev. B* **71**, 245322 (2005).

Intrinsic noise in aggressively scaled field-effect transistors

G Albareda, D Jiménez and X Oriols

Departament d'Enginyeria Electrònica, Escola Tècnica Superior d'Enginyeria,
Universitat Autònoma de Barcelona, 08193 Bellaterra, Spain
E-mail: guillem.albareda@uab.es, david.jimenez@uab.es and
xavier.oriols@uab.es

Received 1 July 2008

Accepted 20 August 2008

Published 7 January 2009

Online at stacks.iop.org/JSTAT/2009/P01044

[doi:10.1088/1742-5468/2009/01/P01044](https://doi.org/10.1088/1742-5468/2009/01/P01044)

Abstract. According to roadmap projections, nanoscale field-effect transistors (FETs) with channel lengths below 30 nm and several gates (for improving their gate control over the source–drain conductance) will come to the market in the next few years. However, few studies deal with the noise performance of these aggressively scaled FETs. In this work, a study of the effect of the intrinsic (thermal and shot) noise of such FETs on the performance of an analog amplifier and a digital inverter is carried out by means of numerical simulations with a powerful Monte Carlo (quantum) simulator. The numerical data indicate important drawbacks in the noise performance of aggressively scaled FETs that could invalidate roadmap projections as regards analog and digital applications.

Keywords: current fluctuations, classical Monte Carlo simulations, mesoscopic systems (theory)

Contents

1. Introduction	2
2. Intrinsic noise in quasi-ballistic devices	3
2.1. Analytical results for noise in analog applications	3
2.2. Analytical results for noise in digital (logic and memory) applications	5
3. Numerical results for nanoscale field-effect transistors	7
3.1. Device description	7
3.2. Numerical Monte Carlo simulation algorithm	8
3.3. DC results	9
3.4. Analog noise results	10
3.5. Digital noise results	10
4. Conclusions	13
Acknowledgment	13
References	13

1. Introduction

The ITRS predicts for the near future the introduction of nanoscale field-effect transistors (FET) with channel lengths below 30 nm, including novel structures with two, three or even four gates provided in order to improve the gate control over the source–drain conductance [1]. The advantages of these nanoscale FETs in overcoming the physical limits of traditional FETs are clearly established in terms of size, speed and power consumption. However, few studies deal with the noise performance of these aggressively scaled FETs. This is the main goal of this work.

At very small (a few nanometers) dimensions of FETs, two important physical features appear in the description of electron transport. On one hand, ballistic transport comes into play. For advanced FETs with channel length smaller than 30 nm, an electron crossing the channel suffers very few inelastic collisions and its total (kinetic plus electrostatic) energy is nearly constant. On the other hand, when the lateral dimensions of the channel are comparable to the de Broglie wavelength of the electron, its wave nature is manifested. The only available energies for electrons are those that provide a solution of the Schrödinger equation whose modulus is zero at the lateral boundaries. The role of such particularities in the noise performance of FET structures will be studied in this work using a powerful Monte Carlo (quantum) simulator. Although there are other sources that provide time-dependent fluctuations of the electronic current in FETs [2], when all those ‘spurious’ sources of noise are eliminated, thermal and shot noise still remain. Therefore, we will consider only these two sources of noise within a particular 3D (bulk) FET and a 1D (quantum wire) FET.

In section 2, we provide analytical estimations for the signal-to-noise ratio (S/N) of a simple analog amplifier, and the bit–error ratio (BER) of a simple CMOS inverter. Then,

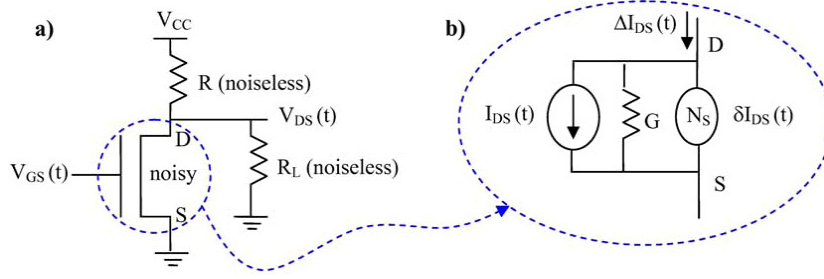


Figure 1. (a) Schematic representation of an analog amplifier. D and S denote the drain and source respectively. (b) Equivalent FET circuit, where $\delta I_{DS}(t)$ and $I_{DS}(t)$ denote noise and signal sources respectively and G represents the FET conductance.

in section 3, we will compute numerical results for the analog and digital applications by means of an electron device Monte Carlo simulator coupled to a full Poisson solver [3] with a novel injection model suitable for electron devices with or without quantum confinement conditions [4]. We conclude in section 4 summarizing the most important results of this work.

2. Intrinsic noise in quasi-ballistic devices

Here, we obtain analytic estimates for the noise performances in both analog and digital FET applications. Such analytic expressions for the S/N ratio and the BER will help in the understanding of the Monte Carlo numerical noise results.

2.1. Analytical results for noise in analog applications

In the present subsection we deduce an analytical expression for the S/N ratio for the analog amplifier depicted in figure 1(a).

The current fluctuations can be extracted from the equivalent circuit shown in figure 1(b):

$$\Delta I_{DS} = G \Delta V_{DS} + \delta I_{DS} \quad (1)$$

where G is the FET conductance, ΔV_{DS} is the source–drain voltage fluctuation and δI_{DS} denotes the intrinsic current noise. At the same time, since the FET is operated in the saturation region,

$$G \equiv \frac{dI_{DS}}{dV_{DS}} \approx 0, \quad (2)$$

we assume that the fluctuation of the drain–source current in (1) will depend not on the drain–source voltage variation, but only on $\delta I_{DS}(t)$. This is a reasonable approximation for the saturation region and the low-frequency limit assumed here. Thus, we can rewrite (1) as

$$\Delta I_{DS}(t) = \delta I_{DS}(t). \quad (3)$$

On the other hand, using the superposition principle, V_{DS} and I_L can be broken down into signal (capital letters) and noise (δ). Removing signal sources from figure 1, it is easy to demonstrate that the noise current on the resistor R_L is

$$\delta I_{R_L}(t) \equiv \frac{\delta V_{DS}(t)}{R_L} = \frac{R}{R + R_L} \delta I(t). \quad (4)$$

Equation (4) can be expressed in the frequency domain as

$$\delta I_{R_L}(\omega) = H(\omega) \delta I(\omega) \quad (5)$$

where $H(\omega)$ is a transfer function. Now, integrating over a bandwidth B associated with a specific amplifier configuration, the resulting total noise power is

$$N_{R_L} = \int_0^B |H(\omega)|^2 S_I R_L \quad (6)$$

which yields, using $H(\omega) = R/(R + R_L)$, the following result:

$$N_{R_L} = \frac{R^2 R_L}{(R + R_L)^2} 2q I_{DS} F B. \quad (7)$$

Note that in equations (6) and (7), we have used the corresponding power spectral density of the thermal noise (S_I), expressed in terms of the Fano factor (F):

$$S_I = 2q I_{DS} F. \quad (8)$$

Now, let us calculate the signal power. First, we express V_{DS} as

$$V_{DS} = \frac{I_{DS} R R_L + V_{CC} R_L}{R + R_L}. \quad (9)$$

Then, we solve (9), obtaining expression for I_{R_L} :

$$I_{R_L} = I_{DS} \left(\frac{R}{R + R_L} \right) + \frac{V_{CC}}{R} \left(\frac{R}{R + R_L} \right). \quad (10)$$

Finally, the signal power $S_{R_L} = I_{R_L}^2 R_L$ can be written as

$$S_{R_L} = \frac{R^2 R_L}{(R + R_L)^2} \left\{ I_{DS}^2 + \left(\frac{V_{CC}}{R} \right)^2 + 2 I_{DS} \frac{V_{CC}}{R} \right\}. \quad (11)$$

Assuming $R \gg R_L$, expressions (7) and (11) reduce respectively to

$$N_{R_L} \approx 2q I_{DS} F B R_L \quad (12)$$

and

$$S_{R_L} = I_{DS}^2 R_L. \quad (13)$$

Finally, the signal-to-noise ratio is

$$\frac{S_{R_L}}{N_{R_L}} = \frac{I_{DS}}{2q B F}. \quad (14)$$

The expression (14) tells us that when the current I_{DS} decreases or the Fano factor (F) increases, the signal-to-noise ratio is degraded.

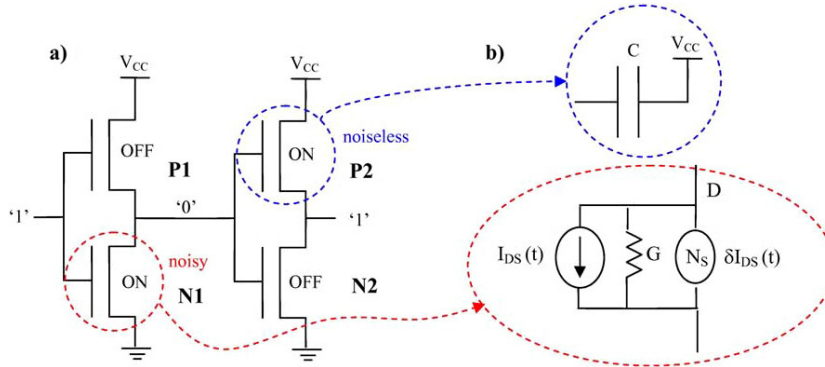


Figure 2. (a) Schematic representation of a digital inverter. (b) Equivalent circuit for N1 and P2, where $\delta I_{DS}(t)$ and $\Delta I_{DS}(t)$ denote noise and signal sources respectively assuming a linear region of operation. G represents the FET conductance and C the associated capacitance for P2 transistors.

Hereafter, we show that, in fact, the downscaling trend of CMOS technology towards low-dimensional active regions provides lower current and also higher Fano factor. For ballistic devices, only the electrons crossing the FET channel contribute to the average and the noise currents [4]. As an example, let us assume a potential barrier within a FET channel. Only those electrons energetically above this barrier will contribute to the current and noise (if tunneling can be neglected). These ‘hot’ electrons come from the Fermi distribution tail. Thus, they are mainly uncorrelated electrons, so they provide little current but a high Fano factor (close to the uncorrelated Poisson value of $F = 1$), resulting in a degraded S/N ratio. Similarly, within a ballistic confined FET system, only those electrons above the confinement energy will enter the channel. In this sense, confinement introduces an additional potential barrier that makes the system deal with a ‘hotter’ region of the fermi distribution, where noise is greater and current lower, giving rise to a degradation of the S/N ratio. On the other hand, bulk FETs do not present potential barriers linked to confinement, resulting in a better S/N ratio. In conclusion, low-dimensional FETs implicitly exhibit higher S/N ratios. Later, in section 3, numerical results obtained with a powerful Monte Carlo (quantum) simulator will be computed for the same system without some of the analytical (low-frequency) simplifications used above.

2.2. Analytical results for noise in digital (logic and memory) applications

Next we deduce analytical expressions for the BER of the digital inverter depicted in figure 2(a), taken as a simple digital circuit for analyzing the role of scaling. When a logical ‘1’ is applied at the first inverter, the P-type transistor P1 is turned off, while the N-type transistor N1 is turned on. N1 is now working in the equilibrium region, giving a logical ‘0’ at the input of the second inverter. Thus, N2 will be turned off while P2 will be turned on. Under these operation conditions, N1 and P2 can be equivalently defined as depicted in the figure 2(b). Transistor N1 can be modeled as the parallel combination of a signal source I_{DS} , a noise source δI_{DS} and a conductance G . On the other hand P2 can be modeled as a capacitor.

Since N1 has its channel completely open, it works within the equilibrium region of operation. Then the current fluctuations around zero mean value, $I_{\text{DS}}(t) \approx 0$, are given by

$$\Delta I_{\text{DS}} = G \Delta V_{\text{DS}}(t) + \delta I_{\text{DS}}(t) \quad (15)$$

where the conductance G is linked with the linear region of operation, i.e. G is roughly constant under small voltage fluctuations. Therefore, G only depends on the applied gate voltage and it can be defined on the equilibrium region, i.e. $G = \partial I_{\text{DS}} / \partial V_{\text{DS}}|_{V_{\text{DS}}=0}$. The first term on the right in equation (15) corresponds to the current fluctuations associated with the voltage fluctuations in the capacitor. The second term corresponds to the intrinsic transistor noise.

Under the equilibrium conditions that we are assuming, noise in the transistor N1 is characterized by the Nyquist–Johnson thermal noise [5]. Then, the corresponding power spectral density for $\delta I_{\text{DS}}(t)$ at low frequencies exhibits the form

$$S_I(0) = 4k_{\text{B}}TG. \quad (16)$$

We can relate variations of the current for the N1 transistor to voltage variations at the capacitor representing P2. Then, making equation (15) equal to the one corresponding to the capacitor current, the intrinsic current noise can be expressed as

$$\delta I_{\text{DS}}(t) = -G \Delta V_{\text{DS}}(t) - C \frac{d(\Delta V_{\text{DS}}(t))}{dt}. \quad (17)$$

The previous expression can be rewritten in the frequency domain as

$$\delta I(\omega) = G \Delta V_{\text{DS}}(\omega) + j\omega C \Delta V_{\text{DS}}(\omega). \quad (18)$$

Therefore, the bias fluctuations are

$$\Delta V_{\text{DS}}(\omega) = \delta I(\omega) \frac{1}{C} \frac{1}{((1/R_T C) + j\omega)}. \quad (19)$$

Combining equations (16) and (19), the total power for the bias fluctuations can be calculated by integrating the spectral density over the frequency:

$$S_V(0) = \frac{1}{\pi} \int_0^{W_t} \frac{1}{C^2} \frac{1}{((1/R_T^2 C^2) + \omega^2)} 4k_{\text{B}}TG \, d\omega. \quad (20)$$

A bit error appears when (during a period $T_C = 1/f_c$ with f_c the clock frequency) the mean value of the bias fluctuations exceeds the threshold value for a logical ‘0’. Therefore, when we use the superior limit of the integral of expression (20) as $W_t = 2\pi f_c$, we obtain

$$S_V(0) = \frac{1}{\pi} \frac{4k_{\text{B}}T}{C} \tan^{-1}(2\pi f_c R_T C). \quad (21)$$

Therefore, the bit error probability can be expressed as [6]

$$P_e = Q \left(\frac{A}{2} \frac{\sqrt{\pi C}}{4k_{\text{B}}T \tan^{-1}(2\pi f_c R_T C)} \right) \quad (22)$$

where A is the bias value associated with the logical value ‘1’, and Q is the error function defined as

$$Q(x) = \frac{1}{\sqrt{2\pi}} \int_x^\infty e^{-\lambda^2/2} d\lambda. \quad (23)$$

From (22) and (23), the BER is higher with higher clock frequencies (see the dependence of expression (22) on the clock frequency through the inverse tangent). For clock frequencies far below the intrinsic frequency $(R_T C)^{-1}$, the following simplification can be made: $\tan^{-1}(x) \approx x$. Then, the total power, obtained from expression (21), can be approximated as

$$S_V(0) \approx 8k_B T f_c R_T. \quad (24)$$

It can be seen from expression (24) that under this frequency limit, there is no capacitance dependence of the BER. On the other hand, for clock frequencies higher than the intrinsic frequency $(R_T C)^{-1}$, then $\tan^{-1}(x) \approx \pi/2$, and the total power can be approximated as

$$S_V(0) \approx \frac{2k_B T}{C}. \quad (25)$$

In expression (25), the variance of the normal distribution shrinks with the capacitance value. In other words, smaller FETs will show higher error probabilities. A similar result, obtained through a different reasoning, has been presented in [7].

So far, analytical estimations for noise performance for analog and digital applications have been deduced. In fact, expressions (14) and (22) will only capture the main trends as regards the understanding of intrinsic noise behavior in nanoscale devices. In view of this, the main goal of the next section is to obtain numerical values for S/N and BER through a much more complex and detailed description of the electron dynamics. Next, we use a Monte Carlo (quantum) simulator which is a powerful and robust technique that allows the study of time-dependent fluctuations without some of the approximations used in this section.

3. Numerical results for nanoscale field-effect transistors

The numerical results presented in this work are computed using a Monte Carlo (quantum) simulator that introduces some features that allow solving a many-electron scenario within 3D and 1D systems. First, we present a brief description of the device under study and the numerical algorithm behind our simulations. Finally we present DC current and noise results for analog and digital applications.

3.1. Device description

We assume that electron transport (from source to drain) takes place along a silicon (100) oriented channel, at room temperature (see figure 3). A double-gate (DG) geometry for the transistor has been considered for numerical simulations, but the qualitative conclusions can be extended to other gate geometries. We assume that electrons can reach the six equivalent ellipsoidal constant energy valleys of the silicon band structure. The effective masses of the ellipsoid are $m_l^* = 0.9163 m_0$ and $m_t^* = 0.1905 m_0$ with m_0 the free electron mass. For details on the particular effective mass value taken by the electrons in each

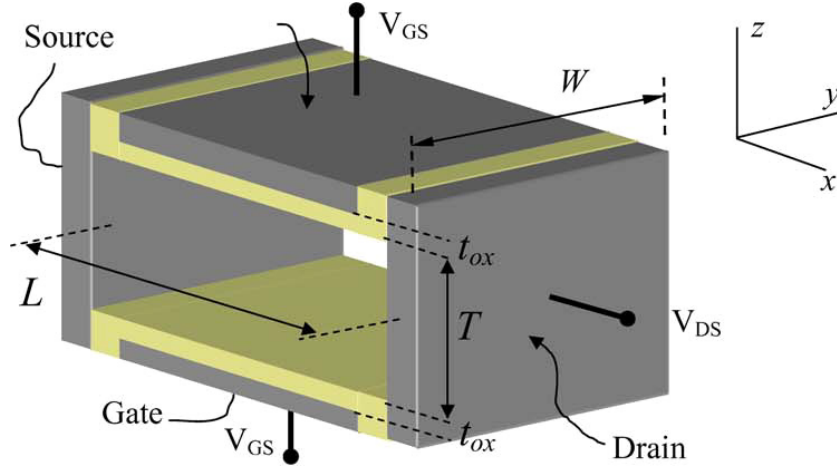


Figure 3. Schematic representation of a DG-FET. Electron transport from source to drain takes place along the x direction. The channel (open system) of the FET has arbitrary lateral dimensions, W and T , determining electron confinement.

direction and valley see [4]. We consider two different geometries to be able to deal with a 3D bulk and a 1D quantum wire, by controlling the electron confinement. When W and T are much larger than the electron de Broglie wavelength, the active region is a three-dimensional (3D) system (bulk) and there is no restriction on the possible values of the energies of an electron in each of the six valleys. The total electron energy for a particular valley is $E = E_x + E_{\perp}$, where the energies E_x and E_{\perp} are defined as $E_x = \hbar^2 k_y / (2m_t)$ and $E_{\perp} = \hbar^2 k_y / (2m_t) + \hbar^2 k_z / (2m_l)$. On the other hand, when T and W are both small enough, the active region becomes a 1D system (a quantum wire) and the energy of an electron in one particular valley is $E = \hbar^2 k_x / (2m_t) + E_{1D}^q$, where $E_{1D}^q = \hbar^2 \pi^2 / (2m_t L_y^2) + \hbar^2 \pi^2 / (2m_l L_z^2)$ represents the minimum energy of the first sub-band, whose value is $E_{1D}^q = 0.182$ eV for $T = 2$ nm and $W = 5$ nm. The energies of the next lowest sub-bands are inaccessible for electrons ($E_{1D}^q = 0.418$ eV or $E_{1D}^q = 0.489$ eV) and only two valleys become relevant. For the quantum wire, the electron velocities in the z and y directions are zero due to the electron confinement¹. Let us notice that we refer to a 3D (bulk) or 1D (quantum wire) system to emphasize the energy confinement in the active region that determines the available energies for electrons. However, the paths of the electrons are defined in the x, y, z directions and, consequently, the electrostatics are obtained through a 3D Poisson solver for all simulations (even for the 1D quantum wire).

3.2. Numerical Monte Carlo simulation algorithm

Our numerical algorithm for solving the dynamics of an ensemble of interacting electrons is quite close, but not identical, to the standard Monte Carlo method applied to

¹ The electron velocity is equal to zero in the direction where there is energy confinement. This is a reasonable assumption that can be formally justified, for example using Bohm trajectories, when the probability of presence in that direction does not change with time. The main approximation here is assuming that the time dependence of the wavefunction involves only one quantized energy in the aforementioned direction, $\exp(iE_{1D}^q t / \hbar)$, because it assumes that the single-particle wavefunction is separable in the 3D space and that only one sub-band is relevant for electron transport. We define the geometries of the 1D system to support these approximations.

semiconductor electron devices. This technique is a powerful method for solving the Boltzmann transport equation, which is developed under the mean-field approximation. In the latter, a unique Poisson equation is solved at each time step of the simulation, while in our many-electron Monte Carlo approach we solve $N(t)$ Poisson equations with $N(t)$ different boundary conditions and charge densities. We use a 3D Poisson solver based on a finite-difference scheme. We divide the whole volume Ω of the scenario drawn in figure 3 into $N_x N_y N_z$ cells. Each 3D cell has spatial dimensions DX , DY and DZ . Thus, the active region of our simulating device has a volume equal to $(N_x DX)(N_y DY)(N_z DZ) = LWT$. The most time-consuming algorithm is that for the solution of the Poisson equation. Therefore, in our algorithm, the simulation time is proportional to $N(t) N_x N_y N_z$, while it reduces to $N_x N_y N_z$ under standard Monte Carlo simulations. As an example, for a total number of cells, $N_x N_y N_z$, on the order of 1000–2000 cells and a number of electrons, $N(t)$, of ~ 20 –50, the computational time is about 2–3 h for each bias point using a state-of-the-art workstation².

At the same time, our numerical algorithm includes electron confinement in the active region. Considering the Bohm trajectory modeling of quantum mechanics, it can be demonstrated that the study of electron transport for confinement conditions can be hugely simplified if only one relevant energy level is meaningful in the confined directions [8] (see footnote 1). In this work we take advantage of this fact by taking into account the same result for the classical Monte Carlo trajectories.

We also use an injection model applicable to systems with arbitrary electron confinement, which is a time-dependent version of the Landauer boundary conditions, valid for degenerate and non-degenerate systems. We inject electrons according to the Fermi–Dirac statistic defined by a Fermi level deep inside the contacts [9, 10]. The applied bias provides a difference between the values of the Fermi level at each injecting surface. Our injection model, coupled to the boundary conditions of the Poisson equation, also assures charge neutrality at the contacts [10].

Finally, as mentioned in the introduction, phonon, impurity, and roughness scattering mechanisms are not taken into account, and only the full (long and short range) Coulomb interaction is considered explicitly. In our algorithm, randomness appears in the rate and properties of the electron injection from the contacts into the volume Ω .

3.3. DC results

In the present section we compute the time evolution of many interacting electrons inside 3D and 1D DG-FETs with the characteristics defined in table 1. The DG-FETs are surrounded by air and metal at the boundary surfaces.

Figures 4 and 5 present the average values for current at different gate and drain voltages for 1D and 3D configurations. V_{GS} represents the saturation gate–source bias and V_{DS} the saturation source–drain bias. The linear region is enclosed below a source–drain bias of 0.1 V while the saturation region is found beyond 0.3 V approximately. On the other hand, saturation gate–source biases are reached around 0.5 V. There, the saturation currents differ between the two configurations. The highest source–drain current is achieved by the 3D configuration, while the lowest is achieved by the 1D system.

² The time is computed using a dual Xenon 3.06 GHz.

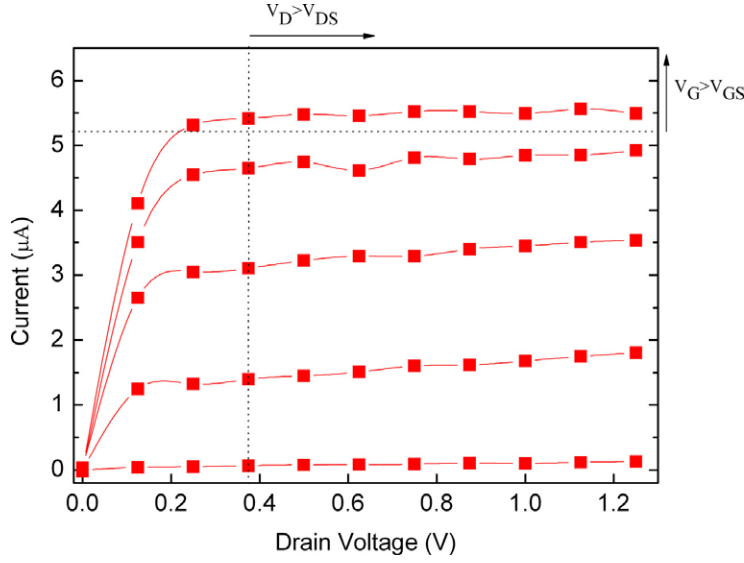


Figure 4. Average current for the 1D DG-FET.

Table 1. Parameters for the DG-FET depicted in figure 3.

	Magnitude	3D bulk	1D Quantum wire
Channel dimensions (nm)	L	30	15
	W	10	5
	T	8	2
	t_{ox}	2	2
Spatial step (nm)	DX	3	3
	DY	2.5	1.6
	DZ	2	1
Doping (cm^{-3})	Channel	1×10^{10}	1×10^{10}
	Contact	2×10^{19}	2×10^{19}
Simulation time (s)	T	3×10^{-10}	5×10^{-10}
Temporal step (s)	Dt	2×10^{-16}	2×10^{-16}

3.4. Analog noise results

As mentioned earlier in section 2.1, differences between confined and non-confined systems are expected. Figure 6 indicates these important differences for 3D and 1D FETs. For our 1D system, the Fano factor is bigger than that of the 3D system and the average current is smaller than the 3D one. Therefore, from expression (14) with a bandwidth $B = 1$ MHz, the 1D S/N ratio is approximately one order of magnitude smaller than the 3D S/N ratio (see figure 7). Hence, the qualitative behavior of the S/N ratio discussed in terms of equation (14) is confirmed numerically by these Monte Carlo results: smaller FETs offer substantially worse analog noise performances than bigger ones.

3.5. Digital noise results

For digital applications (an inverter), a bit error appears when an input voltage ‘0’ or ‘1’ leads to an erroneous interpretation of the output voltage, because of noise. Here we are wondering about those errors due to intrinsic noise fluctuations. In figures 8 and 9 the

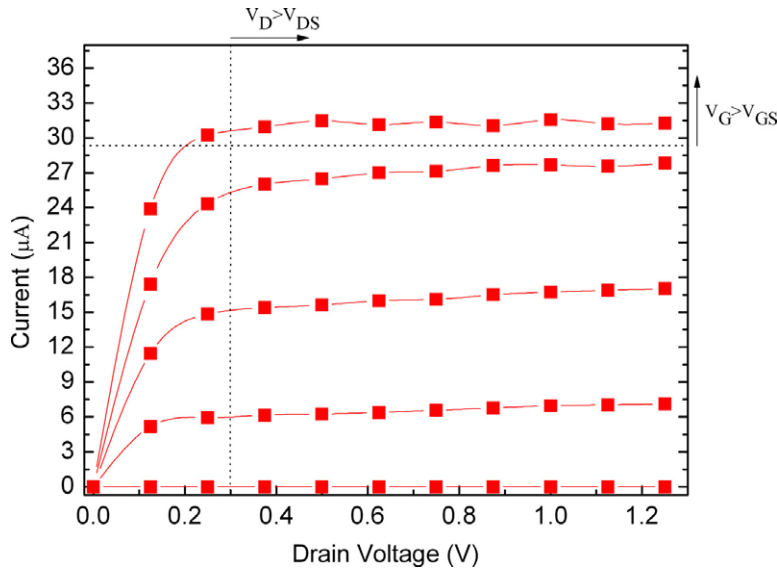


Figure 5. Average current for the 3D DG-MOSFET.

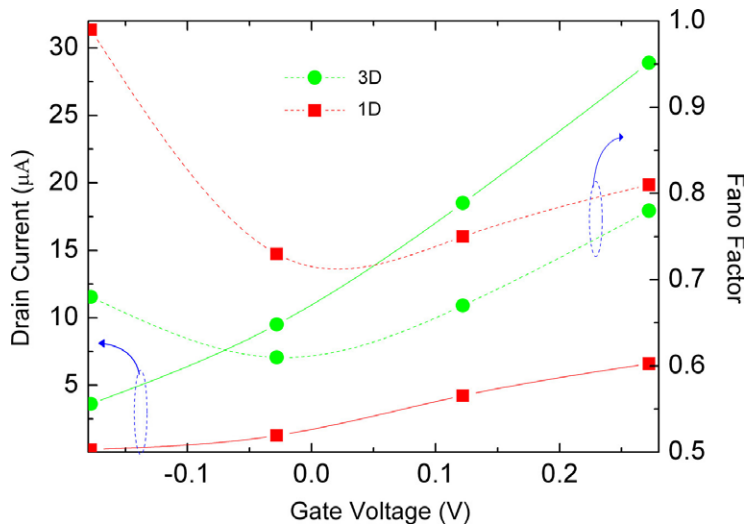


Figure 6. Average current (solid), I , and Fano factor (dashed) as a function of gate voltage for the three double-gate FET geometries mentioned in the text. The oxide thickness is 2 nm. The drain–source voltage is 0.5 V.

probability density for finding certain drain voltages when 0 V is expected is computed for the 1D and 3D systems respectively. Results for two different clock frequencies are presented: 50 and 500 GHz.

On one hand, the clock frequency plays a key role in the BER. As the clock frequency grows, the faster voltage fluctuations are less and less averaged (see the explanation linked to equation (21)). Therefore, the probability of finding higher drain voltages increases with faster switching.

On the other hand, since the voltage fluctuations are directly related to the capacitance value C (see figure 2), different results are obtained for 1D ($C = 1.26 \times$

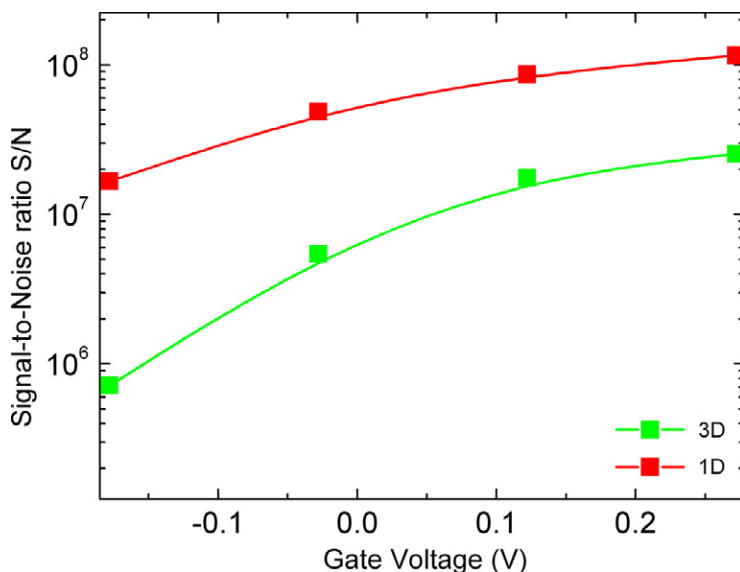


Figure 7. Signal-to-noise ratio for the bulk DG-FET and the quantum wire DG-FET considered here.

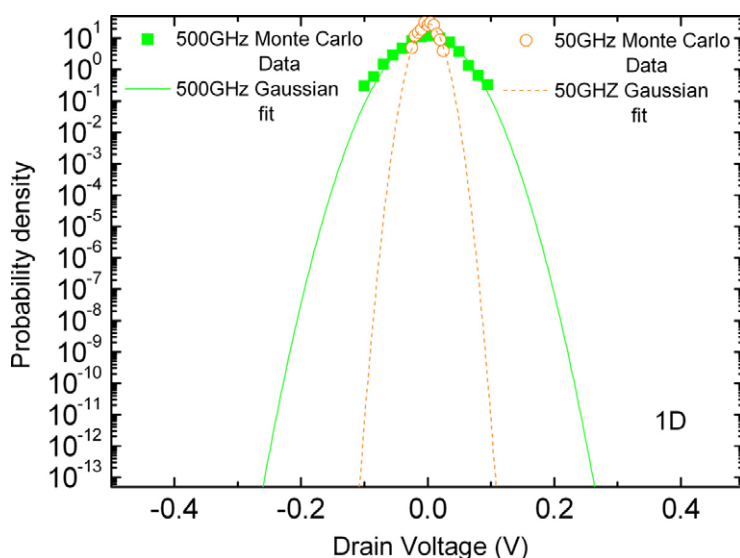


Figure 8. Monte Carlo results for the probability density for finding different drain voltages at 50 and 500 GHz for the 1D system.

10^{-18} F), and 3D ($C = 5.05 \times 10^{-18}$ F) systems. From figures 8 and 9, the corresponding system variance is increased from the 3D configuration to the 1D configuration. Again, the 1D system presents a poorer noise performance behavior. Thus, increasing miniaturization of the FET dimensions implies an important drawback for digital applications, mainly due to a decrease of the associated gate capacitance.

It is worth pointing out that both shrinking dimensions and increasing clock frequencies, two of the principal targets of the ITRS roadmap [1], imply an important increase of the BER due to intrinsic noise.

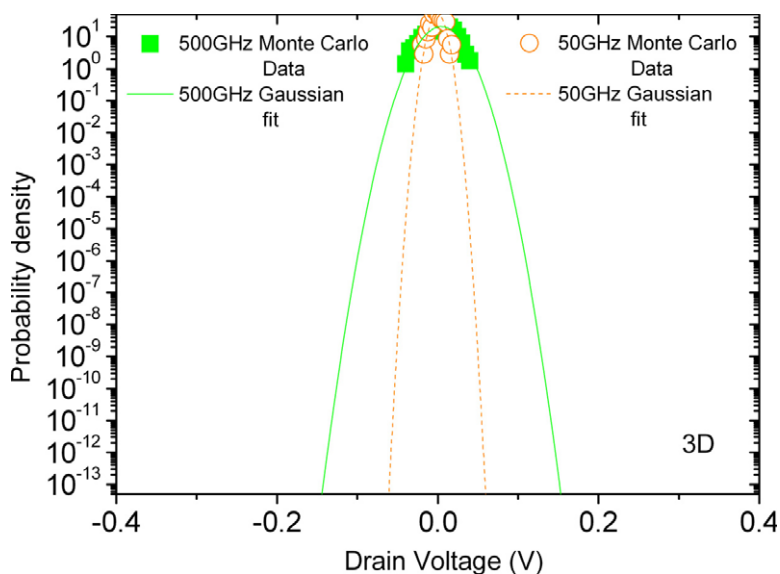


Figure 9. Monte Carlo results for the probability density for finding different drain voltages at 50 and 500 GHz for the 3D system.

4. Conclusions

In this work, we have discussed the noise performance of aggressively scaled FETs (with and without confinement) in digital and analog applications. First, the noise performance for analog applications was discussed in terms of the signal-to-noise ratio. Smaller devices produce a smaller average current and a larger Fano factor, leading to a signal-to-noise (S/N) degradation. Second, the performance for digital applications was analyzed in terms of the bit error probability. Incrementation of the clock frequency and reduction of the FET lateral dimensions result in a drastic incrementation of the BER, mainly because smaller devices (with smaller capacitances) are more sensitive to electrostatics. Our results are supported by analytical estimations and numerical results obtained with a powerful Monte Carlo (quantum) simulator. In summary, our work predicts that smaller FETs are intrinsically noisier. This statement may imply a serious limitation for the continuous shrinking of FET dimensions and increasing of clock speed predicted by the ITRS [1]. In view of these (single-finger-device) results, the consideration of new scaling-related strategies (such as using multi-finger devices) seems mandatory for providing nanoscale devices with acceptable noise performances.

Acknowledgment

This work was partially supported by the Ministerio de Ciencia y Tecnología through project TEC2006-13731-C02/MIC.

References

- [1] *International Technology Roadmap for Semiconductors* 2007 edition. Process integration, devices, and structures
- [2] Hooge F N, 1994 *IEEE Trans. Electron Devices* **41** 1926

- [3] Albareda G, Suñé J and Oriols X, 2008 *J. Comput. Electron.* **7** 197
- [4] Oriols X, Fernandez-Diaz E, Alvarez A and Alarcón A, 2007 *Solid State Electron.* **51** 306
- [5] Blanter Y M and Buttiker M, 2000 *Phys. Rep.* **336** 2
- [6] Carlson A B, 1975 *Communications Systems* (USA: McGraw-Hill)
- [7] Kish L B, 2002 *Phys. Lett. A* **305** 144
- [8] Oriols X, 2007 *Phys. Rev. Lett.* **98** 066803
- [9] Büttiker M, 1990 *Phys. Rev. Lett.* **65** 2901
- [10] López H *et al.*, 2008 *J. Comput. Electron.* **7** 213

Monte Carlo simulations of nanometric devices beyond the “mean-field” approximation

G. Albareda · J. Suñé · X. Oriols

Published online: 6 February 2008
© Springer Science+Business Media LLC 2008

Abstract For nanoscale electron devices, the role of a single-electron (or a single-impurity) can have a large impact on their electrical characteristics. A new method for introducing the long-range and short-range Coulomb interaction in semiconductor semi-classical Monte Carlo simulations is presented. The method is based on directly dealing with a many-particle system by solving a different Poisson equation for each electron. The present work shows the numerical viability of this alternative approach for nanoscale devices with few (<100) electrons. The method is compared with the traditional “mean-field” Monte Carlo simulations. It is shown, numerically, that the “mean-field” approximation produces important errors for aggressively-scaled devices.

Keywords Semiconductor device modeling · Monte Carlo methods · Electron-electron scattering

1 Introduction

For any system of electrons (for example, a nanotransistor), the dynamics of one particular electron is coupled to the rest of electrons (and atoms) of the system because of their mutual interactions. From a computational point of view, the direct solution of such a many-electron quantum system is inaccessible. This issue is at the heart of almost all the unsolved problems in modeling electron transport.

In most semi-classical/quantum electron transport models, the standard solution to overcome this computational

barrier is based on assuming that electrons move according to a unique “average” potential profile (the so-called “mean field” approximation). Nevertheless, in the state-of-the-art nanometric electron devices the output current is carried by very few electrons inside very small (nanometric) regions. In these scenarios, the role of a single electron (or a single-impurity) can have a large impact on the characteristics of these devices. Therefore, the simulation of electron devices using the “mean-field” approximation can be quite inaccurate. For example, experimental phenomena associated to Coulomb Blockade in nano transistors (which completely escape to the “mean-field” approximation) have already been reported [1, 2].

In the literature, several approaches are proposed to include the short-range Coulomb interaction into the traditional Monte Carlo “mean-field” procedure by taking into account the precise location of electrons within the same spatial cell [3, 4]. In this work, we propose an alternative method for the study of the dynamics of a set of electrons inside an electron device: we treat the electron system, directly, as a many-particle system by solving a particular Poisson equation for each electron. Such model is implemented in a semi-classical semiconductor Monte Carlo 3D simulator. The numerical results clearly show that the “mean-field” approximation can be inaccurate for the simulation of aggressively-scaled nanoscale devices.

2 Theoretical background

In this section, in order to provide a common language for a classical and quantum description of electrons, we describe the dynamics of each individual electron in terms of the Hamiltonian of the system of electrons.

G. Albareda (✉) · J. Suñé · X. Oriols
Departament d'Enginyeria Electrònica, Universitat Autònoma de Barcelona, 08193 Bellaterra, Spain
e-mail: guillem.albareda@uab.cat

The whole many-particle Hamiltonian related with a system of electrons inside a semiconductor (involving the atoms) is unsolvable. Therefore, different approximations are mandatory. First of all, the Born-Oppenheimer approximation (being the mass of the atoms much larger than the mass of electrons) assumes that atoms are always at rest in the electronic time scale. Second, the use of the effective mass approximation (for “infinite” structures) decouples the study of the electron transport from that of the electronic structure. Within these approximations, the Hamiltonian that describes the dynamics of a system of electrons inside the device is:

$$H_{\text{exact}} = \sum_{i=1}^{N(t)} \left\{ K(\vec{p}_i) + U_i^{\text{ext}}(\vec{r}_i) + \frac{1}{2} U_i^{\text{int}}(\vec{r}_1, \dots, \vec{r}_N) \right\} \quad (1a)$$

$$U_i^{\text{int}}(\vec{r}_1, \dots, \vec{r}_N) = \sum_{\substack{k=1 \\ k \neq i}}^{N(t)} \frac{q^2}{4\pi \epsilon_r \epsilon_0 r_{ik}} \quad (1b)$$

where the first term of the right-hand side of (1a) is the kinetic energy of the i -electron with \vec{p}_i momentum, the second term is the potential energy at the position \vec{r}_i of the i -electron due to the external bias and the third term is the Coulomb interaction that couples the dynamics of all electrons through $r_{ik} = |\vec{r}_i - \vec{r}_k|$. Hereafter q_i is the electric charge and ϵ_r/ϵ_0 are the relative/vacuum permittivity. For the i th electron, the two potentials terms in (1a) can be computed by solving a 3D Poisson equations taking into account the charge of the other $N(t) - 1$ electrons inside the active region [see the condition $k \neq i$ in (1b)] with the appropriate boundary conditions that accounts for the interaction with external electrons (at the gates or contacts).

2.1 Mean-field approximation

An enormous simplification in the computational procedure of the Coulomb interaction among the electrons can be obtained when the expression of the potential terms in (1a) is assumed to be equivalent for all electrons. Therefore, the solution of a system of $N(t)$ electrons can be obtained from:

$$H_{\text{mean-field}} = \sum_{i=1}^{N(t)} \left\{ K(\vec{p}_i) + U^{\text{ext}}(\vec{r}_i) + \frac{1}{2} U^{\text{int}}(\vec{r}_i) \right\} \quad (2a)$$

$$U^{\text{int}}(\vec{r}_i) = \sum_{k=1}^{N(t)} \frac{q^2}{4\pi \epsilon_r \epsilon_0 r_{ik}} \quad (2b)$$

Notice that we have eliminated the subindex “ i ” in the potentials terms of the Hamiltonian (1a) by omitting the restriction $k \neq i$ in the potential expression in (2b). Then, we

just need to solve a unique Poisson equation for all electrons (at one particular position, all electrons move according to the same electric field). Such enormous simplification comes at the price that the charge of the i th electron is also counted in (2b) and this charge affects the dynamics of the i th electron. This simplification is obviously not exact and it incorrectly treats the short-range Coulomb interactions among electrons. However, it captures most of the long-range component.

In this work, we directly solve the many-particle system (1) by computing an individual 3D potential profile for each electron. From a numerical point of view, the solution of the exact 3D Hamiltonian (1) is accessible for active regions of few nanometers, where the number of electrons is < 100 [5].

Finally, let us mention that the numerical results of this work are obtained taking into account the Coulomb interaction among electrons, but without considering the additional quantum exchange interaction among them (fermions). This is why we say that our treatment of Hamiltonians (1) and (2) is semi-classical.

3 Numerical comparison for nanoscale device

As we mentioned, in this work we want to check the validity of the mean-field approximation for the simulation of nanoscale devices. We compare the results obtained with the exact solution (1) to the results of the approximation (2) with the Monte Carlo technique.

3.1 Comparison for the average current in a nanoscale devices

In Fig. 1, we represent the active region of the nanometric two-terminal N^+NN^+ ($N^+ = 2 \times 10^{19} \text{ cm}^{-3}$, $N = 1 \times 10^{17} \text{ cm}^{-3}$) device that we simulate in the present work. For simplicity, neither (phonon, impurity, surface, ...) scattering nor electron confinement is considered inside the active region. Electron transport (from source to drain) takes place along the Silicon (100) channel orientation at room temperature with a relative permittivity $\epsilon_r = 11.9$. External electrons outside the active region (with volume $L_x \cdot L_y \cdot L_z$) are not explicitly taken into account in the Hamiltonian, but they are considered through the boundary conditions of the Poisson equation. Hereafter, we refer to the results obtained

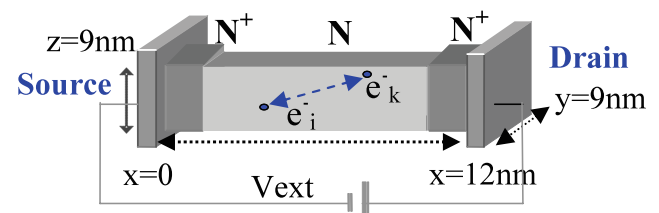


Fig. 1 Schematic representation of a 3D two-terminal nano device

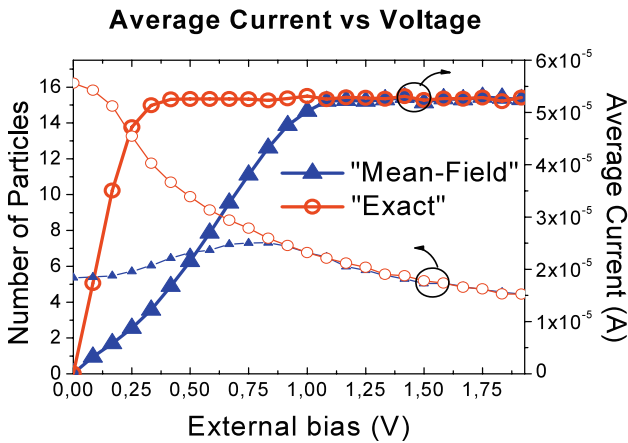


Fig. 2 Average current and number of electrons for the two-terminal device of Fig. 1 using the “exact” Hamiltonian or the “mean-field” approximation

from (1) as “exact” results. Alternatively, the term “mean-field” refers to the solution of (2).

The solution of the 3D Poisson equation is performed with the method of finite-differences. As we will discuss later on, the dimensions of the spatial steps, DX , DY and DZ , that define the grid in the 3D volume of the active region, have important consequences on the modeling of the “short-range” Coulomb interaction.

The electron injection model is based on imposing charge neutrality at the contacts and preserving the Fermi-Dirac distribution there [6]. When dealing with the “exact” Hamiltonian, each electron “sees” a different boundary condition at the contacts.

In Fig. 2, we show the numerical computation of the average current and number of electrons through the device depicted in Fig. 1 using the “exact” Hamiltonian (1) and the “mean-field” approximation (2). We use $DX = DY = DZ = 3$ nm, $L_x = 12$ nm and $L_y = L_z = 9$ nm. In Fig. 2 we see that the “mean-field” approximation gives considerable errors in the output current before saturation. The errors in the output current are closely related to the difference between the computation of the average number of electrons involved in the “mean-field” and the “exact” results.

3.2 Comparison for a two-electron system

In the rest of the manuscript we will explain the origin of the important differences depicted in Fig. 2, by studying the behavior of a simpler two-electron system (just two carriers inside the active region of Fig. 1). One electron (labeled as 1-electron) is injected from the source surface at an arbitrary position. A second electron is injected, arbitrarily, from the drain surface. Within the “mean-field” approximation only one potential profile is calculated for the two electrons (see Fig. 3). Then, each electron can be reflected by an “artificial” alteration of the potential profile due to its own charge.

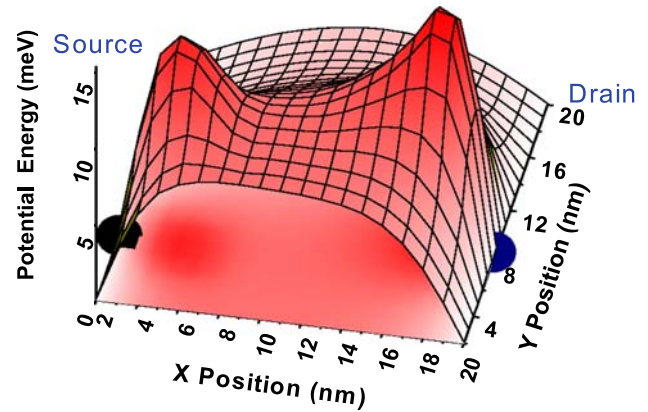


Fig. 3 Common potential energy profile (“mean-field” approximation) in the plane X – Y of the active region of Fig. 1 at $z = 6$ nm at 0.4 fs with $V_{ext} = 0$ V. The solid points are electron positions

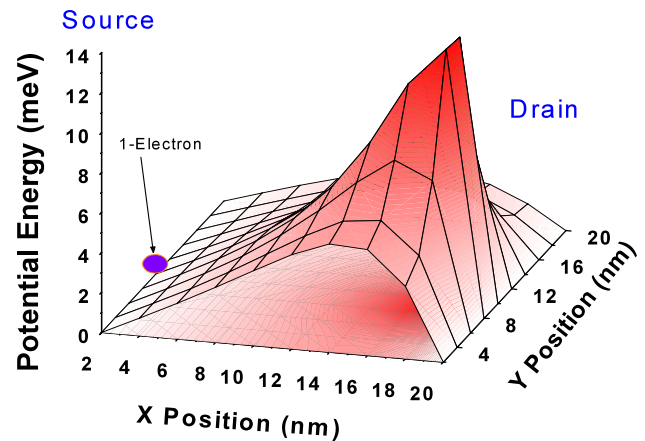


Fig. 4 Potential energy profile (“Exact” Hamiltonian) for 1-electron in the plane X – Y of the active region of Fig. 1 at $z = 6$ nm at 0.4 fs with $V_{ext} = 0$ V. The solid point is the 1-electron position

In Figs. 4 and 5 we have plotted the potential profile “seen” by electron 1 and by electron 2 in the active region of Fig. 1 using the “exact” Hamiltonian (1). Electrons are not affected by their own charge. We clearly see that, within the “mean-field” approximation, electrons are unable to overcome the “large” potential barrier that appears at their own position (due to their own charge). Therefore, the results obtained with the “mean field” approximation are unphysical in some situations (unless a large applied bias minimizes the error).

3.3 The role of the spatial step in the numerical solution

Finally, in order to correctly understand the applicability of the “mean-field” approximation in the traditional Monte Carlo simulation, a comment about the 3D discretization mesh used for the solution of the Poisson equation is needed.

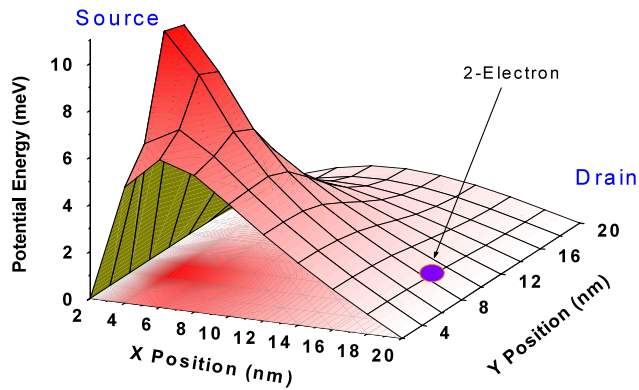


Fig. 5 Potential energy profile (“Exact” Hamiltonian) for 2-electron in the plane X – Y of the active region of Fig. 1 at $z = 6$ nm at 0.4 fs with $V_{\text{ext}} = 0$ V. The solid point is the 2-electron position

For an electron device with a length of hundreds of nanometers, we need a mesh of the 3D active region with spatial step $DX \sim DY \sim DZ > 10$ nm to deal with no more than one thousand nodes in the 3D Poisson numerical solution. This computational limitation in the resolution of the potential is present either when solving (1) or (2). With such spatial resolution, the short-range interaction is missing in both procedures because two electrons inside the same spatial cell will not repel each other. Therefore, we obtain roughly identical results with both schemes. In simpler words, when the spatial cells are large, both schemes correctly model the long-range Coulomb interaction, but both neglect the short-range component.

On the contrary, for electronic device with lengths of 10 to 20 nanometers, we can numerically afford the 3D Monte Carlo simulations with spatial steps $DX \sim DY \sim DZ \sim 3$ nm. Then, the scheme described in (1) takes into account long- and short-range interaction correctly, whereas the description of the short-range component within the “mean-field”

approximation is incorrect (electrons are repelled by themselves!).

4 Conclusion

In conclusion, in this work, the “mean-field” approximation is tested. Our results clearly show that this approximation may imply important errors for nanoscale devices with a small ($DX \sim 3$ nm) spatial step. Within the Monte Carlo technique, the “exact” solution of the many-particle (1) in real 3D scenarios is numerically accessible for nanoscale active regions with < 100 electrons [5].

Acknowledgement This work has been partially supported by the Ministerio de Ciencia y Tecnología through project TEC 2006-13731-C02/MIC.

References

1. Hofheinz, M., et al.: Simple and controlled single electron transistor based on doping modulation in silicon nanowires. *Appl. Phys. Lett.* **89**, 143504 (2006) (October)
2. Oriols, X., Trois, A., Blouin, G.: Self-consistent simulation of quantum noise in nanoscale electron devices. *Appl. Phys. Lett.* **85**(16), 3596–3598 (2004) (October)
3. Gross, W.J., Vasileska, D., Ferry, D.K.: A novel approach for introducing the electron-electron and electron-impurity interaction in particle-based simulations. *IEEE Electron Device Lett.* **20**(9), 463–465 (1999) (September)
4. Wordelman, C.J., Ravaioli, U.: Integration of a particle-particle-mesh algorithm with the ensemble Monte Carlo method for the simulation of ultra-small semiconductor devices. *IEEE Trans. Electron Devices* **47**(2), 410–416 (2000) (February)
5. Simulation time 4 hours in dual Xenon 3.06 GHz for computing the average current at each bias point
6. López, H., Albareda, G., Cartoixà, X., Suñé, J., Oriols, X.: Boundary conditions with Pauli exclusion and charge neutrality: application to the Monte Carlo simulation of ballistic nanoscale devices. *J. Comput. Electron.* (2008, in press)